Dissertation

submitted to the
Combined Faculties for the Natural Sciences and for Mathematics
of the Ruperto-Carola University of Heidelberg, Germany
for the degree of
Doctor of Natural Sciences

put forward by

Neige Frankel

Born in Muret, France

Oral examination:14 October 2020

Forward Modeling

the Secular Evolution of the Milky Way Disk

For my family members, my arms.

Abstract

We know precisely the position of the Sun in our Galaxy. Yet, like for most stars, we cannot tell where it was born. Stars undergo dynamical memory loss: their orbits evolve, because the Milky Way, like many galaxies, has non-axisymmetric structures (e.g. bar, spirals) that shuffle stellar orbits. My thesis quantifies the strength of that process to answer: How (much) do stars change orbit? Can we still infer their birth places, to constrain the formation of the Milky Way disk? I have combined data from the large stellar surveys APOGEE and Gaia, and developed a method to extract the information they contain on the Galactic disk evolution. I forward-modelled the formation of the stellar disk, the stars' elemental abundances and their subsquent orbital diffusion, which then informs us about their birth radii through 'weak chemical tagging'. I have found that stars can change orbits by large amounts, and most of this evolution is cold (the orbits stay near- circular). Secular evolution determines how the Milky Way disk is structued. If the Milky Way is typical this explain what drives disk galaxies in general to their typical exponential disk density profiles.

Abstract

Wir kennen die Position der Sonne in unserer Galaxie genau. Trotzdem können wir nicht sagen, wo sie entstanden ist. Die Sternbahnen in der Milchstrasse erleiden einen dynamischen Gedächtnisverlust: sie entwickeln sich, weil die Milchstrasse, wie viele Galaxien, nicht achsensymmetrisch ist (z.B. Balken, Spiralen), wodurch sich die Bahnen stets Ãd'ndern. Meine Dissertation quantifiziert diesen Prozess umd dann zu beantworten: Wie sehr entwickeln galaktische Orbits von Sternen? Können wir trotzdem die Geburtsorte der Sterne erschliessen, um so die Entstehung der Milchstrassenscheibe verstehen? Ich habe Daten aus den grossen Sterndurchmusterungen APOGEE und Gaia genommen und eine Methode entwickelt um die darin enthaltenen Informationen über die Entwicklung der Milchstrasse zu gewinnen. Mein Modell beschreibt und parameterisiert wann und wo Sterne geboren wurden, wie sich deren ElementhÃd'ufigkeiten entwickelt haben, und wieviel Diffusion der Orbits danach stattfindet. Damit kann ich die Geburtsradien von Sternen durch "weak chemichal tagging" erschliessen. Meine Analyse hat gezeigt, dass sich die Sternbahnenradien in der Milchstrasse stark entwickeln, aber dabei nahezu Kreissbahnen bleiben. Die "säkulare" Entwicklung bestimmt also wesentlich die heutige Struktur der Milchstrassenscheibe. Unter der Annahme, dass diese Prozesse in der Milchstrasse typisch für andere Galaxien sind, kúnnen diese Ergebnisse erklären warum Spiralgalaxienim Allgemeinen exponentielle Dichteprofile haben.

Contents

4

List of Figures

List of Tables

Thesis Manual

To the pressed reader who can only dedicate as much time to read this document as I took to write it: let me recommend going over the blue boxes like this one and the figures. They should hopefully give a suitable idea of the line of reasoning and questions behind this thesis.

Chapter I

Introduction

Astrophysics aims at describing and understanding the origin and evolution of objects in the Universe in terms of physics. The cosmos contains a wide variety of objects and structures on many scales, from the cosmic microwave background fluctuations to galaxies to stars to planets. Galaxies play a central role in this hierarchical structure, showing both diversity and much regularity in their population. Understanding how galaxies, and in particular disk galaxies like our own, came to be is a central theme of astrophysics. Disk galaxies can evolve through different processes: interactions with other galaxies (external interactions), and evolution through internal processes. Like many disk galaxies in a low density environment, the Milky Way has been near isolation for at least the past 7-8 Gyr, leaving much time for internal processes to play an important role. This rises several questions. *How do disk galaxies dynamically evolve when they are nearly isolated? Do internal dynamics play any role? How important are they?* These are the main questions this thesis addresses. In the coming sections, I lay out the observational clues and puzzles posed by galaxies, some solutions brought by theory, and come to a subset of the remaining puzzles.

I.1 Disk Galaxies

As I am writing this thesis in 2020, (to the distant future reader: beware it might have changed), galaxies are defined as gravitationally bound systems comprised of stars, gas, dust and dark matter [1]. Etymologically, "Galaxy" refers to the Milky Way: at some point, astronomers realized that the fuzzy objects seen in the sky are objects of the same nature as the Milky Way. Before then, galaxies used to belong to a more general class of "nebulae" of unknown nature and origin. Galaxies come in various sizes and shapes (e.g. Hubble, 1926; Conselice, 2014) and were found early but characterized very late: already in 1612, using a small telescope, Marius described them (in particular our neighbour, the Andromeda galaxy) as spatially diffuse objects looking like "a candle shining through horn" (Hubble, 1929). It was long debated whether these 'nebulae' were Galactic or extragalactic, until better instruments, and then photography eventually resolved and recorded extragalactic stars, closing the debate: galaxies were then objects that contain the same kind of material as the Milky Way. At that point, they were entirely defined as the stars in them.

Disk galaxies are galaxies whose stellar distribution is highly flattened. An example of our neighbouring disk galaxy, Andromeda, is shown in Figure I.1. Disk galaxies are supported by rotation (to the opposite of spheroidal galaxies, which look like spheroids and are supported by velocity dispersion). The apparent disk, made out of stars (which emit the optical light that we see as a disk), and often gas and dust, sits inside a dark matter halo.
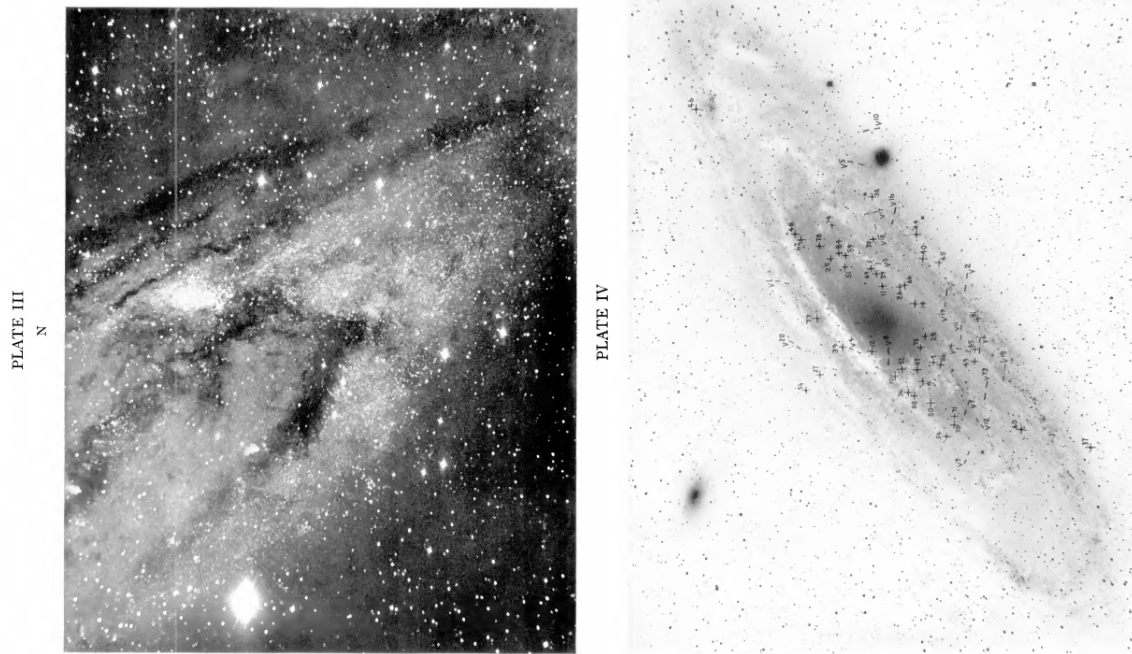
Figure I.1: Andromeda Galaxy photographed by Hubble (1929): the closest spiral galaxy to us, then identified as an extragalactic system.

I.1.1 Observational Characterization of Galaxies

I.1.1.1 Basic Observables

Two complementary families of observations or methods exist to characterize the stellar content of galaxies and understand their formation and evolution: (1) a large number of poorly resolved galaxies at a wide range of redshifts where the light travel time allows the direct observations of the galaxies' past state, and (2) (smaller) samples of local galaxies, seen in greater details. At large distances one can measure surface brightness profiles of the stars (Σ_{bright}) in different color bands and measure galaxy sizes (or half-light radii, also refrerred to as effective radii R_{eff}). The observed volumes are large and so they contain large amounts of of galaxies catalogued by spectroscopic and photometric survey programmes such as 10^4 with 3D-HST

---

[1]The limits of this definition are not sharp. Namely the transition between galaxies and star clusters, or that between galaxies and dark matter haloes devoid of stars can be ambiguous. But I would like to remind the reader that such definitons are only communication shortcuts that changed between the observational discoveries of these objects, their characterizations, and the theories explaining them. The interesting aspect is to consider the entire physical properties of the system (which are better defined), to find out 'how it came to be'.
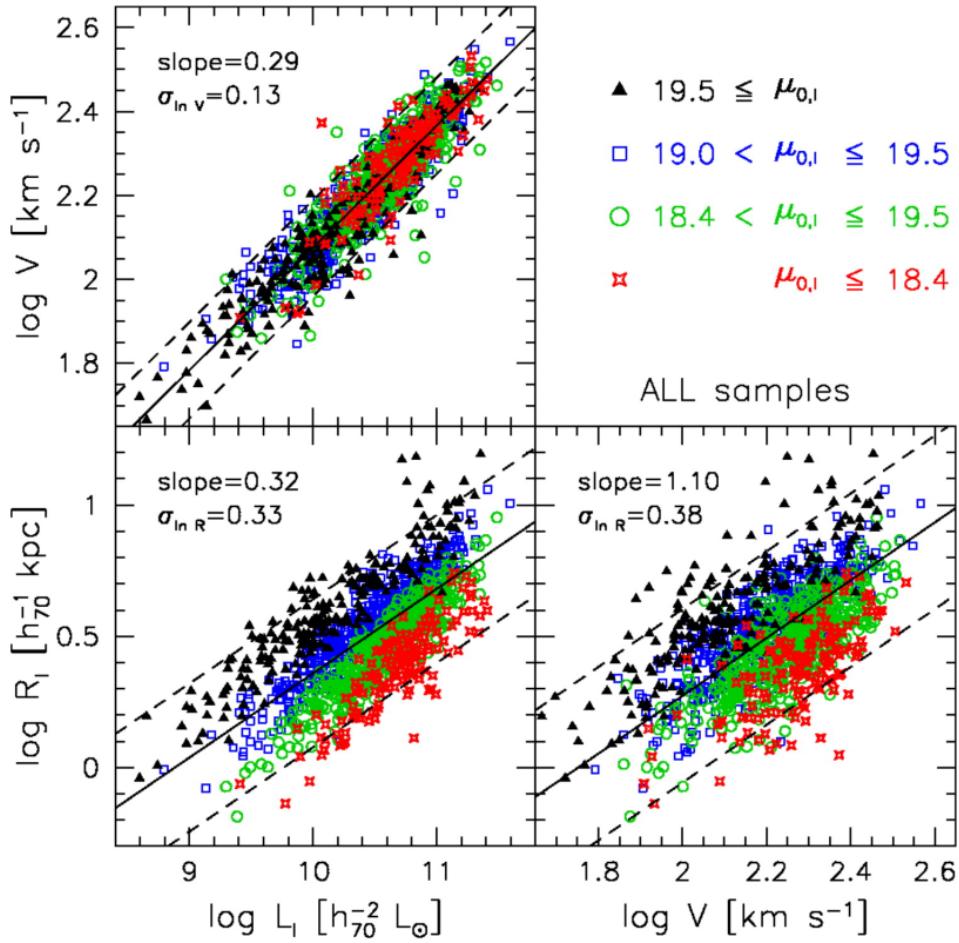
Figure I.2: Example of three 2D projections of galaxies' scaling relations: scatter plots of sizes, luminosities, and rotation velocities of a sample of galaxies. This particular combination constitutes the 'fundamental plane' for disks. Adapted from Courteau et al. (2007).

(Hubble Space Telescope) (Brammer et al., 2012), CANDELS (Grogin et al., 2011), and millions with SDSS (York et al., 2000), allowing to see how the global properties of galaxies correlate, and how these correlations change with redshift, or cosmic time (e.g., van der Wel et al., 2014; Mosleh et al., 2017).

Local galaxies are all observed at the same present-day epoch, which is less convenient to constrain a cosmological model for galaxy evolution. However, they are much better resolved (we can resolve individual stars for the closest galaxies), and the data are rich. Spectra taken in individual pixels with the Integrated Field Unit (IFU) (Courtes, 1982) contain information on the spatially-dependent stellar populations of different metallicities and ages in these galaxies. From a single pixel,

one can infer the distributions of velocity dispersions σ_{vel}, age (τ) and metallicity ([Fe/H]) of the stars in that pixel: $p([\mathrm{Fe/H}], \tau \mid \mathrm{position})$ (e.g., Goddard et al., 2017) and $p(\sigma_{\mathrm{vel}} \mid \mathrm{position})$ (e.g. Shetty et al., 2020). The first method has been well tested by my officemate Boecker et al. (2020) and the encoded information is valuable to constrain galactic archaeologic models: any good model has to reproduce the integrated age-metallicity-position and velocity dispersion-position structure of these galaxies.

I.1.1.2   Not All Galaxies that Could Exist, Do Exist

The observables[2] describing disk galaxies obey regular scaling relations. For instance, at a given redshift z, the masses, luminosities, star formation rates, metallicities, velocity dispersions and sizes of galaxies are tightly correlated, hinting towards more global formation and evolutionary processes relating or co-regulating them. These N-dimensional correlations in data space were discovered and confirmed mostly through 2D projections, such as the luminosity-rotation velocity ($L - V_{\mathrm{rot}}$) relation, named after Tully & Fisher (1977). A subset of these relations are mentioned quickly below. The more visually-oriented reader is invited to jump to Figures I.3 and I.5, which summarize them graphically and present (admittedly simplified) interpretations.

Distance-Redshift Relation   The more distant a galaxy is from us, the faster it recedes from us, on average. This is the redshift - distance (or radial velocity - distance, $v_{\mathrm{radial}} - D$) linear relation found by Hubble (1929), who found distances (D) to galaxies thanks to objects of known absolute luminosity (standard candles), and their radial velocity from us through the redshift method. A radiation of wavelength λ_{emit} emitted by an object moving away from us will undergo the Doppler effect, and be redshifted to the wavelength at which we see it (λ_{obs}). The redshift is quantified as $z = (\lambda_{\mathrm{obs}} - \lambda_{\mathrm{emit}})/\lambda_{\mathrm{emit}}$. This important discovery is not the result of the physics within individual galaxies specifically, but it reveals the large scale

---

[2]Here, I do not mean strictly 'observables' and the quantities I relate to are, also, modelled quantites (and not observables). In this context, I mean 'the most direct basic quantities derived from the observables that make some physical sense in the specific context of galaxy characterization'.
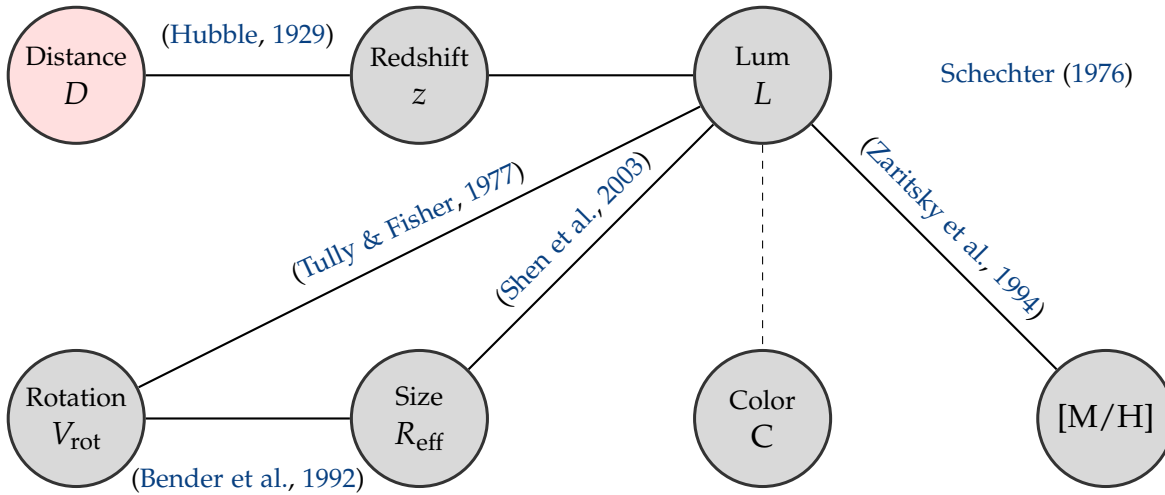
Figure I.3: Schematic illustration of the main 2D planes in which galaxies observables are exploited in the literature. Most variables show to correlate with each other. Two observables found to correlate are related by a line on the schema. For example, the luminosity distribution (L) changes with redshift (z), and correlates with galaxy size (or effective radius, $R_{\rm eff}$), galaxy and gas phase metallicity ([M/H]). Galaxies occupy specific regions in the color-luminosity plane (dashed because this is not exactly a correlation): they have a bimodal distribution that depends on galaxies' shapes. The redshift - distance relation in pink implies more globally the expansion of the Universe.

behavior of the Universe in which galaxies formed and evolved: the Universe is expanding, such that on average, $v_{\rm radial} = H_0 D$, with H_0 the Hubble constant, which is the present-day expansion rate of the Universe constrained today to about 68-74 km/s/Mpc (Planck Collaboration et al., 2016; Riess et al., 2009) .

Galaxy Scaling Relations   The original discovery of the expansion of the Universe pushed astrophysicists to look for ways to find distances to galaxies (in particular, scaling relations involving their absolute luminosities to find photometric distances) and better characterize the expansion rate of the Universe. However, these efforts have lead to important characterizations of galaxies in a different context: their structural properties. The rotation velocity of the stars in their disk correlates to their luminosity with less than 10% scatter (Tully & Fisher, 1977; Giovanelli et al., 1997). Since the luminosity of a galaxy traces its stellar mass, and the rotation velocity traces the overall potential produced by baryonic and dark matter (assumed to be in equilibrium), this relation provides tight constraints on the co-evolution of the baryonic matter and the dark matter halos hosting them: the more massive a halo, the more stars it contains.
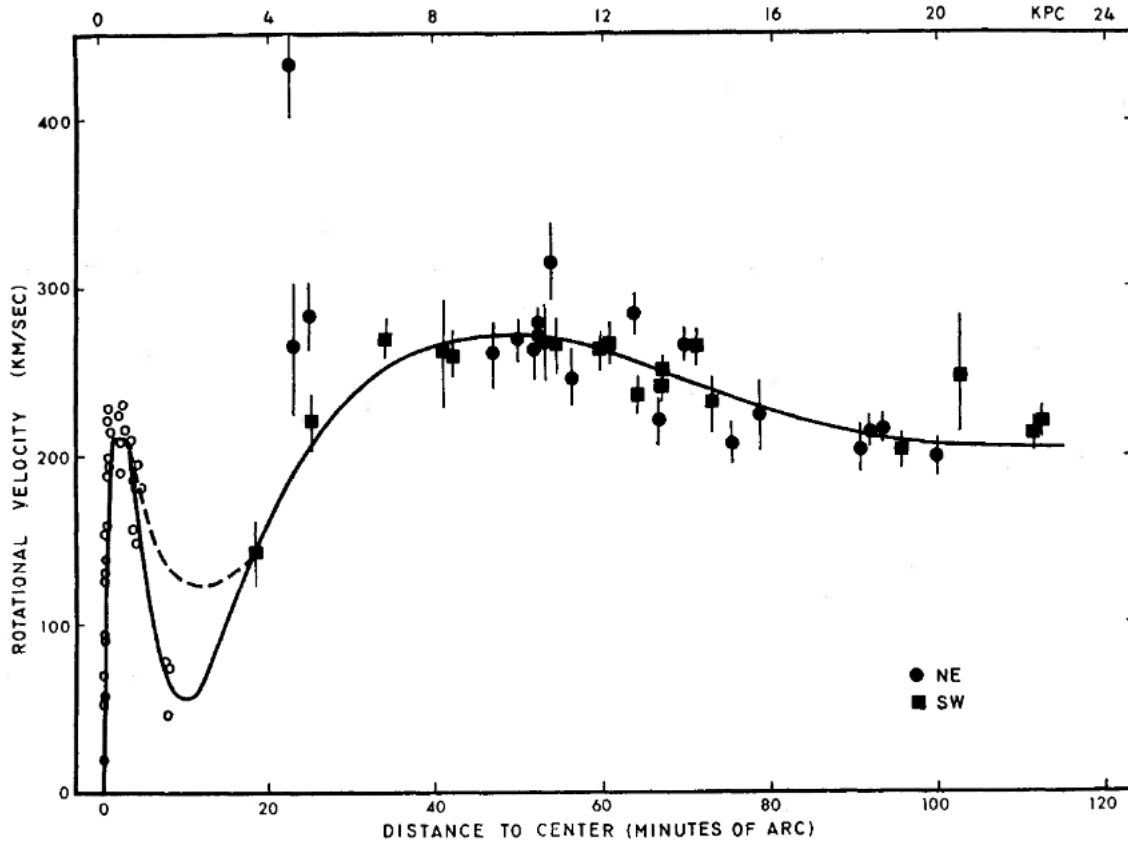
Figure I.4: Rotation curve of the Andromeda Galaxy, from Rubin & Ford (1970), showing a non-Keplerian flat component even at large radii.

Historically, the rotation curves of disk galaxies presented an additional central clue to the nature of galaxies: for most disk galaxies, they flatten at large radii to $V_{\rm rot}(R) \sim$ constant (e.g. Rubin & Ford, 1970, for Andromeda), deviating from the circular velocity curve that one would obtain by summing the luminous mass in that galaxy, which would decay much faster with radius. The additonal mass needed to reproduce these flat rotation curves, dubbed 'dark matter', must consist of a very extended halo with a mass profile leading to these flat rotation curves.

Multiple relations exist connecting the stellar content of galaxies to another of their properties. The luminosity, or stellar mass, of a disk galaxy predicts its size at a given redshift. This is the **mass-size relation** and will be important for Chapter IV of this thesis, which tackles the growth of the Milky Way's stellar disk. Galaxies containing more stars tend to be larger (Barden et al., 2005; Trujillo et al., 2006; van der Wel et al., 2014). This relation varies with redshift, such that **at given stellar**

mass, high redshift galaxies are smaller and less massive than those seen at lower redshift. However, this does not imply a direct evolutionary trend: higher redshift disk galaxies are not necessarily the progenitors of $z = 0$ disk galaxies. Galaxies can undergo metamorphoses through, for example, mergers with other galaxies. Together with the Tully-Fisher relation, the mass-size relation forms a three dimensional correlation between $L - V_{\text{rot}} - R_{\text{eff}}$ dubbed 'the fundamental plane" (Bender et al., 1992; Courteau et al., 2007), illustrated in Figure I.2.

But galaxies also contain gas in various phases, which also can enter scaling relations. The average gas phase metallicity correlates with the luminosity (or stellar mass) of the host galaxy (Zaritsky et al., 1994; Tremonti et al., 2004; Gallazzi et al., 2005; Zahid et al., 2013). Since the elements contributing to increase metallicity are produced and released as stars evolved and during supernovae, a higher metallicity gas indicates that more generation of stars have formed and released their nucleosynthesis products. The metallicity depends on the fraction of these internally produced metals that are retained and not blown out by feedback. The mass-metallicity relation therefore provides important constraints on the internal evolution of galaxies and star formation.

Last but not least, galaxies occupy two distinct areas in the color-magnitude plane (Bell et al., 2005; Kauffmann et al., 2003). Since color is an indication of the age of the stellar populations (bluer and brighter stars are younger), this indicates that galaxies lie in a bimodal distribution in the star formation - stellar mass plane. The color, or star formation rate, correlates strongly with the galaxies' 3D shapes: spheroidal galaxies are in the 'red sequence', with quenched star formation, whereas disk galaxies are mostly in the star-forming region of that plane.

These correlations between the observed properties of galaxies reflect possible relations between the physical properties of galaxies, which are illustrated in Figure I.5. A set of models has been developed to describe these relations and link them to underlying physical processes. These involve the merging (hierarchical growth) of dark matter halos, and relate the stellar component properties to those of the halos, in a cosmological context.

Demographics   Disk galaxies have a limited set of structural properties and morphologies (Hubble, 1926): their disks have a near-exponential profile (Sérsic, 1963; de Vaucouleurs, 1948), and they often host a central bulge, which can be decoupled from the disk in the surface brightness profiles (Kormendy, 1977), or a bar (Kormendy, 1979; Erwin, 2018), which is an inner structure rotating as a solid body. Most disk galaxies have additional non-axisymmetric structures such as spiral arms, which were used to classify galaxies on the so called 'Hubble tuning fork' (Conselice, 2014; Hubble, 1926; Jeans, 1961). Spiral galaxies are often called 'late-type' galaxies[3].

Observational facts

Disk galaxies obey regular scaling relations: their sizes, stellar masses, total masses, gas phase metallicities correlate, such that these properties are not uniformly distributed and lie in a restricted space. Disk galaxies also have a finite set of structures with distinguishable components: exponential disks, bulges, bars, spiral structures, flat rotation curves.

I.1.2   Models of Galaxy Formation and Evolution

The scaling relations introduced above provide tight constraints on the formation and evolutionary[4] processes of galaxies. In the ΛCDM paradigm, galaxies form inside dark matter halos arising from primordial density fluctuations in an expanding Universe. This mass growth later leads to an epoch of mergers, where halos merge

---

[3]This terminology originates from the Hubble sequence, classifying elliptical galaxies as 'early-types' and spiral and irregular galaxies as 'late-types', altough this confusing definition does not refect the evolution processes leading to different morphologies.

[4]In this thesis, I will not differentiate between the words 'formation' and 'evolution': imagine an entity (or a galaxy) that comes from the evolution of its progenitor: did the identity of that progenitor (and of the stars, gas, atoms, particles it contains) changed when it metamorphosed to the newly formed galaxy? Perhaps only its global properties changed? Some of them abruptly, some of them continuously? So instead, I will consider 'properties of the system as a function of time', $p(t)$.
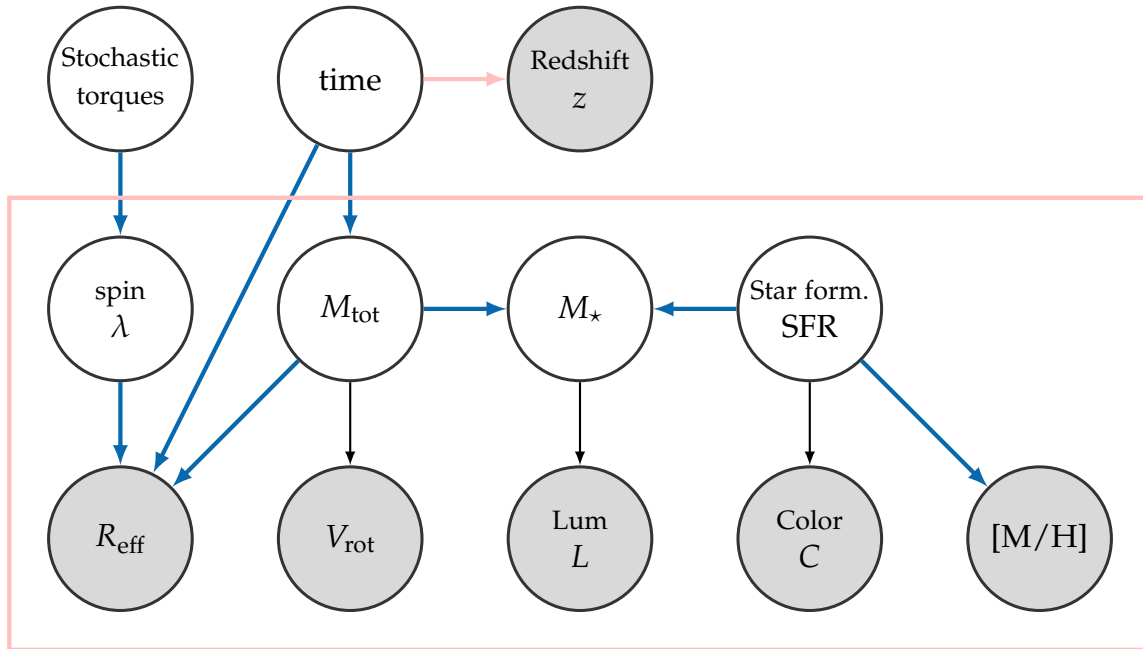
Figure I.5: Schematic interpretation of the correlations between the observables. The observables (filled, grey) are determined by physical quantities that describe galaxies. These relations are illustrated with the black arrows: the rotational velocity (V_{rot}) traces the potential felt by the stars and gas (if in equilibrium), so the overall mass distribution in the galaxies (M_{tot}). The main reason why a galaxy is luminous is because it has stars that shine, therefore the total stellar mass ($M_\star$) determines a galaxy's luminosity (L). And since stars that have a blue color are massive and hot, they must be young, which means that a galaxy that recently formed stars will look bluer: the star formation history (SFH) predicts a galaxy's color (C). The blue arrows link the physical quantities in a more subtle way, and *propose* a description, an explanation, for *how* the galaxy scaling relations come to be. The Tully-Fisher relation implies a close link between the total mass (M_{tot}) and $M_\star$. The SFH determines the number of stars that have formed. The different generations of stars that were produced through the SFH determine the nucleosynthetic products released to the ISM and enrich it, increasing its metal content ([M/H]). As cosmic time increases, galaxies build in mass via hierarchical growth (galaxies merge), increasing the total (and stellar) mass, leading to a redshift-dependent Schechter (1976) function. Their sizes increases at given $M_\star$ as cosmic time increases (van der Wel et al., 2014). And, a cosmological model relates time to the expansion of the Universe, predicting the redshift measurements (z).

and grow hierarchically as they respond to each other's gravitational influence.

I.1.2.1   The Standard ΛCDM Model: Setting the Framework for Galaxy Evolution

Cosmological models are the global framework that sets the boundaries of galaxy evolution. The currently most accepted cosmological model, the Λ Cold Dark Matter model, describes the large scale structure of the expanding Universe under the assumptions that (1) the Universe is homogeneous and isotropic on large scales,

23

(2) general relativity governs the equations of motions, (3) dark matter is cold (its moves much slower than the speed of light), and (4) the Universe's expansion is accelerating (Λ). The equations governing the evolution of the Universe (Friedmann's equations) are

$$
\begin{aligned}
H^2(t) &= \left(\frac{\dot{a}}{a}\right)^2 = \frac{8\pi G}{3\rho} + \frac{kc^2}{a} + \frac{\Lambda}{3}, \\
\frac{\ddot{a}}{a} &= -\frac{4\pi G}{3}\left(\rho + \frac{3p}{c^2}\right) + \frac{\Lambda}{3},
\end{aligned}
\tag{I.1}
$$

where $H(t)$ is the expansion rate of the Universe at a time t. The first equality defines the scale factor $a = 1/(1+z)$. G and c are the gravitational constant and the speed of light, k quantifies the curvature of the Universe, and Λ is the cosmological constant, representing dark energy which drives the acceleration of the expansion of the Universe.

The first of these two equations allows us to relate redshift and cosmic time, provided we know $H(z)$. We have $dt = da/(H(a)a(t)) = -dz/((1+z)H(z))$ that just needs to be integrated between two redshifts to give the time that elapsed between them. This will be useful in Chapter IV, to compare the time evolution of the Milky Way to disk galaxies observed at different redshifts. But this needs to assume a specific cosmological model, with cosmological parameters, that I introduce briefly below.

In the particular case of a flat Universe ($k = 0$) that does not have dark energy ($\Lambda = 0$), the future behavior of the Universe (and whether it continues expanding or collapses back on itself) is only determined by the density ρ. If the density of the Universe is low, it will keep expanding, and if it is large, gravity will make it collapse back onto itself. The specific scenario where the Universe has just enough energy to keep expanding without collapsing happens at the critical density $\rho_{\text{crit}} = 3H^2/(8\pi G)$. The critical density is often used to re-normalize these equations, defining the dimensionless parameters describing matter (m), radiation (r), and dark energy (Λ): $\Omega_m = \rho_m/\rho_{\text{crit}}$, $\Omega_r = \rho_r/\rho_{\text{crit}}$, $\Omega_\Lambda = \rho_\Lambda/\rho_{\text{crit}}$, and the overall density is $\rho = \rho_m + \rho_r + \rho_\Lambda$. The values of these parameters at present time define

the cosmogony in which we are working and sets the boundaries, the context, of galaxy evolution.

I.1.2.2 Reproducing the Scaling Relations with (Semi-)analytical Models and Simulations of Galaxy Formation

What makes galaxies follow $R_{\text{eff}} \sim L^{1/3}$ and $L \sim V_{\text{rot}}^3$ in Figure I.2? In a cosmological framework where the Universe expands at a rate $H(z)$ and galaxies grow through hierarchical accretion, Mo et al. (1998); Kauffmann et al. (1993) and others have constructed global models that reproduce these relations. They are based on the assumptions that galaxies are made of dark matter halos that grow through hierarchical accretion, and that the mass and angular momentum of the baryonic gas that condensates at their center are a fixed fraction of those of the halo. Matter in galaxies acquires angular momentum due to tidal torques (Peebles, 1969), which halts the collapse and leads to a rotationally supported disk (Fall & Efstathiou, 1980). One version of these models consists in a dark matter halo density $\rho(R) = v_{\text{circ}}^2/(4\pi G R^2)$ (the isothermal sphere), which produces a flat circular velocity curve as is common for disk galaxies. The virial radius, defined as the radius of the sphere that contains a mean density, e.g., $\langle\rho\rangle = 200\rho_{\text{crit}}$ is then $R_{200} = v_{\text{circ}}/(10GH(z))$, the total halo mass within the virial radius $M_{\text{tot}} = v_{\text{circ}}^2 R_{200}/G = v_{\text{circ}}^3/(10GH(z))$. A visual summary of such a model is in Figure I.5. Taking the scales predicted by that model and assuming a constant mass-to-light ratio (to convert stellar mass to light), this gives

$$L \propto M_\star \propto M_{\text{tot}} \propto v_{\text{circ}}^3$$
$$R_d \propto R_{200} \propto v_{\text{circ}} \propto L^{1/3}, \tag{I.2}$$

scaling as observed in Figure I.2.

Since the development of the isothermal sphere, more complex and realistic models have been developed (Somerville & Davé, 2015; Somerville et al., 2008), notably the use of more realistic dark matter halo profiles (Navarro et al., 1996) and the inclusion of the self-gavity of the baryons, i.e. baryons have a mass that exerts

gravity on themselves and on the dark matter, affecting the size of disks and halos.

To study the physical processes driving galaxy formation and evolution in greater detail, cosmological simulations have been implemented. The initial conditions of these simulations are set by the cosmic microwave background. Large scale structure forms from the initial density fluctuations, and baryonic particles condense into the potential of the dark matter halos. These simulations encompass physical details on different scales (e.g. the cooling of baryonic gas), allowing a description of disk galaxies in terms of large spatial scales (how environmnent and mergers affect galaxies) to smaller scales (how internal processes in galaxies affect them globally, the impact of secular evolution or stellar feedback), even though they are expensive. They compare well to the galaxy scaling relations (e.g., mass-star formation, mass-size-redshift Pillepich et al., 2019; Buck et al., 2020). Cosmological simulations are constantly being refined and improved and are now reaching resolutions that are interesting to study the long term evolution of galaxies due to their internal and external processes (for example: Illustris TNG50 (Nelson et al., 2019; Pillepich et al., 2019), Eagle (Schaye et al., 2015)). In complement, zoom-in simulations (high resolution) are re-run on a smaller volume extracted from a lower-resolution cosmological simulations (e.g. NIHAO Wang et al., 2015; Buck et al., 2020).

I.1.2.3   How Do Stellar Disks Assemble?

The semi-anaytical models described in Section I.1.2.2 describe galaxies as a population but do not describe the build up of a single galaxy and its time evolution. Similarly, the redshift-size relations (that show that higher redshift disks look smaller, Fig I.6) describe galaxies of different stellar masses, but are not evolutionary tracks for individual galaxies. This hints towards an inside-out build up of stellar disks without proving it. On the other hand, a negative age gradient should qualitatively be expected if the stars in the inner parts of galactic disks formed earlier than the stars in the outer parts of the disks. But disk galaxies seem to be observed with, on average, no (Goddard et al., 2017) or weak (Peterken et al., 2020) age radial gradients that depend on galaxies' stellar mass. Figure I.6 illustrates this apparently conflicting observation.
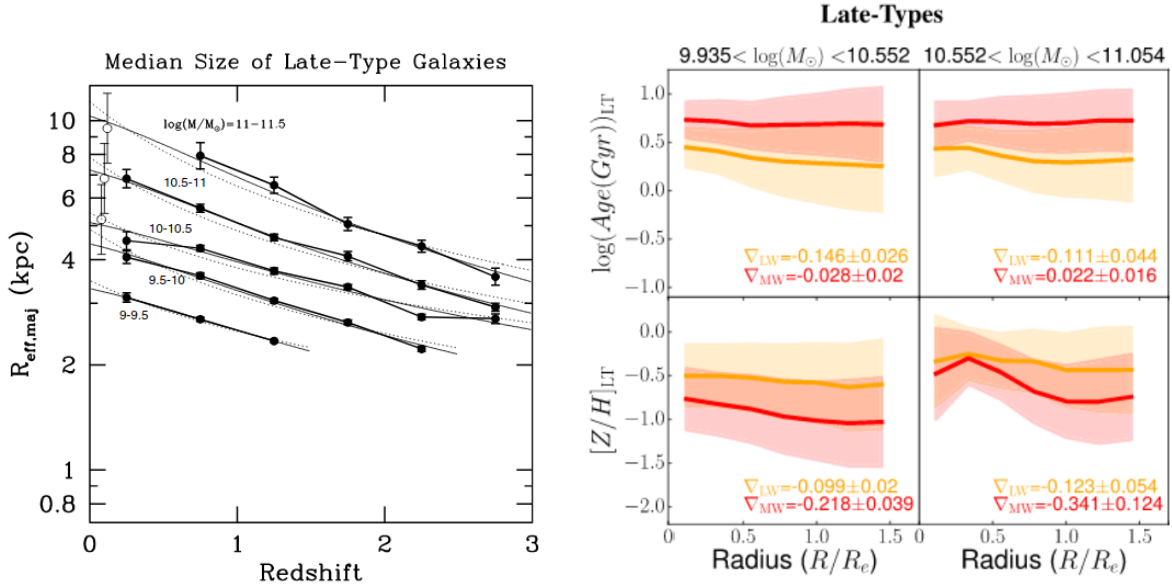
Figure I.6: Left: Redshift-Size relations for disk galaxies in stellar mass bins (taken from van der Wel et al. (2014). At all stellar masses, disk galaxies are smaller at higher redshitft. Right: stacked mass-weighted (red) and light-weighted (yellow) age (top) and metallicity (bottom) profiles of disk galaxies derived from stellar population fits to integrated field units data in the SDSS MsNGA survey, in two stellar mass bins. The mass-weighted age gradients seem, on average, consistent with zero, which means that on average, the stars in the inner disk of these galaxies did not form earlier than those in the the outer disk (not in a measureable manner). Figure adapted from Goddard et al. (2017).

The historical and simplified picture of the 'monolithic collapse' (Eggen et al., 1962) describes how an initially spherically-shaped baryon gas cloud falls rapidly into the potential of a dark matter halo. If it has some initial spin acquired from tidal torques (Peebles, 1969), angular momentum conservation leads that gas to settle into a disk, with low angular momentum gas settling in the disk before higher angular momentum gas (Brook et al., 2012). Observationally, the resulting stellar disks have a near-exponential surface brightness profile (e.g. de Vaucouleurs, 1948), but the physical processes behind this are not clear. What drives stellar disks to these exponential profiles?

Lin & Pringle (1987) showed that if stellar disks form on a star formation time-scale, $\tau_\star$, from a viscous gas disk with a viscous time-scale, τ_ν, then the stellar disk should follow an exponential surface density profile *after all the stars are formed* if $\tau_\star \approx \tau_\nu$. However, this analytic calculation (1) requires fine tuning of the timescales involved in such processes, (2) might not lead to an exponential profile at any time

t before all stars are formed, and (3) might not lead stellar disks to grow from inside-out. Given that the stellar disks observed today are still forming stars, their exponential configuration cannot be fully explained by this argument (but perhaps partly).

Existing models of the formation of stellar disks mentioned previously cannot satisfyingly explain why the resulting surface brightness profile of disks is exponential, nor predict the observed radial gradients of stellar ages and [Fe/H] within galaxies. Nor can they reproduce the fact that stars are observed to form in very structured clouds and clumps (e.g., Elmegreen & Elmegreen, 2019). How the gas falls into the potential well of a galaxy depends on the physical process and timescale on which gas cools and radiates energy. The infalling gas may be stopped or pushed away because of the energy feedback from the stars already exploding in supernovae in the disk of the host galaxy and other highly energetic processes such as supermassive black holes (dubbed 'active galactic nuclei' when they accrete material, transforming large amounts of gravitational energy into high energy radiation). Such self-regulating processes cannot be modelled analytically. Thus, there is a need to simulate the baryonic physics within galaxy scales. Simulations indeed show that (1) at formation, stars are not always born from an exponential profile, (2) they tend to form in highly complex structures, and (3) the resulting mass density profile looks smooth and near-exponential (e.g., Elmegreen & Struck, 2016).

Another possibility is that disks do not *form* with exponential profiles initially, but that they *evolve* towards exponentials through secular processes. If some secular process makes stars' orbits redistribute efficiently in angular momentum over the entire disk, this could lead their angular momentum distribution to tend towards an exponential distribution (Herpich et al., 2017; Elmegreen & Struck, 2013, 2016) (the maximum entropy distribution stars could reach). But this scenario requires that (1) the angular momentum redistribution is asymptotically efficient, (2) the stars in the disk remain on relatively cold orbits, and (3) the galaxy is sufficiently close to isolation that minor mergers or tidal interactions with satellites do not affect it significantly (it has to be near isolation). This effect, dubbed 'radial migration', was shown to be efficient in simulations (e.g. Sellwood & Binney, 2002) and to have more

implications: a global radial diffusion implies important dynamical memory loss of stars birth contitions, which means that the present-day structure of the stellar disk would better reflect dynamical evolution processes rather than its formation. The strength of radial migration has not yet been measured in disk galaxies, so the importance of this process is so far unclear. It is therefore crucial to know how strong radial migration is: can we rewind galactic disks to their birth conditions?

I.1.2.4 The Limitations of External Galaxies as Model Constraints

We saw in the previous sections that disk galaxies have regular properties: their surface brightness profiles look exponential and their global properties are correlated and redshift-dependent, providing stringent constraints on (semi-)analytical models. However, we only have access to their present-day *integrated* properties. The light coming from distant galaxies is integrated over many of their stars with low level of details. As seen in Section I.1.2.3 questions remain. In particular, to which extent do the present-day structures of disk galaxies reflect their initial conditons, angular momentum at formation, and merger history? How important are gradual memory erasing evolutionary processes, and do they play any role in redistributing the stellar content? Which processes set the radial structure of the disk to be approximate exponentials?

> The processes driving the evolution of disk galaxies are difficult to disentangle. This thesis addresses the three questions
>
> 1. What connects the initially structured conditions to the present-day smooth exponential surface brightness profiles of disk galaxies?
>
> 2. Do disk galaxies grow from inside-out?
>
> 3. What processes drive the long-term dynamical evolution of disk galaxies near isolation?

I.2 The Milky Way as a Model Organism

The Milky way is a typical disk galaxy in a low density environment. It has very generic global properties, i.e. mass, size, rotation velocity, metallicity, follow scaling relations (Bland-Hawthorn & Gerhard, 2016; Kormendy et al., 2010) and Tully-Fisher relation (Malhotra et al., 1996; Flynn et al., 2006). It contains most of the structural components identified in other disk galaxies (disks, bulge, bar, halo Gilmore & Reid, 1983; Blitz & Spergel, 1991; Freeman, 1987). However, living inside its disk, we can study it in greater detail than any other galaxy of its kind, down to the individual objects it contains. This motivates the choice made for this thesis to closely inspect the Milky Way and understand how it formed and evolved.

I.2.1 The Milky Way System

The Milky Way is part of a larger group of galaxies called the Local Group. The two most massive galaxies are the Andromeda galaxy and the Milky Way. The Milky Way has a total of about 60 satellites, of which three close satellites: the largest one is the Large Magellanic Cloud (LMC) with a total mass of about $10^{11} M_\odot$ (e.g. Wan et al., 2020) and the other two are the Small Magellanic Cloud (SMC), and the Sagittarius dwarf galaxy. The Milky Way's halo mass is estimated to be between $1 - 1.7 \times 10^{12} M_\odot$ using various methods, ranging from assimilating the fastest halo stars to the escape velocity (e.g., Deason et al., 2019) to measuring the rotation curve (Bland-Hawthorn & Gerhard, 2016). Its stellar mass is estimated to be $5 - 6 \times 10^{10} M_\odot$ and disk has an exponential scale-length of about 3 kpc.

I.2.2 The Milky Way Structure

The stars of which the Milky Way is composed follow a continuous distribution of positions, velocities, abundances ($[\vec{X}/\mathrm{H}]$) and ages $p(\vec{x}, \vec{v}, [\vec{X}/\mathrm{H}], \tau)$ with $\vec{X}$ denoting an array of elements present in the stellar atmospheres. This distribution takes different regimes and shows different components that astronomers have used to dissect the Galaxy: a stellar halo, with stars of low metallicity and orbits that can

be highly eccentric and a nearly spherical distribution, a bulge/bar with stars very centrally concentrated and mostly old, and a stellar disk generally decomposed in two components based on stellar abundances. The so called 'low-α' disk, that is poor in alpha elements (see Section I.3.4) contains mostly stars younger than 8 Gyr, is kinematically cold (it stars have near-circular orbits), and is confined to the mid-plane (small scale-height). The high$-\alpha$ disk is rich in alpha elements and mostly made of old stars (8 Gyr or older), is kinematically hot (the stars orbits are eccentric), and has a higher scale-height than the low-α disk. Most of the stellar mass resides in the disks, and about $1.5 \times 10^{10} M_{\odot}$ in the bulge (Bland-Hawthorn & Gerhard, 2016; Gilmore & Reid, 1983). The overall structure of the Milky Way is far from axisymmetric: the bar is a 5 kpc-long structure that rotates as a solid body at approximately 40 km/s/kpc (Sanders et al., 2019; Bovy et al., 2019), and there is a wealth of evidence that the Milky Way contains spiral arms: overdensities of (young) stars, gas, dust (Oort & Muller, 1952; Morgan et al., 1953; Drimmel, 2000; Binney et al., 1997) that ressemble the spiral shapes seen in exernal galaxies. These overdensities may form due to the dynamical response to (and creation of) a gravitational spiral perturbation: at present, a noticeable spiral dynamical effect on the stars in the Milky Way disk (e.g., Eilers et al., 2020) has been measured over a large radial extent of the Galactic disk. What is the long-term dynamical effect of these non-axisymmetries on the stars?

> Let us use the Milky Way, a typical disk galaxy in many aspects (structure, mass, size, global properties), as a model organism to better understand how disk galaxies form and evolve. Since we see its individual stars, we can effectively model and measure the stellar distributions $p(\vec{x}, \vec{v}, [\vec{X}/\mathrm{H}], \tau)$, unlike other galaxies offering only integrated properties.

I.3   The Milky Way's Stellar Disk

The stellar disk of the Milky Way represents about 75% of the stars in the Galaxy, and is the focus of this thesis. The gas disk, the halo or the bar, are considered as external perturbations applied to the stellar disk system, and the aim is to (1) measure the effect they have on the orbits of stars and (2) understand how these orbital changes affect the shape of the Milky Way's disk over time. The following sections introduce the tools that are commonly used to dissect the Milky Way's disk and to describe the orbits of stars, and how they are distributed.

I.3.1   Stellar Orbits

To describe the dynamical evolution of the stellar disk, we need to describe the orbits of stars and then how they evolve secularly (on long timescales). The typical phase space quantities (3D positions and 3D velocities) are inconvenient because they all vary quickly, on the orbital timescale. In Chapter III, we use 'orbital actions', because they are constant of motions when the stellar system is not perturbed, and their associated 'angles'. When the Galactic disk system is pertuberd due to time-varying non-axisymmetries, the actions change slowly over time. The most important aspects to introduce the angle-action variables are laid out briefly in this section, starting from coordinates, then going from the Lagrangian down to the actions with Hamiltonian mechanics. The interested reader who wants deeper derivations than this short summary is invited to open the lecture book of Binney & Tremaine (2008) that strongly inspired these notes.

Galactocentric and Galactic Coordinate systems   To describe the Milky Way disk, it will be convenient to work in cylindrical coordinates. The distance to the galactic center as projected on the plane of the disk, or Galactocentric radius, is noted as R, the azimuth is ϕ such that for the Sun, $\phi_\odot = 0$. The height above the plane is z with the Sun lying about 20-25pc above the plane (Bennett & Bovy, 2019; Bland-Hawthorn & Gerhard, 2016), and similarly the velocity vector of a star is $\vec{v} = (v_R, v_\phi, v_z)$.

To describe an observational data set of stars, that were observed from the Earth and lie around the Sun, a different coordinate system is more convenient (it will be useful in Chapters III and IV: the Galactic coordinate system. It uses two angles: latitude (l) and longitude (b), and distance to the Sun (D). The direction ($l = 0$, $b = 0$) points to the Galactic center, and the distance between the Sun and the Galactic center is about 8.2 kpc (Gravity Collaboration et al., 2019).

Generalized coordinates The orbits of stars can be described by their 6D phase space made out of their 3D cartesian positions and their 3D velocities $\{\vec{x}, \vec{v}\}$ in an inertial reference frame. Depending on the symmetry properties of the system and on the forces acting on it, it may be more convenient to work in a different coordinate system than the Cartesian coordinate system (e.g., cylindrical coordinates for the Milky Way's stellar disk). Similarly, it may also be more convenient to work in a different reference frame than an Inertial reference frame. For example, if a structure perturbing a star rotates about the Galactic center at a fixed rotation speed, then it may be useful to work in the reference frame that rotates with that perturbation. These considerations are usually applied by means of a coordinate transformation $(\vec{x}, \vec{v}) \longrightarrow (q, \dot{q})$. The phase space can then be described in more general coordinates, q and their time derivatives $\dot{q}$.

Lagrangian In a system described by generalized coordinates $(q, \dot{q})$, which can be functions of more usual coordinates, living in a gravitational potential Φ_{pot} that depends on position and time, the Lagrangian is,

$$\mathcal{L}(q, \dot{q}, t) = E_K(q, \dot{q}, t) - \Phi_{\text{pot}}(q, t) \tag{I.3}$$

with the specific kinetic energy $E_K = \frac{|\tilde{v}|^2}{2}$ of the system in an inertial frame and the potential energy taken here to be the gravitational potential Φ_{pot} of the galaxy at the given positions q. From classical mechanics, the Euler-Lagrange equations,

$$\frac{d}{dt}\left(\frac{d\mathcal{L}}{d\dot{q}}\right) - \frac{\partial\mathcal{L}}{\partial q} = 0 \tag{I.4}$$

yield the equations of motion that describe any system. In Eq. I.4, the quantity $\frac{d\mathcal{L}}{d\dot{q}}$ is the momentum, p, associated to the coordinate, q, which makes this equation analogous to Newton's 2nd law, (here simplified by the mass since $\frac{\partial\Phi_{\text{pot}}}{\partial q}$ is the gravitational acceleration, $\dot{p} =$ acceleration).

Hamiltonian   The Hamiltonian is defined as the Legendre transformation of the Lagrangian:

$$H(q,p,t) = \dot{q}\frac{d\mathcal{L}}{d\dot{q}} - \mathcal{L}, \tag{I.5}$$

and it is a function of the generalized positions q and their canonical momenta p. Combined with Euler-Lagrange equations, this definition leads to Hamilton equations

$$\frac{dH}{dq} = -\dot{p} \qquad \text{(I.6a)} \qquad\qquad \frac{dH}{dp} = \dot{q} \qquad \text{(I.6b)}$$

which yield the equations of motion.

Orbital Actions and Angles   Defining a set of coordinates, θ_i, and their conjugate momenta, J_i, such that J_i is a constant function of time, and consequently θ_i a simple linear function of time, facilitates the description of a stellar system. Such coordinates exist in particular potentials. In particular, the so-called 'action-angle' coordinates with the momenta (actions) are defined as:

$$J_i = \frac{1}{2\pi}\oint p_i \mathrm{d}q_i. \tag{I.7}$$

 with q_i the generalized coordinates and p_i their conjugate momenta. These actions are integrals of motion (not derived here, see Binney & Tremaine, 2008), which means they are conserved along the orbit. Therefore, Hamilton equations in Eq. I.6 yield

$$\frac{dH}{d\theta} = -\dot{J} = 0 \qquad \text{(I.8a)} \qquad\qquad \frac{dH}{dJ} = \dot{\theta}(J) = \Omega. \qquad \text{(I.8b)}$$

Thus, an orbit is fully characterized by its actions J and that the phase of a star along that orbit is simply given by $\theta(J,t) = \Omega t + \text{const}$. Since J is constant along the orbit, $\dot{\theta}(J) = \Omega$ is also a constant, which makes then integral to get $\theta(t)$ very convenient and $\theta(t)$ pleasantly be a linear function of time.

More specifically, in a system that is well described in cylindrical coordinates like the Milky Way disk, the actions we are going to work with are the radial action (J_R), the azimuthal action (J_ϕ) and the vertical action (J_z, which we are less interested in).

For example, in the case of a harmonic oscillator-like orbit of natural frequency κ_0 in an axisymmetric potential (this is the epicycle approximation), we will have $R(t) = A\cos(\kappa_0 t)$ and the azimuthal action will be

$$J_\phi = \frac{1}{2\pi} \oint v_\phi R d\phi = \frac{1}{2\pi} \oint L_z d\phi = L_z = \text{angular momentum}, \qquad \text{(I.9)}$$

and the radial action will be

$$J_R = \frac{1}{2\pi} \oint v_R dR = \frac{A^2 \kappa_0^2}{2}. \qquad \text{(I.10)}$$

The azimuthal action J_ϕ here is reduced to angular momentum, L_z, and quantifies the amount of rotation in the orbit, whereas the radial action, J_R, here quantifies the amount of radial motion: how much a star's orbit deviates from a circular orbit, how eccentric it is. It will be non-zero when the amplitude of the radial motion (A) and when its frequency (κ_0) are non zero. A convenient property of actions that we will use in Chapter III is that these two quantities have the same dimensions (a velocity multiplied by a distance) and units. However, they may be affected by different physical processes, and their respective evolution may affect the shape of the Galactic disk differently. Therefore, working with these actions will be a good way to disentangle the different processes at play in the Milky Way with quantities

that can be compared directly.

In practice, we only know the present-day positions and velocities of the stars in the Milky Way. In order to derive actions for their orbits and compute the integral I.3.1, we need to make assumptions about their orbits: assume a form for the (relevant part of the) gravitational potential of the Milky Way the stars feel on their orbits, and integrate the orbits. Since the potential of the Milky Way is uncertain, any action worked out for a set of data will be only approximate. Furthermore, Eq. I.3.1 implies that actions are only well defined when orbits close, such that we can perform the line integral. However, this is not always the case, so we want to quantifiy the azimuthal, radial, vertical motion for all the stars more generally, by approximating it with the question 'if the orbit could close, what actions would be associated to that motion?'. Several approximations exist.

Approximating Actions   The work in this thesis is mostly interested in the in-plane motions (J_R, J_ϕ) of the stars and not so much in the vertical motions (J_z). Additionally, most stars in the low-alpha disk are young and predominantly lying in the disk midplane. Therefore, their vertical excursions are not very large such that z and v_z are small. We will therefore make the approximation that the in-plane motion of stars is decoupled from their vertical motion (the so called adiabatic approximation (Binney, 2012)). This will allow us to work in the 4D space of (x, y, v_x, v_y) instead of the full 6D space (but the work done in Chapter III could well be generalized to 6D.).

Determining actions for stars in the Milky Way requires additional assumptions because they require us to assume a form of the potential, that we do not know. How to model the potential of the Milky Way? In order to calculate orbital actions quickly for many stars (the integrals over the orbits are computationally expensive), another approximation, called the Staeckel Fudge (Binney, 2012), can be used. It consists in approximating the potential of the Milky Way with a Staeckel potential. It takes the form $\Phi(u, v) = \frac{U(u) - V(v)}{\sinh^2(u) + \sin^2(v)}$ such that the functions $U(u)$ and $V(v)$ depend only on one variable and the resulting Hamilton-Jacobi equations are independent, simplifying the integral computations for the actions (two 1D integral

instead of a nested 2D integral), see Binney (2012) or Binney & Tremaine (2008) for details. This method has been well tested and developed in different softwares or packages like AGAMA (Vasiliev, 2019) and Galpy (Bovy, 2015), both of which are widely used and in this thesis, I will use this as a result.

I.3.2 Distribution Functions

To describe a system of stars in equilibrium in an axisymmetric potential, we use the distribution functions, $f(\vec{x}, \vec{v})\vec{dx}\vec{dv}$, which quantifies the fraction of stars (i) that are at a position $\vec{x}_i \in [\vec{x}, \vec{x} + \vec{dx}]$ and that have velocities $\vec{v}_i \in [\vec{v}, \vec{v} + \vec{dv}]$. This is a distribution in a 6D space, and neither stellar positions $\vec{x}$ or their velocities $\vec{v}$ are conserved along their trajectories. However, it is much more suitable working in action-angle space, and express the distribution functions as a function of actions and angles. This can be done since $\vec{dx}\vec{dv} = \vec{d\theta}\vec{dJ}$, so the distribution functions are

$$f(\vec{x}, \vec{v} \mid \Phi_{\text{pot}})\vec{dx}\vec{dv} = f(\vec{J}, \vec{\theta} \mid \Phi_{\text{pot}})\vec{dJ}\vec{d\theta} = \frac{1}{(2\pi)^3}f(\vec{J} \mid \Phi_{\text{pot}})\vec{dJ}\vec{d\theta}, \qquad \text{(I.11)}$$

since (in the axisymmetric potential Φ_{pot}) the angles $\vec{\theta}$ are uniformly distributed on the orbit (they spend the equal amount of time in different regions of their space). Analytical distribution functions for stars in the Milky Way disk have been developed and fit to local data (Binney, 2010) and used to constrain the potential Φ_{pot} of our galaxy (Ting et al., 2013).

The stellar density Chapters II and IV focus on the positions of stars, so the distribution functions are integrated over velocities: $f(\vec{x})\vec{dx} = \int_{\text{velocities}} f(\vec{x}, \vec{v})\vec{dx}\vec{dv}$. Furthermore, these two chapters describe the Milky Way disk assuming that the stars distribution is axisymmetric, is only a function of Galactocentric radius R and height above the plane z: $f = f(R, z)$. Since Chapter II focuses on the in-plane distributions of the stars, I will further assume that all the stars are in the midplane such that only the radial distribution of stars, $f(R)$, is to be considered. The stellar density is typically modelled with an exponential surface density profile $\Sigma(R) = \Sigma_0 \exp(-R/R_d)$, with a scale-length R_d measured to about 3 kpc.

I.3.3 Stellar Orbit Evolution

The disk of the Milky Way contains giant molecular clouds, a bar, and spiral arms. These structures produce a time-varying potential that induces the stars to scatter and change orbits: they will kick the stars in velocity space, apply torques, exchange angular momentum and so on (see Sellwood, 2014, for a review). On average, the radial action of stars J_R will tend to increase with time as the stars acquire radial random motions, has been noticed early in the Solar neighbourhood as an increase in stellar velocity dispersions with age $\sigma_v \propto \tau^{0.3}$ (Wielen, 1977).

The most important internal processes causing stars to change orbits on long timescales are orbital resonances between stars and structures in the disk. Let us imagine a star orbiting the Galactic disk with an angular momentum L_z and radial action J_R, in the epicycle approximation (harmonic oscillator). Its orbital angles will be linear functions of time with $\phi = \frac{\partial H}{\partial L_z}t = \Omega_0 t$ ($\approx$ azimuthal angle) and $\theta_R = \frac{\partial H}{\partial J_R}t = \kappa_0 t$. The two important orbital frequencies describing the motion of the stars are Ω_0 for the rotation and κ_0 for the radial oscillations. If the star keeps meeting a structure at the same phase, then they are in resonance: their orbital frequencies are related by integers. For example, if a spiral arm that has m arms were to rotate as a solid body with an angular speed of Ω_P, the important resonances (among many others) will be

- $\Omega_0 = \Omega_P$: the corotation resonance [5]

- $\kappa_0 = \pm m(\Omega_P - \Omega_0)$: the Lindblad resonances.

The Lindblad resonances were shown to be efficient at heating stellar orbits: if a star is on some eccentric orbit, and it its pulled out of its orbit at apocenter each time, it becomes even more eccentric. The corotation resonance was shown to be efficient at changing stars' angular momenta, without heating the orbits much (Sellwood & Binney, 2002). When the spiral perturbations that create these resonances are short-lived, stars can undergo many trapping and torquing events over their life time, and change orbits in a random walk-like manner. This effect causing stars to diffuse in

---

[5]see a visual description of corotation resonance trapping at `https://neigef.github.io/post_rm.html`.

orbit space was dubbed 'migration' or 'churning'. In Chapter III, we will measure how strong J_R and L_z redistributions as a function of time are in the disk of our galaxy, providing insights on what mechanisms drive the evolution of the disk.

I.3.4 Stellar Populations

The stellar surface density profile of the Milky Way disk has been well approximated with an exponential surface density profile (Bovy et al., 2012; Bovy, 2016; Mackereth et al., 2017), similarly to the exponential surface brightness profiles that seem to describe so well external disk galaxies. To disentangle evolutionary processes, the density of stars can then be split by populations, as a way to find how stars of presumably different ages and compositions are distributed at present.

Stellar populations refer to generations of stars that were born at the same time and that have similar compositions, such that they were also presumably born from the same gas or in similar conditions. But ages have been difficult to determine, such that much effort was spent on a more practical proxy for stellar populations: mono abundance populations (Rix & Bovy, 2013). Getting stellar spectra on an industrial scale and inferring the stellar atmospheric compositions helped disentangling the formation processes of the Milky Way. In particular, the enhancement of alpha elements[6] compared to iron was a very practical way to infer roughly the birth conditions of a star: the $[\alpha/\text{Fe}]$ ratio correlates with age (e.g., Ness et al., 2019b), which makes sense in terms of chemical enrichment of galaxies: half of iron is produced in Type Ia supernovae (Maoz et al., 2014). Type Ia supernovae are thought to come from thermonuclear exposions of white dwarfs. The delay time between the birth of their progenitors and their explosion is greater than the delay for core collapse supernovae, which produce most of the alpha elements. So since it takes more time to enrich the interstellar gas with iron than with alpha elements, it has been argued that the more a star contains iron compared to alpha, the later it was probably born. Furthermore, the Galactic disk has a $[\text{Fe/H}]$ gradient, such

---

[6]Alpha elements are elements that can be made with many alpha particles: the helium nucleus. These are mostly produced in core collapse supernovae, which explode quickly after the birth of their progenitor star.

that a star with a high [Fe/H] presumably formed in the inner disk and a star with a low [Fe/H] presumably formed in the outer disk. It was found that stars seem to have a bimodal distribution in the [Fe/H]- [α/Fe] plane (e.g., Hayden et al., 2015), with the high-alpha mode being substantially older than the low-alpha mode.

The literature following the disk decomposition into stellar populations (Bensby et al., 2014) then separates in two main research branches that look at the stellar distributions differently:

1. study quantitatively the spatial or kinematic distribution of stars of given abundances or age, $p(\vec{x}|[Fe/H], [\alpha/Fe] \mid model)$(Bovy et al., 2016b; Mackereth et al., 2017). This approach adresses the question 'Where are the stars of a specific composition', where the composition spearation aims at disentangling stars born at different times, from different processes or in different structures.

2. Study the observed abundance (or age) distributions at given position in the disk $p([Fe/H], [\alpha/Fe] \mid R, z)$(Hayden et al., 2015; Ness et al., 2016). This approach addresses the question 'What kind (in terms of age or birth abundances) of stars do we see at this specific locations?'

These two approaches differ mathematically only in which variables are conditionned on which other variables. Statistically, the choice of which variable to bin is difficult: the right hand side of the $p(\mid)$ distribution should have as few uncertainties as possible, and the left hand side should be affected by as few selection effects as possible (unless these selection effects are modelled!). But physically speaking, they differ fundamentally in two aspects. The idea of grouping or binning stars of similar abundances has the same philosophy as the so-called 'chemical tagging' (Bland-Hawthorn et al., 2010): stars born from the same gas cloud should have similar abundances, the gas shows spatial variations of abundances, so stars that have similar abundances were likely born close together spatially. After having formed, then these stars can change orbits and evolve, such that the first approach mostly traces the evolution of the stellar disk in a 'forward' manner.

The second method bins stars in position in the disk and shows their abundances. These studies show that at a given position in the Galactic disk, a wide
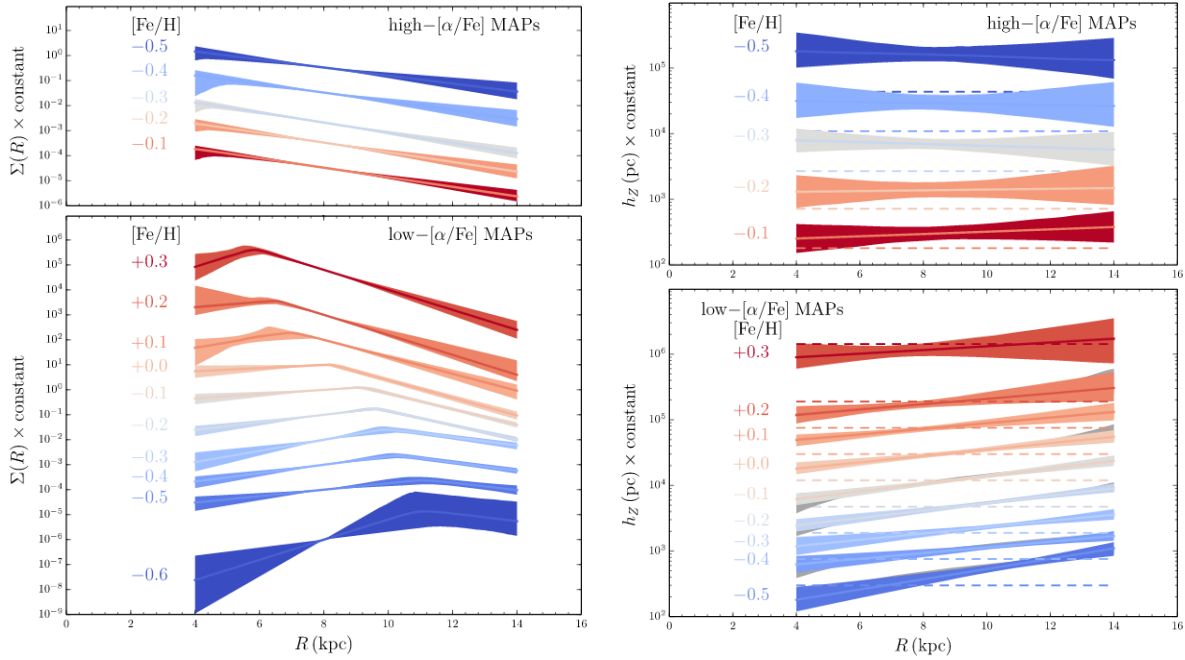
Figure I.7: Surface density profile (left) and scale-height (right) of different stellar populations in the Galactic disk, as a function of Galactocenric radius. The top two panels illustrate that the high alpha populations seem to all have the same radial distribution and their scale-height is uniform as a function of radius. On the other hand, the low alpha populations are concentrated to the inner disk if they are [Fe/H]-rich, and more radially extended if they are [Fe/H]poor. They also seem to flare: their scale-height increases with Galactocentric radius.

range of different abundances occupy the chemical plane: stars born in many different conditions are present at the same position in the disk nowadays. This generalized previous findings in the Solar neighbourhood: around the Sun, stars do not lie on a perfect relation between their age and metallicity (which would be expected: as time goes, supernovae enrich the gas from which later generations of stars form) (Edvardsson et al., 1993; Casagrande et al., 2011).

Stringent constraints on the spatial distribution of mono-abundance populations have been set through forward modelling (Bovy et al., 2012; Bovy, 2016). The chemically older populations seem to be more centrally concentrated and form a thicker disk than the low alpha one. These trends are reflected in Fig. I.7 that shows (1) the surface density of stars in different [Fe/H]-[α/Fe] bins and (2) their scale-height from (Bovy, 2016). These two disks are, in the literature, separated as two different components. But their formation processes are still unknown and debated, and the separation has a number of versions: thin /thick disk, outer/inner disk Haywood

41

(2008); Snaith et al. (2015), and low/high alpha disk. Since (1) the exact formation prosseses are still unknown, and it is not obvious that there is a direct continuity between these two and (2) the high alpha disk seems older than the last important merger (Helmi et al., 2018; Belokurov et al., 2018) which could create discontinuities, I will take the cautious approach in this thesis by modelling only the younger, low-alpha disk's slow, secular dynamical evolution.

I.4   Inferring the Milky Way Disk's History by Forward Modelling the Data

Before the industrial development of spectroscopic and astrometric surveys such as Gaia and APOGEE, our knowledge about the Milky Way was limited by the size and the extent of datasets: how can one learn about the entire Galaxy's history with just a few hundred stars around the Sun? Since approximately 2015, we have access to a lot of information (elemental abundances, ages, positions, kinematics) of tens of thousands of stars over spatial scales of kiloparsecs. Now we need a framework to extract information from large, high-dimenstional data, in a quantitative way. This is the aim of this thesis. I develop and apply a *forward model* for the the dataset. This method describes the entire data distribution (no conditioning) with a parametrized story for the Galactic disk: the joint distribution of the observables in

$$p([\text{Fe/H}], \tau, \vec{x}, \vec{v} \mid \text{parametrized evolution and selection scenario}). \qquad (\text{I.12})$$

I.4.1   From the Idea to the Data to the Data Usage

With the recent arrival of new, large scale, high quality data from space and ground-based surveys (e.g. Gaia, GALAH, APOGEE, LAMOST...), the field of Galactic Archaeology and more generally astrophysics has reached a new scientific potential that is no longer based on exploring a new wavelength range for the first time, obtaining a new dimension in the observable space, but that is rather based on large numbers. Datasets reach extremely large sample sizes (millions of stars) and

are homogeneous (collected with the same instrument and reduced with the same pipelines). It has therefore become important to develop a framework to use the information content of these data (Ness et al., 2019a; Rix & Bovy, 2013). In view of the next generation surveys (SDSSV, 4MOST, WFIRST etc.), there are a number of challenges to overcome. These can be grouped in a few main points (e.g. Ness et al., 2019a) listed in the blue box below.

> Current challenges/requirements of the industrial Galactic Archaeology:
>
> 1. Designing surveys and targeting strategies allowing to use the maximum of the information content (reconstructible selection function)
> 2. Collecting high quality data
> 3. Storing these data, in publily accessible large databases;
> 4. Extracting the basic information from the raw data at an industrial level and calibrating these data globally across products from different surveys with suitable pipelines;
> 5. **Developing a framework to fully utilize these data products and interpret them in terms of physics: where this thesis contributes.**
> 6. Developing the theoretical models that will allow a deep understanding of these observational results and guide the next generations of observational programs.

The projects described in this thesis are aimed at a small-scale exploration to explore and develop the 5th item of this list.

Items 3-4 of the above list have made tremendous progress over the past years. And the return of statistics, machine learning and data science into astrophysics have made possible to deliver fast and precise stellar physical quantities from large sample sizes (millions of stars), where classical techniques would now fail (e.g. Ness et al., 2015, 2016; Ting et al., 2019).

However, the last two items of this list, data exploitation for physcial interpretation are not fully developed yet, at least in the field of Galactic Archaeology. Once

we have all these data, what do we do with these? The large amounts of data that have already been collected in the past years have mostly been interpreted qualitatively and under-utilized, by looking at trends in the quantities derived. For example, using the APOGEE-DR12 data products, which were released in 2015 already (Hayden et al., 2015), the spatial variations of [Fe/H]-[α/Fe] have brought qualitative evidence that the Milky Way disk grew from inside-out and for radial migration (Hayden et al., 2015). Only three years later, did we actually quantify these clues using the same dataset (by then outdated), with a model parameterizing the time evolution of the disk scale-length and time-dependent distribution of stars around their birth radius (?Frankel et al., 2019): this multi-dimentional dataset had not been fully utilized, more data were already being released and used (in part) to confirm qualitatively known global trends. The lack of quantitative measurements have made difficult the interpretation of these results. There is now a need to optimize our extraction of data information content for the surveys in the coming years.

I.4.2   Modelling and Inference

Most of the results presented in this thesis are based on the same method: forward modelling (and fitting) the observations we have from the Milky Way, based on a background scenario that is parametrized. Let $\{\vec{x}_{i,obs}\}$ be a set of observables that we have for a star i. It can be for example its position, its velocity, the elemental abundances in its atmosphere etc (the specific quantities I worked with are described in each chapter and selected to tackle a specific question). And let $\mathbf{p_m}$ be the parameters that answers the question: 'how did stars end up with these $\{\vec{x}_{i,obs}\}$'? The model will propose a scenario with parameters that describe quantitatively the formation and evolution of the Galactic disk, the subsequent selection of the dataset into our catalogs, and the data uncertainties.

$$p(\vec{x}_{i,obs} \mid \text{parametrized evolution and selection scenario}). \qquad (I.13)$$

From this model, we can build a likelihood function for the dataset

$$p_{\mathcal{L}}(\{\vec{x}_{i,\text{obs}}\} \mid \text{parametrized scenario}) = \prod_i p_{\mathcal{L}}(\vec{x}_{i,\text{obs}} \mid \text{parametrized scenario}),$$

(I.14)

and using prior knowledge on what is a physically acceptable parameterized scenario (for example, distances, sizes, timescales should be positive and finite), we can build a posterior for the model parameters given the dataset we are working with

$$\begin{aligned} p_{\text{pos}}(\text{parametrized scenario} \mid \{\vec{x}_{i,\text{obs}}\}) \\ \propto p_{\text{prior}}(\text{parametrized scenario}) p_{\mathcal{L}}(\{\vec{x}_{i,\text{obs}}\} \mid \text{parametrized scenario}). \end{aligned}$$

(I.15)

This summarises in broad lines the overall method used to constrain the evolution of the Milky Way disk in my thesis. However, a few aspects make this inference procedure difficult: probabilities need to be normalized to the volume expected to be occupied by the data. Said differently: we need to account for the fact that we do not see all the stars of the Milky Way disk, but only those that are selected and end up in the data set. The difficulties are (1) the selection of the data made by astrophysicists, and (2) the natural properties of the galaxy that prevents stars from entering our catalog. In particular, dust in the Milky Way extinguishes stellar light at certain wavelengths such that the stars do not meet the selection criteria. Thus, we need to also know the 3D spatial distribution of dust in the Milky Way disk. These two aspects are developed briefly in the coming two sections. They are useful for chapters III and IV.

I.4.3   A Magnitude Limited Dataset

We cannot see all the stars in the Milky Way. Our instruments can only detect stars that are bright enough, and therefore any dataset we chose to work with will be characterized by its selection function, that is the probability that a star makes it to the dataset given its properties (brightness, color, etc). It needs to be well understood before drawing physical conclusions. I will enter in the details of this

concept here, because it will be very important in Chapters III and IV where it is not explained because these chapters focus on the physics of the Galactic disk.

Generally if a survey is limited by magnitude, it sees stars of a given intrisic brightness up to a certain distance only. How bright a star is depends (among other aspects) on its mass, its age, and its metalicity. Therefore, a survey that is magnitude- or color-limited may target stars of specific ages and metallicities, and not all the stars. To relate statistically the ages and metallicity of the stars in a survey dataset to the underlying population in the Galaxy, one needs to account for stellar evolution and the distribution of stars in the color-magnitude plane. Stars burning hydrogen in their core are on the main sequence, and the more massive they are, the hotter (bluer) and brighter they are (and also short-lived), such that at large distances, one primarily sees young stars. After low mass stars exhaust the hydrogen in their core, hydrogen burning continues in a shell surrounding it and stars move off the main sequence and see their envelope expand and cool: they become redder and brighter, moving to their next evolutionary phase: the red giant phase. As soon as their core temperature is high enough, they start burning helium in their core. Low mass stars burning helium in their core are on the red clump stage. Red clum ans red giant branch stars are useful because (1) they are bright so they can be seen from far, and (2) they are red, so the light they emit is less extinguished by the dust present in the Galaxy (see next Section, I.4.4). This makes them ideal targets for stellar surveys whose aim is to cover large extent of the Galactic disk, which brings us to the APOGEE survey (named after the Apache Point Observatory Galactic Evolution Experiment).

Figures I.8 and I.9 illustrate schematically the process of data selection. The first panel of Figure I.8 describes (qualitatively and obviously not to scale) a disk of stars (what we want to model and understand) and a telescope inside that disk of stars (which is going to shape our perception of the stellar disk). Say this telescope is designed to look at specific directions on the sky and has a limited set of stars to observe (we cannot observe all the stars in the Milky Way: we do not have the time or sensitivity for this, so we have to choose). The second panel of that figure shows an example of 'survey footprint': the green areas show the directions in

which the telescope is designed to observe (this is done by human decision). The other regions, which also contain stars, will not be observed. Since the telescope is not sensitive to all stars, it won't see all the stars that are in the green cones that it targets, but only a subset of these. This is illustrated in the top panel of Figure I.9 that color codes which stars end up eligible for targeting: some are not simply because they live outside the footprint, some of them are too faint given their distance, and some other stars may be hidden behind a cloud that contains dust (see legend). In the end, the stars that actually end up in the catalogue and have suitable data are represented in green and shown in the bottom panel of the same Figure (I.9). As the reader can see, the green stars distribution no longer reflects the distribution of the underlying population in the Galactic disk! Therefore, to understand the Galactic disk, one needs to model all the decisions that were made during the selection of the dataset, and the possible effects happening to the data until they enter the catalog.

The data used in this thesis comes primarily from two surveys: the APOGEE spectroscopic survey and Gaia. These two surveys are both magnitude limited, but Gaia can see stars fainter than APOGEE (in the limits where I have used them in the present thesis), so the survey limiting the sample size is APOGEE. APOGEE took stellar spectra in near-infrared light, the part of the electromagnetic spectrum least affected by dust extinction (Section I.4.4), but it is still affected. This survey targeted stars in specific regions of the sky as illustrated in Figure I.8.

I.4.4 The Effects of Dust and Interstellar Extinction

The Milky Way contains dust. The Milky Way's disk contains, in addition to stars and gas, dust mostly distributed in the midplane (e.g., Green et al., 2019). The dust absorbs and re-emits light over the entire continuum of the spectrum (unlike the gas, that is more abundant than dust but less worrying: it absorbs and emits radiation at specific frequencies), scattering photons on their way between the stars and us, the observers. The star will look fainter and redder than it is. Therefore, to evaluate the brightness and color of a star, one needs to know by how much it has been extinguished and reddenned.

a) Milky Way Disk if we were to see all its stars

Criteria:
– Only stars in specific directions (l, b)
– Only stars within some magnitude range
– Only stars within some color range
– Only N stars per pointing (limited number of fibers)

b) Survey selection function: footprint

Pointing direction: field selected by targeting
strategy prior to the survey
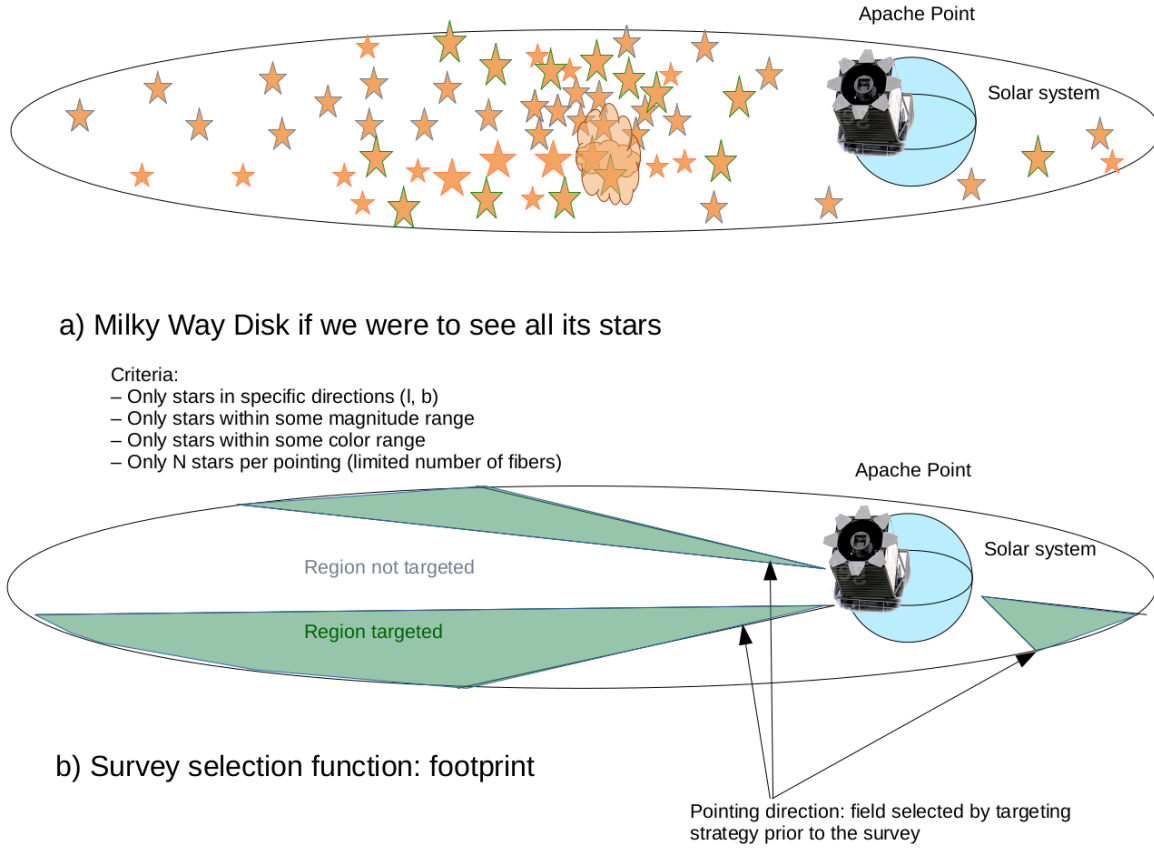
Figure I.8: Schematic illustration of the impact of a selection on a dataset. Top: schema of a galactic disk with stars of different ages, metallicities, brightnesses, with a dust cloud and a telescope. Bottom: lines of sight where astronomers decided to point the telescope to and observe stars (green) or not (white).

Dust is responsible for extinction. A light beam of frequency ν and intensity I_ν that travels through absorbing medium, like dust, will see a fraction of its intensity be absorbed or scattered over some travel distance. So after travelling a path length s, the light beam has an intensity $I_\nu(s) = I_\nu(0) \exp(-\tau_\nu(s))$ with τ_ν being the optical depth of the medium, wich depends on both the frequency of the radiation and the nature of the medium (for example, the size of dust grains). Similarly, the flux of light we receive, as observers $F_\nu(s)$ is related to the flux we would see if there were no dust $F_\nu(0)$ by $F_\nu(s) = F_\nu(0) \exp(-\tau_\nu(s))$. We can relate this to the magnitude m of the stars through $m = -2.5\log(F) + \text{const}$, and get:

$$m - m_0 = -2.5\log(F_\nu/F_{\nu,0}) = 2.5\log(e)\tau_\nu = A_\nu. \tag{I.16}$$

c) Stars eligible for targeting or not

d) Stars actually observed: MW disk seen through the catalogued stars
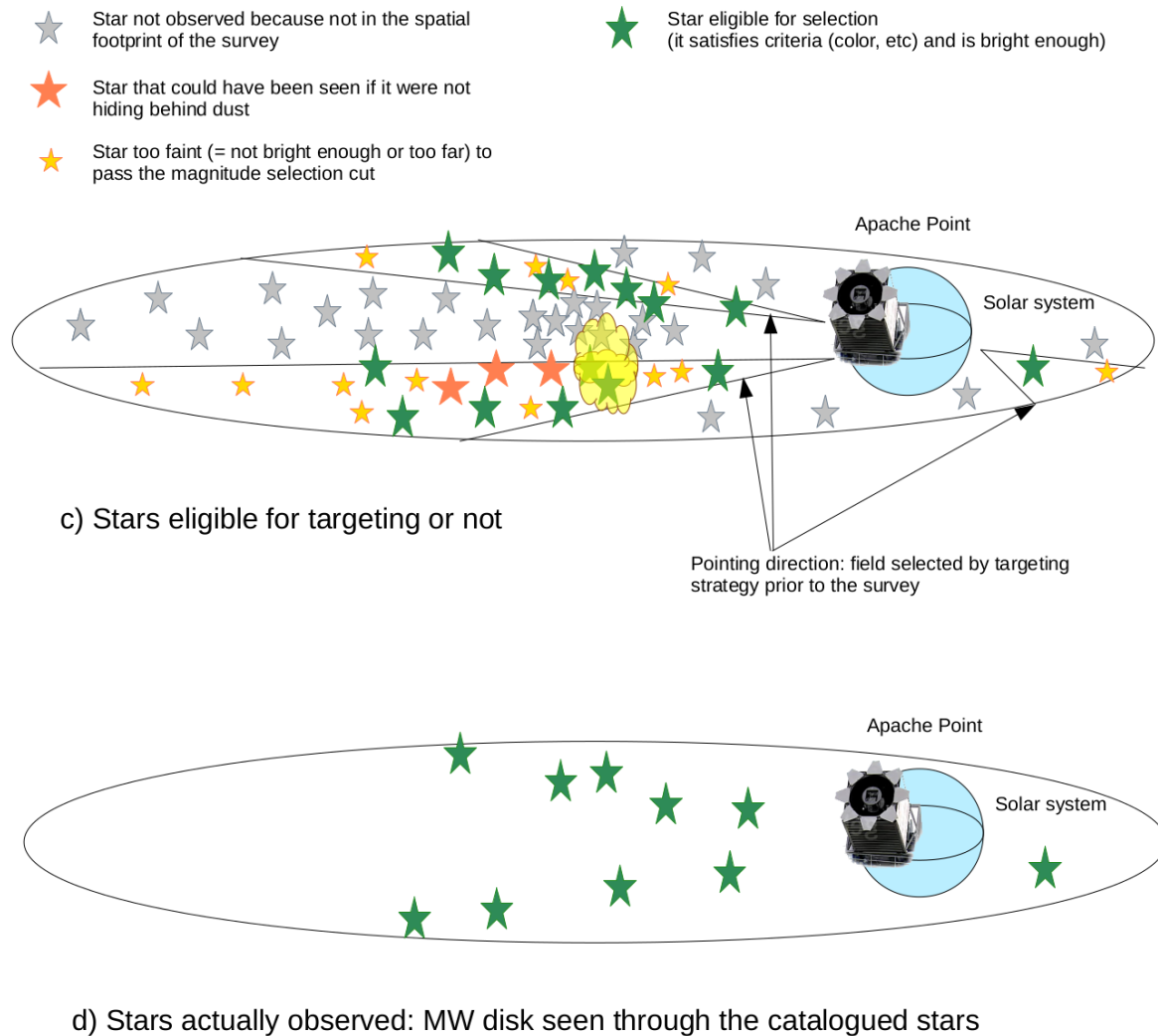
Figure I.9: Schematic illustration of the impact of a selection on the final dataset: top: same as Figure I.8, but stars are color coded by outcome: they pass selection criteria (green) or not (other colors) for various reasons. Bottom: final dataset that does not directly reflect the Galactic disk but does contain information about it, if we know and model the selection that lead to it.

A_ν is the extinction coefficient, and quantifies how much fainter a star looks (when seen through a filter for frequency ν), after the light it emits has travelled through dust.

Dust is responsible for reddening. Since the optical depth τ_ν is a function of ν, the spectrum of a star will be affected differently at different frequencies. Therefore, the apparent color of the star will be different from its intrinsic color. Typically, dust scatters short wavelengths more effectively than long wavelengths, so a star

will look redder than it is. If we are looking at the star in two different filters, say J and K near-infrared bands, the observed color of the star will be $(J - K) = (J_0 - K_0) + (A_J - A_K) = (J - K)_0 + E(J - K)$. The new term $E(J - K)$, 'color excess' or reddening, indicates how much redder the stars looks than if it were not hiding behind dust.

Accounting for these obstacles.   The dust leads to two complications for the modeling in the coming chapters: first, to find the distance to a star, one needs to know by how much it is obscured by dust. Second, to know how many stars are in a given line of sight, one needs to also know how many stars are there, but not seen, because dust hides them.

In the coming chapters, we use several tricks to mitigate the effects of dust. First, all the data I used were taken in near-infrared wavelengths, which are, as we have seen before, less affected by extinction. Secondly, the stars I have used are red clump stars: these are giant stars, which are bright and mostly red. But this does not bring extinction and reddening to zero. The effects can be accounted for by de-reddening the stars, to get their true color, using the assumption that in the Rayleigh-Jeans limit, all stars have the same intrinsic color, giving the $E(J - K)$ term by simply taking the difference between stars observed and true colors. Applying our favoured extinction law allows us to determine A_K, which can in turn be used to determine distances to red clump stars. To know how many stars are hidden behind dust and thus unseen, one needs to have a clear view of the 3D dust distribution in the Milky Way disk. This has been determined by several works (e.g. Green et al., 2018; Rezaei Kh. et al., 2017).

Pioneering efforts have developed methodologies to infer the Milky Way's properties (Sanders & Binney, 2015; Bovy et al., 2014; Bovy, 2016; Mackereth et al., 2017; Rix & Bovy, 2013). But such studies are still rare and focused at the time on *describing the present-day Milky Way*, or forward modelled only for a subset of the available dimensions in the data (e.g., binning in mono-abundance populations) and presented qualitative discussions of the implications for the Milky Way's disk formation and evolution. In many aspects, the limitations partly resided in

- the lack of precise stellar ages in large spatial volumes
- the low precision to which one can approximate surveys selection functions, partly due to a limited knowledge of the 3D extinction in the Milky Way disk
- the lack of precision in the data

At present, 3D extinction in the Milky Way disk is mapped more precisely (Green et al., 2019), stellar ages can be determined to 30%-40% for samples with wide spatial coverage (Ness et al., 2015, 2016; Ting & Rix, 2019), the Gaia space mission delivered precise kinematics for millions of stars (Lindegren et al., 2018): it is **now** very timely to build on and extend the previous inference efforts with an **evolutionary** model for the Milky Way's disk.

I.5 Introduction Summary and Thesis Outline

Disk galaxies, including the Milky Way, lie in restricted regions of the observational space. Their formation and evolution processes are not fully understood, in particular the origin of exponential surface brightness profiles, the inside-out growth processes and the internal dynamical processes driving the secular evolution. This thesis uses the Milky Way as a model organism to address these questions, taking advantage of the fact that we have access to the full distributions $p(\vec{x}, \vec{v}, [\mathrm{Fe/H}], \tau)$

for many of its stars.

The following chapters build incrementally a statistical model for the Milky Way disk stars from their birth conditions to their present-day properties, tackling at each step a different question. Chapter II investigates how strongly stars diffuse in radius.

In Chapter III, I build on this model to investigate further *how* the orbits evolve and disentangle heating processes from cold radial migration processes: orbit diffusion goes as radial action change, and angular momentum diffusion.

In Chapter IV, I rewind stars to their birth properties to infer how the Milky Way disk assembled, and quantify the amount of inside-out growth in the Galactic disk.

In Chapter V, I synthetize the results obtained in this PhD and put them in a larger context of galaxy formation and evolution. I discuss the limitations of the method used in this thesis and suggest possible improvements, for the statistical methods and drawing physical inspiration from cosmological simulations.

Chapter VI concludes on this PhD thesis and discusses briefly the implications and future steps for this research field.

Chapter II

Radial Redistribution of Stars

Science Question   We have seen in Chapter I that the birth conditions of stars in disk galaxies (highly structured) are different from their present-day conditions (very smooth). And we have also seen that in the Milky Way, stars at a given radius and age have a large scatter in [Fe/H]. This could be explained if stars were to redistribute, or diffuse, in radius. Since physical scatter cannot be measured for external galaxies, we are now looking at the Milky Way, to ask: **"Do stars in the Milky Way disk redistribute in radius, and by how much?"**

Publication   This Chapter was published in a similar form in The Astrophysical Journal in Frankel et al. (2018) and presents the construction of a global model for the Milky Way disk, to assess how fast stars change Galactocentric radius in the Galactic disk.

Contributions

- I conducted the research reported in this paper: adapting and extending a Galactic disk model from Sanders & Binney (2015) and from notes that were written before hand by my advisor Hans-Walter Rix. I coded the equations, took major technical decisions independently, produced the plots and wrote the article.
- Hans-Walter Rix supervised the project by giving me regular guidance on the

next steps or helping solving problems I encountered. He also contributed significantly to editing the early drafts of this paper and helped constructing the outline.

- Yuan-Sen Ting contributed through machine-learning guidance, regular interactions which cleared up my mind, and detailed comments on the manuscript.
- Melissa Ness provided the data and comments on the manuscript.
- David Hogg contributed through (1) discussions with my primary advisor leading to the birth of this project (before I start working on it), and (2) through useful comments on the draft and help drawing the graphical models (Fig. II.7 and II.8).

Abstract We develop and apply a model to quantify the global efficiency of radial orbit migration among stars in the Milky Way disk. This model parameterizes the possible star formation and enrichment histories, radial birth profiles, and combines them with a migration model that relates present-day orbital radii to birth radii through a Gaussian probability, broadening with age τ as $\sigma_{\text{Lz12}} \sqrt{\tau/8\text{Gyr}}$. Guided by observations, we assume that stars are born with an initially tight age–metallicity relation at given radius, which becomes subsequently scrambled by radial orbit migration, thereby providing a direct observational constraint on radial orbit migration strength σ_{Lz12}. We fit this model with MCMC to the observed age–metallicity distribution of low-α red clump stars with Galactocentric radii between 5 and 14 kpc from APOGEE DR12, sidestepping the complex spatial selection function and accounting for the considerable age uncertainties. This simple model reproduces well the observed data, and we find a global (in radius and time) radial orbit migration efficiency in the Milky Way of $\sigma_{\text{Lz12}} = 3.6 \pm 0.1$ kpc when marginalizing over all other model aspects. This shows that radial orbit migration in the Milky Way's main disk is indeed rather strong, in line with theoretical expectations: stars migrate by about a half-mass radius over the age of the disk. The model finds the Sun's birth radius at ~ 5.2 kpc. If such strong radial orbit migration is typical, this mechanism plays indeed an important role in setting the structural regularity of disk galaxies.

II.1   Introduction

To understand how disk galaxies formed and evolved (e.g., Mo et al., 2010a; Schön-
rich & Binney, 2009b), we need to understand how our Milky Way, typical disk
galaxy, formed and evolved. In particular, we need to identify and characterize
the processes setting the radial and vertical structures of the Galactic stellar disk in
terms of stellar ages and abundances.

The present-day structure must at some level reflect both the global initial con-
ditions such as the cold gas' total angular momentum and distribution, and the hi-
erarchical merging during the early turbulent phases of the Milky Way's formation
(Brook et al., 2004; Bird et al., 2013; Stinson et al., 2013). The stars' age distribution
obviously reflects the overall star formation history of the Galaxy. In addition, the
stars' photospheric element abundances trace the gradual enrichment of the Milky
Way, which proceeded differently in different parts of the galaxy (e.g., Chiappini
et al., 2001; Schönrich & Binney, 2009b).

But for the last ~ 8 Gyr, the Milky Way's dynamical history has been quite
quiescent, with the large majority of stars formed since then residing in a thin disk
(e.g., Rix & Bovy, 2013; Bland-Hawthorn & Gerhard, 2016). However, even in this
quiescent regime, we cannot expect the stars' present-day orbits to reflect their birth
orbits, as first detailed by Sellwood & Binney (2002) (SB02): there may be a great
deal of dynamical evolution on timescales longer than a dynamical time because
the Galaxy is not axisymmetric, called "secular evolution".

In particular, radial orbit migration has been recognized as a potentially very
important process in both analytic and simulation work (Sellwood & Binney, 2002;
Roškar et al., 2008a; Minchev & Famaey, 2010a). Even if a star was born on a
circular orbit, its present-day radius may differ from its birth radius for basically
two reasons: first, a variety of perturbations in the in-plane or vertical direction
may cause increasing epicycles, a process dubbed "blurring" by SB02 to refer to
orbital heating. We know from the velocity dispersion in the Galactic disk that
for "middle-aged" stars (~ 5 Gyr), this leads to radial excursions of about 1 kpc.
But SB02 emphasized another process, which they dubbed "churning", that occurs

in the presence of changing, fleeting or complex non-axisymmetric patterns (over-densities) such as spiral arms; these exert torques on stars, and lead to an effective change in a star's angular momentum or mean orbital radius, without inducing much "blurring". Here, we focus on the changes in the (instantaneous) orbital radius, and refer to this combined effect of "churning" and "blurring" as "radial orbit migration" or "radius migration" throughout the present analysis.

N-body and cosmological simulations imply that radial orbit migration is very important: the angular momentum (and hence orbit-size) may change of order unity for any star over time-scales as short as a few Gyr (Grand et al., 2012, 2016; Kubryk et al., 2013), in detail depending on the non axis-symmetric structures' properties such as their pattern speeds and strengths. But to predict the actual degree of radius migration in any galaxy *quantitatively*, one would need to have an inventory of all the past spiral and bar pattern speeds and strengths.

There is well established observational evidence for the relevance of this process. In external galaxies, it makes predictions for the outermost radial density and age profiles of the stellar disk, which are in qualitative agreement with observations (e.g., Herpich et al., 2017; Ruiz-Lara et al., 2017). In our Galactic disk, there is the remarkable, longstanding observation that there is no distinct age–metallicity relation of stars in the Solar neighbourhood (few 100 pc around the Sun); and that there is a wide spread of metallicities at the Solar radius (Edvardsson et al., 1993; Haywood, 2008; Casagrande et al., 2011). Both observations would be puzzling if stars – at a given time and Galactocentric radius – were born with a very small spread in metallicities. This is expected from both chemical evolution models (Matteucci & Francois, 1989) and from observations of the interstellar gas and young stars in galaxies (e.g., Przybilla et al., 2008).

But if there is an important radial gradient in the metallicities (as observed in the Milky Way, (e.g., Genovali et al., 2014)) then extensive radius migration, scrambling the orbital radii of stars while keeping their [Fe/H] unchanged, could explain the lack of an age–metallicity–(present-day) radius relation at given radius. This has been advocated and worked out by Schönrich & Binney (2009a,b); Roškar et al. (2008c); Minchev et al. (2013); Hayden et al. (2018). They laid out a picture where

three basic ingredients can explain the present-day orbit–age–abundance distribution of Galactic disk stars: 1) disk stars at all epochs and Galactocentric orbit radii were born with a well-determined metallicity ($[Fe/H](R_0, \tau)$), 2) there has always been an evolving outward metallicity gradient, 3) extensive subsequent mixing of orbital radii occurred.

Much of the best observational constraints on such radial orbit migration in the Galaxy stems from very local samples (Nordström et al., 2004; Sanders & Binney, 2015), with stars that have both abundance and age estimates; and indeed these analysis imply very effective radius migration. But if radial orbit migration is a global phenomenon across the Galactic disk, then it calls for a "global" test, i.e. a test with observational data that cover Galactocentric radii that encompass a good fraction of the Galactic disk.

Here we propose *measurement* of the average, or global, efficiency of radial orbit migration, based on data over a very wide Galactocentric radial range ($5 \leq R \leq 14$ kpc), with age estimates from spectroscopy. APOGEE (Majewski et al., 2017) spectra provide the first large ($\sim 20,000$) sample with consistent age estimates, τ (Ness et al., 2016) across a large radial range in the Galaxy. Qualitatively, the young stars $\tau \leq 1$ Gyr show a well defined radial metallicity gradient ($[Fe/H]$ decreasing outward), with a modest scatter in $[Fe/H]$ at any given radius (see Figure II.2). "Old" stars (≥ 10 Gyr) show no discernable metallicity – radius relation, or at least enormous scatter in $p([Fe/H] \mid R)$. The basic idea (Schönrich & Binney, 2009a; Sanders & Binney, 2015) is that extensive radius migration has largely erased the original radius–$[Fe/H]$– age relation.

This approach is related to, but not the same as "chemical tagging" (Freeman & Bland-Hawthorn, 2002; Ting et al., 2015), which aims at identifying stars that were born in the same cluster by their near-identical, detailed abundance patterns, even if they are now on widely different orbits. While stars from the same cluster were manifestly born at the same epoch and the same Galactocentric radius, the approach in the present analysis makes a different assumption: that stars born at the same epoch at the same Galactocentric radius have very similar $[Fe/H]$ (e.g., Przybilla et al., 2008).

Any radius migration over the course of a star's life is best thought of as a combination of diffusion of orbital angular momentum, or guiding radius (churning) and orbital heating (blurring), presuming it was born on a near-circular orbit. These are two distinct processes of different amplitudes, which can be measured separately using stellar angular momenta and radial action. But here, we focus on the stars' Galactocentric radii R as a proxy, as these quantities are currently available with great fidelity and across a wide range of radii. We also restrict our analysis to stars with ages $\tau \leq 8$ Gyr, as a model of gradual, secular orbit evolution may not be applicable to the earliest phases of the Galactic (thick) disk formation.

Here we construct a forward-model that incorporates the main processes that set the age- and abundance-dependent structure of the Galactic disk: the global star-formation history, inside-out growth, gradual chemical enrichment and radial orbit migration. In important aspects, this model draws on the ideas laid out in Sanders & Binney (2015). We then compare this model to APOGEE data, thereby constraining the strength of radial orbit migration from data across the Galaxy. The data are presented in Section IV.2. The methodology is laid out in Section II.3. We then present our results in Section IV.4 that quantitatively constrain radius migration and affirm how effective it seems to be in the Galaxy. We conclude and comment in Section II.5

II.2 Data: APOGEE red clump giants

Global constraints on radius migration of stellar orbits call for a sample of stars that covers a wide range in Galactocentric radii at low latitudes and with precise distances, and that has consistent [Fe/H] and age estimates. The APOGEE (Apache Point Observatory Galactic Evolution Experiment Majewski et al., 2017) sample of red clump giants (Alam et al., 2015; Bovy et al., 2014) is, by design, very well suited for this purpose. Observing at near-infrared wavelengths for which dust is nearly transparent, the APOGEE spectrograph delivered spectra for giant stars with Galactocentric radii from ~ 5 kpc to ~ 14 kpc, as illustrated in Figure II.2. Stellar parameters and abundances for this sample (originally from APOGEE DR12, Alam

et al., 2015) were re-derived using *The Cannon* Ness et al. (2015). Importantly, consistent ages were derived by Ness et al. (2016), using the same data-driven approach to calibrate spectroscopic age estimates to asteroseismic data; the spectroscopic age signature of red clump giants resides in the C and N abundances (at given [Fe/H]), reflecting mass (and hence age) dependent dredge-up (Masseron & Gilmore, 2015; Martig et al., 2016). Uncertainties in metallicity are of about 0.05-0.10 dex, and those in ages ($\log \tau$) are 0.2 dex.

Red clump giants are reliable standard candles, see for example Girardi (2016), with photometric distances precise to within 5%. The 3D position in the Galaxy can be obtained from these, assuming the Sun is at a Galactocentric distance $R_\odot = 8$ kpc and height $z_\odot = 25$ pc. Bovy et al. (2014) identified $\sim 20{,}000$ red clump giants in APOGEE with a contamination fraction between $\sim 3\%$ and 10% by red giant branch stars.

The above elements provide us with a set of about 20 000 data $\{[Fe/H], \tau, R\}$, and their uncertainties. For our modelling at hand, it seems sensible to apply a few more cuts to the sample. As we are interested in radial orbit migration as the possibly dominant orbit evolution process in the more quiescent phase of the Galactic disk evolution (the last $\sim$8 Gyr), we eliminate stars with high $[\alpha/Fe]$, as illustrated by the grey dots in Fig II.1. Additionally, we select stars well in the Galactic plane with altitude $|z| < 1$ kpc.

II.2.1   Sidestepping the complex spatial selection function

Given a set of data $\{[Fe/H], \tau, R\}$, the obvious approach would be to construct a parameterized model to predict $p(\{[Fe/H], \tau, R\} | \mathbf{p_m})$, where $\mathbf{p_m}$ are various model parameters describing the possible evolution histories of the Galactic disk (see Section II.3) including radial orbit migration. But such direct comparison of model predictions to data requires to account for the selection function: the probability that any star in the sky enters the survey catalog, given its physical properties. In the case of the APOGEE data at hand, the selection function is (inevitably) complex: stars must (1) belong to the red clump population, and (2) be the pointing directions of APOGEE and have color and magnitudes to fit the APOGEE survey selection.
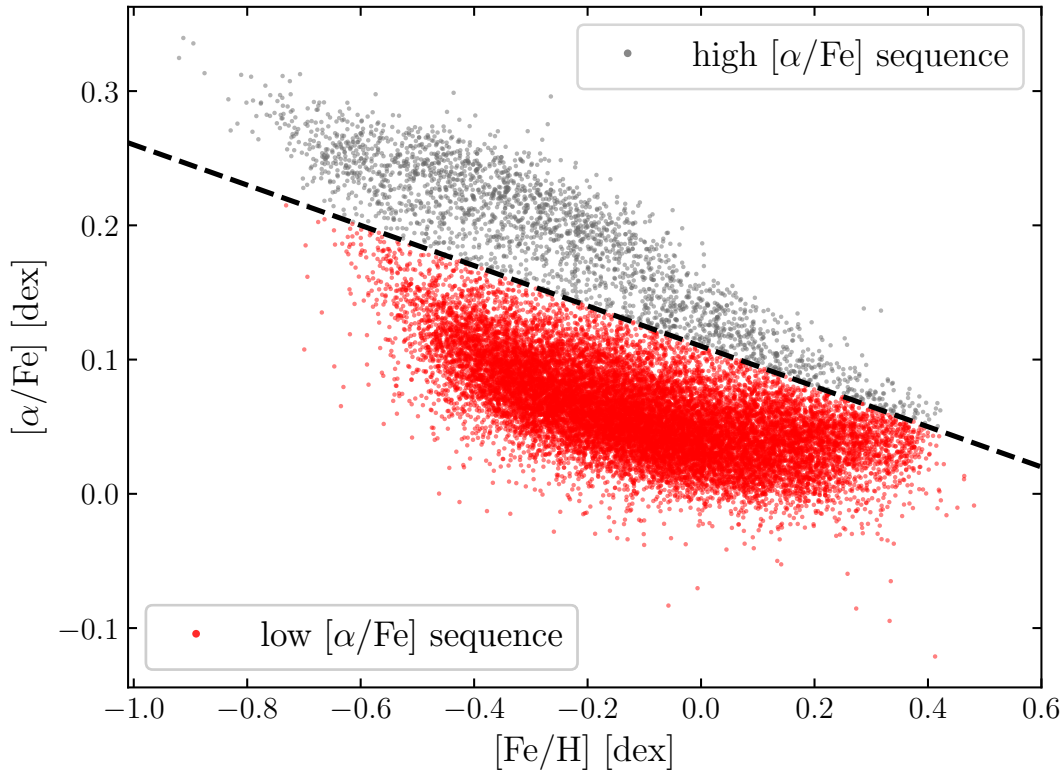
Figure II.1: Illustrating the abundance-based selection of about 17,500 low-[ff/Fe] red clump stars among the 20,000 APOGEE red clump giants (in red, below the dashed line) for this study. We focus on those "thin disk" stars, as describing orbit evolution via gradual, secular radial orbit migration may not be applicable to the turbulent early phases of Milky Way formation, when most high-[ff/Fe] presumably formed.

Firstly, the number of red clump stars per unit mass of a stellar population is a strong function of age (Girardi & Salaris, 2001). Bovy et al. (2014) have calculated with stellar evolutionary models the relative fraction of stars which are in this evolutionary stage in function of their age for a flat star formation history (this is illustrated by the dashed line in Figure II.3).

Secondly, the APOGEE spatial selection function was shown to be a complex function (Bovy et al., 2016a). The consequences of spatial distribution on the radial distribution of the APOGEE red clump sample used in our study is visible in Figure II.2 where there is, for example, an over-density of stars observed at the position of the Sun (≈ 8 kpc). Therefore, we opt not to model this complex distribu-
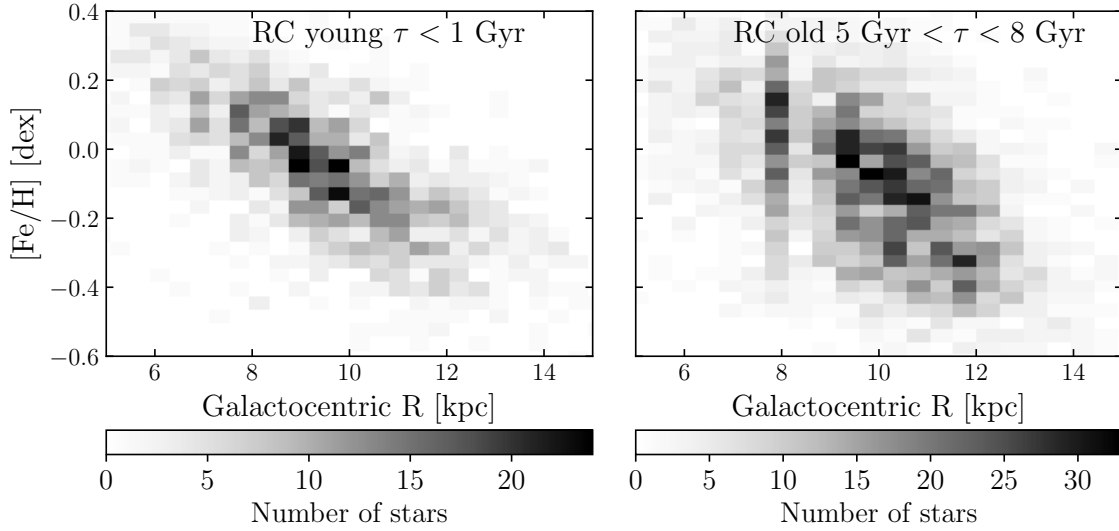
Figure II.2: Number density distribution of RC stars in the plane of metallicity ([Fe/H]) and Galactocentric radius, for two ages bins: young stars (less than 1 Gyr, left), and older stars (measured age between 5 and 8 Gyr, right), assuming a solar position of $R_\odot = 8$ kpc and $z_\odot = 25$ pc. Measurement uncertainties are of about 5% in radius and 0.1 dex in metallicity. This Figure, adapted from Ness et al. (2016), shows that (1) there is a well-defined metallicity gradient among young stars; (2) at a given metallicity, the (horizontal) spread in Galactocentric radii is larger for old stars than that for young stars (which we interpret and model as a consequence of radius migration); and (3) the stellar density at different radii is dominated by the complex spatial selection function of APOGEE (e.g., the manifest over-density at 8 kpc, reflecting the location of the Sun).

tion. Instead, we work only with the age–metallicity distribution given stellar radii $p(\{[\text{Fe/H}], \tau\} \mid \{R\})$. The advantage is that the model construction is technically simpler and more robust; but not all of the information contained in the data is used. In particular, we are not exploiting the present-day radial distribution of stars in the Milky Way disk $p(\{R\})$.

II.3   A model for the Galactic disk evolution, including radial orbit migration

We now lay out a simple parameterized model for the age–abundance–radius structure of the Galactic disk of low-[α/Fe] stars. This model specifies different formation and evolution aspects: when, and at what metallicity stars were born, with which radial profile they were born, and how much they migrated, ultimately pre-

dicting the joint distribution $p([\text{Fe/H}], \tau, R)$ and $p(\{[\text{Fe/H}], \tau\} \mid \{R\})$. In many ways, this model draws on the approach laid out by Sanders & Binney (2015).

We start by stating the main assumptions underlying our model. We then specify the individual model aspects, each described by a set of functional forms, which result in a vector of model parameters, $\mathbf{p_m}$. We then combine these aspects to predict the age-metallicity distribution at any given Galactocentric radius, $p([\text{Fe/H}], \tau \mid R, \mathbf{p_m})$, which allows us to calculate the data likelihood for the APOGEE sample given any $\mathbf{p_m}$ and apply Bayes' theorem to infer the posterior probability function for the model parameters, given the data

$$
\begin{aligned}
p_{po}(\mathbf{p_m} \mid \{[\text{Fe/H}], \tau, R\}) = {} & p_{\mathcal{L}}(\{[\text{Fe/H}], \tau\} \mid \{R\}, \mathbf{p_m}) \\
& \times p_{pr}(\mathbf{p_m}) / p_{pr}(\{[\text{Fe/H}], \tau\}),
\end{aligned}
\tag{II.1}
$$

with p_{po} the posterior probability density function of the model parameters, $p_{pr}(\mathbf{p_m})$ our prior knowledge on the model parameters, and $p_{pr}(\{[\text{Fe/H}], \tau\})$ the evidence. Such inference operation requires to account for data uncertainties. We assume in the present study that the uncertainties in R and $[\text{Fe/H}]$ are negligible (red clump stars have $\sim 5\%$ and $\sim 0.05 - 0.1$ dex uncertainties in distance and $[\text{Fe/H}]$ respectively). We presume that the uncertainties in $\log \tau$ dominate and are described by a Gaussian with $\sigma_{\log \tau} = 0.2$ dex (Ness et al., 2016).

II.3.1 Basic model assumptions

In order to describe the evolution of the Galactic disk with a parametrized model, we made several assumptions on the nature and strength of the processes at play. Obviously, the astrophysical inferences from our modelling are only as valid as the assumptions.

- We assume that the metallicity $[\text{Fe/H}]$ of the interstellar medium has negligible variations with azimuth; this is perhaps the strongest assumption involved in the modelling. This assumption is supported by observations of young stars in the Galaxy (e.g., Luck et al., 2006; Przybilla et al., 2008; Genovali et al., 2014). Azimuthal variations in rapidly produced α-elements have been claimed (Ho

et al., 2017; Sánchez-Menguiano et al., 2016), but those in [Fe/H] should be less strong.

- We do not treat or model explicitly the vertical structure of the Milky Way disk, though there are of course vertical (populations) gradients in it (e.g. Ness et al., 2016), which are affected by radial migration (e.g., Schönrich & McMillan, 2017a; Kawata et al., 2017a). Such gradients will only appear as scatter at given radius, interpreted as consequence of radial orbit migration in the present work.

- Secular evolution has been the dominant orbit evolution effect for the past 8 Gyr, which implicitly assumes that the Milky Way had a relatively quiescent life for the past 8 Gyr. We therefore restrict our analysis to stars younger than 8 Gyr, neglecting possible recent external interactions that could be responsible for shaping the Milky Way disk.

It follows from these assumptions that we model radial orbit migration as the only mechanism responsible for the scatter in age–metallicity at given radius. In this work, we interpret all scatter with radius migration, and therefore provide an upper limit on its strength, which should reflect the distance over which stars have migrated radially.

II.3.2 Functional Forms for the Different Aspects of the Model

In the following, we use the assumptions stated above and lay out our adopted functional forms for different aspect of the Galactic disk's formation and evolution: the distributions of (1) the global disk star-formation rate, (2) birth radii distribution as a function of time, (3) birth metallicities at a given epoch and radius, and (4) the strength of radial orbit migration. We summarize these functional forms in Table II.1. These functions are combined to produce Eq II.1, from which we can sample the posterior probability distribution function of the parameters $\mathbf{p_m}$.

II.3.2.1   Star formation history and the age distribution of red clump stars

We parameterize the possible age distribution of red clump stars by

$$p(\tau \mid \mathbf{p_m}) \equiv c_1 \cdot \text{SFH}(\tau, \mathbf{p_m}) \cdot f_{RC}(\tau), \qquad (\text{II.2})$$

where SFH is the star formation history of the Milky Way thin disk, f_{RC} is the relative mass of stars at the red clump stage, and the normalization requires

$$c_1^{-1} \equiv \int_0^{\tau_m} \text{SFH}(\tau, \mathbf{p_m}) f_{RC}(\tau) \, d\tau. \qquad (\text{II.3})$$

The star formation history (SFH) of the Milky Way thin disk is thought to be extended in time (Bland-Hawthorn & Gerhard, 2016) and is manifestly still ongoing. This motivates our choice (Mo et al., 2010b) to conventionally parametrize the star formation rate in the Milky Way disk as a slowly decreasing exponential with time, for which we fit the exponential decay time-scale τ_{SFR}. This is a simplification of the Sanders & Binney (2015) model, who go further in detail and include thick disk star formation. We write the star formation history

$$\text{SFH}(\tau, \mathbf{p_m}) = \exp\left[-(\tau_m - \tau)/\tau_{SFR}\right], \qquad (\text{II.4})$$

where τ_m is the maximum disk age, set to 12 Gyr; τ_{SFR} is the model parameter setting the star formation history, and is to be fit (i.e. it is an element of $\mathbf{p_m}$).

The expected number of red clump stars per unit stellar mass, $f_{RC}(\tau)$, is a distinct function of age (and a weaker function of metallicity); it has been derived and parametrized in eq (11) of Bovy et al. (2014). We illustrate $f_{RC}(\tau)$ in Figure II.3 (dashed line) together with one particular choice of a star formation history SFH (solid line).

II.3.2.2   Radial Birth profile and inside-out growth

We presume that disk stars are born on near-circular orbits near the mid-plane of the disk. The sizes of their orbits is determined by the angular momentum of the
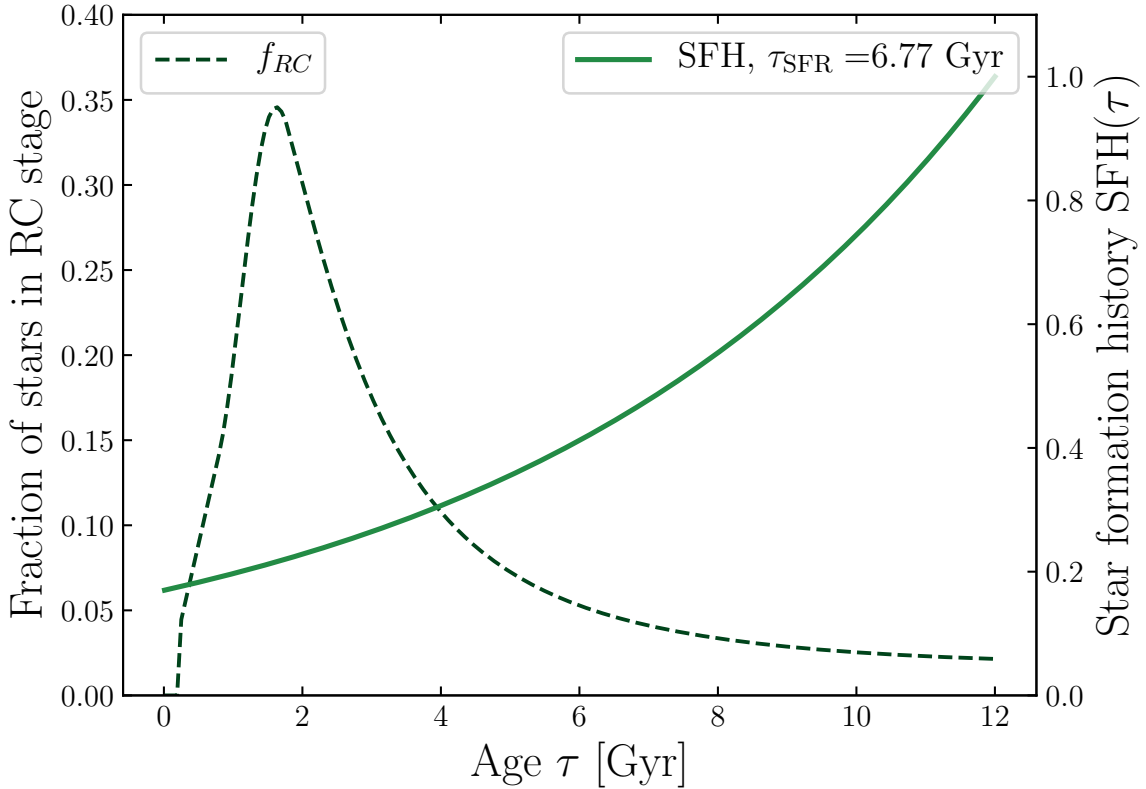
Figure II.3: Model for the global star formation history and the age distribution of red clump stars. We assume that the global star formation history of the (low-α) Galactic disk can be described (see Eq II.4) by a model family SFR $\propto \exp\left(-t/\tau_{SFR}\right)$, illustrated by the solid line for a star formation time-scale $\tau_{SFR} = 6.8$ Gyr. The dashed line shows the theoretically expected relative number of red clump stars per unit mass for a constant star formation history. The normalized product of these two functions gives the current age distribution of red clump stars.

gas from which they formed. We therefore need to parametrize the radial profile of the star-forming gas in the Galactic disk at any time. The Galactic disk is thought to build from inside-out, as gas of first low then higher angular momentum cools and falls into the potential of the dark matter halo (White & Frenk, 1991; Mo et al., 1998; Muñoz-Mateos et al., 2007a; Fraternali & Tomassetti, 2012). This inside-out growth is thought to play a determining role in the gas and stars metallicity profile (Schönrich & McMillan, 2017a), so it is important to incorporate this aspect into our disk model. We parametrize the possible radial birth profile of stars at any given epoch as a decreasing exponential with Galactocentric radius, with a scale-length

R_{exp},

$$p(R_0 \mid \tau, \mathbf{p_m}) = \exp\left(-R_0/R_{\mathrm{exp}}(\tau)\right)/R_{\mathrm{exp}}(\tau). \tag{II.5}$$

We then parameterize inside-out growth by allowing the scale-length to increase (linearly) with time,

$$R_{\mathrm{exp}}(\tau) = 3 \text{ kpc} \left(1 - \alpha_{R_{\mathrm{exp}}}\left(\frac{\tau}{8 \text{ Gyr}}\right)\right). \tag{II.6}$$

The relative size of the disk today and at early times is set by the free parameter to be fit $\alpha_{R_{\mathrm{exp}}}$ (Eq II.6), bound to the interval $[0, 1]$ with the current star-forming disk scale-length set to $R_{\mathrm{exp}}(\tau = 0) = 3$ kpc. Note that we do not attempt to model the radial profile of the disk beyond 8 Gyr ago, because we deem our secular evolution model inapplicable at such early epochs. The radial scale-length of the Milky Way stellar disk is not well constrained (see Bland-Hawthorn & Gerhard (2016) for a review). It was shown that such scale-length varies with stellar populations (Bovy et al., 2012). We adopt here the suggested value for the younger stars (in the chemical sense: with low $[\alpha/\mathrm{Fe}]$) in the disk of ~ 3 kpc from Bovy et al. (2012), to model the present-day star-forming gas profile. The possible distributions of stars at birth 8 Gyr ago and today are shown in Figure II.4 for a specific choice for $\alpha_{R_{\mathrm{exp}}}$.

II.3.2.3   Metallicity–radius–age relation

We also need to specify with what [Fe/H] stars were born at time τ ago at Galactocentric radius R_0. At present, disk stars in the Milky Way are born with a tight relation between their birth radius and their metallicities. This is qualitatively seen in data: young sub-populations (e.g., Cepheids, Genovali et al. (2014)) of a given [Fe/H] cover a small range of galactic radii. Open clusters metallicity spreads were shown to be about 0.03 dex (Bovy, 2016; Ness et al., 2017; Ting et al., 2018a). This motivates our assumption that the metallicity profile of the interstellar medium (and hence the metallicity stars have at birth) can be modelled at any time through a tight relation. Following the general reasoning of Sanders & Binney (2015) who approximate the output of a simulation of Schönrich & Binney (2009a), we describe the metallicity profile in the star-forming gas disk as the product of a radial profile,
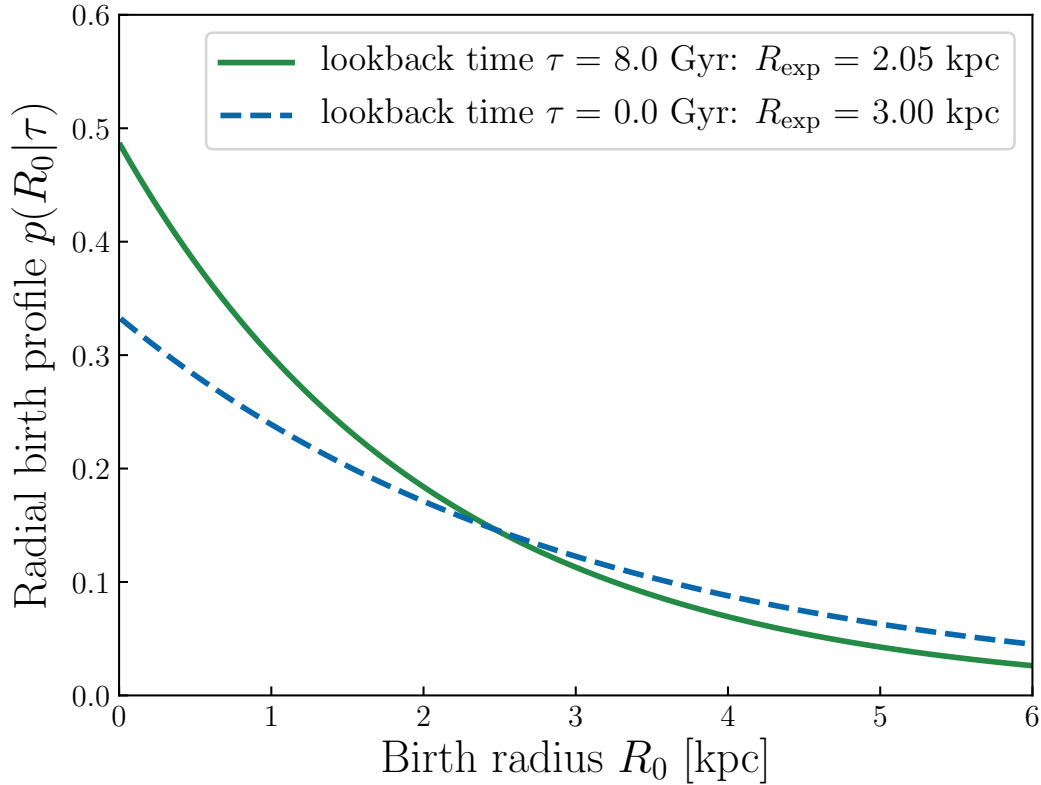
Figure II.4: Illustration of the models for the birth-radius distribution of stars. At any given point in time, the radial birth profile is assumed exponential, with a scale-length growing with time to reflect inside-out growth (here, $\alpha_{R_{\exp}} = 0.3$, see Eq II.6). Stars were born in more centrally concentrated regions 8 Gyr ago (solid line) with a radial scale length of 2 kpc, which is about 30% smaller than today's assumed birth scale length of 3 kpc (dashed line).

and of a term describing the time dependency of chemical enrichment

$$
\begin{aligned}
[\text{Fe/H}] =& F_m - (F_m + \nabla[\text{Fe/H}]R^{\text{now}}_{[\text{Fe/H}]=0})f(\tau) \\
& + \nabla[\text{Fe/H}]R.
\end{aligned}
\tag{II.7}
$$

Here, F_m represents the metallicity of the gas at the center of the disk at $\tau = 12$ Gyr. We assume it to be fixed at -1 dex, a choice supported by the age–metallicity relation of globular clusters at the center of the Milky Way (e.g., Kruijssen et al., 2018). The parameter $\nabla[\text{Fe/H}]$ is the interstellar medium metallicity gradient in dex kpc^{-1}, is negative, and is to be fit with the other parameters in $\mathbf{p_m}$. We do not specify the physical mechanisms behind the origin and maintenance of the (birth)

gas metallicity gradient. Simulations show such a gradient to be a robust prediction (Grand et al., 2015). It is presumed here to be constant in radius and time, although the metallicity gradient may have evolved over the life time of the Galactic disk (Minchev et al., 2018; Grisoni et al., 2018a). We discuss the possible impact of this assumed form in Section IV.4, where different expressions are tested. We expect young stars across the Galactic disk to provide the strongest constraints on this model parameter. Then, $R^{\text{now}}_{[\text{Fe/H}]=0}$ is the radius at which the present-day (birth) metallicity is solar ([Fe/H]= 0). We expect this parameter to be constrained by the current radii of the youngest red clump stars of solar metallicity. We assume the time dependency of the enrichment to follow the power law

$$f(\tau) = \left(1 - \frac{\tau}{\tau_m}\right)^{\gamma_{[\text{Fe/H}]}}$$

with the parameter (to fit) $\gamma_{[\text{Fe/H}]}$ controlling the time dependency of chemical enrichment with time: linear if $\gamma_{[\text{Fe/H}]}$ is 1, and faster at early times if $\gamma_{[\text{Fe/H}]}$ is less. Overall, this encapsulates that there is a metallicity gradient in the interstellar medium in the disk, and that enrichment proceeded gradually over time, as illustrated in Figure II.5.

With this parametrization, we now assume that there is an exact birth metallicity at a given stellar age τ and birth radius R_0, i.e. $p([\text{Fe/H}] \mid R_0, \tau, \mathbf{p_m})$ is a δ-function at the value of [Fe/H] that satisfies Eq IV.17. To study radial orbit migration ($R - R_0$), we use this functional form of the metallicity profile of the interstellar medium as a function of time to find stellar birth radii, given stellar metallicities and stellar ages. In other words, we invert the age–metallicity relation in Equation IV.17 and construct the inverse relation $\tilde{R}_0([\text{Fe/H}], \tau)$, which is a δ-function in R_0, centered on:

$$\tilde{R}_0 = \frac{[\text{Fe/H}] - F_m + (F_m + \nabla[\text{Fe/H}]R^{\text{now}}_{[\text{Fe/H}]=0})f(\tau)}{\nabla[\text{Fe/H}]} \tag{II.8}$$

Such inversion requires

$$\tau \leq \tau_{\max}([\text{Fe/H}], \mathbf{p_m}),$$

for $\tilde{R}_0$ to be positive. Here, $\tau_{\max}([\text{Fe/H}], \mathbf{p_m})$ is the maximum stellar age deemed
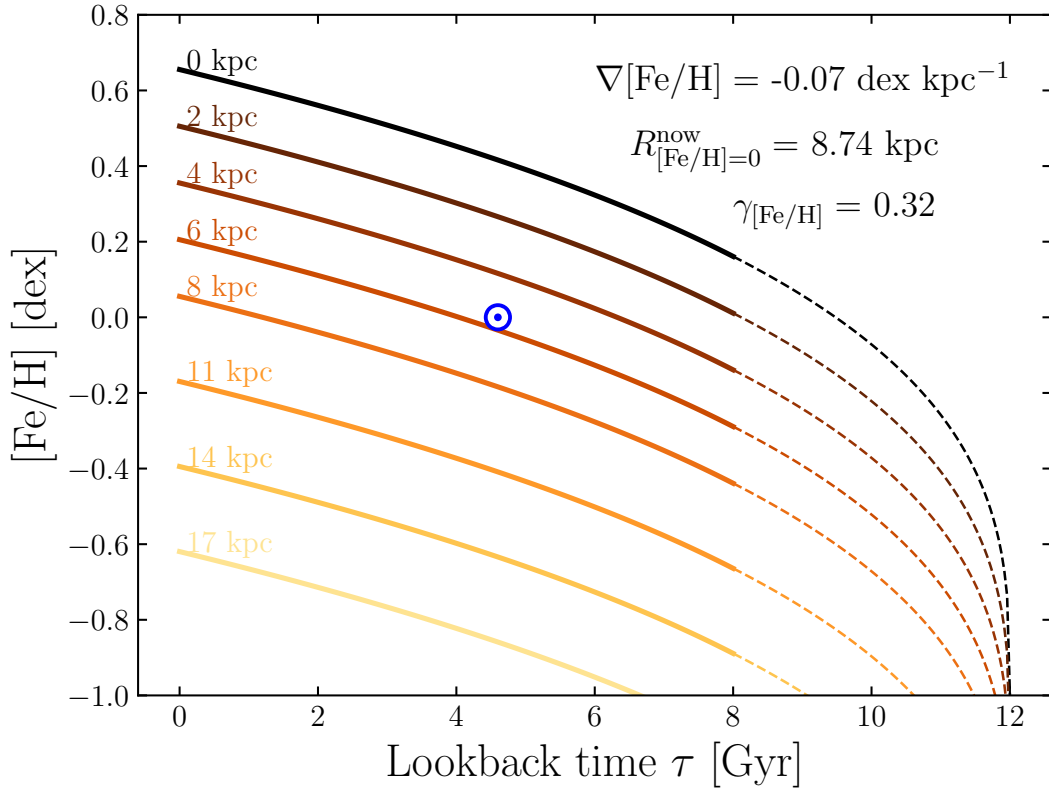
Figure II.5: Model family for the "chemical enrichment", i.e. the relation between age, birth radius and metallicity, shown for eight different birth radii and a fiducial set of model parameters (see inset and Eq IV.17). At all times there is a radial metallicity gradient ([Fe/H] decreases towards larger radii), and at any radius (line of a given color) the interstellar medium gets enriched with time. The position of the Sun in this plane is indicated by the blue ⊙ marker. Combinations of ages and metallicities above the black 0 kpc line would be deemed unphysical by the model.

physical by our model evaluated for $\mathbf{p_m}$, given a metallicity [Fe/H]. Solving the inequality $\tilde{R}_0([Fe/H], \tau) > 0$ for τ at a given metallicity in Eq II.8,

$$\tau_{max}([Fe/H], \mathbf{p_m}) = \tau_m \left(1 - \frac{[Fe/H] - F_m}{F_m - \nabla[Fe/H] R^{now}_{[Fe/H]=0}}\right)^{1/\gamma_{[Fe/H]}} \quad \text{(II.9)}$$

where we used the assumption that the metallicity gradient in the star-forming gas is always negative; [Fe/H] decreases outward. This inequality can be visualized in Figure II.5: combinations of [Fe/H] and τ above the 0 kpc line are deemed unphysical. This condition, that is a function of $\mathbf{p_m}$, will therefore provide strong
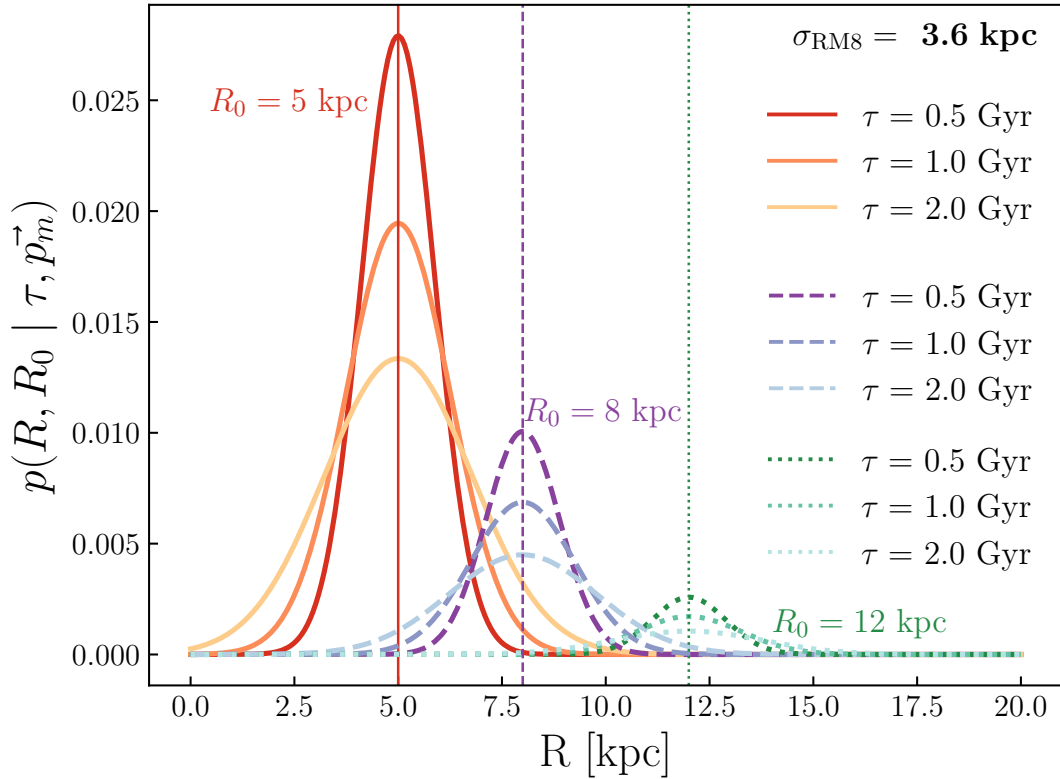
Figure II.6: Simple model family for radial orbit migration, illustrated by the orbit radius probability distributions of stars born respectively at 5, 8 and 12 kpc (plain red, dashed purple and dotted green) as a function of time after birth: 0.5, 1 and 2 Gyr (darker to lighter). The radial orbit migration strength σ_{Lz12} to be fit (Eq IV.13, here 3.6 kpc) determines the rate at which the distributions broaden with time. Near the center of the Galactic disk, the distributions become asymmetric because stars have a null probability to migrate to negative radii (e.g., discontinuity of the yellow line at $\tau = 2\,\mathrm{Gyr}$ and $R = 0\,\mathrm{kpc}$). The distributions are modulated by the exponential radial birth profile, with an inside-out scale parameter $\alpha_{R_{\mathrm{exp}}}$ of 0.3, and the current disk scale-length 3kpc.

constraints on the parameters to fit in the age–metallicity – birth radius relation, in particular on $\gamma_{[\mathrm{Fe/H}]}$.

II.3.2.4   Radial orbit migration

We now introduce the central part of our model: radial orbit migration in order to quantify how far stars move from their birth radii as a function of their age. Theoretical and observational arguments suggest that radial orbit migration can be modelled as a diffusion process. Sellwood & Binney (2002) first demonstrated

Table II.1: Summary of the important aspects of the model.

Question tackled by the model	Describing model parameter	Parameter of $\mathbf{p_m}$ to fit	Relevant appearance in the parametrized equations	Model aspect / Eq reference
When did stars form?	Star formation timescale	$\dfrac{\tau_{SFR}}{\mathrm{Gyr}}$	$\mathrm{SFH}(\tau, \mathbf{p_m}) = \exp\left[-(\tau_m - \tau)/\tau_{SFR}\right]$	Star formation history, Eq II.4
Where did stars form?	Relative size of the disk at birth and present-day	$\alpha_{R_{exp}}$	$p(R_0 \mid \tau, \mathbf{p_m}) \propto \exp\left(-R_0/R_{exp}\right)$ $R_{exp} \propto \left(1 - \alpha_{R_{exp}} \cdot \dfrac{\tau}{8\mathrm{Gyr}}\right)$	Inside-out growth, Eq II.5
With what [Fe/H] were stars born?	Present-day radius of solar metallicity in ISM	$\dfrac{R^{now}_{[Fe/H]=0}}{\mathrm{kpc}}$	$[\mathrm{Fe/H}] = F_m + \nabla[\mathrm{Fe/H}]R$ $- \left(F_m + \nabla[\mathrm{Fe/H}]R^{now}_{[Fe/H]=0}\right)f(\tau)$	Tight age-metallicity relation at birth, Eq IV.17
	Metallicity gradient in the ISM	$\dfrac{\nabla[\mathrm{Fe/H}]}{\mathrm{dex.kpc}^{-1}}$		
	Enrichment power law index	$\gamma_{[Fe/H]}$	$f(\tau) = \left(1 - \dfrac{\tau}{\tau_m}\right)^{\gamma_{[Fe/H]}}$	Chemical enrichment
How far did stars orbit migrate over the disk life time?	Diffusion scale length migration distance over the past 8 Gyr	$\dfrac{\sigma_{Lz12}}{\mathrm{kpc}}$	$p(R \mid R_0, \tau, \mathbf{p_m}) \propto$ $\exp\left(-\dfrac{(R - R_0)^2}{2\,\sigma^2_{Lz12}\,\tau/8\mathrm{Gyr}}\right)$	Diffusion in radius, radial migration, Eq IV.13

that non-axisymmetric structures such as spiral arms can, through repeated and transient torques on stars at co-rotating with them, induce large changes in their angular momenta. Further simulations confirmed this diffusion aspect of radial migration (Schönrich & Binney, 2009a; Brunetti et al., 2011). Qualitatively, data show that at a fixed metallicity, a spread in stellar radii increases with stellar ages. This is qualitatively evident in the different [Fe/H]–R spread between the two panels in Figure II.2. Motivated by these arguments, we follow Sanders & Binney (2015) and adapt their parametrization to Galactocentric radius coordinate. In its simplest form, a solution to the diffusion equation in radius gives the following probability for a star to be currently at a Galactocentric radius R, given that it was born at R_0 a time τ ago:

$$p(R \mid R_0, \tau, \mathbf{p_m}) = c_3 \, \exp\left(-\frac{(R - R_0)^2}{2\,\sigma_{\mathrm{Lz12}}^2\,\tau/8\,\mathrm{Gyr}}\right), \tag{II.10}$$

where σ_{Lz12}, the radial orbit migration strength (our main astrophysical goal, to fit), represents the extent of radial orbit migration for a star after 8 Gyr (the width of the Gaussian function in Equation IV.13 at age $\tau = 8$ Gyr). As its age increases, the probability for a star to be on a different orbit than its birth orbit increases, because it had more time to radial migrate. An illustration of the radial spread of different orbits with, for example, $\sigma_{\mathrm{Lz12}} = 3.6$ kpc is shown in Figure II.6, where the distributions are modulated by the radial birth profile across the disk. Finally, the normalization constant c_3 satisfies

$$c_3^{-1} = \sigma_{\mathrm{Lz12}}\sqrt{\frac{\pi}{2}\,\frac{\tau}{8\,\mathrm{Gyr}}} \cdot \left(\mathrm{erf}\left(\frac{R_0}{\sigma_{\mathrm{Lz12}}\,\sqrt{2}\sqrt{\tau/8\,\mathrm{Gyr}}}\right) + 1\right),$$

to ensure that stars do not migrate to negative radii. This parametrization implies a (presumably unphysical) net motion outwards, which has a very limited impact on the results as discussed in Section II.5.

In this most restricted form, the only free parameter describing radial orbit migration is σ_{Lz12}.

II.3.3 Constructing the Data Likelihood Function

We use the above elements to build a parameterized model that predicts the joint distribution $p([\mathrm{Fe/H}], \tau \mid R, \mathbf{p_m})$ at a given Galactocentric radius R for the low-α Galactic disk. The model consists of two distinct components. The first component is built from the aspects described in the above section for the disk younger than 8 Gyr and is aimed to be informative about the evolution of the Milky Way disk. The second component is a simple model for the disk older than 8 Gyr; the model laid-out above may not apply to the early phases of the evolution of our Galaxy. As this old disk component model is a "nuisance" aspect of the current work, the model is fairly simple and uninformative. However, as age uncertainties grow with age (0.2 dex), one cannot assign stars to a particular component of the model based on the most likely age. We must marginalize over age uncertainties, in Equation II.24. As the red clump sample is a fairly young population (with an age distribution that peaks around 2 Gyr, see Figure II.3), the total likelihood will be dominated by terms from younger stars.

We start using Bayes' rule on

$$
\begin{aligned}
p([\mathrm{Fe/H}], \tau \mid R, \mathbf{p_m}) &= \frac{p([\mathrm{Fe/H}], \tau, R \mid \mathbf{p_m})}{p(R \mid \mathbf{p_m})} \\
&= \frac{p(\tau \mid \mathbf{p_m}) \cdot p([\mathrm{Fe/H}], R \mid \tau, \mathbf{p_m})}{p(R \mid \mathbf{p_m})}.
\end{aligned}
\tag{II.11}
$$

And we will now construct both the numerator and the denominator as two distinct models, summarized respectively in Figures II.7 and II.8. The numerator is the joint distribution of all data given the model parameters $p([\mathrm{Fe/H}], \tau, R \mid \mathbf{p_m})$. But as we do not model the spatial selection function of APOGEE, we should keep the Galactocentric radius R as given, hence the ratio with $p(R \mid \mathbf{p_m})$. The first term in the numerator of Eq II.11 is the age distribution of red clump stars, given in Eq II.2. The second term in the numerator and the denominator are constructed below. We separate stars younger and older than 8 Gyr in two terms p_y (young) and p_o (old), as we believe that the model of secular evolution we have laid out is only applicable to $\tau < 8$ Gyr. But, in the presence of significant age uncertainties, we

must acknowledge the existence of older stars in the Galactic disk without making assumptions on their possible birth radii, enrichment history, and subsequent radial orbit migration. For those we specify a less informative metallicity-radius distribution

$$p([\text{Fe/H}], R \mid \tau, \mathbf{p_m}) = \begin{cases} p_y([\text{Fe/H}], R \mid \tau, \mathbf{p_m}) & \tau \le 8\text{Gyr} \\ p_o([\text{Fe/H}], R \mid \tau, \mathbf{p_m}) & \tau > 8\text{Gyr}, \end{cases} \quad (\text{II.12})$$

where the young term $p_y([\text{Fe/H}], R \mid \tau, \mathbf{p_m})$ is derived by marginalizing the joint distribution of metalliticy and birth radii at given time (the age-metallicity-radius relation) $p([\text{Fe/H}], R_0 \mid \tau, \mathbf{p_m})$ over stellar birth radii R_0. Using $p([\text{Fe/H}] \mid R_0, R, \tau, \mathbf{p_m}) = p([\text{Fe/H}] \mid R_0, \tau, \mathbf{p_m})$, i.e. the metallicity of stars born at a given birth radius R_0 and time τ does not depend on their present-day position R, we marginalize

$$\begin{aligned} p_y([\text{Fe/H}], R \mid \tau, \mathbf{p_m}) = \int_0^\infty & p(R \mid R_0, \tau, \mathbf{p_m}) \\ & \times p(R_0 \mid \tau, \mathbf{p_m}) \\ & \times p([\text{Fe/H}] \mid R_0, \tau, \mathbf{p_m}) \mathrm{d}R_0, \end{aligned} \quad (\text{II.13})$$

with the three terms in the integral being the different aspects of the model. The first two terms are radial orbit migration (Eq IV.13) and the radial birth profile (Eq II.5), respectively. The third term is the metallicity at birth (a Dirac function due to the tight relation Eq IV.17, or equivalently Eq II.8), which we express as a probability distribution function for R_0: $p([\text{Fe/H}] \mid R_0, \tau, \mathbf{p_m}) = \delta(\tilde{R}_0 - R_0) \cdot |R_0'|$, with $\tilde{R}_0$ the analytical solution for the tight relation, defined in Eq II.8, and $|R_0'|$ the Jacobian term relating the distribution in [Fe/H] and $\tilde{R}_0([\text{Fe/H}], \tau)$. R_0' is defined as the inverse of the metallicity gradient

$$R_0' \equiv \frac{\mathrm{d}R_0}{\mathrm{d}[\text{Fe/H}]} = \frac{1}{\nabla[\text{Fe/H}]}.$$

The Dirac function makes the computation of the integral trivial, simply evaluating
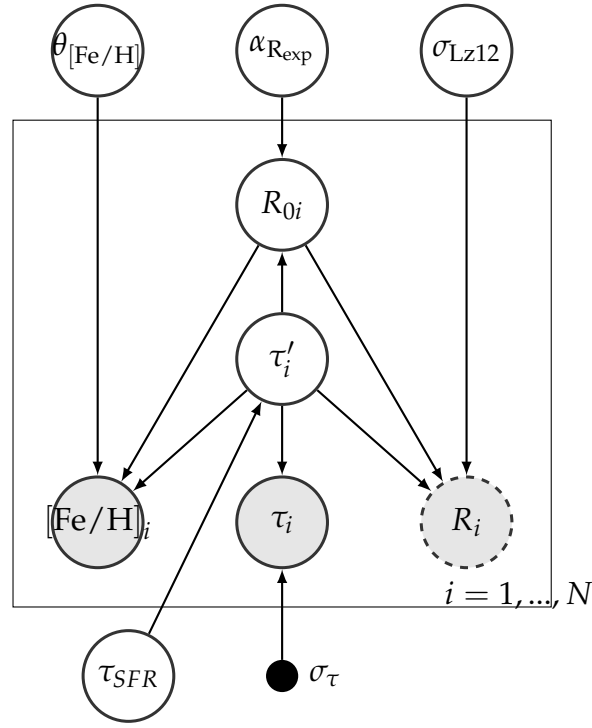
Figure II.7: Probabilistic graphical model for the joint distribution $p(\{[Fe/H]_i, \tau_i, R_i\} \mid \mathbf{p_m})$ for the < 8 Gyr Milky Way (thin) disk. Our likelihood is the ratio between this model and the model for $p(\{R_i\} \mid \mathbf{p_m})$ presented in Figure II.8. The observed quantities are in grey circles and model parameters are in white circles. The present-day Galactocentric radius R_i is in a dashed circle as a reminder that the final likelihood does not predict the present-day observed radial distribution of red clump stars. The filled black dot represents a fixed quantity, here the assumed age errors, from (Ness et al., 2016). The $\theta_{[Fe/H]}$ circle represents the three enrichment parameters $R_{[Fe/H]=0}^{now}$, $\gamma_{[Fe/H]}$, $\nabla[Fe/H]$. R_0 are birth radii, τ_i' are the true ages and τ_i the measured ages. We infer the parameters which are outside of the box, the others are marginalized-out.

the integrand at $R_0 = \tilde{R}_0$ defined in Eq II.8:

$$
\begin{aligned}
p_y([Fe/H], R \mid \tau, \mathbf{p_m}) = & \; |\tilde{R}_0'| \, p(R \mid \tilde{R}_0, \tau, \mathbf{p_m}) \\
& \times p(\tilde{R}_0 \mid \tau, \mathbf{p_m}).
\end{aligned}
\tag{II.14}
$$

All elements are spelled-out to be recast in p_y of Eq II.12, and we can now do the same exercise with p_o. Guided by the data, we presume that the old term $p_o([Fe/H], R \mid \tau, \mathbf{p_m})$ of Eq II.12 can be well described by a Gaussian distribution in metallicity and a decreasing exponential in radius. We deem this approximation sufficient for the purpose at hand: this old component is uninformative on radial orbit migration (our interest) and is constructed in order to allow us to treat the large age uncertainties of the data appropriately: with important age uncertainties,
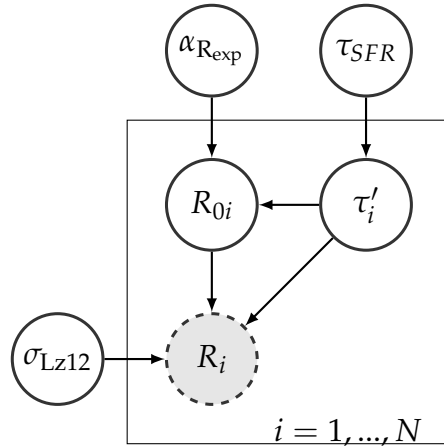
Figure II.8: Sub-model from the model shown in Figure II.7 which is used as the denominator $p(\{R_i\} \mid \mathbf{p_m})$ in the ratio of probabilities used as the likelihood in this inference (see Eq II.11 and the related text). The nomenclature is the same as in Figure II.7.

we expect a significant number of stars younger than 8 Gyr to have measured ages greater than 8 Gyr, and *vice versa*. We define

$$
p_o([\text{Fe/H}], R \mid \tau, \mathbf{p_m}) = p_o(R|\tau, \mathbf{p_m}) \\
\times p_o([\text{Fe/H}]|\tau, \mathbf{p_m}),
\tag{II.15}
$$

with a radial distribution of old stars (where we keep the variable τ given, even if there is no explicit dependency, as a reminder that this expression holds given ages greater than 8 Gyr.)

$$
p_o(R \mid \tau, \mathbf{p_m}) = \frac{1}{R_{\text{old}}} \exp(-R/R_{\text{old}})
\tag{II.16}
$$

with a scale-length R_{old}, and similarly the metallicity distribution common to all old stars,

$$
p_o([\text{Fe/H}] \mid \tau, \mathbf{p_m}) = \mathcal{N}([\text{Fe/H}], \overline{[\text{Fe/H}]}, \text{std}([\text{Fe/H}])).
\tag{II.17}
$$

The model parameters part of $\mathbf{p_m}$ here are the old stars scale length R_{old}, their mean metallicity $\overline{[\text{Fe/H}]}$ and their metallicity dispersion $\text{std}([\text{Fe/H}])$. Now, Eq II.12 can be fully written and reintegrated into Eq II.11.

Finally, we move on to the denominator in Eq II.11, which is the predicted radial

distribution of stars, and can be calculated by over time:

$$p(R \mid \mathbf{p_m}) = \int_0^{\tau_m} p(R \mid \tau, \mathbf{p_m}) p(\tau \mid \mathbf{p_m}) \mathrm{d}\tau \qquad \text{(II.18)}$$

with the radial distribution of stars being determined by radial orbit migration. Since we presume that conditions at birth are known only for $\tau \leq 8$ Gyr, we separate out older stars again:

$$p(R \mid \tau, \mathbf{p_m}) = \begin{cases} p_y(R \mid \tau, \mathbf{p_m}) & \tau \leq 8 \text{ Gyr} \\ p_o(R \mid \tau, \mathbf{p_m}) & \tau > 8 \text{ Gyr.} \end{cases} \qquad \text{(II.19)}$$

The old component $p_o(R \mid \tau, \mathbf{p_m})$ is the exponential profile introduced above in Eq II.16 with a scale-length R_{old}. The radial distribution of $\tau \leq 8$ Gyr stars is given by the model described in the above subsection. It is determined by the birth radii of stars of age τ, and by their further radial orbit migration after a time τ:

$$\begin{aligned} p_y(R \mid \tau, \mathbf{p_m}) = \\ \int_0^\infty p(R \mid R_0, \tau, \mathbf{p_m}) \, p(R_0 \mid \tau, \mathbf{p_m}) \, \mathrm{d}R_0. \end{aligned} \qquad \text{(II.20)}$$

When this expression is inserted back into Equation II.18, it leads to a double integral function (extracted in Eq II.21) of the four variables (R, τ_{SFR}, $\alpha_{R_{\exp}}$, σ_{Lz12}).

The evaluation of such function is computationally expensive: a single evaluation takes about the order of a second, making MCMC sampling on thousands of stars and tens of thousands of MCMC steps rather slow. We therefore precompute the integral

$$\int_0^8 \int_0^\infty p(R \mid R_0, \tau, \mathbf{p_m}) \, p(R_0 \mid \tau, \mathbf{p_m}) \, p(\tau \mid \mathbf{p_m}) \mathrm{d}R_0 \mathrm{d}\tau \qquad \text{(II.21)}$$

on a large number of points in the 4D space of $\vec{x} = (R, \tau_{SFR}, \alpha_{R_{\exp}}, \sigma_{Lz12})$ to interpolate it with precision 0.4% using a family of highly flexible non linear functions,

$$f(\vec{x}) = \mathbf{W_0} \tanh \left[\mathbf{W_1} \tanh(\mathbf{W_2} \vec{x} + \mathbf{b_2}) + \mathbf{b_1} \right] + \mathbf{b_0}, \qquad \text{(II.22)}$$

where $\mathbf{W_i}$ and $\mathbf{b_i}$ are matrices of coefficients found by minimizing the difference between Eq II.21 and II.22 on the pre-computed points, using a regression gradient descent algorithm. The interpolation intervals in the parameter space are chosen large enough for our analysis: $3 < R < 15$ kpc, $4 < \tau_{SFR} < 14$ Gyr, $0 < \alpha_{R_{exp}} < 1$ and $2 < \sigma_{Lz12} < 8$ kpc. Possible error propagations during the sum of log likelihood over all data (Eq II.23 just below) are discussed in section IV.4.

We can now recast all the elements spelled-out above into Eq II.11 and build the likelihood function.

The overall likelihood of all the data is given by

$$
\begin{aligned}
&\ln p_{\mathcal{L}}\left(\{[\text{Fe/H}], \tau\} \mid \{R\}, \mathbf{p_m}\right) = \\
&\sum_{i=1}^{N_{data}} \ln p_{\mathcal{L}}\left(\{[\text{Fe/H}], \tau\}_i \mid \{R\}_i, \ \mathbf{p_m}\right),
\end{aligned}
\tag{II.23}
$$

where $p_{\mathcal{L}}\left(\{[\text{Fe/H}], \tau\}_i \mid \{R\}_i, \ \mathbf{p_m}\right)$ is the likelihood of the data on one object, given the model. Our data $\{[\text{Fe/H}], \tau, R\}$ also have uncertainties, dominated by τ (we neglect those in metallicity and radius as a first approximation) and, therefore, we need to marginalize over these uncertainties. This marginalization smooths out the effects of our 8 Gyr cut: stars will have a non-zero contribution to each component, and this contribution is weighted by its possible age distribution $p_{\text{obs}}(\tau_i \mid \tau)$. Therefore, even if an old star had its age underestimated, instead of fully constraining our disk evolution model, it will contribute to both the young and the old component, which prevents from giving zero net likelihood values to the informative (young) model. This is analogous to the role of an outliers model. Of course, such non-zero contribution of old stars to the young likelihood component may have an effect on our inference, especially if their enrichment history differs significantly from that of younger stars. However, this effect should be limited by the facts that (1) red clump stars are mainly a young population, reflecting the recent history of the Milky Way disk, and (2) we are considering only low-α stars at $|z| < 1$ kpc, filtering out a large

fraction of the old stars of the red clump sample.

$$
\begin{aligned}
p_{\mathcal{L}}\left(\{[\text{Fe/H}], \tau\}_i \mid \{R\}_i, \mathbf{p_m}\right) = \\
\int p_{\text{obs}}(\tau_i \mid \tau) \cdot p([\text{Fe/H}]_i, \tau | R_i) d\tau,
\end{aligned}
\tag{II.24}
$$

where τ_i, $[\text{Fe/H}]_i$ and R_i are the measured age, metallicity and Galactocentric ra-
dius (the values in our red clump catalog) and τ is the potentially true age of the
star. Here, $p_{\text{obs}}(\tau_i \mid \tau)$ is the error distribution in age: the probability to measure an
age τ_i given that the possible true stellar age is τ and measurement uncertainties.
This distribution is a Gaussian function in log space, such that for $a = \log_{10}(\tau)$,
$a_i = \log_{10}(\tau_i)$, $\sigma_{a_i} = 0.2$ dex the error in age, we have $p_{\text{obs}}(a_i \mid a, \sigma_{a_i}) = \mathcal{N}(a_i, a, \sigma_{a_i}^2)$.
As this noise model may underestimate the errors of very young stars, we apply a
different model for stars younger than 0.5 Gyr where errors are Gaussian in linear
space with a standard deviation of $\sigma_{\tau_i} = 200$ Myr, $p_{\text{obs}}(\tau_i \mid \tau, \sigma_{\tau_i}) = \mathcal{N}(\tau_i, \tau, \sigma_{\tau_i}^2)$.
Both noise models are normalized to physically plausible age ranges: between the
theoretical minimum red clump age (Figure II.3) and the age of the Universe. Inte-
gral II.24 gets evaluated separately for each data point (given each $\mathbf{p_m}$). In practice,
we do not need to compute this integral over all the terms in the expression of the
distribution $p([\text{Fe/H}]_i, \tau | R_i)$ (Eq II.11), but only its numerator because the denom-
inator does not depend on age τ (hence, we do not propagate the interpolation
errors of the term in Eq II.21 along this marginalization over age uncertainties).

II.3.4 Sampling the Parameter *PDF*

We apply Bayes' theorem on the likelihood function constructed with the analytical
disk evolution model described in Section II.3, and APOGEE red clump giants, to
express a posterior probability distribution on the global efficiency of radial orbit
migration.

The posterior probability distribution on the model parameters is given by

$$p_{po}(\mathbf{p_m} \mid \{[\text{Fe/H}], \tau, R\}) =$$
$$\frac{p_{\mathcal{L}}(\{[\text{Fe/H}], \tau\} \mid \{R\}, \mathbf{p_m}) \cdot p_{pr}(\mathbf{p_m})}{p_{pr}(\{[\text{Fe/H}], \tau\})}, \tag{II.25}$$

where we presume $p_{pr}(\{[\text{Fe/H}], \tau, R\})$, the evidence term that does not depend on the model parameters, to be a constant. We sample the vector of the 9 free parameters $\mathbf{p_m} \equiv \{ \tau_{SFR}, \alpha_{R_{\exp}}, R^{\text{now}}_{[\text{Fe/H}]=0}, \tau_{[\text{Fe/H}]}, \nabla[\text{Fe/H}], \sigma_{Lz12}, \overline{[\text{Fe/H}]}, \text{std}([\text{Fe/H}]), R_{\text{old}} \}$, by means of Equation II.1, and then marginalize over all nuisance parameters $\{ \tau_{SFR}, \alpha_{R_{\exp}}, R^{\text{now}}_{[\text{Fe/H}]=0}, \tau_{[\text{Fe/H}]}, \nabla[\text{Fe/H}], \overline{[\text{Fe/H}]}, \text{std}([\text{Fe/H}]), R_{\text{old}} \}$ to extract a posterior distribution for radial orbit migration $p_{po}(\sigma_{Lz12} \mid \{[\text{Fe/H}], \tau, R\})$. This is done using the MCMC sampler package Emcee (Foreman-Mackey et al., 2013). In practice, we first perform a maximum likelihood estimation of the parameters using the Nelder-Mead method (Nelder & Mead, 1965), and sample initial walker positions for 20 Markov chains within small intervals around the best fit results. To compromise the precision of our results and computational time, we perform several fits on different subsets of stars. For each fit, we use a subset of 1500 stars from our low $[\alpha/\text{Fe}]$ sample, after having selected further those well in the Galactic disk with $|z| < 1$ kpc. Each chain is sampled with 7000 iterations. We then marginalize over the nuisance parameters to infer the radial orbit migration strength σ_{Lz12}. Our prior on σ_{Lz12} is set by the restricted space where the interpolation of equation II.21 is valid: $2 < \sigma_{Lz12} < 8$ kpc. Other priors are $0 < \alpha_{R_{\exp}} < 1$, $3 < \tau_{SFR} < 12$ Gy. The priors on other model parameters are also flat, we only constrain distances and durations to be positive. As can be seen in Figure II.9, the posteriors are tightly constrained even though we had fairly broad priors.

II.4   Results

We now summarize the results obtained from fitting our disk evolution model to the low-α APOGEE red clump data, described in Section IV.2. The maximum likelihood estimates (Eq II.23) for the model parameters are presented in Table IV.2. All 20
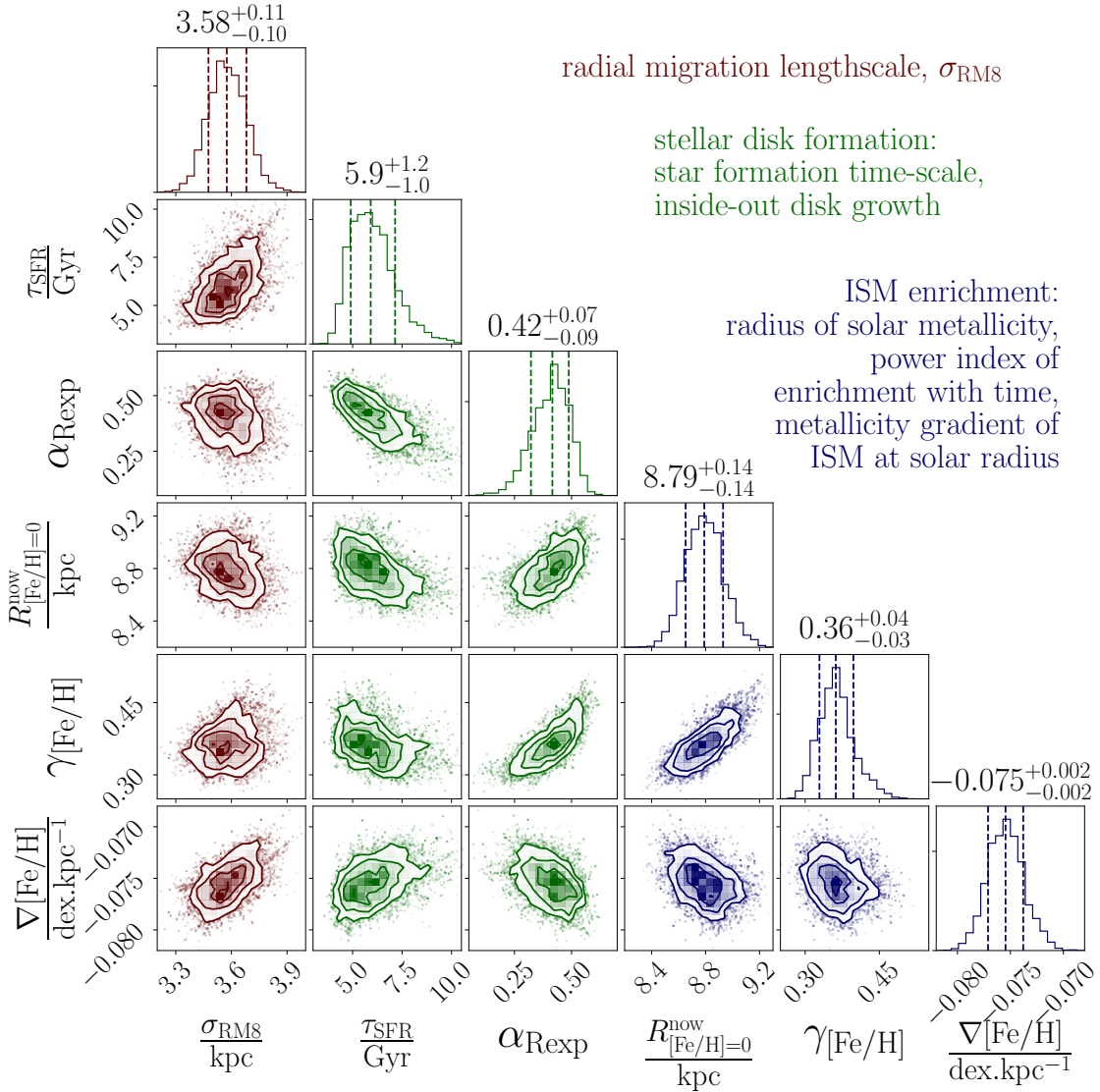
Figure II.9: Posterior distribution of the 6 parameters of the Galactic disk evolution model. From left to right: the main parameter of interest for radial orbit migration strength σ_{Lz12} in kpc (Eq IV.13), followed by the nuisance parameters: star formation time-scale τ_{SFR} in Gyr (Eq II.2), the parameter characterizing inside-out disk growth α_{Rexp} (the Miky Way disk was approximately 40% smaller at its possible formation 8 Gyr ago, Eq II.5). Then come the three parameters characterizing the enrichment of the interstellar medium (ISM) as a function of time and galactic radius (Eq IV.17): the radius where the ISM metallicity is solar $R^{\text{now}}_{[\text{Fe/H}]=0}$ in kpc, the power index characterizing the gradual chemical enrichment of the ISM with time $\gamma_{[\text{Fe/H}]}$, the metallicity gradient of the ISM at the solar radius $\nabla[\text{Fe/H}]$ in dex kpc^{-1}. A complete version of the posterior in the 9D parameter space (that includes the parameters of the less informative component for old stars) is in appendix.

Table II.2: Best fit MLE parameters

p_m	Best fit	Description
τ_{SFR}/Gyr	6.8	Star formation time-scale
$\alpha_{R_{\mathrm{exp}}}$	0.3	Inside-out growth
$R^{\mathrm{now}}_{[\mathrm{Fe/H}]=0}/\mathrm{kpc}$	8.7	$R([\mathrm{Fe/H}]=0, \tau=0)$
γ	0.3	Enrichment power index
$\nabla[\mathrm{Fe/H}] /\mathrm{dex\ kpc}^{-1}$	-0.075	$[\mathrm{Fe/H}]_{\mathrm{ISM}}$ gradient
$\sigma_{\mathrm{Lz12}}/\mathrm{kpc}$	3.5	radius migration strength
$R_{\mathrm{old}}/\mathrm{kpc}$	2.5	Scale-length old disk
$\overline{[\mathrm{Fe/H}]}/\mathrm{dex}$	-0.05	Mean metallicity $\tau > 8$ Gyr
$\mathrm{std}([\mathrm{Fe/H}])/\mathrm{dex}$	0.15	std metallicity $\tau > 8$ Gyr

chains of the MCMC converged with 7000 iterations on subsets of 1500 stars out of the 17,500 low-α available stars of the sample. We show the posterior distributions for the parameters of immediate interest in Figure II.9; it shows that all parameters are well constrained by the data, with some covariances but no degeneracies. The full version of the figure, that shows the exploration of the whole parameter space including all nuisance parameters, can be found in Figure II.16 in the Appendix.

We first focus on quantifying on radial orbit migration, show the model calculation for the best fit parameters, and then comment briefly on the other parameters.

II.4.1   Radial orbit migration

Fig II.9 shows that the inferred strength of radial orbit migration is very well constrained. Marginalizing the posterior distribution over the nuisance parameters gives an estimate of σ_{Lz12} of about 3.6 ± 0.1 kpc (see Figure II.9). This represents the length-scale over which the oldest stars (8 Gyr) have spread around their birth radii. This radius spread could be caused by either churning, or blurring. But we know from the stellar radial velocity dispersion in the Solar neighborhood that orbit eccentricities (blurring) have a radial amplitude of about 1 kpc. Therefore, we infer that churning needs the dominant mechanism in explaining the measured value of σ_{Lz12}. In Fig II.10, our radial orbit migration estimate $\sigma(\tau) = 3.6\,\mathrm{kpc}\sqrt{\tau/\,8\mathrm{Gyr}}$ is illustrated by sampling from posterior distribution, i.e. the MCMC chains in Figure II.9). This result quantifies that the present-day radius is a poor proxy for the birth
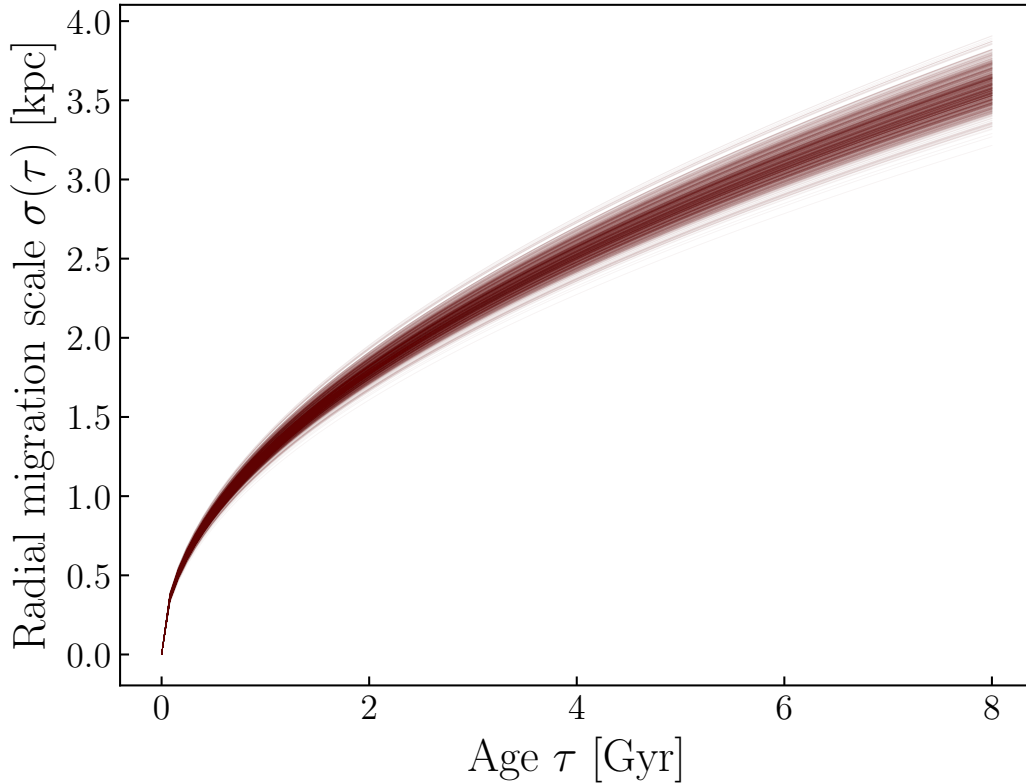
Figure II.10: Radial orbit migration strength inferred in this study with respect to stellar ages.
radius, compared to the metallicity at given age.

Mathematically, σ_{Lz12} quantifies the distance between the present Galactocentric radius of a star and the birth radius *expected* from the global model fit. Whenever the quantity of interest is a "scatter" one must explore to which extent it is attributable to other model shortcomings. We have therefore explored model variants and have found that this radial orbit migration strength estimate is rather robust. We exercised MCMC estimates holding other model parameters fixed to diverse values, leaving the radial orbit migration strength estimate robust.

II.4.2 Other parameters

But along with the radial orbit migration strength, the model also constrains all other aspects: star formation history, inside-out growth, and the enrichment history

of the Galactic disk. While these are mere nuisance parameters when constraining radial orbit migration strength, they are informative about the Galactic disk evolution over the last 8 Gyr.

Star formation history: τ_{SFR} The data favor a star formation time-scale $\tau_{SFR} = 6 \pm 1$ Gyr for the Galactic low $[\alpha/\text{Fe}]$ disk. This value seems rather low given prior expectations of an extended star formation in the thin disk. We find that this estimate depends strongly on the assumed form of the age distribution at young ages (< 1 Gyr); and it is sensitive to the details of the selection: e.g., we find a larger star formation time-scale if we select $|z| < 1$ kpc stars rather than if we select $|z| < 1.5$ kpc; this should be expected as the proportion of young stars is larger near the mid-plane. Given the age distribution varies with Galactocentric radius and height above the plane, the uneven APOGEE pointings could induce some τ_{SFR} bias for which we do not correct. Additionally, this estimate is degenerate with the old stars scale-length parameter R_{old} (Figure II.16 in Appendix). This is due to the spatial selection function limited to 5 kpc from the center of the disk: predicting a fast star formation (many old stars) with a small scale-length is, according to this model, roughly equivalent to predicting a slow star formation (less old stars) but more extended in the disk, preserving the overall observed ratio of young to old stars (the Galactocentric radius ranges are 5-14 kpc: we do not see an old stellar population when it is well concentrated in the inner disk). This is because these two scenario will predict the same amount of old stars in the *observed* regions of the Galactic disk. However, even if our estimate of τ_{SFR} is questionable, we note that (1) this does not seem to affect our radial orbit migration strength estimate, and (2) the observed age distribution of red clump stars is well reproduced, as illustrated in Figure II.11 which shows a comparison of the observed age distribution of red clump stars to the one predicted by the model (the details of this procedure are described in subsection II.4.3.2).

Inside-out growth: $\alpha_{R_{\text{exp}}}$ The growth (i.e. star formation) of the Galactic disk was modelled by the scale-length parameter $R_{\text{exp}}(\tau) = 3\text{kpc}(1 - \alpha_{R_{\text{exp}}} \frac{\tau}{8\text{Gyr}})$ of newborn
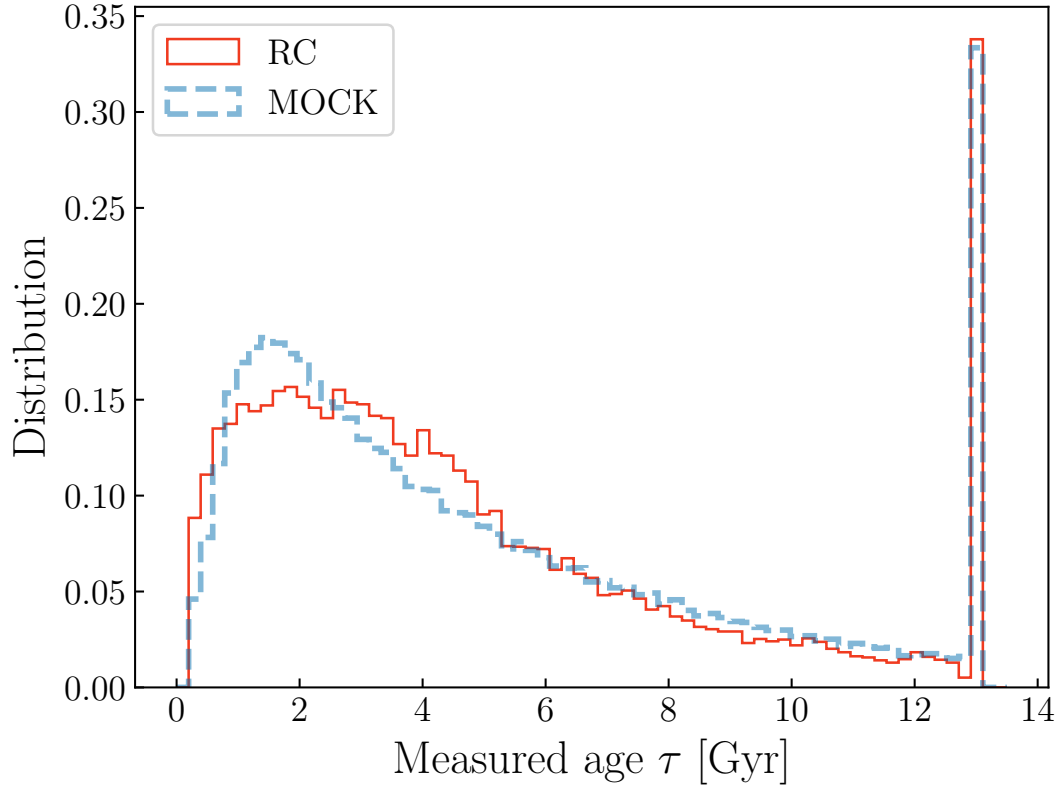
Figure II.11: Age distribution of the low-α APOGEE red clump stars sample: observed (red) and predicted (blue) by the model evaluated at the best MCMC parameters and with reproduction of the effects of the spatial selection function (subsection II.4.3). The peak of stars at 13.4 kpc are stars with initially measured age greater than the age of the Universe, of which the age was brought back to this exact value, see Ness et al. (2016).

stars. We find $\alpha_{R_{exp}} = 0.42 \pm 0.09$. This implies that the disk was about 40 % smaller 8 Gyr ago. This is consistent with observations of high redshift disk galaxies (e.g van Dokkum et al., 2013). However, we report that the estimate for this parameter was very sensitive to the assumed functional form for the metallicity profile combined with the age distribution, with covariances with τ_{SFR}.

Metallicity profile and enrichment history: $\{R^{now}_{[Fe/H]=0}, \nabla[Fe/H], \gamma_{[Fe/H]}\}$ The metallicity profile of the cold gas in the disk is described in our model by a simple straight line in radius with a negative gradient. The two model parameters that characterize the metallicity profile are $R^{now}_{[Fe/H]=0}$: the Galactocentric radius at which the star-forming gas metallicity is solar, corresponding to an arbitrary zero point,
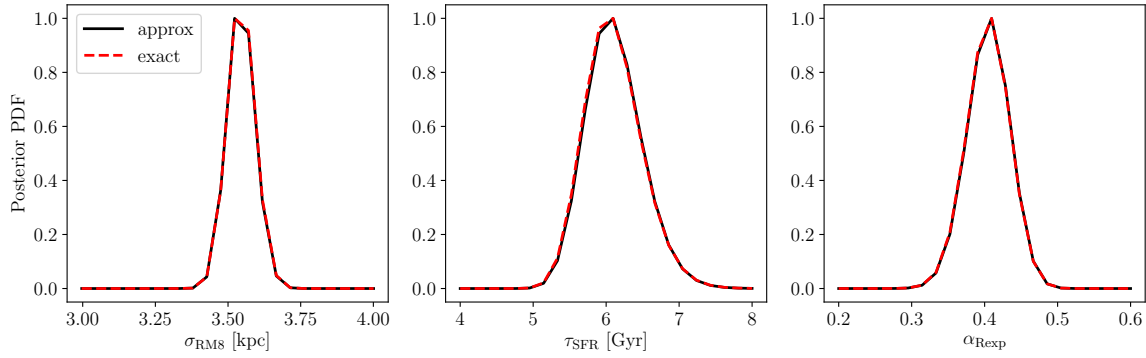
Figure II.12: Comparison between the posteriors that contain an approximated term in black (for computational optimization purpose) and the exact posteriors in dashed red (not normalized). We take cuts in the posterior probability density in the three dimensions that were approximated in Eq II.21 and compute them on 22 points for each panel. From left to right: σ_{Lz12}, τ_{SFR}, $\alpha_{R_{exp}}$. All other parameters in $\mathbf{p_m}$ were taken at their best MCMC value. The black and red lines overlap well: the interpolation errors, even after a sum of log likelihoods over 1500 stars, propagate slowly and have no effect on where the posterior maximum is located, nor on the width of the distribution. This gives us confidence that the 'best MCMC' parameters and their corresponding errors were evaluated well enough, without dramatic effects from the interpolation of Eq II.21.

and $\nabla[\text{Fe/H}]$: the present-day metallicity gradient at $R^{\text{now}}_{[\text{Fe/H}]=0}$. As these are two "present-day" properties, the youngest stars of our sample are expected to provide the strongest constraints on these parameters. We find the radius of solar metallicity to be about $R^{\text{now}}_{[\text{Fe/H}]=0} = 8.8 \pm 0.2$ kpc. The metallicity gradient $\nabla[\text{Fe/H}]$ is found to be $-0.075 \pm 0.002\text{dex.kpc}^{-1}$. The values of these two parameters are consistent with the left panel of Figure II.2, for which we plot the metallicity profile of the young red clump stars. The densest region for [Fe/H]= 0 dex is close to 8kpc. We note that Sanders & Binney (2015) find different results with their model on the Geneva-Copenhagen Survey data (Nordström et al., 2004), with the radius of solar metallicity of 7.37 kpc and a shallower metallicity gradient of -0.064 dex · kpc^{-1}, and Genovali et al. (2014) measure a gradient of $-0.060 \pm 0.002\text{dex} \cdot \text{kpc}^{-1}$. More recently, Anders et al. (2017) measured the stellar metallicity gradients for red giants in different stellar age bins, and found about $-0.058 \pm 0.008\text{dex} \cdot \text{kpc}^{-1}$ for stars younger than 1 Gyr.

The enrichment history at any radius of the disk is described in our model by a power law of time with index $\gamma_{[\text{Fe/H}]}$. The best MCMC value is $\gamma_{[\text{Fe/H}]} = 0.36 \pm 0.04$. The metallicity of the interstellar medium is plotted with respect to look-back time in Figure II.5 (using the MLE results). This result is different from (semi) analytic

models used previously in the literature (Schönrich & Binney, 2009a,b; Sanders & Binney, 2015), where the enrichment of the interstellar medium generally increases faster at early times and is almost flat at late epochs. Here, we find that the gas metallicity grows continuously at all radii up to the present day. This is, however, very much consistent with Milky Way-like simulations (Grand et al., 2018), and further tests with different metallicity profile forms would be interesting.

The nuisance model for the disk before 8 Gyr ago   We built a less-informative "nuisance" model the Milky Way disk older than 8 Gyr, to avoid sharp age cuts. But these stars enclose information on the star formation history of the Milky way: in essence, they help to constrain the τ_{SFR} parameter only. The other three model parameters that correspond to our old stars model are $\overline{[Fe/H]}$, std($[Fe/H]$), R_{old}. The mean and variance of the old stars metallicity appear to be robust estimates and do not show degeneracies with other parameters. The MCMC exploration shows R_{old} to be about 2.4 kpc (see the full corner plot in appendix, Figure II.16). This value is physically coherent with our prior knowledge on the disk. We note that this R_{old} parameter, which we model as the "old disk scale-length", is strongly covariant with τ_{SFR}: τ_{SFR} sets the relative fraction of old and young stars in the Milky Way disk, and the scale-length R_{old} determines the present-day radial distribution of old stars. But the *observed* relative fraction of old and young stars in the data is fixed. In turn, lower values for τ_{SFR} (predicting more old stars than observed) lead the model fitting procedure to compensate by placing the overpredicted number of old stars at Galactocentric radii not covered by the survey (e.g. the inner 5 kpc). This results in a small old disk scale-length estimate R_{old}. Conversely, higher values for τ_{SFR} (less old stars in the disk) need the fitting to compensate by placing more old stars at Galactocentric radii where data are seen (5 – 14 kpc) and this results in a large scale-length estimate R_{old}. This is an expected short-coming when fitting directly a scale-length without accounting explicitly for spatial selection effects.

This parameter covariance could also be a manifestation that the scale-length of the disk is a function of the ages of the stellar population used to determine it: old stars are more concentrated in the inner disk than young stars (Bovy et al., 2012).
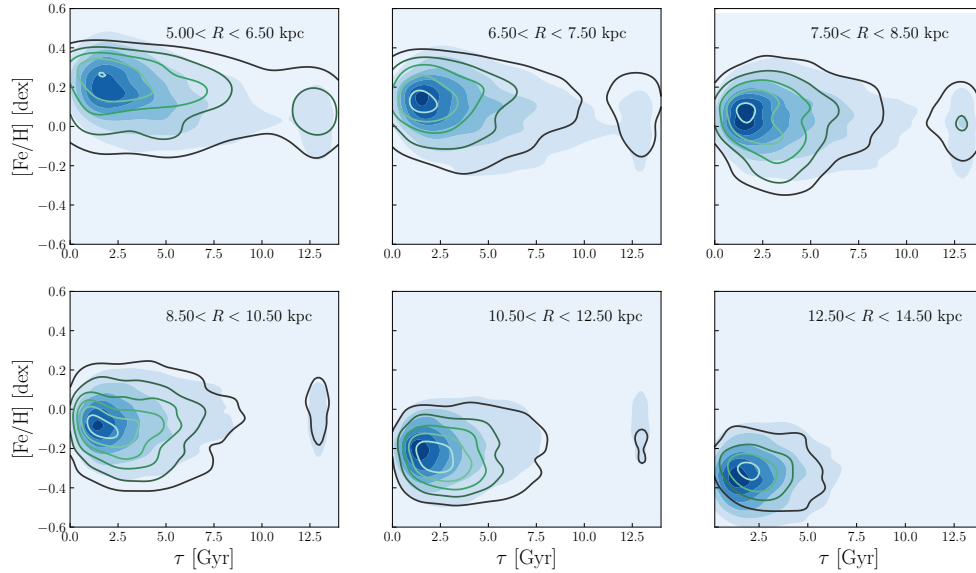
Figure II.13: Density of red clump stars in the age–metallicity plane at six Galactocentric radii: 6, 7, 8, 9, 11 and 13 kpc. The model predictions using the best MCMC values are represented by the shaded background. Isolines on the foreground represent smoothed isocontours of [Fe/H]–τ distributions of red clump stars data in the different radial bins. The scatter in age–metallicity is well reproduced through the effect of radial orbit migration. The over-density (dark area) predicted by the model (background) for ages near 2 Gyr is the effect of the selection of red clump population (see Figure II.3 for their age distribution that peaks near 2 Gyr).

II.4.3   Tests and verifications

In this section, we examine some of the model and methodological shortcomings or restrictions that could bias our inferences, such as the approximations made to minimize the computational cost of likelihood evaluations and the convergence of the MCMC. We further address the robustness of the radial orbit migration strength estimate. Finally, we confront the predictions of our model evaluated at the best MCMC values in the space of the data.

II.4.3.1   Technical verifications

The term $p(R \mid \mathbf{p_m})$ in likelihood function (Eq II.21, represented in Figure II.8), was interpolated. Interpolation errors on a set of 20,000 test points are less than 0.4%. To see whether interpolation errors have propagated during the overall product of

the likelihood over the 1500 stars used for inference, we choose slices in the parameter space at the best MCMC values, and compare the (expensive) true likelihood evaluations to the approximated values. The relative differences are small, as can be seen in Figure II.12 that shows three slices of the posterior distribution. Additionally, the generation of mock data and the model itself $p([\text{Fe/H}], R, \tau | \mathbf{p_m})$ do not rely on the approximation in $p([\text{Fe/H}], \tau | R, \mathbf{p_m})$, so comparisons between the model prediction and the data in Section II.4.3.2 also give us confidence that the posterior was approximated well enough for our purpose.

To address the question of the MCMC convergence and the exploration of the parameter space, we have run several more MCMC chains, where the walkers were started in more extended ranges than just the MLE neighborhood. The results remained close to those presented in Fig II.9. We have also performed MCMC on three different random batches of 1500 stars. We found that radial orbit migration strength σ_{Lz12}, the present-day cold gas metallicity gradient at solar radius $\nabla[\text{Fe/H}]$, and the radius of solar metallicity in the interstellar medium $R^{\text{now}}_{[\text{Fe/H}]=0}$ were extremely well constrained. However, the star formation time-scale τ_{SFR} showed some variability (the best τ_{SFR} varied between 5 Gyr and 7.5 Gyr) depending on the sets of stars used, but as discussed in the subsection above, this parameter showed to be sensitive to biases and has 1 Gyr uncertainty. Finally, we calculated the potential scale reduction factor, estimating the ratio of variances within single chains and between several chains to about < 1.03 and the autocorrelation time, to 180 steps (where the MCMC ran 7000 iterations).

II.4.3.2 Model predictions in the data space

We generated a mock data set to compare with APOGEE red clump sample, using rejection sampling on the different aspects of the model evaluated at the best MCMC values. For comparison with APOGEE data, we reproduced the age distribution of red clump stars using the same functional form as in (Bovy et al., 2014), and introduced some scatter for the age uncertainties using our noise model (a Gaussian of width 0.2 dex in $\log_{10}$ age, and a floor of $\sigma_\tau = 200$ Myr uncertainties for stars younger than 0.5 Gyr). We imitated the possible effect of the radial selec-
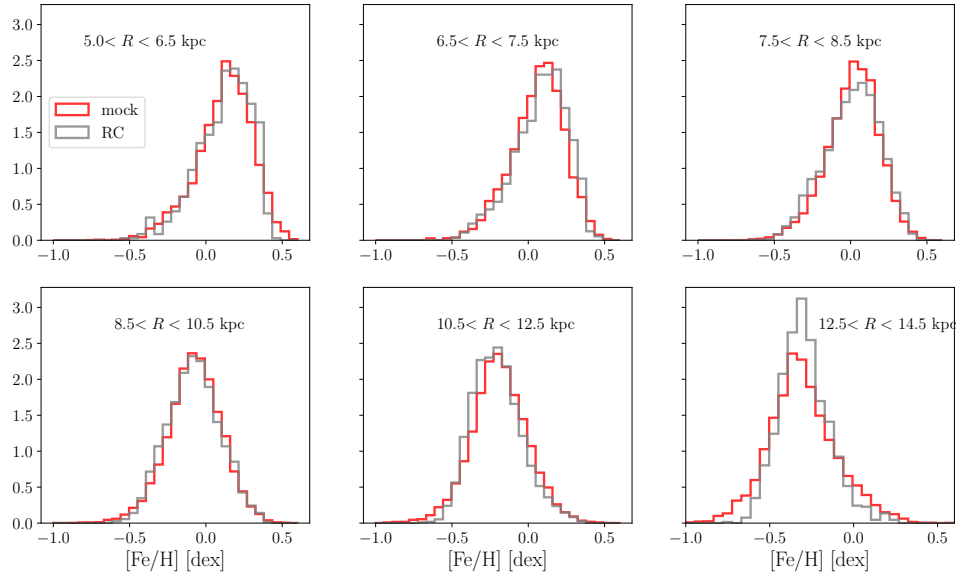
Figure II.14: Metallicity distribution functions (MDFs) at six Galactocentric radii: 6, 7, 8, 9, 11 and 13 kpc. The model predictions using the best MCMC values are represented by the red histograms. Red clump stars MDFs are shown in grey. The metallicity distribution functions are well reproduced and a metallicity gradient is visible (shift of the MDFs maxima to lower metallicities as R increases), except for the outer disk where the data show the limitations due to the rigidity of our model.

tion function in our data set using importance sampling (thereby reproducing the radial distribution of stars in our data set). This is a relevant test to do, as inference of the parameters was performed only on a small fraction of the overall catalog: the MCMC was performed (multiple times) on 1500 low-α stars randomly selected in the red clump catalog. Asking if the model can describe the rest of the 17,500 stars is therefore an interesting test. We show the results in three different plots allowing data comparison. First, we map the age–metallicity plane $p([\mathrm{Fe/H}], \tau | R)$ with contours of both our mock data and the APOGEE red clump sample in different radial bins, see Figure II.13. The observed trends are well reproduced in the Solar neighborhood and inner disk, but the last panel (13 kpc) shows that the model predicts a distribution broader (in metallicity, so in the vertical direction in Figure II.13) than the observed distribution. We suspect that the main differences between our predictions and the data come either from our restrictive model for the evolution of metallicity gradient, or from the fact that radial orbit migration strength could

depend on radius whereas we fitted a global value. The effect of the metallicity profile will be investigated in the subsection II.4.3.3.

Secondly, we integrate the age–metallicity plane $p([\text{Fe/H}], \tau \mid R)$ with respect to age to show the metallicity distribution functions at given radii $p([\text{Fe/H}] \mid R)$. These distribution functions are well reproduced in most of the disk, showing the expected positive skewness appearing due to radial orbit migration (Hayden et al., 2015; Loebman et al., 2016; Toyouchi & Chiba, 2018). The difference between observed and predicted metallicity distribution function at 13 kpc is more obvious here.

Finally, we compare the prediction in the radius – metallicity plane; in Fig II.15, where the radial spread at fixed metallicity clearly increases with age at similar rates both for the observed and mock data; and the overall metallicity gradient and the broadening of distributions with time seems to be well reproduced. At young ages, the spread of radii at given metallicity is slightly underestimated by the model. This is because (1) our model assigns any metallicty scatter at given radius and age to radius migration, and at young ages, the probability distribution of a star tends to a Dirac function (Eq IV.13) and (2) we neglected measurement errors in metallicity. We note that if star clusters are intrinsically homogeneous but data show additional metallicity spread at young ages for a given Galactocentric radius, azimuthal variations of metallicity could be probed by adding one more parameter accounting for scatter in the metallicity-radius-age relation.

II.4.3.3 Model variant

The tests presented above showed that (1) the fitting procedure went well for most parameters and the model describes the observations well for most of the Galactic disk, (2) the estimate of radial orbit migration strength is robust, but (3) the model does not reproduce the outer disk observed metallicity distribution functions. This can be interpreted in several ways: (a) The metallicity profile functional form that we assumed is rigid: it describes a straight line for which we fit the gradient $\nabla[\text{Fe/H}]$, the zero point (after translation of $R^{\text{now}}_{[\text{Fe/H}]=0}$) and the time evolution of the zero point $\gamma_{[\text{Fe/H}]}$. But the gradient itself could evolve with time, as pointed
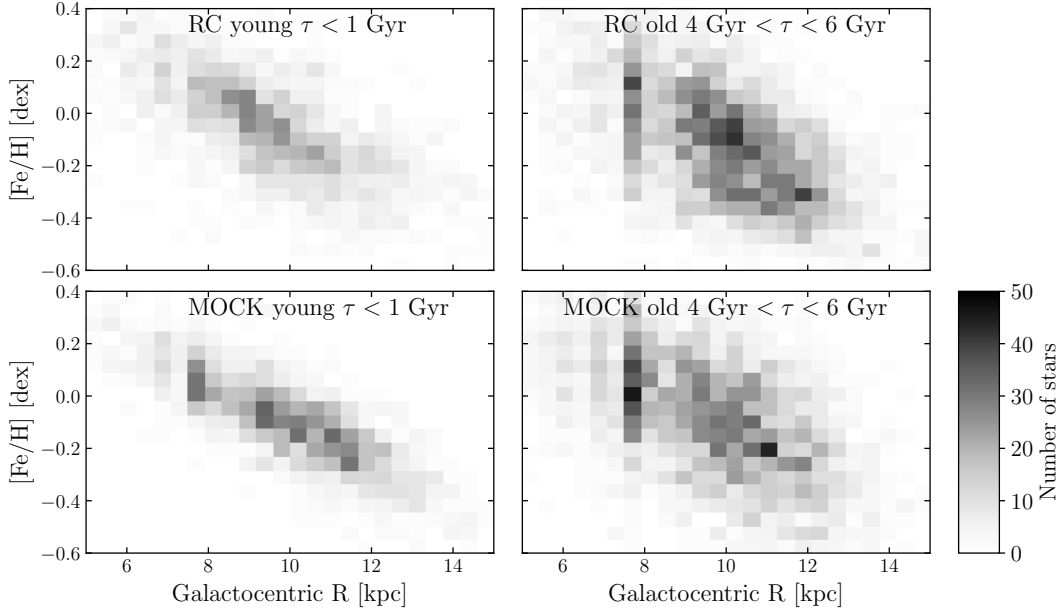
Figure II.15: Number density distribution of red clump (RC) stars (top) and mock data (bottom) in the plane of metallicity ([Fe/H]) and Galactocentric radius, for two ages bins: young stars (less than 1 Gyr, left), and older stars (measured age between 4 and 6 Gyr, right). The total number of mock stars equals the total number of red clump stars.

out in Minchev et al. (2018); Pilkington et al. (2012); Wuyts et al. (2016). Or the assumption that the metallicity profile is well described by straight line could be a too simple extrapolation of the observed gradients. Sanders & Binney (2015) used a different functional form describing a decreasing exponential in radius:

$$[\text{Fe/H}] = F_m\Big(1 - \exp(-\frac{-\nabla[\text{Fe/H}](R - R^{\text{now}}_{[\text{Fe/H}]=0})}{F_m})f(\tau)^1\Big) \qquad (\text{II.26})$$

We tested this form with several MCMC procedures, and the estimate of radial orbit migration with this model was $\sigma_{\text{Lz12}} = 4.0 \pm 0.1$ kpc, which remains close to our current result and confirms the robustness of the estimate of σ_{Lz12} in the present study. Additionally, the outer disk was very well described by mock data from a fit to this model. However, the model predictions in the inner disk were problematic: we systematically overestimated the metallicity of stars born in the inner disk.

---

[1]with a different enrichment prescription $f(\tau)$, which we also tested separately

Sanders & Binney (2015) reported the same high metallicity trend while modelling the Solar neighborhood. This gives us confidence that the metallicity profile description is a key ingredient in such modelling, and any model-induced rigidity can affect the results significantly (here: reproducing the metallicity distribution functions, even though the estimate of radial orbit migration strength was affected by less than 15%). (b) Another interpretation for the disagreement between model predictions and observed metallicity distribution at 13 kpc could be that radial orbit migration occurs differently at different strengths at different radii. We note we used only one global parameter to describe radial orbit migration over the whole disk, and that outer disk stars are not well described by our global fit, suggesting that a σ_{Lz12} is a spatial average of a Galactocentric radius-dependent radial orbit migration strength.

II.5 Discussion and conclusions

II.5.1 Summary and implications

In this study we have quantified the global efficiency of radial orbit migration in the Galactic disk. We have built an analytical disk evolution model, in good part inspired by Sanders & Binney (2015), which combines the distribution of star formation in radius and time with the chemical enrichment of the ISM, and with subsequent diffusive migration of the stars' orbital radii. Our model does not attempt to differentiate explicitly whether changes in the orbital radius are to be attributed to churning or blurring.

We have applied this to a set APOGEE red clump stars with age estimates, a large sample with precise distances (covering $5 \text{ kpc} \lesssim R \lesssim 14 \text{ kpc}$) and metallicities; this is the first time that such a large and radially extensive data set with consistent estimates of [Fe/H] and τ has been available. We sidestepped the complex spatial selection function of this survey and accounted for the 0.2 dex age uncertainties.

This has enabled for the first time an estimate of the overall radial orbit migration efficiency throughout the Galaxy, using $\{R, [\text{Fe/H}], \tau\}_i$. Previous studies

of radial migration focused on the Solar neighborhood (Sanders & Binney, 2015, Geneva-Copenhagen Survey data). Other studies of large radial extent in the Galactic disk, using e.g., APOGEE, had focused mainly on recovering the present day stellar metallicity distribution functions without the explicit use of stellar ages (Hayden et al., 2015; Toyouchi & Chiba, 2018). The model draws its constraints from the mean metallicities at each age and (present-day) radius, and from the spread of these metallicities (growing with age).

Our basic result is that APOGEE data tell us quite directly in this modelling context that radial orbit migration in the Galactic (low-α) disk is strong, $\langle |R(\tau) - R_0| \rangle \approx 3.6 \text{ kpc} \sqrt{\tau/8 \text{ Gyr}}$. This means that the characteristic distance over which stars migrate over the age of the disk is comparable to the half-mass radius of the Milky Way disk. Qualitatively, this has of course been implied by a number of earlier studies, (e.g., Schönrich & Binney, 2009a); and it has been implied by numerical studies of disk dynamics (e.g., Roškar et al., 2008c; Minchev & Famaey, 2010b). But a stringent and global modelling-based estimate of this efficiency from stellar data across the Galactic disk had not been explored before.

This result has a number of astrophysical implications. First, it tells us that for disk stars older than a few billion years, the current radius is not a particularly good indicator of the stars' birth radii. The combination of age and metallicity should be a better predictor of R_0.

For example, the Sun's age (4.6 Gyr) and [Fe/H]$\equiv 0$ implies in our model context that it was born at 5.2 ± 0.3 kpc: it has migrated outward by about 3 kpc since. While it is true that [Fe/H]$_{\text{now}}(R_\odot) \approx 0$ dex, the continuous ISM enrichment at all radii does not imply $R_\odot \approx R_{\text{birth}}$. This quite precise R_{birth}(Sun) estimate is in agreement with the broad prediction from chemo-dynamical simulations of Minchev et al. (2013) (between 4.4 and 7.7 kpc), but has 2 kpc difference with the recent results of Minchev et al. (2018) (7.3 $\pm$ 0.6 kpc). Nieva & Przybilla (2012) derived analogous constraints from chemical evolution arguments and data in the Solar neighbourhood, inferring a birth radius between 5 and 6 kpc. These chemical evolution arguments are in seeming tension with Solar birth location predictions based on backward integration of Martínez-Barbosa et al. (2015), finding that the

Sun should come from the outer disk rather than from the inner disk.

Further, our results show and confirm that – even in the absence of any significant violent relaxation in the last ~ 8 Gyr – the stellar distribution in the Galactic disk experiences significant "dynamical memory loss"; the angular momentum of stars in the disk is not even approximately conserved, though many of these stars may now still be on near-circular orbits. The value of σ_{Lz12}, when combined with the radial velocity dispersion of the disk, implies that churning is a considerably stronger effect than blurring in the Galactic disk.

We derived these results without having to drawing on detailed chemical tagging (Freeman & Bland-Hawthorn, 2002). Instead, we relied on the assumption that the spread in birth metallicities among stars born at the same time at the same radius was small over the last 8 Gyr; this is in some sense the most elementary version of chemical tagging.

To the extent that our Galactic disk is typical for large disk galaxies (Rix & Bovy, 2013; Bland-Hawthorn & Gerhard, 2016), this result helps explain why the stellar mass density profiles of disks are smooth and approximately exponential. Elmegreen & Struck (2013, 2016); Herpich et al. (2017) have shown that asymptotically efficient radial migration leads to exponential profiles. Of course, this "thermodynamic limit" of maximal angular momentum entropy would erase all abundance gradients, in conflict with observations. Our analysis here shows that strong radial orbit migration may happen, and still match the radial abundance gradients (at least [Fe/H]) in detail.

II.5.2   Current limitations and future prospects

In concluding, it may be good to recall some of our main model assumptions and simplifications and possible limitations due to the dataset used for inference: (1) We used a very specific radial orbit migration description, assuming it to be constant across the disk and with a specific time dependency. Describing this as a Gaussian diffusion equation in radius is strictly valid only at large radii in cylindrical coordinates (Brunetti et al., 2011). Here, we instead renormalized the solution for small radii (constant c_3 in Eq IV.13). We expect our results to robust against this

approximation, as most of our data constraints are more than 5 kpc away from the Galactic center, a distance that is larger then the radial migration strength after 8 Gyr. Further, we deem it is plausible that radial orbit migration occurs over wide range of radii and over much of the disks' evolution history. Nonetheless, it would be good to explore whether the extensive orbit-abundance data sets allow to constrain the presumably more complex radial or temporal dependence of radial orbit migration efficiency (Brunetti et al., 2011; Kubryk et al., 2013; Toyouchi & Chiba, 2018). For example, a bar could drive enhanced migration near its resonance, but also increase radial motions. To address this question, a modelling context that focuses near the resonances with the bar and that considers diffusion in angular momentum (rather than radius) and accounts for blurring would seem more appropriate. (2) At a basic level, our model explained "scatter" in data with radial orbit migration. This always begs the question whether other sources of scatter have been considered exhaustively. For example, we treated the (dominant) age uncertainties by explicit marginalization in the model, but did not do the same for [Fe/H] uncertainties to save computational expense. Also, future work could generalize the assumption that the abundance scatter at a given birth radius and epoch was zero, to the assumption that it was merely "small". And, (3) we restricted our radial orbit migration analysis to modelling of Galactocentric radius, while angular momentum and radial action should be modelled to best differentiate churning from blurring. The arrival of data from Gaia DR2 (Gaia Collaboration et al., 2018a) suggests such a generalized analysis as the next step.

We also eliminated the explicit R_i-dependence of the model, to eliminate the model's dependence on the detailed spatial selection function. But this approach "to ignore the observed radius distribution" also eliminates much valuable information. Future modelling could tackle the spatial selection function head-on (e.g. Bovy et al., 2016a).

Our inferences are based on APOGEE-DR12 red clump stars only: while these tracers provide excellent distances, they trace their underlying population in a very age-biased way, which we modeled. Nonetheless, the dependence of the star formation history τ_{SFR} and inside-out growth $\alpha_{R_{exp}}$ on the age distribution of the stars (Sec-

tion IV.4, suggests to repeat this analysis with other tracers, such as RGB stars. This is not expected to affect our findings on radial migration, and τ_{SFR} and $\alpha_{R_{exp}}$ were treated as nuisance here. But we hope that future data sets can better constrain the star formation history and inside-out growth of the stellar disk.

Finally, we have only considered [Fe/H] in this work. The vast stellar data sets of more detailed element abundance measurements must contain much information about where stars were born and how much they migrated. This, too, bears detailed modelling.

Acknowledgements

II.6   Appendix

We include here the full results of the MCMC procedure with all nuisance parameters, including those describing the old low-α stars in the Galactic disk, see Figure II.16. This figure essentially shows that all nuisance parameters are rather well constrained, but there is a degeneracy between the old disk scale-length and the star formation time-scale, as explained in Section IV.4.
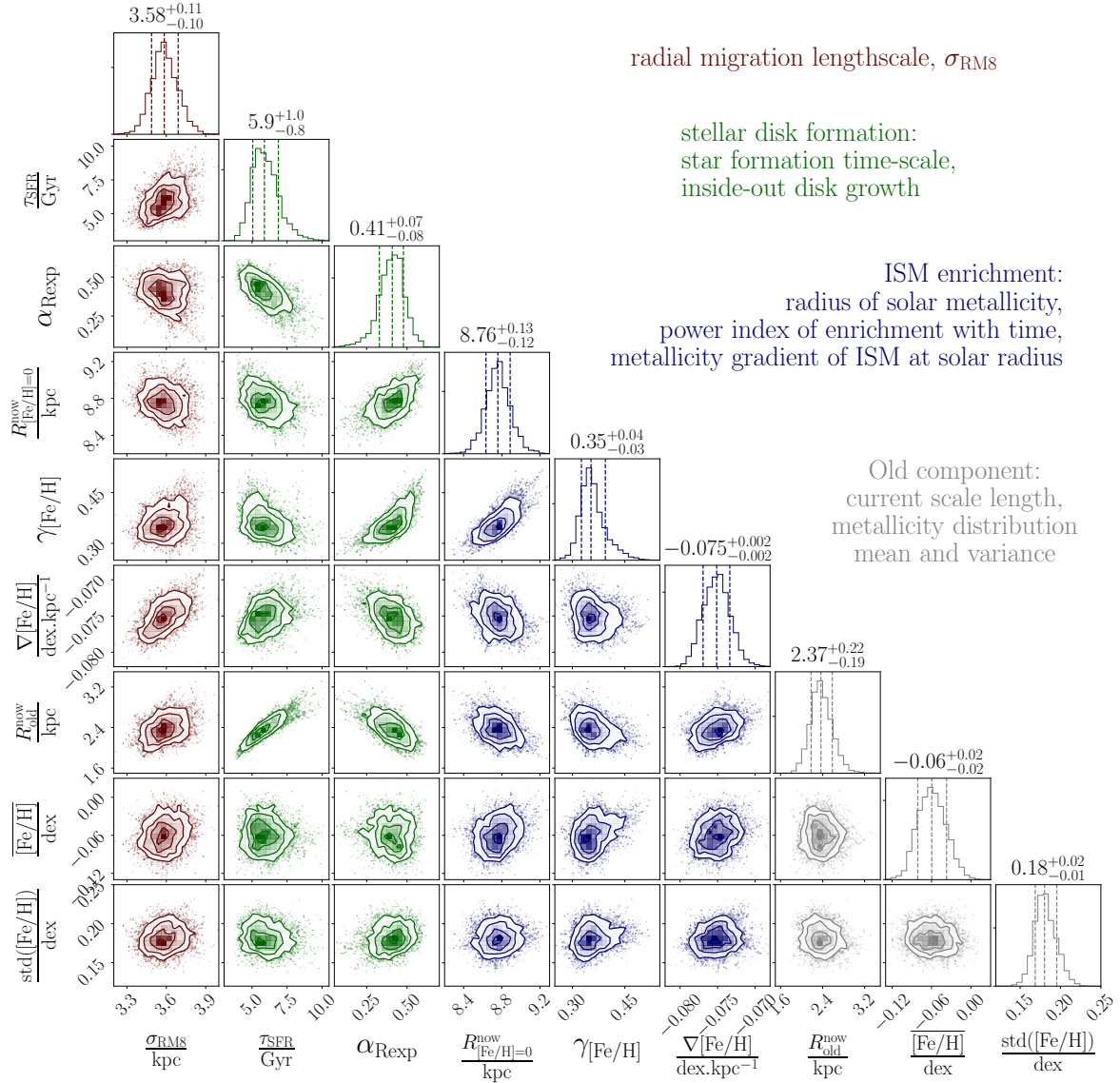
Figure II.16: Posterior distribution of the 9D parameter space. From left to right: the parameter of interest σ_{Lz12} for radial orbit migration in kpc (Eq IV.13), followed by the nuisance parameters: star formation time-scale τ_{SFR} in Gyr (Eq II.2), the parameter characterizing inside-out disk growth α_{Rexp} (the Miky Way disk was approximately 40% smaller at its formation 8 Gyr ago, Eq II.5). Then come the three parameters characterizing the enrichment of the ISM as a function of time and galactic radius (Eq IV.17): the radius where the ISM metallicity is solar $R^{\mathrm{now}}_{[\mathrm{Fe/H}]=0}$ in kpc, the power index characterizing the gradual chemical enrichment of the ISM with time $\gamma_{[\mathrm{Fe/H}]}$, the metallicity gradient of the ISM at the solar radius $\nabla[\mathrm{Fe/H}]$ in dex kpc^{-1}. The three last parameters are those characterizing the old star: the scale length of the old disk R_o in kpc, mean metallicity of old stars $\overline{[\mathrm{Fe/H}]}$ and its standard deviation std$([\mathrm{Fe/H}])$ in dex.

99

Chapter III

Disentangling Orbital Changes in the Milky Way Disk

Science Question   In Chapter II, I showed that stars in the Milky Way disk mix in radius very efficiently, which implies that dynamical effects causing them to change orbits are important. However, this is not enough to know *how* stars change orbits. In particular, two different processes must be disentangled: cold migration (stars diffuse in angular momentum, with orbits that remain roughly circular), from heating (stars' eccentricities or random motion increase). This chapter tackles this question by building on the previous model, including kinematics of stars (available thanks to the Gaia space mission).

Publication   This chapter was published in a similar form in Frankel et al. (2020).

Contributions

- I conducted the research presented in this paper: I thought about the science question and various concepts to sort which assumptions could be made, adapted the model of Frankel et al. (2019), coded it, produced the figures and the text.

- Jason Sanders contributed through regular guidance, help building the dynamical model and communicating enthusiasm.

- Yuan-Sen Ting provided the data and helped understanding their limitations, and commented on the draft.

- Hans-Walter Rix contributed through regular guidance and comments on the draft.

Abstract   A star in the Milky Way's disk can now be at a Galactocentric radius quite distant from its birth radius for two reasons: either its orbit has become eccentric through radial heating, which increases its radial action J_R ('blurring'); or merely its angular momentum L_z has changed and thereby its guiding radius ('churning'). We know that radial orbit migration is strong in the Galactic low-α disk and set out to quantify the relative importance of these two effects, by devising and applying a parameterized model ($\mathbf{p_m}$) for the distribution $p(L_z, J_R, \tau, [\text{Fe/H}]|\mathbf{p_m})$ in the stellar disk. This model describes the orbit evolution for stars of age τ and metallicity $[\text{Fe/H}]$, presuming coeval stars were initially born on (near-)circular orbits, and with a unique $[\text{Fe/H}]$ at a given birth angular momentum and age. We fit this model to APOGEE red clump stars, accounting for the complex selection function of the survey. The best fit model implies changes of angular momentum of $\sqrt{\langle \Delta L_z \rangle^2} \approx 619\,\text{kpc km/s}\,(\tau/6\,\text{Gyr})^{0.5}$, and changes of radial action as $\sqrt{\langle \Delta J_R \rangle^2} \approx 63\,\text{kpc km/s}\,(\tau/6\,\text{Gyr})^{0.6}$ at 8 kpc. This suggests that the secular orbit evolution of the disk is dominated by diffusion in angular momentum, with radial heating being an order of magnitude lower.

III.1   Introduction

What dominates the secular orbit evolution of nearly isolated disk galaxies? The Milky Way's last major merger is thought to have occurred before 7-8 Gyr ago (e.g. Rix & Bovy, 2013; Bland-Hawthorn & Gerhard, 2016; Belokurov et al., 2018; Helmi et al., 2018), leaving a long subsequent period for internal processes to dominate the dynamical evolution of the disk: non-axisymmetries (e.g. , bar, spiral arms) and giant molecular clouds can rearrange stellar orbits in different ways (e.g. Sellwood, 2014; Sellwood & Binney, 2002), as they resonantly interact or scatter.

The change in a star's orbit can be decomposed into (1) 'cold processes': the orbit's size or angular momentum changes, but remains circular, and (2) 'heating processes': the orbit's eccentricity and vertical extent change. Sellwood & Binney (2002) dubbed the first process "radial migration" and postulated that it could be important for restructuring stellar discs. Pure radial migration occurs when stars are near corotation of a non axisymmetry and can change angular momentum (L_z) by some amount ΔL_z, without significant change in their radial action (J_R): $\Delta J_R = 0\Delta L_z$. Such secular change of angular momentum can be very substantial – at least in dynamical simulations – indeed of order unity (Roškar et al., 2008b; Minchev et al., 2011; Kubryk et al., 2013; Halle et al., 2015; Loebman et al., 2016). Nonetheless, the bar, and coupling between non-axisymmetries including the bar, can boost radial migration significantly in N-body simulations (Minchev & Famaey, 2010b; Minchev et al., 2011; Brunetti et al., 2011). Additionally, Daniel et al. (2019) showed that radial migration should come with non-zero changes in J_R due to possible resonance overlaps between, for example, co-rotation and Lindblad resonances of different non-axisymmetries, or higher order resonances. But this effect could also increase the angular momentum changes. Heating processes could arise from interactions with non-axisymmetric perturbations through other resonances, or other heating agents such as satellites (e.g. Velazquez & White, 1999). The different components of the velocity dispersion have been measured to increase with stellar ages both in the Solar neighbourhood and over the disk (Wielen, 1977; Soubiran et al., 2008; Sanders & Das, 2018; Ting & Rix, 2019; Mackereth et al., 2019).

There is now persuasive evidence that *radius* migration in the Galactic disk is strong. In **?** we measured this radius migration, which must be the combined effect of radial heating and angular momentum diffusion. We modeled radial migration as a global process, fitting the distributions $p(R|R_0, \tau)$ of present-day Galactocentric radii (R) as a function of their birth radii (R_0) and age (τ) over a wide range of radii. We assumed that stars were born on initially tight metallicity-birth radius relations, and it is the radial diffusion that introduces the observed present-day scatter in this relation (Edvardsson et al., 1993; Casagrande et al., 2011). Inferring radial migration this way was originally proposed in the seminal paper by Sellwood & Binney (2002). Our global model fits turned out to constrain the overall migration scale well, to $\sigma_{RM} = 3.6\text{kpc}\sqrt{\tau/8\,\text{Gyr}}$: the typical star migrates about by a scale-length over the age of the disk.

However, this work did not disentangle diffusion in angular momentum from the increase in radial action, but only measured the combined effect of 'heating' and 'cold L_z diffusion' as 'orbit migration'. Therefore, the relative contributions of ΔJ_R (or 'blurring' in the terminology of Sellwood & Binney, 2002; Schönrich & Binney, 2009a) and ΔL_z (or 'churning') to the evolution of the stars' orbits in the Milky Way has yet to be quantified. Indeed, whether heating alone is sufficiently strong to account for all observed radial mixing is still questioned (Haywood et al., 2013, 2016). Here we set out to separate the importance of these two processes quantitatively.

We now ~~set out to~~ build on the model of **?**Frankel et al. (2019) and disentangle the strength of diffusion in angular momentum from that of increase in radial action. We will do this by generalizing the model of F18 from constraining the radius migration, i.e. the 'diffusion rate' in R, to constraining the secular orbit evolution in the disk plane, by quantifying the diffusion rates of both actions L_z and J_R. In Section IV.2, we describe our data set. We then construct the model and data likelihood in sections III.3 and III.4 and present the result best fit model in section III.5. We discuss the implications in Section III.6.
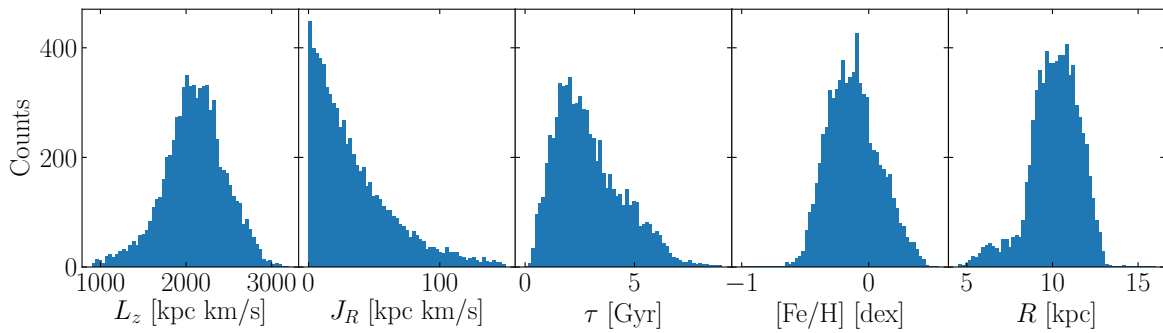
Figure III.1: Distributions of the adopted sample of red clump stars (drawn from APOGEE DR14, low-α) in angular momentum (L_z), radial action (J_R), age (τ), [Fe/H], and Galactocentric radius (R). The L_z and R distributions are clearly affected by spatial selection effects due to APOGEE's footprint. The sample's age distribution, with a prominent peak at 2 Gyr, reflects the combination of the 'underlying' age distribution and (most prominently) the age- or mass-dependent time duration of the core helium burning evolutionary stage (red clump).

III.2 Data: APOGEE-DR14 Red Clump Giants

Since the disk build up and its secular dynamical evolution involve processes occurring on large spatial and time scales, our science case requires a sample of stars with extensive coverage of the Galactic disk, a wide range of ages, and accurate and reliable 6D phase-space coordinates to calculate orbits. In practice, this requires spectroscopic and astrometric information, precise distances (as these are the dominant uncertainty in the action determination, as shown in e.g., Coronado et al., 2018), and a way to limit the impact of dust extinction at low Galactic latitudes. A crossmatch of the APOGEE-RC catalogue (Bovy et al., 2014; Majewski et al., 2017; Abolfathi et al., 2018) with Gaia DR2 (Gaia Collaboration et al., 2018b; Lindegren et al., 2018) satisfies these desiderata: red clump stars are bright standard candles and APOGEE collected their spectra in near-infrared (limiting the effect of extinction).

III.2.1 Data Selection and Catalogs

We start with the stars from the 14th data release of the APOGEE near-infrared spectroscopic survey and restrict to the low-α sample as in **?**, with stars mostly born between ~ 8 Gyr ago and now. We further select high-fidelity red clump stars derived by Ting et al. (2018b) cross-matched with Gaia DR2.

Red clump stars are low-mass stars in the core helium burning stage. They are good standard candles (to ~ 0.1 mag, Girardi, 2016; Hawkins et al., 2017; Hall et al., 2019; Sanders et al., 2019; Chan & Bovy, 2020), allowing the determination of a precise photometric distance. The identification of the red clump stage, done in Ting et al. (2018b), relies on spectroscopic estimates of the asteroseismic parameters Δv and ΔP which contain information on the evolutionary stage and stellar mass.

We further restrict our sample to the low latitude ($|b| < 25$ deg) "short cohort" (as defined in Zasowski et al., 2013) fields of APOGEE, which consists of the brightest stars with H band apparent magnitude $7 \le H \le 12$ to ease our modeling and reduce the fraction of stars with large uncertainties. Stars in longer cohorts are fainter, so at larger distances, have greater distance uncertainties and are more extinguished. Including them would increase computational expenses and complicate the selection function without commensurately increasing the information content. So we restrict the analysis to the short cohort stars for which we can work out the probability that they were selected for targeting in APOGEE (*i.e.* we can determine the selection function). We reject all APOGEE "special targets" in our data set as well as all the stars that are in APOGEE fields for which we could not work out a probability of selection (see Frankel et al., 2019). Since the number of cross-match failures between the red clump sample and Gaia DR2 is negligible ($< 1\%$), we assume in the following that the selection of our data is purely determined by APOGEE selection function, and that Gaia is complete within the APOGEE's short cohort selection cuts.

III.2.2   Basic Data and their Uncertainties

We use eight basic pieces of information: Galactic longitude (l), Galactic latitude (b), distance (D), line of sight velocity (v_{los}), metallicity ([Fe/H]) from APOGEE, proper motion in right ascension (μ_α) and declination (μ_δ) from Gaia, and age (τ) derived from the full spectrum in Ting & Rix (2019), which are calibrated to asteroseismology.

The photometric distances (D) were determined to about 7% in Ting & Rix (2019), using near-infrared and Gaia G photometry for red clump stars as standard candles, exploiting the fact that interstellar extinction is weaker at longer wavelengths (e.g., Indebetouw et al., 2005; Wang & Chen, 2019). The line of sight velocity (v_{los}) is taken from the APOGEE-DR14 catalog, and the proper motions (μ_α, μ_δ) from Gaia DR2. Spectroscopic age estimates τ for this sample were obtained by Ting & Rix (2019) from a data-driven method built to determine ages from the APOGEE spectra, trained on the APOKASC2 red clump sample (Pinsonneault et al., 2018); this approach has a precision of about 0.15 dex, with possible systematics at large ages, because the C and N spectral features tracing the age, (e.g. Martig et al., 2016; Ness et al., 2016) vary more weakly at large ages and hence contains less information. A more extensive discussion on the possible implications of such systematics on the modeling, and comparisons of different age estimates can be found in Frankel et al. (2019). The metallicity estimates ([Fe/H]) are taken from the ASPCAP pipeline with typical uncertainties below 0.05 dex (Holtzman et al., 2018).

III.2.3   Galactocentric Rest Frame and Orbital Actions

From these basic data, we extract and pre-compute the quantities that are more directly used in our model, and propagate uncertainties via Monte Carlo sampling of 80 points. In particular, we compute the Galactocentric radius (R), height above the plane (z), azimuthal velocity (v_ϕ) and radial velocity (v_R) in Galactocentric coordinates, assuming the distance between the Sun and the Galactic center $R_\odot = 8.2$ kpc (Gravity Collaboration et al., 2019), and the Sun's height above the Galactic plane $z_\odot \approx 20.8$ pc (Bennett & Bovy, 2019). We also assume the Solar velocity with respect to the Local Standard of Rest $v_\odot = [-11.1, 12.24, 7.25]$ km.s^{-1}(Schönrich et al., 2010) and the tangential velocity of the Sun 247.4 km/s (Gravity Collaboration et al., 2019; Reid & Brunthaler, 2004).

We further compute the orbital parameters relevant to our modeling of the Galactic disk; going from phase-space coordinates ($\vec{x}$, $\vec{v}$) to orbits, as quantified *e.g.* by their actions, requires the adoption of a gravitational potential. We compute the stars' angular momenta (L_z, which are the azimuthal actions J_ϕ in an axissymmet-

ric potential) and radial actions (J_R) using the Python package *Galpy* (Bovy, 2015) based on the algorithm of Binney (2012). The orbits are integrated over the potential *MWPotential2014* of this package, which is also the potential used in our model, scaled to the Galactocentric rest-frame as described above. The 1D marginal distributions of angular momentum, radial action, age, [Fe/H] and Galactocentric radius are illustrated in Figure III.1. The distributions in angular momentum and Galactocentric radius are directly affected by the APOGEE on-sky footprint and implicit distance limit; else we would expect these distributions to be approximately exponential. The age distribution shows a prominent peak at at ~ 2 Gyr, reflecting the mass dependence of the RC lifetime (Girardi, 2016; Bovy et al., 2014).

III.3 Chemo-dynamical Model for the Evolution of the Galaxy's Low-α Disk

We now present a global model for the formation and evolution of the Galaxy's low-α disk, building directly on Sanders & Binney (2015), **?** and Frankel et al. (2019). The most important astrophysical assumption of the model is that stars form on near-circular orbits from chemically well mixed cold gas with an inside-out star formation history. Over time, the orbits of stars evolve, and the gas is enriched in metals. The combination of age and [Fe/H] in this model implies a birth angular momentum $L_{z,0}$ or a birth radius. *Radial heating* of stellar orbits is modeled as an increase of their mean radial action J_R and *radial migration* is modeled as a global diffusion process in angular momentum L_z. In our modeling, vertical heating is only implicit: we ignore the (weak) coupling between in-plane and vertical motions, and model an age-dependent vertical profile for the disk to incorporate the 3D spatial selection function (see Section III.4). The overall model for the dataset $p_{\mathrm{dataset}}(l, b, D, [\mathrm{Fe/H}], \tau, v_R, v_\phi | \mathbf{p_m})$, and how it is combined with the Galactic disk model $p_{MW}(L_z, J_R[\mathrm{Fe/H}], \tau | \mathbf{p_m})$ is summarized in Figure III.2 and in Table III.1. The model aspects are then combined together in the following section in a likeli-
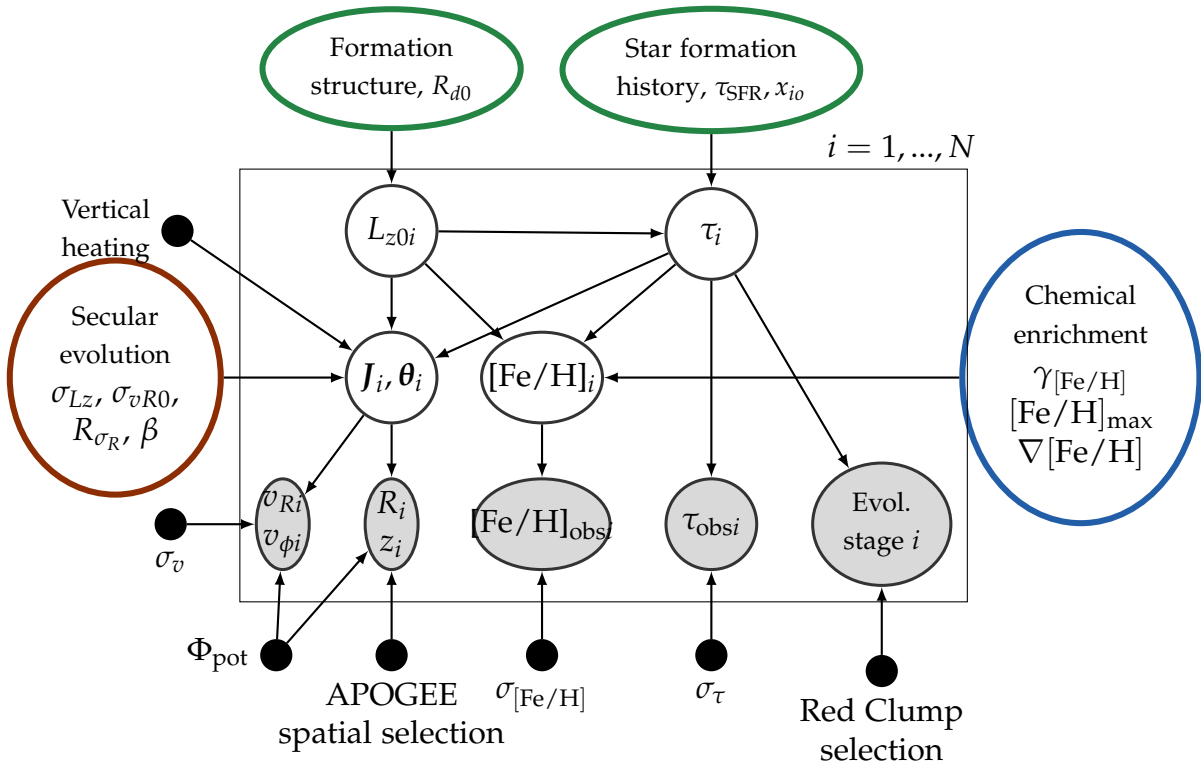
Figure III.2: Probabilistic graphical model for the joint distribution $p(\mathbf{x_i}, \mathbf{v_i}, [\text{Fe/H}]_i, \tau_{\text{obs}i}\} \mid \mathbf{p_m})$ of the APOGEE data set. This simplified model reflects the combination of a global model for the Milky Way disk, APOGEE selection function, and the marginalization over the data uncertainties. The circles filled in gray contain the APOGEE red clump stars' observables to be modelled. The circles inside the large contain the variables in which model is cast : the true birth angular momentum, true age, true action vector, true metallicity. The ellipses outside the rectangle contain the global model parameters to be fit: scale length at birth, star formation time-scale, inside-out parameter, secular evolution parameters and chemical enrichment parameters. The black points are fixed aspects of the model: present-day potential of the Milky Way, noise model and APOGEE selection function.

hood function, used to constrain its parameters. In this way we can disentangle the strength of radial migration and radial heating and compare them, but only under a set of (physically sensible) assumptions that we will now lay out in some detail.

III.3.1 Model Assumptions

Our modelling assumptions are as follows:

1. Stars are born with a tight relation between [Fe/H] and $L_{z,0}$ at any given τ. This is a 'weak chemical tagging' assumption, supported by Krumholz & Ting (2018) and Ness et al. (2019b), who showed that in the low-α disk, [Fe/H]and age can predict present-day L_z precisely (and we here attribute the scatter in

that relation to radial migration). This assumption is also well supported by extragalactic observations of a sample of spiral galaxies, which showed that the azimuthal variations and scatter in the interstellar medium's [O/H] is low (< 0.05 dex in e.g. Kreckel et al., 2019) . We parametrize this tight relation (Section III.3.6) and fit for the parameters.

2. Secular processes (processes happening on time scales longer than a typical orbital time scale) have dominated the evolution of the Galaxy's low-α disk. As the last major merger presumably occurred before the formation of the low-α disk (e.g., Rix & Bovy, 2013; Bland-Hawthorn & Gerhard, 2016; Belokurov et al., 2018; Helmi et al., 2018), the Milky Way is thought to have evolved in near isolation (i.e. interacting mainly with itself and occasionally with lower mass satellites, e.g., the Sagittarius dwarf galaxy) for the past 7-8 Gyr, which leaves a lot of time for slower, more gradual processes to occur and affect the Galaxy's evolution. We assume that secular processes cause orbits to diffuse, and set out to measure the strength of this diffusion, but we do not make assumptions on the nature of this process nor try to identify the agents driving them.

3. We assume that the present-day potential of the Milky Way is sufficiently well approximated by the axisymmetric potential *MWPotential2014* in the *Galpy* package (Bovy, 2015), and that the present equilibrium state of the Milky Way disk can be described by separable distribution functions

$$p(\mathbf{J}) = p(L_z)p(J_R|L_z)p(J_z|L_z), \tag{III.1}$$

where the vertical motion is independent of the radial action (the so-called adiabatic approximation, Binney, 2010). This is manifestly an approximation since we know the disk is not axisymmetric, nor in equilibrium: there are spiral perturbations, a bar and a warp (Bland-Hawthorn & Gerhard, 2016; Beane et al., 2019).

4. When computing the actions, we use the Stäckel approximation (Binney, 2012) as implemented in the *Galpy* package (Bovy, 2015). Furthermore, we implicitly

assume in the models that the height above the plane z and vertical velocity v_z are independent of the radial action (the adiabatic approximation, Binney, 2010). We use this approximation because we wish to focus on the in-plane distributions $p(J_R|L_z)p(L_z)$ and for our considered orbits, which predominately lie close to the Galactic plane, the approximation is valid.

III.3.2 Modeling the Gradual Build-up of the Stellar Disk

We now describe the parameterized version of our modeling for the successive build-up of the Galactic stellar disk, encompassing the star-formation history with inside-out growth.

We model the time-integrated distribution of angular momenta at birth as

$$p(L_{z,0}|\mathbf{p_m}) = \frac{L_{z,0}}{\langle L_{z,0}\rangle^2} \exp\left(-\frac{L_{z,0}}{\langle L_{z,0}\rangle}\right), \tag{III.2}$$

where we define the mean angular momentum at birth as $\langle L_{z,0}\rangle = R_{d0} \times 235\mathrm{km.s^{-1}}$, to fit for and interpret the parameter R_{d0} as a global scale-length. This scale-length is time-integrated and reflects the global profile of the disk after all stars are born. For a cold disk at birth, this model is approximately equivalent to an exponential surface density profile ($\Sigma(R_0) \propto \exp(-R_0/R_{d0})$) with a scale-length R_{d0}. But the actual spatial scale-length of the disk at birth may be different since the spatial distribution of stars will depend on gradual changes of the potential due to the ongoing build up of the disk. The possible inside-out growth (illustrated in Fig. III.5) is modeled through an $L_{z,0}$-dependent star formation, where the star formation time-scale depends linearly on birth angular momentum, causing the inner disk to form stars on shorter time-scales than the outer disk. The star formation history is adapted from Frankel et al. (2019), but now taken to be a function of birth angular momentum (rather than birth radius):

$$\mathrm{SFH}(\tau \mid L_{z,0}, \mathbf{p_m}) = c(L_{z,0}, \mathbf{p_m})$$
$$\times \exp\left[\frac{1}{\tau_{SFR}}\left((1 - x_{io}\frac{L_{z,0}/235\ \mathrm{km\,s^{-1}}}{8.2\ \mathrm{kpc}})\tau - \tau_m\right)\right]. \tag{III.3}$$

Here, $c(L_{z,0}, \mathbf{p_m})$ is a normalization constant such that $\int \text{SFH} d\tau = 1$ at any given $L_{z,0}$. Since the star formation history is not the primary focus of this work, we treat it as a nuisance aspect of the model. We fit for and marginalize over the parameters x_{io} and τ_{SFR}. The parameter τ_m corresponds to the maximum stellar age we consider in the low-α disk, fixed to 6 Gyr.

III.3.3   Present-day Gravitational Potential

We assume that the present-day gravitational potential of the Milky Way disk is well described by the *MWPotential2014* in the *Galpy* Package. In the present work, we only use the present-day potential of the Milky Way disk and its derived quantities (circular velocity v_{circ}, epicyclic frequencies κ and ν etc.) and make no assumptions about its past evolution.

As the Milky Way's stellar disk has gradually grown from inside-out over the past 7-8 Gyr (Subsection III.3.2), the mass distribution of the stellar and gas disks have changed, and the potential $\Phi_{\text{pot}}(\tau)$ has evolved accordingly. Linking stellar birth radii R_0 to their birth angular momenta $L_{z,0}$ would require to know exactly how the potential has evolved. This could be done by modeling the mass distribution in different Milky Way components, including a growth for the stellar disk. But the present-day contributions of each component of the Milky Way are already fairly unconstrained today (e.g., de Salas et al., 2019; Eilers et al., 2019), so we do not attempt to infer them in the past. Instead, our modeling is fully based on linking birth actions to present-day actions rather than birth positions. In an axisymmetric potential, if the gradual build up of the disk is slow and adiabatic, then the actions of stars should be conserved: stars on the same orbit but at different phases will, if the change in potential is sufficiently slow, experience the same changes of potential (averaged over a period) and thus conserve their actions. However, stellar velocities and positions should change: as the disk mass increases, stars will on average sink to orbits closer to the Galactic center. Therefore, measuring a change of orbital action ΔJ bypasses other orbital changes of the stars and gives direct insights into the secular processes in the disk.

III.3.4   Modeling the Angular Momentum Evolution

We follow the argument of Sellwood & Binney (2002) that the radial orbit redistribution of stars is caused by a sequence of stochastic processes, of some nature that we do not determine (which could be, for example, short-lived spiral perturbations). In this limit, stars follow a random walk in angular momentum so that radial migration can be modeled as a diffusion process in angular momentum, dubbed "churning" by Sellwood & Binney (2002). Following Sanders & Binney (2015) we adopt the parameterized angular momentum diffusion equation

$$\frac{\partial f}{\partial t} = \frac{\partial}{\partial L_z}\left(-D^{(1)}f + \frac{\sigma^2}{2}\frac{\partial f}{\partial L_z}\right). \tag{III.4}$$

The nature of the radial migration process determines the diffusion coefficients of this diffusion equation. For simplicity, we assume that the diffusion coefficients in the equation above do not depend on L_z and that σ is independent of time. These assumptions imply that we are only constraining an effective global mean (in radius and time) of the overall L_z diffusion.

Herpich et al. (2017) showed that if radial migration were asymptotically efficient, the angular momentum distribution in a disk should go as

$$f(L_z) = \exp(-L_z/\langle L_z\rangle)/\langle L_z\rangle, \tag{III.5}$$

and their model predictions match the observed angular momentum profile of external galaxies well. On the other hand, surface brightness profiles of disk galaxies have been observed to have exponential or de Vaucouleur profiles (de Vaucouleurs, 1948), which would correspond to (in the limit of circular orbits) an angular momentum distribution $f(L_z) \propto L_z \exp(-L_z/\langle L_z\rangle)$ to which a bulge could be added at the center. Since we are not modeling a bulge in the present work, our model will in any case be inadequate in the inner few kpc of the Milky Way.

Drawing on these considerations, we impose that the steady state solution for the L_z diffusion equation is either the exponential distribution in L_z, or the expo-

nential surface density profile. At $L_z \gg \langle L_z \rangle$[1], these distribution are similar and constrain the diffusion coefficient $D^{(1)}$ to $D^{(1)} = \frac{-\sigma_{Lz12}^2}{2\langle L_{z,0} \rangle \tau_m}$, where we pose the mean specific angular momentum $\langle L_{z,0} \rangle = 235 \text{km.s}^{-1} R_{d0}$. This ensures approximate conservation of angular momentum. In the microscopic limit, Schönrich & Binney (2009a) model this process with each star having a probability to move to a radius r_i proportional to the stellar mass m_i at that radius. This ensures that the number of stars migrating from radius i to radius j is proportional to $m_i m_j$, which is equal to the number of stars migrating from j to i, thereby conserving the total disk profile. However, in reality the total disk angular momentum need not be conserved, as external torques, e.g. exchanges with the halo, could change it; here we do neglect this effect, since it is not well quantified or understood even in simulations: Buck et al. (2020) show that some Milky Way-like simulated galaxies see their scale-length increase over time (net outward migration), while others don't. Here, with our fixed choice of $D^{(1)}$ disk profile remains constant with a mean angular momentum $\langle L_{z,0} \rangle$. But individual populations of age τ born on profiles with $\langle L_{z,0} \rangle (\tau) < \langle L_{z,0} \rangle$ will, on average, broaden, and those born with $\langle L_{z,0} \rangle (\tau) > \langle L_{z,0} \rangle$ will, on average, shrink.

The present day angular momentum of a star of age τ would then be related to its birth angular momentum by

$$
\begin{aligned}
p(L_z \mid L_{z,0}, \tau, \mathbf{p_m}) = N(\mathbf{p_m}) \\
\times \exp\left(-\frac{(L_z - L_{z,0} - D^{(1)}\tau)^2}{2\sigma^2(\tau)} \right)
\end{aligned}
\tag{III.6}
$$

where $\sigma(\tau) = \sigma_{Lz12}\sqrt{\frac{\tau}{\tau_m}}$ is the radial migration strength in angular momentum units (kpc km/s^{-1}). The parameter σ_{Lz12} is to be fit and $N(\mathbf{p_m})$ is a normalizing constant such that $\int_0^\infty p(L_z \mid L_{z,0}, \tau, \mathbf{p_m}) dL_z = 1$ (there are no counter rotating stars in the disk). τ_m is the maximum age of the disk we consider, which is fixed to 6 Gyr here since there are so few constraining stars in the data at larger ages (see 3rd panel in Fig. III.1).

---

[1]The region $L_z \leq \langle L_z \rangle$ corresponds to the inner 3 kpc of the disk, where we currently do not have data, see the right most panel of Fig. III.1

III.3.5 Radial Heating

We assume that stars are born on near-circular orbits, and that their mean radial action increases with time as their orbits are kinematically heated (dubbed "blurring" by Sellwood & Binney (2002)). We adopt the isothermal disk model from Sanders & Binney (2015); Binney (2010), and we fit for the increase of mean radial action as a function of age and final position. The radial action distribution is then written as

$$p(J_R \mid \tau, L_z, \mathbf{p_m}) = \frac{1}{2\pi} \frac{\kappa}{\sigma_R^2} \exp\left(-\frac{\kappa J_R}{\sigma_R^2(\tau, L_z)}\right), \tag{III.7}$$

with $\kappa = \kappa(R_{\mathrm{circ}}(L_z))$ the frequency of radial motion (the epicycle frequency), which depends on the guiding radius R_{circ}, the radius of circular orbit of angular momentum L_z. The velocity dispersion $\sigma_R = \sigma_R(\tau, R_{\mathrm{circ}}(L_z))$ traces the heating history of stars in the disk:

$$\begin{aligned}
\sigma_R(\tau, R_{\mathrm{circ}}(L_z)) = {} & \sigma_{\mathrm{vR0}} \left(\frac{\tau + \tau_1}{\tau_m + \tau_1}\right)^{\beta} \\
& \times \exp\left(\frac{8\,\mathrm{kpc} - R_{\mathrm{circ}}}{R_{\sigma_R}}\right),
\end{aligned} \tag{III.8}$$

where σ_{vR0} is the velocity dispersion of stars of age $\tau_m = 6$ Gyr in the Solar neighbourhood (to be fitted), τ_1 is set to reflect a dynamical time, ~ 110 Myr, as in Sanders & Binney (2015) and allows stars to be born with small but non-zero eccentricity. The scale R_{σ_R} represents a possible decay of the velocity dispersion with Galactocentric radius, as in Sanders & Binney (2015) (to be fitted). Note again that the radial actions are adiabatic invariants, and so the gradual build up of the disk should not influence the radial action of stars after their birth.

III.3.6 Weak Chemical Tagging: [Fe/H]-τ-$L_{z,0}$ Relation

For the current modeling, we use [Fe/H], and assume that it is approximately only a function of time and $L_{z,0}$; in some sense, this is the weakest form of "chemical tagging".

We model the [Fe/H]-τ-$L_{z,0}$ relation as a a power law in time and a broken line in
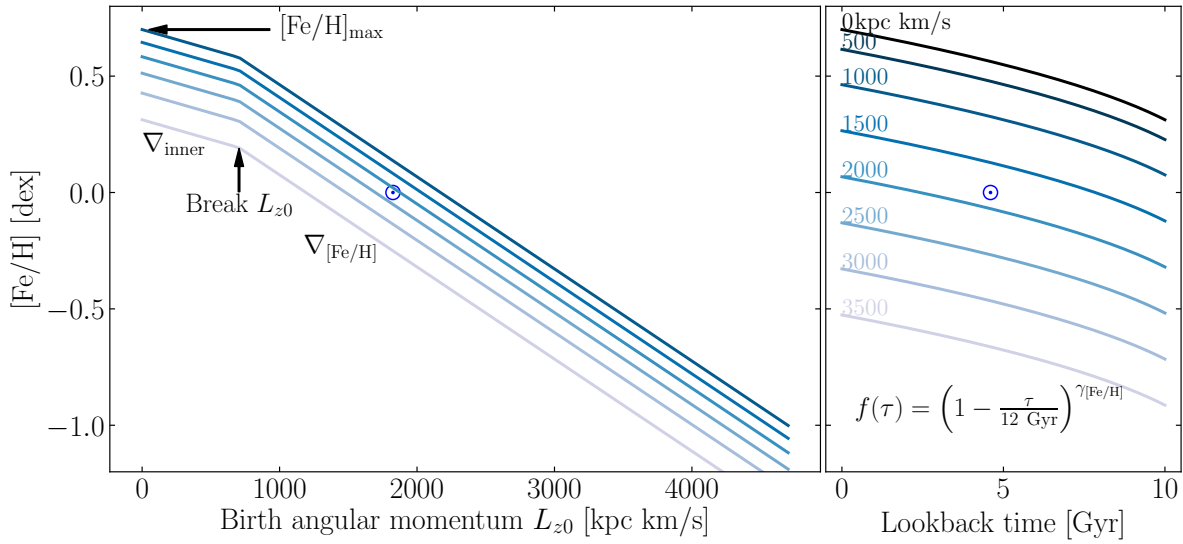
Figure III.3: Functional forms to fit for $[\text{Fe/H}](L_{z,0}, \tau, \mathbf{p_m})$, showing $[\text{Fe/H}]$ as a function of $L_{z,0}$ in the left panel, and as a function of look-back time in the right panel (for a set of birth angular momenta). The model parameters chosen here are $\gamma_{[\text{Fe/H}]} = 0.45$, $\nabla[\text{Fe/H}] = -0.093$ dex.kpc^{-1} and $[\text{Fe/H}]_{\text{max}} = 0.70$ dex. The present-day gradient $\nabla[\text{Fe/H}]$ sets the 'outer' metallicity profile, the power index $\gamma_{[\text{Fe/H}]}$ sets the time dependence and $[\text{Fe/H}]_{\text{max}}$ sets the present-day $[\text{Fe/H}]$ at the center of the Galaxy. We show the position of the Sun marked with an $\odot$ symbol, at $[\text{Fe/H}]_{\odot} = 0$ dex and $\tau_{\odot} = 4.6$ Gyr.

the variable $L_{z,0}$ with an inner disk radial gradient of -0.03 dex/kpc for $L_{z,0} < 3 \times 235$ kpc km/s. Since we have no constraining data on the inner metallicity profile in the disk, we use two external arguments to motivate this imposed flattening in the inner disk: (1) the observed metallicity profile in the stars is flatter in the inner disk/bulge (Pietrukowicz et al., 2015), and (2) chemical evolution models predict a flatter metallicity profile in the gas in the inner disk (e.g., Schönrich & Binney, 2009a). Namely,

$$
\begin{aligned}
[\text{Fe/H}] = &[\text{Fe/H}]_{\text{max}} f(\tau) + b_{[\text{Fe/H}]} \\
&+ \nabla[\text{Fe/H}](L_{z,0}) \frac{L_{z,0}}{235 \text{ kms}^{-1}}
\end{aligned}
\tag{III.9}
$$

where the gradient

$$
\nabla[\text{Fe/H}](L_{z,0}) = \begin{cases} \nabla\text{inner} & \frac{L_{z,0}}{235\text{km.s}^{-1}} < 3 \text{ kpc} \\ \nabla[\text{Fe/H}] & \text{otherwise.} \end{cases}
\tag{III.10}
$$

116

with the inner metallicity gradient ∇inner fixed at -0.03 dex.kpc^{-1} and the outer metallicity gradient $\nabla[\text{Fe/H}]$ is to be fitted. As in **?**, $\nabla[\text{Fe/H}]$ is assumed constant in time, since its time dependence is poorly constrained with a variety of chemical enrichment models predicting different time evolution, (e.g. Pilkington et al., 2012; Schönrich & Binney, 2009a; Grisoni et al., 2018b). $b_{[\text{Fe/H}]}$ is introduced so the overall profile is continuous at $L_{z,0} = 3 \times 235$ kpc km/s:

$$b_{[\text{Fe/H}]} = \begin{cases} 0 & \frac{L_{z,0}}{235\text{km.s}^{-1}} < 3 \text{ kpc} \\ \frac{(\nabla_{\text{inner}} - \nabla[\text{Fe/H}])L_{z,0}}{235 \text{ km s}^{-1}} & \text{otherwise.} \end{cases} \tag{III.11}$$

The central metallicity is governed by the parameter $[\text{Fe/H}]_{\text{max}}$ and we use a time dependence of

$$f(\tau) = \left(1 - \frac{\tau}{12 \text{ Gyr}}\right)^{\gamma_{[\text{Fe/H}]}}. \tag{III.12}$$

The set of model parameters we fit for are $\nabla[\text{Fe/H}]$, $\gamma_{[\text{Fe/H}]}$, and $[\text{Fe/H}]_{\text{max}}$. These functions are plotted in Fig. III.3.

III.3.7 Vertical Distribution of Stars

The vertical distribution of stars in the Milky Way disk is not the primary focus of this work (since we are essentially interested in the in-plane motions), but we must model it because the spatial selection of our data is in three spatial dimensions and so we require a 3D model for the disk. For simplicity, we model the vertical distribution of stars in the disk with the best fit model of Ting & Rix (2019) in the regime of the isothermal disk:

$$p(z \mid L_z, L_{z,0}, \tau, \mathbf{p_m}) = \frac{1}{2h_z(L_z, L_{z,0}, \tau)} \\ \times \text{sech}^2\left(\frac{z}{h_z(L_z, L_{z,0}, \tau)}\right), \tag{III.13}$$

where the scale height

$$h_z = a_z\sqrt{\frac{2\overline{J_z}(L_z, L_{z,0}, \tau)}{\nu(R)}}, \tag{III.14}$$

with the vertical frequency ν defined such that $\nu^2 = \frac{\partial^2 \Phi}{\partial z^2}$. $\overline{J_z}(L_z, L_{z,0}, \tau)$ is the mean vertical action of stars of angular present momentum L_z, birth angular momentum $L_{z,0}$ and of age τ. Ting & Rix (2019) studied the vertical heating history of the Galactic disk using an APOGEE red clump data set, and published an analytic fit for $\overline{J_z}(L_z, L_{z,0}, \tau)$. We model the age- and radial-dependent vertical distribution of red clump stars according to this form. Since the model of Ting & Rix (2019) used different age dependencies and birth radii scales than those in our work, we allow for an overall scaling of their heating law parametrized by a_z, which we anticipate will be near unity (see resulting fits in Table III.1).

III.4   The Likelihood of the APOGEE-RC $\times$ Gaia DR2 Data

To determine how this model is constrained by our data, we must construct the data's likelihood for any given set of model parameters, and on this basis sample the parameter's posterior probability distribution, *pdf*. We now lay out how to implement this.

For each star, our 'data' are

$$\mathcal{D} = \{l, b, D, \tau, [\text{Fe/H}], v_R, v_\phi\} \tag{III.15}$$

with their associated uncertainties (see Section IV.2). As noted in Section IV.2, these data are not sampled directly from the underlying Milky Way disk distribution: the sample very much reflects both the distribution of stars in the Milky Way $p_{MW}(\mathcal{D})$, and the selection process $S(l, b, D, \tau) \equiv p(\text{select}|\mathcal{D})$. Therefore, the probability distribution of the data given our model parameters is

$$
\begin{aligned}
p_{\text{dataset}}(\mathcal{D} \mid \mathbf{p_m}) = C \cdot p_{\text{MW}}(\mathcal{D} \mid \mathbf{p_m}) \\
\times S(l, b, D) f_{RC}(\tau)
\end{aligned}
\tag{III.16}
$$

where $p_{\text{MW}}(\mathcal{D} \mid \mathbf{p_m})$ is the model of the Galactic disk, which is a combination of

Model aspect	Functional Family	Model Parameters	Max. Likelihood Value
Global structure at birth	$p(L_{z,0}\|\mathbf{P_m})$ $\propto L_{z,0}\exp\left(-L_{z,0}/v_{\rm circ}R_{d0}\right)$	Birth scale-length R_{d0}	2.8 kpc
Inside-out star formation history	$p(\tau\|L_{z,0},\mathbf{P_m})$ $\propto \exp\left[\frac{1}{\tau_{SFR}}\left(\left(1-x_{io}\frac{L_{z,0}/v_{\rm circ}}{8.2\,{\rm kpc}}\right)\tau-\tau_m\right)\right]$	Inside-out coefficient x_{io} SFR time-scale τ_{SFR} Maximum age τ_m	0.65 1 Gyr Fixed to 6 Gyr
Angular momentum diffusion	$p(L_z\|L_{z,0},\tau,\mathbf{P_m})$ $\propto \exp\left(-\frac{(L_z-L_{z,0}-D\tau)^2}{2\sigma_{Lz12}^2\tau/\tau_m}\right)$	Diffusion strength σ_{Lz12}	582 kpc km/s
Radial heating	$p(J_R\|L_z,\tau,\mathbf{P_m})$ $\propto \exp(-\kappa J_R/\sigma_R^2)$ $\sigma_R=\sigma_{\rm vR0}\left(\frac{\tau+\tau_1}{\tau_m+\tau_1}\right)^{\beta}\exp\left(\frac{8\,{\rm kpc}-R_c}{R_{\sigma_R}}\right)$	Time dependence β Velocity dispersion $\sigma_{\rm vR0}$ Radial dependence R_{σ_R}	0.3 49 km/s 19 kpc
Vertical heating	$p(z\|L_z,L_{z,0},\tau,\mathbf{P_m})$	a_z (scaling)	1.16
Weak chemical tagging	$p([{\rm Fe/H}]\|L_{z,0},\tau,\mathbf{P_m})$ $[{\rm Fe/H}]=[{\rm Fe/H}]_{max}\left(1-\frac{\tau}{12\,{\rm Gyr}}\right)^{\gamma_{[{\rm Fe/H}]}}$ $+\nabla[{\rm Fe/H}](L_{z,0})\frac{L_{z,0}}{v_{\rm circ}(L_{z,0})}+b_{[{\rm Fe/H}]}$	Time dependence $\gamma_{[{\rm Fe/H}]}$ Radial gradient $\nabla[{\rm Fe/H}]$ Max [Fe/H] $[{\rm Fe/H}]_{max}$	0.456 -0.0936 dex/kpc 0.7 dex

Table III.1: Summary of the main model aspects (described in Section III.3) and best-fit parameters

the model aspects described above as detailed in Appendix III.8. C is a normalizing term specified in Eq. III.17 and Section III.4.1. $S(l, b, D) = p(\text{select}| \, l, b, D)$ is the selection function, or the probability that a star ends up in the catalog given its observable properties. The observables for each star are a combination of its intrinsic properties and its position and velocity with respect to us, and the evolutionary stage is determined using the spectrum (Ting et al., 2018b). Typically the selection function is a strong function of apparent magnitude. In the case of standard candles where the apparent magnitude is a function of distance (and extinction) only, such as RC stars, the selection function essentially reduces to a function of (l, b, D). Finally, the term $f_{RC}(\tau)$ is the probability of a star to be on the red clump evolutionary stage given its age τ (Bovy et al., 2014).

We determine the spatial selection function of APOGEE following the methods laid out in Rix & Bovy (2013); Bovy et al. (2014) and Frankel et al. (2019), and extend the methodology to the DR14 data which includes APOGEE-2. The main difference in the APOGEE-2 target selection for the main disk fields with respect to APOGEE-1 is the inclusion of two color bins: blue ($(J - K_s) < 0.8$ mag) and red ($(J - K_s) > 0.8$ mag) (Zasowski et al., 2017). This makes the selection function more complex because the fraction of selected stars of different stellar types differs between APOGEE fields. However, we are not affected by this complexity because we are working with RC stars, assumed perfect standard candles (with $(J - K)_0 = 0.68$ mag, Hawkins et al., 2017) lying fully in the blue color bin, such that we need not account for the selection fractions of the red color bin. In practice, the spatial selection function, $S(l, b, D)$, is a piece-wise function in each APOGEE field, such that for a field i centred at $(l, b)_i$ it can be expressed solely as a function of distance $S_i(D)$. The dependence on distance is more complex than a constant between D_{min} and D_{max} set by the stars absolute magnitude and the survey's magnitude cuts, due to the 3D spatial distribution of dust, which limits the fraction of stars seen at a given absolute magnitude and distance. We model this using the 3D dust map of Green et al. (2019). A detailed description of how this is incorporated into the model can be found in Frankel et al. (2019)[2].

---

[2]The selection function is published with a tutorial of its use at `https://github.com/NeigeF/`

III.4.1   Normalization of the PDF: Survey Volume

To make p_{dataset} a probability density function, it must be normalized by

$$C^{-1} = V_S(\mathbf{p_m}) = \int_{\mathcal{D}} p_{\text{MW}}(\mathcal{D} \mid \mathbf{p_m})S(l,b,D)\mathrm{d}\mathcal{D} \qquad (\text{III.17})$$

which is a 7-dimensional integral over all the physical properties of the data We refer to V_S as the 'survey volume'. Two of the integrals (l,b) can be transformed into a sum over APOGEE fields, if we assume that the properties of stars in the sky within a single APOGEE pointing are uniform. This is a valid assumption as the APOGEE fields are typically 3 deg across. We compute V_S in the next subsection, and assemble the data likelihood in Subsection III.4.2.

Expanding Eq. III.17, the survey volume can be written

$$V_S(\mathbf{p_m}) = \sum_{\text{field } i} \int_{\text{Data space}} p_{\text{MW}}(\tau, L_{z,0}, J_R, L_z, z, \mid \mathbf{p_m})$$
$$\times S_i(D) f_{RC}(\tau)\Omega_i D^2 \mathrm{d}L_{z,0}\mathrm{d}D\mathrm{d}v_R\mathrm{d}v_\phi\mathrm{d}\tau, \qquad (\text{III.18})$$

This integral is not straightforward to compute. The integrand is proportional to a probability density that we cannot fully compute, but that we can sample. Therefore, we compute this integral through iterative importance sampling (details in Appendix III.9). We start with a 'blind' optimization of the data likelihood by normalizing the likelihood with samples generated from a model with initial plausible guesses for the model parameters $\mathbf{p_{m,prop}}$. We then use these best fit parameters to generate new samples, which better reflect the shape of the likelihood and can be used normalize the likelihood for further calculations.

III.4.2   Data Likelihood Function and Parameters Posterior

The overall Milky Way disk model combined with the selection function predicts the likelihood of the data for any star in the sample. Assuming all measurements are independent, we write the total likelihood of the entire data set given our model

---

`apogee_selection_function`
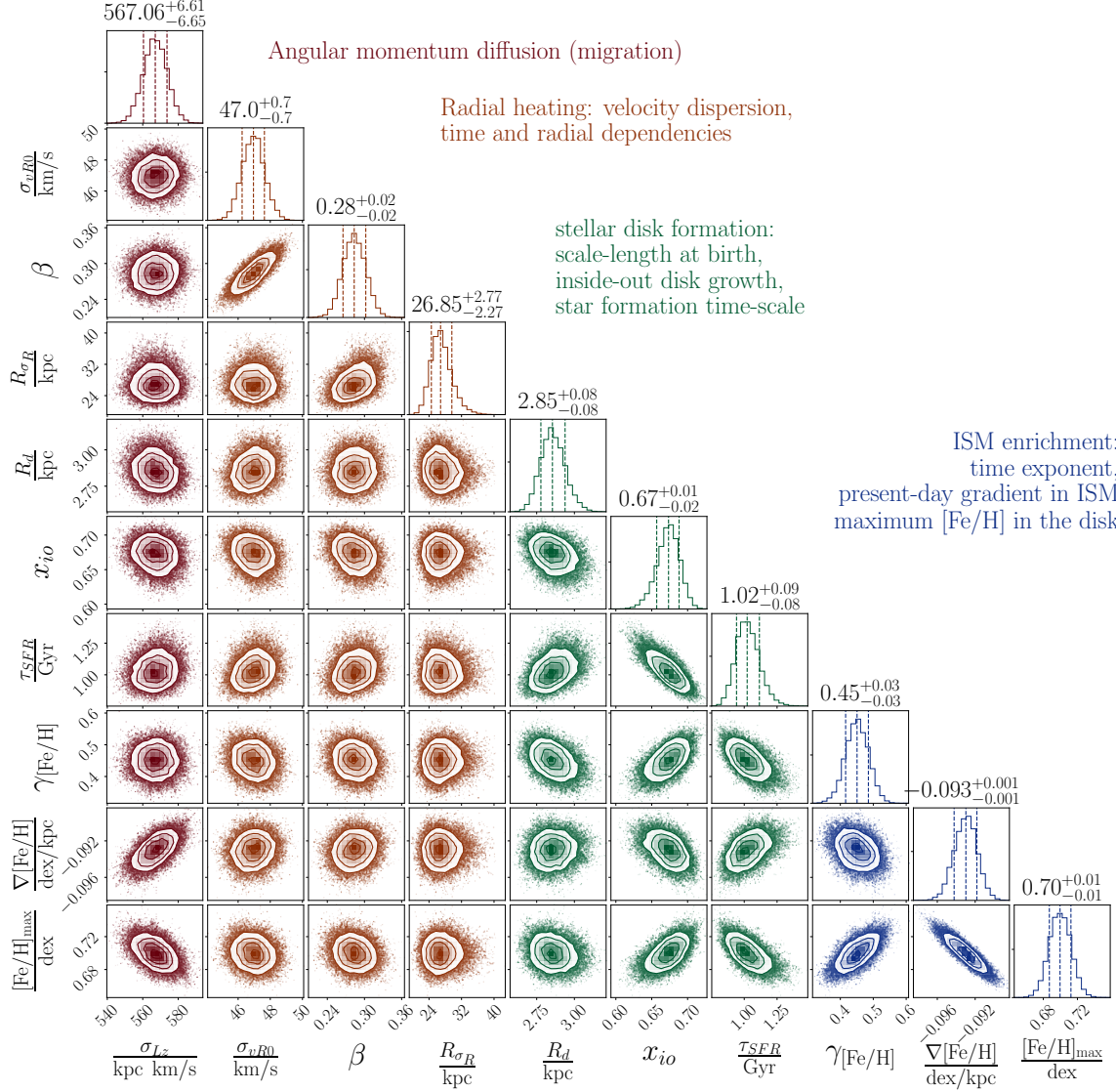
Figure III.4: Posterior distribution of the parameters from a model fit to 7000 stars from APOGEE DR14. σ_{Lz12} is the diffusion coefficient in angular momentum in kpc km/s. The other parameters are: radial velocity dispersion [km/s], time exponent for heating, scale-length of heating, disk scale length at birth, inside-out linear parameter, star formation time-scale, and enrichment parameters. Some parameters have important covariances, but all are well-constrained.

with parameters $\mathbf{p_m}$ as

$$p_{\mathcal{L}}(\{[\text{Fe/H}], \tau, l, b, D, v_R, v_\phi\}|\mathbf{p_m})$$
$$= \prod_{i=1}^{N_{\text{stars}}} p_{\text{dataset}}([\text{Fe/H}]_i, \tau_i, l_i, b_i, D_i, v_{R,i}, v_{\phi,i}|\mathbf{p_m}). \tag{III.19}$$

We use uniform priors with wide ranges in the parameter space, and enforce distances, spatial scales and time-scales to be positive. We first maximize the likelihood (Nelder & Mead, 1965), which gives the results in Table III.1. We start the optimizer from different initial conditions to lower the chances of the optimizer becoming stuck in local maxima. Using the MCMC sampler *emcee* (Foreman-Mackey et al., 2013), we then sample the posterior,

$$p_{\text{pos}}(\mathbf{p_m} \mid \{[\text{Fe/H}], \tau, l, b, D, v_R, v_\phi\})$$
$$\propto p_{\text{prior}}(\mathbf{p_m})p_{\mathcal{L}}(\{[\text{Fe/H}], \tau, l, b, D, v_R, v_\phi\} \mid \mathbf{p_m}) \tag{III.20}$$

using 12,000 iterations (> 50 times the auto-correlation time) and 52 walkers. We initialize the MCMC sampling uniformly in a hypercube (of size greater than 8 times the error bars quoted in Fig III.4) centered on the maximum likelihood estimates.

The posteriors of the model parameters are illustrated in Fig. III.4. The parameters of interest are the dynamical parameters: $\{\sigma_{\text{Lz12}}, \sigma_{vR0}, \beta, R_{\sigma_R}\}$, in red and orange in Fig. III.4. We treat the other model parameters as nuisance parameters and marginalize over them, although we comment briefly on them in Section III.5. There are no degeneracies and only weak covariances. In particular, the estimate of radial migration (or spread in angular momentum) σ_{Lz12} is slightly correlated with the metallicity gradient. This is expected because the information on radial migration comes from the scatter in metallicity. Stars born in a galaxy with a shallower metallicity gradient will need to migrate larger distances to produce the same metallicity spread. The other notable covariance is between σ_{vR0} and β, which together quantify heating in the radial direction: σ_{vR0} is the strength, and β the time dependency. If most of the sample is dominated by stars of a given age (here 2

Gyr), then the two ways to reproduce the local velocity dispersion of stars of that age is to either have a greater strength, and a faster time evolution (small β), or a smaller strength and a more linear time evolution (larger β).

The other model aspects also seem well fitted since the overall distributions of the data are well recovered by the model (Fig. III.1) and their estimate is robust to the tests we have performed (Subsection III.5.4). This shows that the best fit model is also qualitatively a good fit. The parameter analogous to the scale-length of the disk at birth is about 2.9 kpc. The covariances are more important for the inside-out growth model aspects, which are treated as nuisance parameters in the present work. The measurements of inside-out growth are consistent with our previous estimate in Frankel et al. (2019) with $x_{io} \approx 0.7$, where the implications and shortcomings of fitting data with large age uncertainties are discussed extensively.

III.5   Best fit Milky Way Disk Model

Fig. III.4 illustrates that all model parameters are well constrained, that the *pdfs* are approximately Gaussian, and that for most parameter combinations the covariances are small. The model seems to be well-posed for and well-constrained by the data set. This holds true for its dynamical aspects (brown in Fig. III.4), inside-out growth (green), and ISM enrichment (blue). The best fit model is illustrated in a schema in Fig. III.5.

In the following subsections, we look at these different aspects more closely.

III.5.1   Migration strength and Age-Radial Velocity Dispersion

The strength of radial migration is encompassed in the model aspect $\sigma_{\mathrm{Lz12}}(\tau)$, the width of the distribution of stars of age τ about their mean angular momentum. We find $\sigma_{\mathrm{Lz12}}(\tau) = 567 \text{ kpc km/s} \sqrt{\tau/6 \text{ Gyr}}$. With a circular velocity of about 235 km/s, this corresponds to a migration scale of 2.4 kpc for the 6 Gyr stars.

Radial heating leads stars to increase their random motion in the radial direction. Using Eq. III.8, we find that the velocity dispersion at the Sun is about 43 km/s for
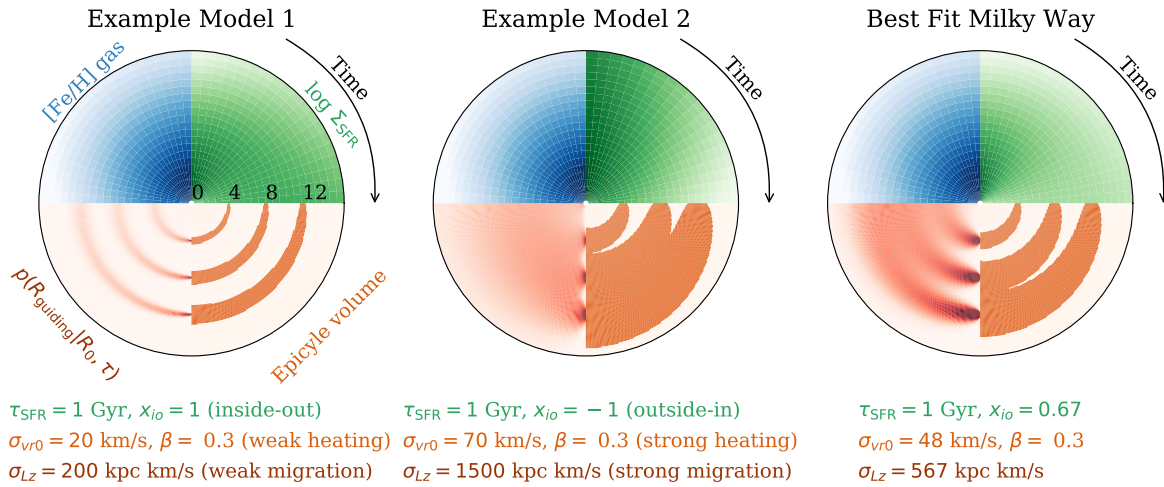
Figure III.5: Schematic illustration of the four main model aspects (left and middle panels), shown for the best-fit model in the right panel. Each panel represents a realization of the Milky Way disk model presented in Section III.3 with given model parameters (see legend). The radial axis in polar coordinates is Galactocentric radius. The angle in each quadrant represents time, increasing clockwise. For the top quadrants, time follows the evolution of the Galaxy. For the bottom quadrants, time is time since the birth of a star, tracing the evolution of its orbit. Each quadrant of the disk is color-coded by one of the model aspects. Going clockwise from top left, they display (i) the gradual enrichment of the gas in iron (top left, blue), (ii) the gradual build up of the disk (top right, green), (iii) the radial range occupied by stars born at 4, 8, and 12 kpc due to their radial motion (epicycle volume, bottom right, orange) and (iv) the probability density of the same stars to have their guiding radius at different places in the disk due to radial mixing (bottom left, red). At birth, stars are assumed to be on near circular orbits so, as can be seen in all panels, the three orbits born at 4, 8, and 12 kpc can be easily disentangled. Model 2 (middle) is undergoing strong radial mixing and strong radial heating, which mixes the orbits such that the *pdfs* of the stars cover almost the entire disk. Model 1 (left) has only modest radial heating and migration. The actual best fit model (right) falls in between these two regimes, where stars mix significantly, but not enough to erase all dynamical memory of their birth conditions.

the ~ 6 Gyr stars, in line with Nordström et al. (2004) and Mackereth et al. (2019), and that the age dependency is $\tau^{0.3}$. In the epicycle approximation, radial heating leads to epicycle amplitudes typically of $A_{\mathrm{epi}} = \sqrt{\sigma_r^2(\tau)/\kappa^2} \approx 1.5$kpc for the older stars, as illustrated in Fig. III.5. The parameter R_{σ_R} best fit value is ≈ 27 kpc, whereas it has been commonly assumed to be of order $2 \times$ disk scale length ($\sim 6 - 7$ kpc). The original motivation for the exponential decay of the radial velocity dispersion was to keep a n overall disk with a constant global scale height h_z and a constant ratio σ_r/σ_z (van der Kruit & Searle, 1982), with $\sigma_z \propto h_z \sqrt{\rho} \propto \exp(-R/2R_d)$. But (1) the agents driving the evolution of the vertical and radial motion are likely different (e.g Sellwood, 2014) so σ_r and σ_z need not be related, and (2) populations of given age in the Galactic disk are now known and expected to flare (Ting

& Rix, 2019; Minchev et al., 2015; Bland-Hawthorn & Gerhard, 2016; Bovy et al., 2016b; Kawata et al., 2017b; Sanders & Das, 2018; Mackereth et al., 2017, 2019): the scale height of coeval stellar populations increases with radius, hence there is no expectation for R_{σ_R} to be small at a given age. This is distinct from the population-integrated properties of the Galaxy, which, in a manifestation of Yule-Simpson's paradox, can even show opposite trends to the coeval populations (see Fig. 1 of Minchev et al., 2019).

III.5.2 Inside-out Growth and the Metallicity Profile

The model fit favors a global inside-out growth of the disk, where stars formed first from low angular momentum gas, and star formation moved gradually to higher angular momentum ($x = 0.68$). This is in accord with the results of Frankel et al. (2019), who used a similar model in radius on the APOGEE-RC data set of the 12th data release. Our model is illustrated for different values of x, as well as for the best fit, in Fig. III.5 in green (top right quadrants). As the disk forms from inside-out, the enrichment in metals (here iron, [Fe/H]) proceeds with a radial gradient and still on-going enrichment (Figure III.3).

III.5.3 The Orbit-Age-Abundance Distributions

The distributions most directly affected by radial mixing are the metallicity distribution functions of stars at given radius $p([\text{Fe/H}]|R)$ (Hayden et al., 2015; Loebman et al., 2016), whose shape is influenced by the amount of metal-rich stars incoming from the inner disk the metal-poorer stars coming from the outer disk, and the initial metallicity profile of the gas from which stars formed, set by the inside-out star formation history (Schönrich & McMillan, 2017a; Schönrich & Binney, 2009a).

The available data, and the framework we developed in this work, allow us to make comparisons in more dimensions, reproducing the entire data set's 5-dimensional distribution $p([\text{Fe/H}], \tau, J_R, L_z, R)$ resulting from the global evolution of the Milky Way disk (and selection procedures). Figure III.6 illustrates the distributions $p([\text{Fe/H}], \tau, J_R, L_z, R)$ observed in the data set (brown) and predicted by
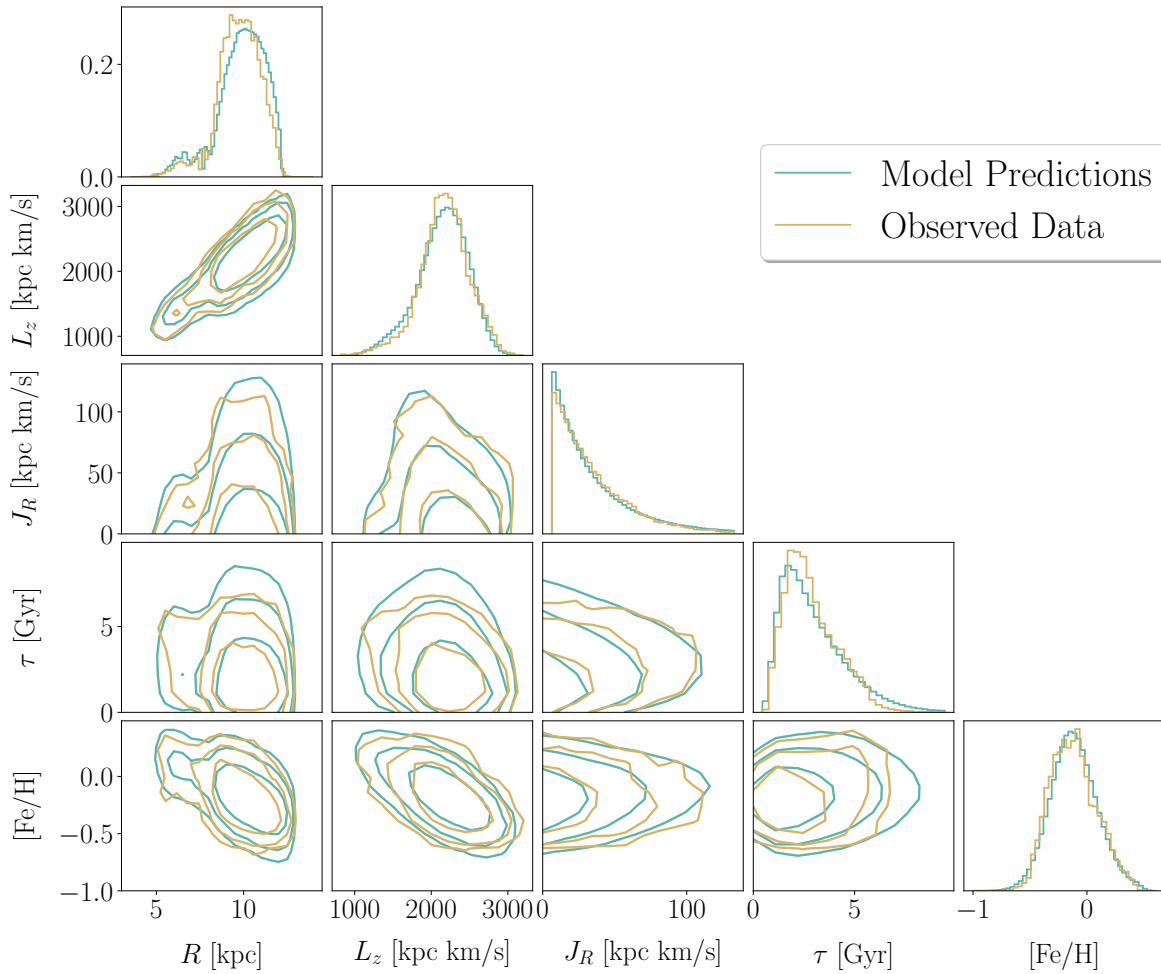
Figure III.6: Best fit model predictions in data space (brown), generated from the MLE estimates of Table III.1, compared with observed densities in APOGEE DR14 data (brown). The model agrees remarkably well with the data: the 1D distributions are generally well reproduced, but more importantly the 2D dististributions and the entire shape of the density the 5 dimensional data space agrees well. The age-metallicity-orbit structure of the dataset seems well recovered.

the best fit model for the data set (green). Overall, the observed distributions are globally well recovered by the model fit. The metallicity radial profile (bottom left panel of the corner plot in Fig III.6), which arises from (1) chemical evolution and (2) subsequent orbit evolution is well described, and illustrates that the metallicity distribution functions $p([Fe/H], R)$ and the age-metallicity distributions (4th panel, bottom), usually the main diagnostic used in the literature, are all well reproduced. The distributions in L_z and J_R reflect both the secular evolution of the disk and APOGEE's spatial selection function.

III.5.4 Verifications: Model Variants and Parameter Recovery

During the construction of this model, we tested a set of model variants. We first tested the parameter recovery on noised mock data, and rejected all models for which we could not recover the true parameters. For example, we could not add a parameter to quantify how much angular momentum is actually conserved while stars diffuse in angular momentum (by e.g., fitting for a simple form of diffusion coefficient $D^{(1)}$ from Eq. (III.4)) because there is a degeneracy with the enrichment model.

Once the best model candidate (which is presented in Section III.3) was identified, the best fit parameters found with MLE, and the posterior sampled with MCMC, we performed a series of additional tests to verify different aspects of our results. We investigated whether uncertainties in our integral calculations introduced systematics or biases in the estimation of the parameters, by computing it using different model realizations (by changing the model parameters) and Monte Carlo samples of different sizes, and found no change in the results within 1σ (for both the data used in the present paper and mock samples generated from our model). We generated and fitted mock data with different noise levels (increasing or decreasing the formal uncertainties by a few percent), and the best fit parameters are well recovered too.

We studied the effect of varying the model of the potential on the estimates of the dynamical parameters. Using the default *MWPotential2014* in *Galpy* with a circular velocity of 220 km/s at 8 kpc, we found small changes in the estimates of $\sigma_{\text{Lz}12}$. These changes are however expected and quantifiable. The estimate for radial migration dropped by about $\sigma_{Lz220} \approx \sigma_{\text{Lz}12} \times \frac{220}{235}$, which is what one expect since the metallicity scatter, and the radial metallicity gradient in the stars are the same, and $\sigma_{\text{Lz}12} \approx \sigma_{[\text{Fe/H}]}v_{\text{circ}}/\nabla[\text{Fe/H}]$. But a full exploration of alternate gravitational potentials is beyond the scope of the present work. The potential model we are currently using is well constrained by external data (Bovy & Rix, 2013; Bovy, 2015).

III.5.5 Model Limitations

Forward modeling the orbit-age-[Fe/H] structure of the APOGEE×Gaia dataset, with an interpretable model that accounts simultaneously for diverse aspects of Galaxy evolution, data uncertainties and the survey selection function, provides a framework with a great potential for Galactic archaeology. The best fit model is well tested and reproduces the observed trends and distributions of the data set well. However, at present our model lacks some features that one might desire from a full physical model of the Galaxy:

1. Radial migration of stars in the Milky Way is measured indirectly through its impact on the age-metallicity distributions. The strongest assumption we have made in that direction is that the birth age-metallicity relation was tight and monotonic, and that our choice of functional forms to model the evolution of [Fe/H] were flexible enough and adequate. However, any inadequacy or inappropriate rigidity in that model will be measured as radial migration in this context, so $\sigma_{\mathrm{Lz}12}$ could be a lower limit on the strength of radial migration.

2. Our description of L_z change is only an approximation of the solution to the diffusion equation (Eq. III.4) that is valid far from the Galactic center, and is not self-consistent. It is likely that the strength of migration is a function of radius and time (e.g. Kubryk et al., 2013; Toyouchi & Chiba, 2018), which in our simple diffusion picture is ignored. Additionally, Eq. III.4 should contain a source term for star formation, which we have modeled separately. This should not impact the results drastically, as the two extreme regimes are recovered: in the limit where radial migration is asymptotically inefficient, stars' current L_z distribution is a Dirac function of their birth distribution, and the overall L_z distribution is the exponential profile used for initialization in Eq. III.2. In the limit where radial migration is asymptotically efficient, our imposed steady state solution for the L_z distribution recovers the results of Herpich et al. (2017) for a flat circular velocity curve, with the same scale length R_{d0}.

3. The secular evolution processes in the disk (diffusion in L_z and increase in J_R) were treated independently. However, they are expected to be covariant. The covariance depends both on the heating agents, (e.g. as in Eq. III.27) and the likelihood of a star of given actions to be trapped at corotation resonance and thereby migrate radially (Daniel & Wyse, 2018; Solway et al., 2012; Vera-Ciro et al., 2016; Minchev et al., 2012a) . Ideally, we should treat the entire Fokker-Planck equation in action space. However, we argue that this should have only a small impact on the present results, because the disk remains relatively cold (J_R does not increase much) and L_z diffusion is stronger by an order of magnitude. Additionally, in our modelling, both heating and migration are conditioned on time, making their conditioning on each other included implicitly . This may blur out such covariances on large spatial and time-scales. However, in the Solar neighbourhood, there are indeed clear over-densities in the $L_z - J_R$ plane, some of them arising along Lindblad resonances with the bar or other non-axisymmetries (Sellwood & Binney, 2002; Trick et al., 2019a,b)). These portray the impact of the most recent set of non-axisymmetries.

4. The treatment of radial heating, with the time dependence β could depend on angular momentum. Indeed, as shown in simulations, the heating time dependence β could depend on spiral arms and Galactocentric radius (Aumer et al., 2016a; Binney & Tremaine, 2008). The radial dependence of β in the age-velocity dispersion relation in the Milky Way disk was confirmed in Mackereth et al. (2019). The present model fit leads to $\beta \approx 0.3$, which is typical and agrees with the largest part of the disk values in Mackereth et al. (2019), but not in the outer disk where their β decreases, possibly due to the weakening of spiral strength.

III.6   Astrophysical Implications and Discussion

Secular processes drive stellar orbits to evolve, which can have a large impact on a disk galaxy's evolution. If strong, such diffusion processes lead to a near complete
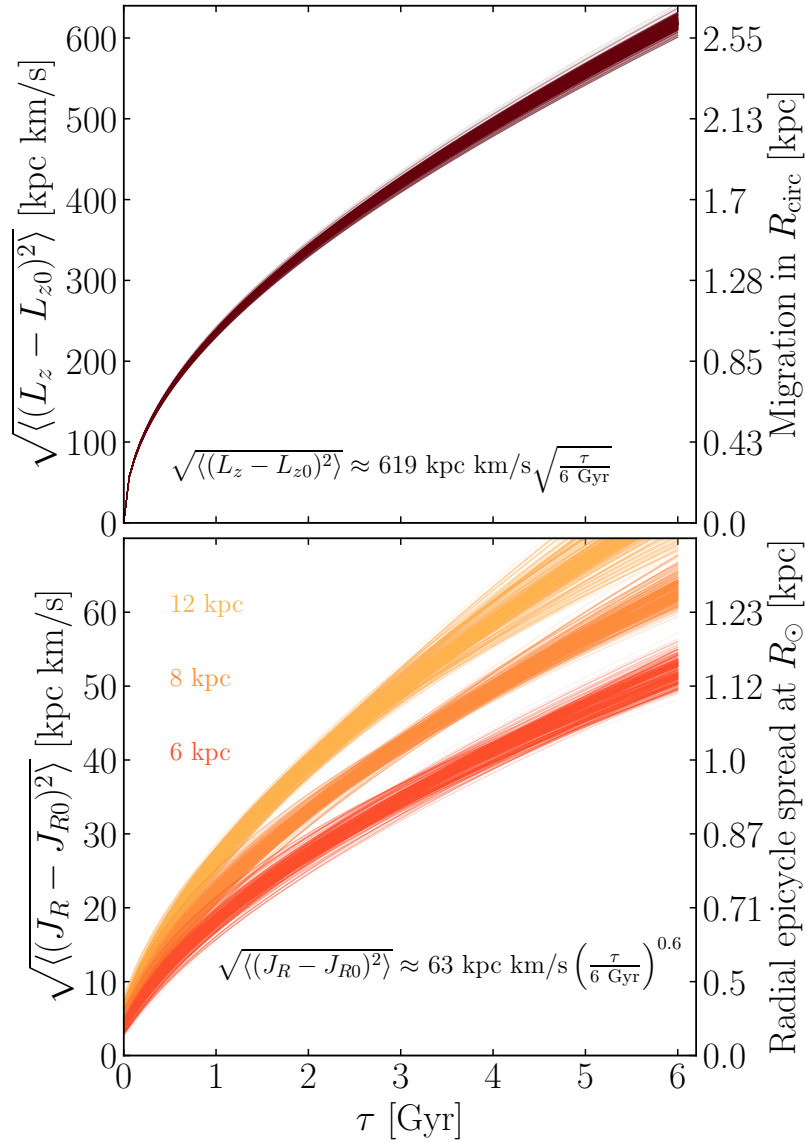
Figure III.7: Secular evolution of the Milky Way disk implied by the best fit model, as diffusion in angular momentum (top) and radial action (bottom) drawn from the MCMC samples illustrated in Fig III.4 and using the model equations, Galactocentric radii 6, 8 and 12 kpc. The right-hand side y axis shows the equivalent in distance units. Top: we assumed a constant circular velocity curve $R_{\rm circ} = L_z/v_{\rm circ}$ with $v_{\rm circ} = 235$ km/s. Bottom, shown for the Solar Galactocentric radius: we assume the radial spread about the guiding radius due to the epicycle motion corresponding to a radial action J_R at R is $\sqrt{\langle (R - R_g)^2 \rangle} = \sqrt{J_R/\kappa} = A/\sqrt{2}$ with κ the epicycle frequency and A the epicycle amplitude.

dynamical memory loss, challenging efforts in Galactic archaeology to try to infer a galaxy's history from its present-day properties. Radial migration is such a process and was shown to be strong in simulations (e.g. Minchev et al., 2013), but had not been well quantified across the Milky Way disk.

We have presented the first global model relating stellar ages, chemistry, and dynamics, which we have fitted to high-quality data over a large extent of the Galactic's low-α disk, accounting rigorously for data uncertainties and selection effects. The model builds on and extends Sanders & Binney (2015)'s pioneering framework. The previous modeling to **?** was based on more local data and did not incorporate stellar ages. In this work, we have forward-modelled the distributions of stellar ages, [Fe/H], L_z and J_R with a radially-dependent star formation history accounting for the inside-out growth of the disk, a parametric chemical evolution model, and birth and action-based radial heating and radial migration orbit-evolution model. We have fitted all aspects of this model simultaneously, but focus on the orbit evolution, and treated the other model aspects as a nuisance. We have used the APOGEE×Gaia red clump sample, a dataset that covers a large part of the Galactic disk, from $R \sim 4$ kpc to 13 kpc, a scale larger than the typical radial migration scale of a few kpc.

Large efforts have been made to measure the strength of radial migration in the Milky Way, but previous works lacked data on large spatial scales, making quantifying a large scale diffusive process a hard task. Furthermore, previous approaches did not use stellar ages (e.g. Sanders & Binney, 2015) instead relying more tangentially on the known local relationships between stellar age and kinematics. Other methods measured a scatter in the [Fe/H]-[α/Fe]-R directly, but without accounting simultaneously for the galactic evolution processes that could contribute to it, thus lacking a framework that could use and describe the entire dataset (e.g. Hayden et al., 2015). In **?**Frankel et al. (2019), we developed a framework accounting for the main evolution aspects of the Milky Way disk, with a radially-dependent star formation history, chemical evolution of the disk, and evolution of the stars' Galactocentric radius. This model constrained a global orbit migration scale of about 3 kpc $\sqrt{\tau/6\,\mathrm{Gyr}}$, implying that radial mixing happens on scales comparable to the

scale-length of the Milky Way disk. However, this description of the disk only measured diffusion in Galactocentric radius, and not angular momentum, so failed to disentangle the two major processes causing stars to change Galactocentric radius ('churning' and 'blurring').

III.6.1   Secular Dynamical Evolution

Our model describes the in-plane secular evolution of the Milky Way's low-α disk and disentangles the contributing processes: diffusion in angular momentum ('churning') and increase in radial action ('blurring', or 'radial heating'). As both processes are diffusion in action space, we can quantitatively compare their strengths in a meaningful way, and here we choose to inspect the root-mean-squared (rms) deviation in the actions.

We first work out the rms deviations of the actions expected in the Solar neighbourhood from external data, and will then show that our more global model recovers this particular case. From a simplistic perspective, the rms deviation in the radial action is related to the disc properties as

$$\sqrt{\langle (\Delta J_R)^2 \rangle} \approx \frac{\sqrt{2}\sigma_R^2}{\kappa}. \tag{III.21}$$

Taking the 'textbook' quantities for the radial epicyclic frequency $\kappa \approx 37\,\text{km/s/kpc}$ and $\sigma_R \approx 38\,\text{km/s}$ for old stars from Binney & Tremaine (2008), we find $\sqrt{\langle (\Delta J_R)^2 \rangle} \approx 55\,\text{kpc km/s}$. Likewise, the rms deviation in the angular momentum can be simply expressed as

$$\sqrt{\langle (\Delta L_z)^2 \rangle} \approx \frac{v_{\text{circ}}\sigma_{[\text{Fe/H}]}}{|\mathrm{d}[\text{Fe/H}]/\mathrm{d}R|}. \tag{III.22}$$

Using approximate values for the solar neighbourhood of $\sigma_{[\text{Fe/H}]} = 0.2\,\text{dex}$ for the metallicity dispersion (Nordström et al., 2004), $|\mathrm{d}[\text{Fe/H}]/\mathrm{d}R| = 0.062\,\text{dex/kpc}$ for the radial metallicity of young stars (Luck & Lambert, 2011) and $v_{\text{circ}} = 235\,\text{km/s}$ we find $\sqrt{\langle (\Delta L_z)^2 \rangle} \approx 750\,\text{kpc km/s}$. These simple calculations confirm that plausibly $\sqrt{\langle (\Delta L_z)^2 \rangle}$ is an order of magnitude larger than $\sqrt{\langle (\Delta J_R)^2 \rangle}$.

Expanding to the greater extent of the disk with our full model, from Eq. III.6,

the variance of the angular momentum distribution of a stellar population of age τ is

$$\langle (L_z - L_{z0})^2 \rangle = \sigma(\tau)^2 + (D\tau)^2. \tag{III.23}$$

where the drift term $(D\tau)^2$ is subdominant, contributing only $\sim 20\%$ to $\langle (L_z - L_{z0})^2 \rangle$.

Similarly, the variance of the radial action of a population of age τ is

$$\langle (J_R - J_{R0})^2 \rangle = 2\langle J_R \rangle^2 + 2J_{R0}^2 - 2J_{R0}\langle J_R \rangle, \tag{III.24}$$

with J_{R0} the radial action at birth, which we assume here is zero since in the model stars are born on near-circular orbits. $\langle J_R \rangle = \sigma_R^2/\kappa$ is the mean radial action as defined in Eq. III.7. Both of these quantities are plotted as functions of τ in Fig. III.7. Using a reference age of $\tau_m = 6\,\text{Gyr}$, we find at 8 kpc (see Fig. III.7 for the spatial variations)

$$\begin{aligned}
\sqrt{\langle (L_z - L_{z0})^2 \rangle} &\approx (619 \text{ kpc km/s}) \left(\frac{\tau}{6\,\text{Gyr}} \right)^{0.5}, \\
\sqrt{\langle (J_R - J_{R0})^2 \rangle} &\approx (63 \text{ kpc km/s}) \left(\frac{\tau}{6\,\text{Gyr}} \right)^{0.6}.
\end{aligned} \tag{III.25}$$

We note that up to a factor between 1.2 and $\sqrt{2}$, these quantities are very close to $\sigma_{\text{Lz12}} = 572$ kpc km/s and the mean radial action $\langle J_R \rangle = \sigma_R^2/\kappa = 45$kpc km/s respectively, so our general conclusions do not depend much on the details of our choice of reference quantities (i.e. σ_{Lz12}versus $\sqrt{(\Delta L_z)^2}$).

A spatial representation of the diffusion in angular momentum and increase of radial action is illustrated in Fig. III.5. We show two examples for the secular evolution of the disk for the first two panels (weak mixing and heating, and strong mixing and heating), and the best fit in the third panel. The second y axis of Fig. III.7 also illustrates this more quantitatively.

Using the same APOGEE RC dataset, ?Frankel et al. (2019) measured a migration strength in Galactocentric radius of 3.1 kpc$\sqrt{\tau/6\,\text{Gyr}}$, which is slightly larger than we have found here. These models were purely spatial and ignored the dynamics.

The spreads in the metallicity distributions in these models are wholly accounted for by the radius migration and its strength is more simply linked to the radial metallicity gradient (as in Eq. (III.22)). In the new dynamical model presented here, spreads in the metallicity distribution are due to a combination of both migration and heating, the latter of which introduces more extreme metallicity stars from the inner and outer disc at their apo- and pericentres respectively, and so further broadens the metallicity distributions. This reduces our measured radial migration strength to $\sqrt{\langle(\Delta L_z)^2\rangle}/v_{\text{circ}} = 2.6 \text{ kpc}\sqrt{\tau/6\,\text{Gyr}}$ with the difference coming from the radial heating.

III.6.2   Implications of a Strong L_z Diffusion Process

If the strength of angular momentum diffusion, of the order of the mean angular momentum of the Galaxy, is typical to all disk galaxies, this redistribution has important implications for galactic archaeology for external galaxies. For the Milky Way, the strength of radial migration can be measured through a physical [Fe/H]-age-L_z scatter, obtained by data for individual stars. Such a framework may not be applicable in external galaxies beyond the Local Group, where all properties are integrated. Studying stellar populations in external galaxies may lead to good present-day age histograms and present-day mass-weighted age gradients, but reflect only mildly the formation of galaxies due to important dynamical memory loss: i.e. age and metallicity radial gradients weaken (Frankel et al., 2019).

As argued in Herpich et al. (2017), an asymptotically strong redistribution of stellar angular momenta in cold disks could naturally lead disk profiles to follow exponential distributions, as is observed in disk galaxies (e.g., de Vaucouleurs, 1948; Freeman, 1970). Since disks are not always expected to form with exponential profiles (e.g. Roškar et al., 2008b), a strong diffusive process that leads to an exponential profile irrespective of the initial conditions could reconcile the observations with simulations of galaxy formation.

Even though mixing processes are strong, they are not strong enough to erase all gradients in which case even using chemical-age information would not rewind stars back to their birth conditions because the final state of the system would be

independent from its initial state. In the Milky Way, metallicity and age radial gradients are weakened, but not erased.

However, any modelling of the Milky Way's chemical evolution requires us to account for the strong radial orbit redistribution. For instance, a local age distribution might reflect better the global star formation history of the disk rather than the local star formation history, as a local sample of stars, even those on circular orbits, may contain stars born kiloparsecs away and lack stars born locally.

III.6.3   Disentangling L_z-Diffusion from Heating

Dynamical processes produce correlated changes in the actions of stars. Assuming $\Delta J_R = f(\Delta L_z)$, the general function f will depend on the specifics of the dynamical interaction. In the present work, we do not explicitly model the possible interactions leading to radial heating and angular momentum diffusion; we only measure their effect over 6 Gyr of evolution with an effective model, and find that across the disk

$$\sqrt{\langle (J_R - J_{R0})^2 \rangle} \approx 0.1 \sqrt{\langle (L_z - L_{z0})^2 \rangle}. \tag{III.26}$$

This result can already provide some global constraints on the nature of dynamical processes across the Milky Way, but not on the details of the secular interactions. The net changes are not directly comparable to the changes expected over single migration events $\Delta J_R = f(\Delta L_z)$. To zeroth order, near the main resonances of a non-axisymmetry rotating at a constant pattern speed Ω_P (e.g. the bar or a spiral wave), the change of radial action is related to the change in angular momentum through (e.g. Sellwood & Binney, 2002)

$$\Delta J_R = \frac{\Omega_P - \Omega}{\kappa} \Delta L_z. \tag{III.27}$$

Here κ and Ω are the radial and azimuthal frequencies. Sellwood & Binney (2002) point out that near corotation ($\Omega = \Omega_P$), ΔJ_R should be very small even though ΔL_z can be large – a star can move from circular orbit to circular orbit. Therefore, there is no <u>dynamical</u> evidence that a star found on a near circular orbit at radius R

today was not born on a different circular orbit. Around the Lindblad resonances, where $\kappa = \pm m(\Omega - \Omega_P)$, interactions with non-axisymmetries tend to heat the disk $\Delta J_R = \pm \Delta L_z / m$. More recent works argue that $\Delta J_R = f(\Delta L_z)$ is not necessarily linear, and that angular momentum redistribution at corotation might not always occur without changes in J_R: resonances can overlap, leading to non-linear effects and stochastic motions of the stars (e.g Minchev et al., 2011, 2012b; Daniel et al., 2019). In this model context, our findings suggest that migration near corotation was important.

In addition to these non-linear effects, ΔL_z and ΔJ_R may deviate from Eq. III.27 if spiral perturbations do not rotate as solid bodies as seen in simulations (i.e. with a pattern speed that changes with Galactocentric radius Quillen et al., 2011; Grand et al., 2012) or indirectly with extragalactic observations (Merrifield et al., 2006; Masters et al., 2019), or if their pattern speed is a function of time.

The simulations described above, as well as those of Brunetti et al. (2011) and Loebman et al. (2016), have brought understanding of the processes involved in the secular evolution of disk galaxies and the processes at play in radial orbit migration, and have pioneered qualitative comparisons with Milky Way data. However, they are not directly comparable to observed data in the Milky Way because observed data are noisy and do not represent the full Milky Way disk. More importantly, the present view of the Milky Way only represents the equivalent of the final snapshot of a simulation ~~as argued in~~ and must be modeled as such (e.g. Aumer et al., 2016a). This means age-kinematic relations differ from heating histories (as much as time differs from age) and our effective models cannot be used to recover robustly the full evolutionary history of the Galaxy. Simulations are necessary to guide the construction of realistic and physically motivated forward models and to make the link between the global measure of $\sqrt{\langle (J_R - J_{R0})^2 \rangle}$, $\sqrt{\langle (L_z - L_{z0})^2 \rangle}$ and the instantaneous changes ΔJ_R and ΔL_z.

III.6.4 Implications for the Sun and the Solar System

In a model with significant radial migration, the Sun potentially formed quite far from its present Galactocentric radius. Here we analyse the most likely history of

the Sun using our model.

Using Eq. IV.17 with the Sun's age of $\tau_\odot = 4.6$ Gyr (Bonanno et al., 2002) and $[\mathrm{Fe/H}]_0 = 0 \pm 0.05$ dex (Asplund et al., 2009), we find the birth angular momentum of the Sun was $L_{z0\odot} \approx 1824 \pm 127$ kpc km/s . If, at the time of its formation, the circular velocity corresponding to this angular momentum were 235 kpc km/s, this would correspond to a birth Galactocentric radius of 7.8 ± 0.6 kpc, which is 5% closer to the Galactic center than today. This is quite different from previous estimates of the Solar birth location in **?** (5.3 kpc), but in better agreement with Minchev et al. (2018) (7.3 kpc) and Haywood et al. (2019a). We interpret this significant change of Solar birth location from our previous estimates as a consequence of two model modifications. Firstly, the introduction of the drift term D towards the inner disk in the diffusion equation III.4. In **?**, D was set to zero, which resulted in global outwards migration due to the negative density gradient, with a disk profile that broadens with time. Here, we approximately conserve angular momentum, with a disk profile remaining approximately constant over time. As a result, stars have a higher probability to migrate inwards than outwards. Secondly, our chemical enrichment description (Section III.3.6) is different: it is a function of birth angular momentum and not birth Galactocentric radius, and we have imposed a flattening of the [Fe/H] profile in the inner disk, which is more physically and observationally motivated.

The Solar birth Galactocentric radius is still widely debated and not well constrained. Most chemical evolution arguments lead to birth radii estimates between its present-day radius and 3 kpc closer to the Galactic center (e.g. Wielen, 1977; Nieva & Przybilla, 2012; Minchev et al., 2018; Sanders & Binney, 2015; Feltzing et al., 2020; Kubryk et al., 2015; **?**), except for Haywood et al. (2019a) who argue that the Sun is a typical outer disk star. Even though different models infer different birth radii for individual stars, the overall radial migration rate estimate remains similar in all models, as shown in Feltzing et al. (2020). Finally, Martínez-Barbosa et al. (2015) use backward integration over the Sun's lifetime, concluding that the Sun was born in the outer disk. However, without knowledge of the past evolution of the Milky Way's potential, such an exercise is not trivial. Better estimates of the

Solar birth place may additionally produce tighter constraints on the environment in which the solar system has evolved (e.g. encounters with Giant Molecular clouds Kokaia & Davies, 2019). However, knowing both the Solar birth and current orbits does not imply that the Sun has always remained between the two: it could well have migrated back and forth to the same place, since the typical migration distance for a 4.6 Gyr old star is about 2 kpc .

III.6.5   Application to the Solar Siblings' Orbit Distributions

We estimate the possible present-day L_z and J_R ranges occupied by stars that were born with the same $L_{z,0}$, the same [Fe/H], and at the same time as the Sun with Eq. III.6. Assuming solar siblings undergo phase mixing rapidly (the Sun has undergone $\sim$ 20 Galactic orbits), there is then no dynamically noticeable difference between 'sharing the same birth cluster as the Sun' and 'being born with the same $L_{z,0}$, and time'. From our model fit, 95% of these stars should currently have $550 \leq L_z \leq 2770$ kpc km/s and $J_R \leq 130$ kpc km/s. This is roughly consistent with the results of Webb et al. (2019), who used simulations to investigate the present-day positions of solar siblings in the (L_z, J_R, J_z) space in different possible potentials and constrained present-day solar siblings angular momenta to $353 \leq L_z \leq 2110$ kpc km/s and $J_R \leq 116$ kpc km/s. The exact values of these bounds should depend on the detailed history of the Milky Way disk, but their model gives an angular momentum range of about 2000 kpc km/s, which is close to our $2\sigma(\tau)$ value.

However, if the abundance profile of the gas in the Galactic disk is really axisymmetric, then there is no chemical information on the phase to disentangle whether a star is born in the same birth cluster as the Sun, or just at the same Galactocentric radius (or $L_{z,0}$). Therefore, the Sun could well have been born in a (possibly now fully disrupted) birth cluster that is different from the usual candidate cluster M67, which is known to have a similar age and metallicity as the Sun (Yadav et al., 2008; Heiter et al., 2014). Recent work has shown M67 is unlikely to be the Sun's birth cluster, but this is not fully ruled out (Webb et al., 2019; Jørgensen & Church, 2020). Instead the Sun's birth cluster could have formed at the same radius and time, but at a distinct azimuth from M67 . The recent analysis of Ness et al. (2019b) shows

that stellar orbits and abundances can be well predicted with only [Fe/H] and age, implying that our present analysis contains the most essential elements for chemical tagging.

III.6.6   Limitations and caveats

The physical limitations of our modeling were discussed extensively while presenting the best fit Milky Way disk model in Subsection III.5.5: the model could improve by allowing a time- and radius-dependent strength of radial migration and radial heating.

We now discuss another approximation we have made while constructing the model: the model for the population selection of the red clump stars. In practice, the red clump selection is based on a neural network trained to classify stellar evolutionary stage from their spectra, trained on asteroseismic data (Ting et al., 2018b). In the model, we have approximated the selection of red clump stars as a cut in logg-Teff-color space as in Bovy et al. (2014). This approximation is well motivated because (1) the classifier is currently one of the best methods to obtain a pure and complete sample of red clump stars given their spectra (Ting et al., 2018b), and (2) the modeled cut in logg-Teff-color space is, in theory, a good approximation to selecting core helium burning stars.

However, this approximation is conceptually not satisfying (as for other methods based on data driven selection functions), and with no known applicable and rigorous solution: our treatment of the population selection function in the model is conceptually inconsistent with the actual selection of stars. The actual data-driven selection of stars is not trivial to forward model: this method takes a star's spectrum as input and returns asteroseismic parameters $\Delta\nu$ and ΔP, thereby disentangling RC and secondary RC. Therefore, to assess selection effects in our forward model properly, we should generate a set of theoretical spectra of various ages, T_{eff}, $\log g$ and various abundances, add noise and instrumental effects, and then pass these spectra to the neural networks that selected the red clump stars to evaluate the fraction of generated stars that becomes classified as red clump, as a function of age and metallicity (or any stellar quantity that we wish to model). Hence, if for example

the neural networks were to fail in some areas of the parameter space (where e.g. the training data are sparse), the effects would be fully modelled.

As machine learning-based selection functions are (justifiably) becoming important in the field of astrophysics, they will also need come with a consistent modeling framework in the future.

Instead, we have approximated this population selection effect as a function of age from Bovy et al. (2014) as in **?**Frankel et al. (2019) and assumed it was sufficient for the purpose of our work. We argue qualitatively that this should have only a small impact on the present work: such a selection should mainly affect the distribution of ages (at large ages, were the training sample was sparse) of our sample, that is most closely linked to the star formation history in our modeling context. However, we treat this star formation history as a nuisance aspect and marginalize over it, and assume the red clump selection does not bias significantly the dynamical parameters of the stars (beyond the covariances between age and kinematics, which we do model), and we focus on radial migration and diffusion in action space. As can be seen in Fig. III.4, the dynamical parameters are not correlated with the star formation history.

III.7   Summary

We have presented and applied a global model for the secular evolution of the Milky Way's low-α disk. The model accounts for an inside-out star formation history, [Fe/H] gradual enrichment, and the subsequent evolution of a stars' orbits as diffusion in action space. Applying this model to the APOGEE red clump stars, we have fully accounted for the selection function of the survey and for data uncertainties. The data are constraining, and the model fit with MCMC implies, in this context, that

1. L_z redistribution evolves as $\sqrt{\langle (L_z - L_{z0})^2 \rangle} \approx (619 \text{ kpc km/s}) \left(\frac{\tau}{6 \text{ Gyr}} \right)^{0.5}$, which corresponds to a migration distance of about 2.6 kpc for the 6 Gyr old stars (see Fig. III.7). In other words, for a coeval population of stars, 68% of them

will be within $2.6 \text{ kpc} \sqrt{\tau/6 \text{ Gyr}}$ of their birth radius and the remaining 32% will have migrated further;

2. J_R evolves as $\sqrt{\langle (J_R - J_{R0})^2 \rangle} \approx$ $(63 \text{ kpc km/s}) \left(\frac{\tau}{6 \text{ Gyr}} \right)^{0.6}$. This shows that redistribution in angular momentum is stronger than increase of radial action, by a fator ~ 10, leading us to conclude that radial migration dominates the evolution of the Galaxy's low-α disk. This leads the disk to remain kinematically cold, but with a strong dynamical memory loss, making it necessary to use chemical and age information to recover the birth conditions;

3. the Sun's birth angular momentum inferred from the best fit is relatively close to its present-day angular momentum with $L_{z0,\odot} \approx 1824 \pm 127 \text{ kpc km} s^{-1}$, but its siblings may have a large distribution in action space with a width of 2000 kpc km/s in L_z and 130 kpc km/s in J_R.

We have demonstrated that our approach can disentangle the diversity of dynamical phenomena that have shaped the Milky Way's disk. However, our parametric model is purely effective so does not capture the real complexities of individual dynamical processes, but only their average effect on the Milky Way. We hope that this may be solved in the future, by applying and coupling this model to more detailed simulations of galaxy evolution.

Acknowledgements

III.8   Combining the Model Aspects into a Global PDF

III.8.1   Global Milky Way Disk model

We show here how the different model aspects presented in subsections (III.3.2, III.3.4, III.3.6, III.3.5, III.3.7) are combined together to build the overall model for the Milky Way disk. Applying the probabilistic chain rule, and marginalizing over the dummy variable $L_{z,0}$, the different aspects of the model appear:

$$
\begin{aligned}
p_{\mathrm{MW}}(\tau, [\mathrm{Fe/H}], J_R, L_z, z | \mathbf{p_m}) &= \int p(L_{z,0}|\mathbf{p_m}) p(\tau|L_{z,0}, \mathbf{p_m}) \\
&\quad \times p([\mathrm{Fe/H}], J_R, L_z, z | R_0, \tau, \mathbf{p_m}) \mathrm{d}L_{z,0} \\
&= \int p(L_{z,0}|\mathbf{p_m}) p(\tau|L_{z,0}, \mathbf{p_m}) p([\mathrm{Fe/H}]|L_{z,0}, \tau, \mathbf{p_m}) \\
&\quad \times p(z|L_{z,0}, \tau, \mathbf{p_m}) p(J_R, L_z|L_{z,0}, \tau, \mathbf{p_m}) \mathrm{d}L_{z,0}.
\end{aligned}
$$

$$(\text{III.28})$$

The first term on the right hand side is the stars' birth angular momentum distribution (the first part of Subsection III.3.2). The second is the star formation history conditioned on birth angular momentum, resulting from an inside-out star formation history (second part of Subsection III.3.2). The third term is the distribution of metallicity in the star forming disk in function of time (modeled here as a Dirac function, since we are assuming a tight $L_{z,0} - \tau - [\text{Fe}/\text{H}]$ relation, Subsection III.3.6), the fourth term is the vertical distribution of stars in the disk, and the last one is the joint distribution of in-plane orbital properties (which we take as the azimuthal action, or angular momentum, and the radial action). It can be split

$$p(J_R, L_z \mid L_{z,0}, \tau, \mathbf{p_m}) = p(J_R \mid L_z, L_{z,0}, \tau, \mathbf{p_m}) p(L_z \mid L_{z,0}, \tau, \mathbf{p_m}), \qquad \text{(III.29)}$$

where the first part corresponds to radial heating, and is conditioned on both birth angular momentum and present-day angular momentum. Heating through scattering should happen over the entire trajectory of the star, so in some sense at an average of the birth and final angular momenta, but we will drop the dependence on birth angular momentum as an approximation (see Subsection III.3.5). The second term corresponds to radial migration, modelled as diffusion in angular momentum. Here it shows the probability of a star to be at angular momentum L_z given it was born at $L_{z,0}$ a time τ ago (see Subsection III.3.4). Each of these model aspects are presented in Section III.3 and assembled together to form the Milky Way model in Section III.4.

III.8.2 Modeling the Dataset: Noise Model, Selection Function, and the Observables

The Milky Way model described above cannot be directly applied to our dataset, since the stars were selected in a given survey and the data are noisy. We therefore write the model for the data set, in the space of the noisy observables (with subscript 'obs'). We (1) marginalize over uncertainties, and (2) apply the selection function to

the model:

$$
\begin{aligned}
p_{\text{dataset}} &= p_{\text{dataset}}(l, b, D_{\text{obs}}, v_{X,\text{obs}}, v_{Y,\text{obs}}, [\text{Fe/H}]_{\text{obs}}, \tau_{\text{obs}} | \mathbf{p_m}, \boldsymbol{\alpha}) \\
&= \int p_{\text{dataset}}(l, b, D_{\text{true}}, v_{X,\text{true}}, v_{Y,\text{true}}, [\text{Fe/H}]_{\text{true}}, \tau_{\text{true}} | \mathbf{p_m}) p_{\text{noise}}(\text{obs} \mid \text{true}, \boldsymbol{\alpha}) d^n\text{true} \\
&= \frac{1}{V_s(\mathbf{p_m})} \int p_{\text{MW}}(l, b, D_{\text{true}}, v_{X,\text{true}}, v_{Y,\text{true}}, [\text{Fe/H}]_{\text{true}}, \tau_{\text{true}} | \mathbf{p_m}) \\
&\quad \times S(l, b, D_{\text{true}}) f_{RC}(\tau_{\text{true}}) p_{\text{noise}}(\text{obs} \mid \text{true}, \boldsymbol{\alpha}) d^n\text{true} \\
&= \frac{1}{V_s(\mathbf{p_m})} \frac{1}{(2\pi)^2} \int p_{\text{MW}}(L_z, J_R, z, [\text{Fe/H}]_{\text{true}}, \tau_{\text{true}} | \mathbf{p_m}) D_{\text{true}}^2 \cos(b) \\
&\quad \times S(l, b, D_{\text{true}}) f_{RC}(\tau_{\text{true}}) p_{\text{noise}}(\text{obs} \mid \text{true}, \boldsymbol{\alpha}) d^n\text{true}.
\end{aligned}
\tag{III.30}
$$

From the first to the second line, we marginalize over data uncertainties with a noise model $p_{\text{noise}}(\text{obs} \mid \text{true}, \boldsymbol{\alpha})$ where 'noise' denotes all the noisy variables used here (those which have subscript 'obs'), and the uncertainty parameter array σ reflects the uncertainties described in the Section IV.2. From the second to the third line, we split the dataset model as the product of the Milky Way model extensively described in Section III.3 and the selection function $S(l, b, D, \tau)$. From the third to the fourth line, we describe the disk in the 2D space of actions (J_R, L_z) instead of the 4D phase space (x, y, v_x, v_y). We note the slight inconsistency in the actual action calculation based on the Staeckel approximation (Binney, 2012) which uses the full 6D phase space information, and our simplified modelling assumption based on the adiabatic distribution functions (Binney, 2010). This assumption should not matter much since we restrict to the thin ($|b| < 25$ deg), young (red clump), low-α disk where vertical excursions are very limited. The $D_{\text{true}}^2 \cos(b)$ term is the Jacobian to change from Galactic to Cartesian coordinates. In practice, we perform this integral by sampling the true values (in phase space and propagating directly to action space) from an approximate noise model $p(\text{true}|\text{obs})$, and then we use importance sampling (weighting the integrand with $p(\text{obs}|\text{true})/p(\text{true}|\text{obs})$) and Monte Carlo integrate by summing the remaining terms over these samples. The $p(\text{obs}|\text{true})$ term is the uncertainty model as described in Section IV.2.

III.9   Accounting for the Survey Volume $V_S(\mathbf{p_m})$

The survey volume in Eq. III.17 is a 7 dimensional integral (or 5, after having integrated over (l, b) by assuming the distribution function does not vary over an individual APOGEE field). We choose to compute this integral by importance sampling. This method works best if the proposal distribution p_{proposal} is similar to the target distribution. Ideally, we would like to generate from our full models using a set of realistic parameters $\mathbf{p}_{\mathrm{prop}}$. We could then systematically use these samples in a Monte Carlo integration of the survey volume corresponding to a new set of model parameters. The advantage of this method is that our samples approximately trace the best fit model so provide an accurate computation of the normalization with a minimal number of samples. It also provides a tractable way to handle the selection function in the survey volume which is automatically incorporated in our sampling distribution.

However, one cannot sample points directly from our full models because they are constructed in a complex and un-normalized way. As a workaround, we choose to sample from the full model in two steps, using a simpler Galaxy model as an intermediate distribution. First, we sample stars from the simple proposal distribution that is easy to normalize. Then, we down-sample these data through importance sampling using our proposal model. The simple Galaxy model p_s is an exponential disk of constant scale length R_{ds} and scale height h_{zs} chosen close to the analogous parameters in the overall model (e.g. $R_{d,\mathrm{prop}}$). Given their positions in the disk, stars velocities are sampled from a Gaussian centered on $(v_R, v_\phi) = (0, v_{\mathrm{circ}}(R))$ with large standard deviations that envelope the known velocity dispersion.

To generate N_{prop} samples from our proposal distribution, we use the following procedure:

1. For every APOGEE field i, we sample on-sky positions (l, b) using boundaries defined by the selection function. We then sample distances D using the

cumulative distribution function of

$$p_s(D \mid l, b) \sim D^2 \cos(b) \exp(-R(l, b, D)/R_{ds})\text{sech}^2(z(l, b, D)/h_{zs}). \quad \text{(III.31)}$$

2. We down-sample from these positions using the relative normalization of the simple model in each field. The field that contains the greatest number of stars is not down-sampled, and the other fields are down-sampled by accepting the points with probability

$$P_{\text{accept}}(\text{point} \mid \text{field i}) = F_{\text{proposal}}(l_i, b_i)/F_{\max}, \quad \text{(III.32)}$$

where
$$F_{\text{proposal}}(l_i, b_i) = \int_{D_{\min,i}}^{D_{\max,i}} p_s(D \mid l_i, b_i) S(l_i, b_i, D)\mathrm{d}D \quad \text{(III.33)}$$

and $F_{\max} = \max(F_{\text{proposal}}(l_i, b_i))$. After this step, the samples have a distribution that follows our simple Galaxy model but now accounts fully for the spatial selection function of APOGEE and the 3D extinction.

3. We now sample the remaining variables from our simple model before a further downsampling. Ages are sampled from a uniform distribution. Birth angular momenta $L_{z,0}$ are sampled from a normal distribution centered on $R \times 235$ kpc km/s with a standard deviation that increases as $\sigma \sim \sqrt{\tau}$ (to mimic radial migration). The strength σ is chosen larger than the analogous parameter in the global model (σ_{Lz12}) such that this distribution envelopes the radial migration model. Radial and azimuthal velocities (v_R, v_ϕ) are sampled from normal distributions centered on 0 and $v_{\text{circ}}(R)$ respectively.

4. We further down-sample these points by accepting them with a probability

$$P_{\text{accept}} = \frac{p_{\text{proposal}}(L_z, J_R, \tau, L_{z,0}, z \mid \mathbf{p}_{\text{prop}})f_{RC}(\tau)}{p_s(L_{z,0}, R, z, v_r, v_\phi)}, \quad \text{(III.34)}$$

where $p_{\text{proposal}}(L_z, J_R, \tau, L_{z,0}, z \mid \mathbf{p}_{\text{prop}})$ is our full proposal model with fixed parameters $\mathbf{p}_{\text{prop}}$. The term $f_{RC}(\tau)$ contains the age-dependent fraction of

stars on the red clump evolutionary stage. This down-sampling leads to a set of N_{prop} points.

Our N_{prop} samples are now drawn from the pdf $S(l, b, D) f_{RC}(\tau) p_{\text{proposal}}(L_z, J_R, \tau, L_{z,0}, z \mid \mathbf{p}_{\text{prop}})$, so we can calculate the survey volume as

$$
\begin{aligned}
V_S(\mathbf{p_m}) &= \int_{\mathcal{D}} p_{\text{model}}(\mathcal{D} \mid \mathbf{p_m}) S(l, b, D) f_{RC}(\tau) \mathrm{d}\mathcal{D} \\
&= \int_{\mathcal{D}} \frac{p_{\text{model}}(L_z, J_R, \tau, L_{z,0}, z \mid \mathbf{p_m})}{p_{\text{proposal}}(L_z, J_R, \tau, L_{z,0}, z \mid \mathbf{p}_{\text{prop}})} \\
&\quad \times S(l, b, D) f_{RC}(\tau) p_{\text{proposal}}(L_z, J_R, \tau, L_{z,0}, z \mid \mathbf{p}_{\text{prop}}) \mathrm{d}\mathcal{D} \\
&\approx \frac{1}{N_{\text{prop}}} \sum_{i}^{N_{\text{prop}}} \frac{p_{\text{model}}(L_{z\text{prop}i}, J_{R\text{prop}i}, \tau_{\text{prop}i}, L_{z0\text{prop}i}, z_{\text{prop}i} \mid \mathbf{p_m})}{p_{\text{proposal}}(L_{z\text{prop}i}, J_{R\text{prop}i}, \tau_{i\text{prop}}, L_{z0\text{prop}i}, z_{\text{prop}i} \mid \mathbf{p}_{\text{prop}})}.
\end{aligned}
$$

(III.35)

This integration has several advantages over using a regular grid (which is inefficient as the number of dimensions in the data increases) or re-sampling the normalization sample each time with new parameters. First, we only need to produce Monte Carlo samples once, not each time we need to evaluate the model, which is computationally more efficient. Secondly, since the initially generated samples are fixed, we need not recompute actions from these samples each time the model is evaluated, which saves additional computation time. Thirdly, as highlighted by McMillan & Binney (2013), for fixed samples the stochastic noise is limited and the overall normalized model is a smooth function of the model parameters which is a desirable property when we want to optimize the likelihood to fit the model parameters).

Step 2 of our procedure (down-sampling from the points generated at step 1) is in principle not mandatory. But in practice, the more alike the two distributions in the integral are, the greater the effective sample size.

We have tested this integration method on mock data, and the results remain robust as long as the proposal distribution is broad enough to envelope the distribution that we want to normalize. Additionally, we have tested the overall optimization scheme (MCMC ran on a model using this integration method) on mock

data, and recovered the true parameters largely within the uncertainties.

Chapter IV

Quantifying the Inside-out Growth of the Milky Way Disk

Science question   In the previous two chapters, I have shown that most of the dynamical evolution of the Galactic disk was cold and kinematically untractable (diffusion). However, using the metallcity and age of stars combined with their kinematics made it possible to rewind stars to their birth positions. This gives us a direct insight into the build up of the Galactic disk. We can now use the Galaxy as a model organism, quantify whether it grew from inside-out and by how much, and compare it to both the z=0 IFU galaxies and the redshift-size relations of Figure I.6.

Publication   This chapter was published in a similar form in Frankel et al. (2019).

Contributions

- I conducted the research presented in this paper: I spent time pondering on the scientific question, adapted the model of Frankel et al. (2018), coded it, produced the figures and the text.

- Jason Sanders contributed through regular guidance, and patiently let me explain to him each step I had taken to derive the selection function of APOGEE survey, advising and validating the procedure. He also indirectly contributed to the draft through paper discussions that benefited to my scientific maturity.

- Hans-Walter Rix contributed through regular guidance and comments on the draft, helping with the science more broadly.

- Yuan-Sen Ting provided the data and helped understanding their limitations, and commented on the draft.

- Melissa Ness provided additional comparison data and commented on the draft.

Abstract   We quantify the inside-out growth of the Milky Way's low-α stellar disk, modeling the ages, metallicities and Galactocentric radii of APOGEE red clump stars with $6 < R < 13$ kpc. The current stellar distribution differs significantly from that expected from the star formation history due to the redistribution of stars through radial orbit mixing. We propose and fit a global model for the Milky Way disk, specified by an inside-out star formation history, radial orbit mixing, and an empirical, parametric model for its chemical evolution. We account for the spatially complex survey selection function, and find that the model fits all data well. We find distinct inside-out growth of the Milky Way disk; the best fit model implies that the half-mass radius of the Milky Way disk has grown by 43% over the last 7 Gyr. Yet, such inside-out growth still results in present-day age gradient weaker than 0.1 Gyr kpc^{-1}. Our model predicts the half-mass and half-light sizes of the Galactic disk at earlier epochs, which can be compared to the observed redshift -size relations of disk galaxies. We show that radial orbit migration can reconcile the distinct disk-size evolution with redshift, also expected from cosmological simulations, with the modest present-day age gradients seen in the Milky Way and other galaxies.

IV.1   Introduction

The star formation history is a key formation and evolution aspect for any disk galaxy, as it governs its resulting stellar structure. Subsequent orbit mixing processes can redistribute the stars and remove dynamical memory of their birth conditions. Constraining galaxy evolution requires knowledge of both the initial formation distribution and the importance of orbit mixing.

Galaxy disks are thought to grow from inside-out. Peebles (1969) first postulated that gas disks acquire their angular momenta from tidal torques; with the low angular momentum gas cooling, settling and forming stars on shorter time-scales than the high angular momentum gas (Larson, 1976). (semi-)Analytic hierarchical models for disk formation in a cosmological context (e.g., Fall & Efstathiou, 1980; Mo et al., 1998; Somerville et al., 2008; **?**) have predicted that galaxy disks must grow from inside-out to reproduce the observed size-luminosity-velocity relations (Tully & Fisher, 1977; Courteau et al., 2007). Similarly, cosmological and zoom-in simulations show disks with star formation time-scales that increase with the distance to the galactic center or gas accretion of higher angular momentum at later times (Avila-Reese et al., 2018; Grand et al., 2017; Aumer et al., 2014; Brook et al., 2006, 2012; Pilkington et al., 2012; **?**). Measuring the rate at which stellar disks grow can give insight to constrain the interplay between the physical processes involved in gas accretion, cooling and forming stars, as well as the global evolution of disk galaxies.

Observationally, a number of independent measurements suggests that disk galaxies grow from inside-out. Several studies indicate that disk galaxies of a given stellar mass are smaller at higher redshift (Ferguson et al., 2004; Barden et al., 2005; Franx et al., 2008; Buitrago et al., 2008; van Dokkum et al., 2013; van der Wel et al., 2014; Rodríguez-Puebla et al., 2017). Likewise, in massive disk galaxies of the local Universe, integrated light from older stellar populations, as traced by color, is more centrally concentrated than that of younger populations, and star formation is more spatially extended than the overall stellar distribution (e.g. MacArthur et al., 2004; Muñoz-Mateos et al., 2007b; Boissier et al., 2008; Muñoz-Mateos et al.,

2011; **?**; Pezzulli et al., 2015). Similarly, resolved stellar observations of Local Group galaxies (e.g, NGC300, M33 and more recently NGC7793) using the *Hubble Space Telescope* showed that old populations are often more centrally concentrated than young populations (Gogarten et al., 2010; Williams et al., 2009; Sacchi et al., 2019). However, this does not appear to be the case in M31 (Bernard et al., 2015). Finally, integral field spectroscopy surveys, such as MaNGA (Bundy et al., 2015) and CALIFA(Sánchez et al., 2012) have led to the detection of mostly weak age radial gradients in massive disk galaxies (Goddard et al., 2017; García-Benito et al., 2017; González Delgado et al., 2014; Pérez et al., 2013).

Most of the described galaxy observations are consistent with inside-out growth, but are restricted to studying present-day galactocentric radii of stellar populations, instead of considering their (unknown) birth sites. Dynamical processes in disk galaxies rearrange the stars, often weakening or erasing any formation gradients (e.g. **?**). Therefore, to state anything quantitative about inside-out growth from these observations requires knowledge of the strength of these dynamical processes. The importance of dynamical heating from non-axisymmetric perturbations such as spiral arms and molecular clouds has long been recognised (e.g. Lacey, 1984; Carlberg & Sellwood, 1985; Sellwood, 2014; Aumer et al., 2016b). Transient spiral patterns produce changes in angular momentum and heating around the Lindblad resonances, restructuring the disc (Lynden-Bell & Kalnajs, 1972). Sellwood & Binney (2002) recognized that at corotation, a star could be scattered in angular momentum without associated increase in random motion. This process is known as 'radial migration' or 'churning' and is generally distinguished from 'blurring' which describes changes in angular momentum with associated heating. A truly radial-migrated population will appear dynamically identical to a population that has not experienced any dynamical mixing (Sellwood, 2014), making their separation hard. In this work, we ignore kinematics of the stars so cannot distinguish between the different dynamical processes that scatter stars radially, and consider the combined effect as 'radial orbit migration'. If radial mixing is strong, then the age gradients expected from inside-out growth can be severely weakened. An old star at a large Galactocentric radius can have formed at a smaller radius, erasing

evidence for inside-out growth. All these aspects (inside-out star formation, radial migration) must be accounted for simultaneously in any modeling as demonstrated in Schönrich & McMillan (2017a); **?**); Frankel et al. (2018).

For the Milky Way, we have an opportunity to disentangle the effect of inside-out formation from radial orbit migration as we have access to positions, chemical compositions and ages of individual stars from spectroscopic observations. Although dynamical processes cause stars to lose dynamical memory of their birth sites, they are thought to retain chemical memory. With assumptions on the past history of the Galaxy, these observations allow the linking of stars to their birth locations from their chemistry or ages through 'weak chemical tagging', (different from the classical 'chemical tagging' as described in Freeman & Bland-Hawthorn (2002) and Ting et al. (2015) for example) such that the dynamical processes can be 'rewound' and the formation properties measured (e.g., Schönrich & Binney, 2009a; Sanders & Binney, 2015; Hayden et al., 2015; Schönrich & McMillan, 2017b; Frankel et al., 2018; Minchev et al., 2018).

The recent advance of wide spectroscopic surveys of the Milky Way disk has produced pioneering work in Galactic archaeology enabled by unprecedented samples samples of $\sim 10^5 - 10^6$ stars well beyond the solar neighbourhood. Earlier work considered the distribution of abundances at each Galactic location $p([\alpha/\text{Fe}], [\text{Fe}/\text{H}] \mid R)$ (e.g. Hayden et al., 2015) or $p(R \mid [\alpha/\text{Fe}], [\text{Fe}/\text{H}])$ (e.g. Bovy et al., 2012), finding that stars with high $[\alpha/\text{Fe}]$ were more centrally concentrated. But $[\alpha/\text{Fe}]$ was used as a chemical clock proxy for stellar age, and the focus was on the basic differences between the high-α and the low-α disks. More recently, stellar ages have become available for many stars, making it feasible to study the age distribution at different locations, and the spatial distributions of mono age populations $p(R \mid \tau, [\text{Fe}/\text{H}])$ – a more explicit measure of the history of the Galaxy (e.g. Bergemann et al., 2014; Bensby et al., 2010; Mackereth et al., 2017). However, as the Galaxy evolves it is nontrivial to relate these distributions to the star formation history of the disk. Here, we set out to build a model for where and when stars were born over a large range of Galactocentric radii $p(R_0.\tau)$, with direct use of stellar ages, and accounting for radial orbit migration. We focus on the low-α disk only (the last 8 Gyr of the Milky

Way evolution), propose an evolution scenario through parametrized equations and fit the parameters using APOGEE data.

This paper is the second in a series, developing and applying a framework for a global evolutionary Milky Way disk model introduced in Frankel et al. (2018), with emphasis on inside-out growth. We present the data we model in Section IV.2. In Section IV.3, we describe aspects of the model itself: (1) the survey selection function and (2) the Galactic disk; this model is an extension of Frankel et al. (2018), where it is described in some detail. We then present the results of the model fit to the data in Section IV.4. Finally, we interpret these in a more global context of galaxy disk formation and evolution and compare them to disk galaxies observed at different redshifts in Section IV.5, and discuss the limitations in Section IV.6.

IV.2   Data: APOGEE Red Clump Giants

We use asteroseismically calibrated ages, [Fe/H] and 3D positions of red clump stars from the 12th data release of the APOGEE near-infrared spectroscopic survey (Apache Point Observatory for Galactic Evolution Experiment, Alam et al., 2015; Majewski et al., 2017). Red clump stars are low mass core helium burning stars that have gone through the helium flash. Since they have similar core masses, they have similar luminosities, which make them good standard candles and suitable for Galactic archaeology studies that require precise distances. The core helium burning stage life-time is longer for initially more massive stars. Therefore, the overall red clump population is fairly young, with an age distribution that peaks around 2 Gyr (Girardi, 2016), as can be seen in Fig. IV.1.

Bovy et al. (2014) describes the selection of the red clump population from the APOGEE data. It is based on cuts in stellar parameters $\log g$, T_{eff} and infra-red photometry $(J - K)_0$ and H. We cross-match this red clump catalog with that of Ting et al. (2018b) to remove possible contaminants. Ting et al. (2018b) used a data-driven approach trained on APOKASC2 (Pinsonneault et al., 2018) to predict asteroseismic parameters (and hence the evolutionary stage) from stellar spectra, and evaluate their contamination fraction to 3%.
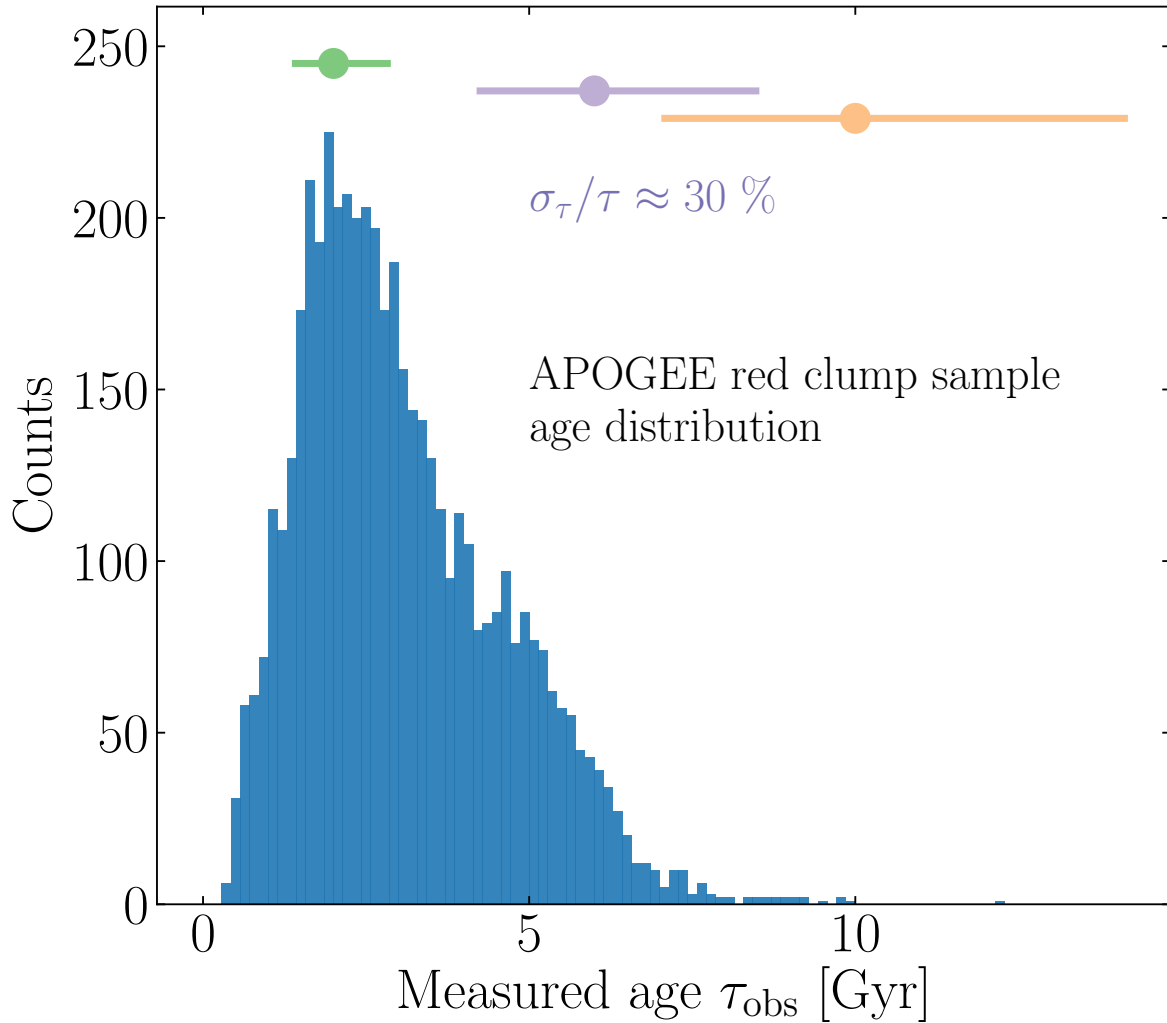
Figure IV.1: Age distribution of the APOGEE red clump stars from the low-α Galactic disk, used in the analysis presented here. These ages were determined in Ting & Rix (2019), tied to asteroseismic mass estimates. Age uncertainties are $\sigma_{\log_{10} \tau} \approx 0.15$ dex, resulting in about 30% age uncertainties, as illustrated for three ages: 2 Gyr (green), 6 Gyr (purple), 10 Gyr (orange). The peak in the distribution at 2 Gyr does not reflect the age distribution of the "underlying" stellar population, but is expected from theory and can be modeled quantitatively: it reflects the mass dependence – and thereby age dependence – of the life time of the core helium burning evolutionary stage that defines red clump stars.
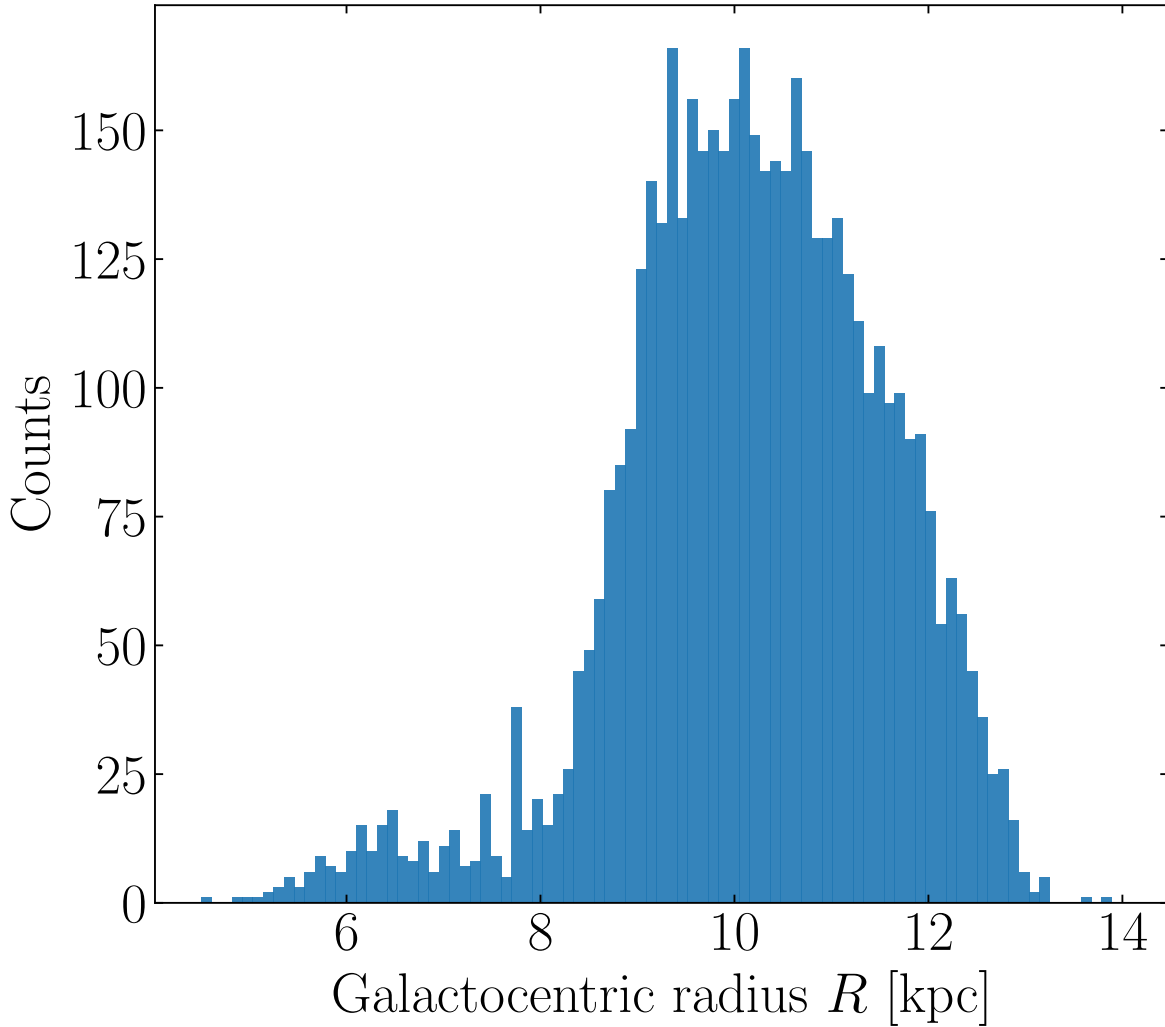
Figure IV.2: Galactocentric radius distribution of the red clump stars (as in Fig. IV.1), used in this analysis. They span a range of 6 kpc to 13 kpc, with the vast majority of sample stars beyond the Solar radius; this latter property traces back to the Galactocentric radius R distribution of the initial Bovy et al. (2014) parent sample and the subsequent selection cuts we have imposed (Section IV.2).

We further restrict our sample to the low alpha stars as in Frankel et al. (2018), tracing the most recent evolution of the Milky Way disk, in order to cut down undesired information from older stars. In addition, we consider only the 'short cohort' fields of APOGEE, as defined in Zasowski et al. (2013), which contain the brightest and closest objects (with approximately $7 < H < 12$). Stars further away, in longer 'cohorts' because they are fainter, may have higher extinctions, at a level where modeling extinction may be challenging. We restrict our sample to the APOGEE fields where the median extinction of APOGEE stars is less than ≈ 0.6 in H band.

After these cuts, our sample consists of ~ 5381 stars in 142 APOGEE fields.

We use metallicities [Fe/H] known to about ± 0.05 dex and 3D positions (l, b, D) with (l, b) standing for Galactic longitude and latitude and with photometric distances D, known to about 7% for such standard candles, from Ness et al. (2016). The ages τ_{obs} known to about 30% are taken from Ting & Rix (2019). APOGEE has delivered measurements of 15 chemical abundances, which we could, in principle, use. We choose to restrict to [Fe/H]and age, because they are sufficient for our purpose: at given [Fe/H]and τ, other abundances [X/Fe] of the low-α disk can be predicted with good precision (Ness et al., 2019b).

The ages were determined using neural networks trained on stars that have asteroseismic age estimates from APOKASC2 (Pinsonneault et al., 2018). The neural networks were trained to predict ages from stellar spectra in Ting & Rix (2019). This age determination method applies the same philosophy as the work described in Ness et al. (2016), who used a quadratic model to map from stellar spectra to ages rather than non-linear functions. It was shown, in a separate works using respectively asteroseismic ages (Martig et al., 2016; Silva Aguirre et al., 2018) and Bayesian isochrone fitting (Feuillet et al., 2016; **?**), that most of the spectral information on the stellar mass (and hence stellar age) comes from surface abundances of the CNO cycle elements brought up during the mass dependent dredge-up process.

Since the largest source of uncertainties comes from the ages (i.e. the age uncertainties are much larger than metallicity and distance uncertainties), we will account for them through a noise model, and treat the distances and metallicities as noise-free variables. The observed age distribution of the resulting sample is illustrated in Figure IV.1, and the Galactocentric radius distribution is shown in Figure IV.2. Most of the stars of our sample are young and located in the outer 8-12 kpc of the Milky Way disk. Therefore, our modeling will describe mainly the recent evolution of the outer disk. Our final data set consists of these 5381 stars with $\mathcal{D} = \{l, b, D, [\mathrm{Fe/H}], \tau_{\mathrm{obs}}\}$.

Symbol	Name	Type and appearance in the text
l, b, D	Galactic longitude, latitude, distance from the Sun	Assumed noise-free observables
X, Y	Cartesian coordinates for stellar positions in the plane	Disk model variables
R, Z	Galactocentric radius, height above the Galactic plane	Disk model variables
R_0	Galactocentric radius of a star at its birth	Disk model variable
$[\text{Fe/H}]$	Metallicity of stars	Assumed noise-free observable
τ_{obs}	Measured stellar age	Observable that has errors
τ	Modeled true age	Disk model variable
$\sigma_{\log_{10}\tau}$	Uncertainties in measured log age	Noise model parameter, fixed
R_d	Integrated scale length of the star-forming disk	Element of $\mathbf{p_m}$ in Eq. IV.10, to fit
τ_{SFR}, τ_m, x	Star formation time-scale, onset time, inside-out degree	Elements of $\mathbf{p_m}$ in Eq. IV.11, to fit
$h_z(a_z)$	Disk scale height as a function of the scaling parameter a_z	Nuisance parameter in Eq. IV.16, to fit
R_{old}	Scale length of the disk for $\tau > \tau_m$	Nuisance parameter in Section IV.3.2.5, to fit
σ_{Lz12}	Strength of radial orbit mixing	Element of $\mathbf{p_m}$ in Section IV.3.2.2, to fit
$\gamma_{[\text{Fe/H}]}$	chemical evolution parameter time dependency	Nuisance parameter in Eq. IV.18, to fit
$R^{now}_{[\text{Fe/H}]=0}$	Radius of solar metallicity in the star-forming gas	Nuisance parameter in Eq. IV.17, to fit
$\nabla[\text{Fe/H}]$	[Fe/H] radial gradient in the star-forming gas	Nuisance parameter in Eq. IV.17, to fit
Ω_i	Solid angle of APOGEE pointing i	Selection function parameter, fixed
H_{RC}	Red Clump absolute magnitude in H band	Selection function parameter, fixed
A_H, A_K	Extinction in H and K bands	Selection function variable
$(J-K)_0$	Deredenned color of a star	Selection function variable

Table IV.1: Main variables and parameters used in the model.
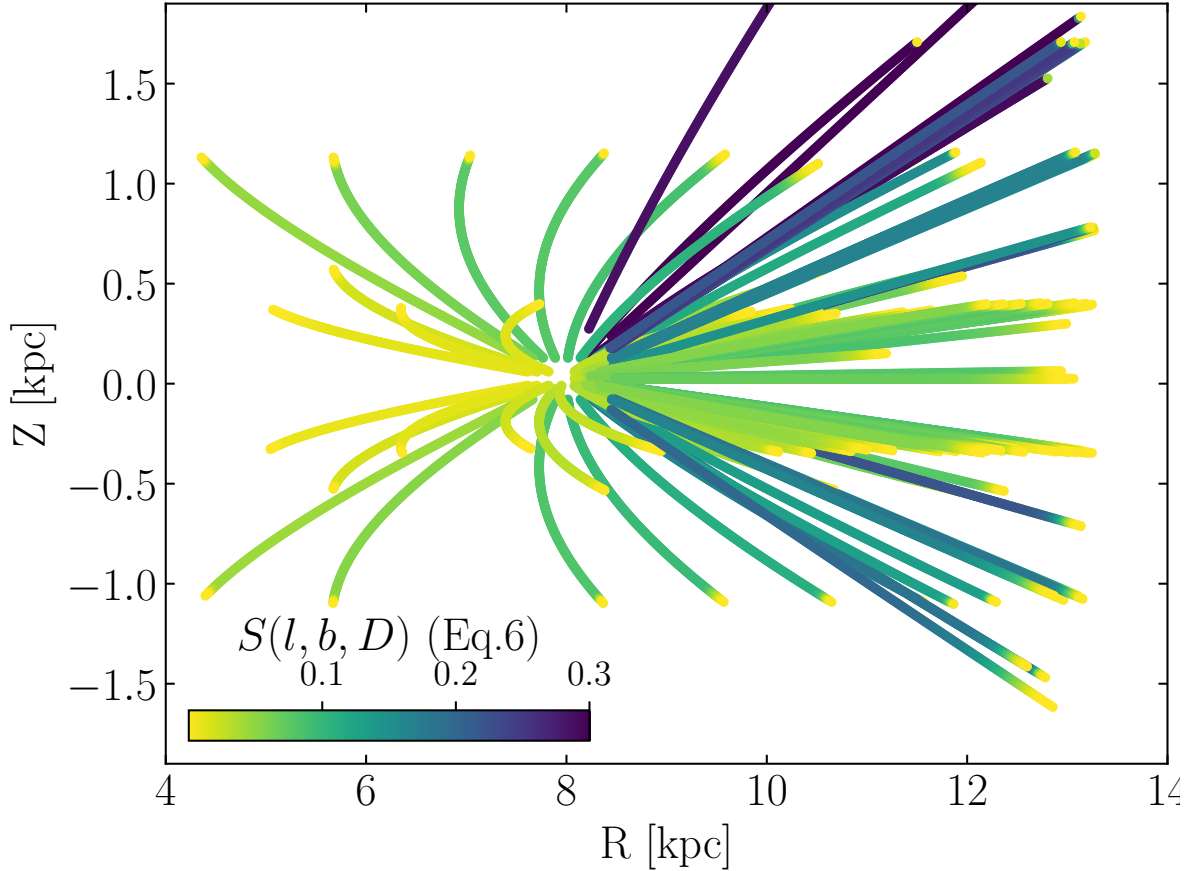
Figure IV.3: Distance-dependent fraction of observed red clump stars in the APOGEE pointings used here. This is the product of the fraction of photometrically eligible stars in each of the 142 fields that were spectroscopically targetted (Eq. IV.4), and the distance-dependent probability that a star of red clump luminosity does not have prohibitive dust extinction, as calculated from the Green et al. (2018) extinction map (Eq. IV.5).

IV.3 Modeling the Data Set

We set out a global model for the data described above: $\mathcal{D} = \{l, b, D, [\text{Fe/H}], \tau_{\text{obs}}\}$ and their uncertainties. We make a clear difference between the measured age τ_{obs} and the true age τ that we use for the modeling, to account rigorously for age uncertainties (see Section IV.3.3). For clarity, all the model variables and parameters are summarized in Table IV.1. We start by splitting this model in three main terms: (1) the model for the selection of the disk stars in the APOGEE survey, (2) a global forward model for the Galactic disk with model parameters in an array $\mathbf{p_m}$ and (3) the normalization constant over the observable space limited by the selection as in

Rix & Bovy (2013).

$$p(\mathcal{D} \mid \mathbf{p_m}, \text{ selection}) = \frac{S(l, b, D) f_{\text{RC}}(\tau) p(\mathcal{D} \mid \mathbf{p_m})}{V_s(\mathbf{p_m})} \qquad \text{(IV.1)}$$

where $p(\mathcal{D} \mid \mathbf{p_m}, \text{ selection})$ is the normalized model of the data set, $V_S(\mathbf{p_m})$ is a normalization constant, $p(\mathcal{D} \mid \mathbf{p_m})$ is the physical model for the Galactic disk, and $S(l, b, D) = p(\text{selection} \mid l, b, D)$ is the survey selection function: the probability that a star ends up in the catalog, given its properties: position (l, b), magnitude H or distance D in our particular case for a standard candle, deredenned color $(J - K_s)_0$, and integrated extinction $A_H(D)$ along the line of sight (Section IV.3.1). The term $f_{\text{RC}}(\tau)$ is the fractional stellar mass contained in the red clump population at given age. It can be determined assuming an initial mass function and using stellar isochrones. Generally, selecting stellar populations through cuts in observables implies biasing the sample in age and metallicity. For the red clump population, Bovy et al. (2014) showed that f_{RC} is as strong function of age, and a weak function of metallicity. Therefore, we neglect the weak metallicity dependence and adopt the fit of f_{RC} as a function of age from Bovy et al. (2014).

The normalization constant (or survey volume) can be computed by integrating the unnormalized model over the observable space:

$$V_S(\mathbf{p_m}) = \int_{\mathcal{D}} p(\mathcal{D} \mid \mathbf{p_m}) S(l, b, D) f_{\text{RC}}(\tau) d\mathcal{D}, \qquad \text{(IV.2)}$$

which is a 5 dimensional integral over all the physical properties of the data. The integrals over (l, b) are obtainable analytically and can be transformed into a sum over APOGEE fields, assuming that the properties of stars do not vary in (l, b) over a single APOGEE pointing (of about 1.5 degree radius). We evaluate this integral in subsection IV.3.4. Expanding out the data and writing the spatial distributions in Cartesian coordinates (X, Y, Z), we have

$$\begin{aligned} p(l, &b, D, \tau_{\text{obs}}, [\text{Fe/H}] \mid \mathbf{p_m}) \\ &= D^2 \cos(b) p(X, Y, Z, \tau_{\text{obs}}, [\text{Fe/H}] \mid \mathbf{p_m}), \end{aligned} \qquad \text{(IV.3)}$$

where $p(X, Y, Z, \tau, [\text{Fe/H}] \mid \mathbf{p_m})$ is our model for the Galactic disk described in Section IV.3.2, and its relation to the similar term in Eq. IV.3 is the convolution over age uncertainties as described in Section IV.3.3.

IV.3.1   Modeling APOGEE Selection Function

The APOGEE survey targeted stars in different lines of sights, or pointings, centered on directions (l, b). Therefore, a spatial histogram of the stars contained in the APOGEE catalog does not reflect the spatial density of stars in the Milky Way disk. Using these stars to infer the spatial structure of the Milky Way disk requires forward modeling of this selection process.

The details of the APOGEE-1 selection function are described in Zasowski et al. (2013). We apply and summarize here the general method laid-out in Rix & Bovy (2013); Bovy et al. (2014) and refer the reader to these references for details [1]. For most stars of the APOGEE sample, we can assign a probability that this star was observed given its location, magnitude and color (selection function), which is then combined with a probability for this star to be at this location (the density model). In most APOGEE disk fields, stars were selected according to simple magnitude cuts in the H band and cuts in dereddened $(J - K)_0$ color from the photometric sample 2MASS (Skrutskie et al., 2006) which is assumed complete within these cuts. The de-reddened colors were obtained in Zasowski et al. (2013) using the Rayleigh Jeans Color Excess method (Majewski et al., 2011), based on combinations of photometry in different near- and mid-infrared bands and on the assumption that most stars have a similar intrinsic color in the Rayleigh-Jeans part of their spectrum. When too many stars in a pointing satisfy these criteria, the subset of stars to observe was drawn roughly randomly from the 2MASS. This subset contains a fraction S_i of all available stars, $\star$,

$$S_i = \frac{\# \star \text{ in APOGEE field i}}{\# \star \text{ in 2MASS matching selec. criteria in i}}. \tag{IV.4}$$

---

[1] we have additionally made the selection function for fields used here available as a fits table at https://github.com/NeigeF/apogee_selection_function with a tutorial

We focus on the main disk fields of APOGEE that are not dominated by ancillary programs (Eq. IV.4 is approximately valid only for targets drawn randomly from 2MASS, not for targets chosen for a specific purpose). We also remove the fields for which the selection criteria were complex to model (see a detailed description of the numerous particular cases in Zasowski et al. (2013)) or irrelevant to the scope of the present work, e.g., halo fields which contain fewer disk stars.

In addition, a fraction of stars in each field in the Milky Way disk is too extinguished by interstellar dust to be detectable within the magnitude limits of APOGEE (Bovy et al., 2016a). This is a function of distance, and can be modeled, if we have a model for the extinction spatial distribution in H band. We use the Bayestar17 3D extinction map (Green et al., 2018), which predicts the extinction distribution in different bands at any (l, b, D). We convert the map's output values to H band using the extinction coefficient 0.468 and assume the extinction law of Indebetouw et al. (2005) ($A_H/A_K = 1.55$) to convert the K band extinction values stated by APOGEE, to the H band. Assuming red clump stars are standard candles of magnitude $H_{RC} = -1.49$ (Laney et al., 2012), the probability that a red clump star can be seen at a given distance D within APOGEE magnitude limits H_{min} and H_{max} is the fractional area of the field at this given distance that is not hidden by dust extinction A_H. The map's highest resolution (3.4′) allows computation of this ratio by counting the distance-dependent fraction of pixels that satisfy the inequality

$$f_i(D \mid \text{field i}) = \frac{\# \, \text{pix}(H_{min} < H(D, H_{RC}, A_H) < H_{max})}{\# \, \text{pix in field i}}. \tag{IV.5}$$

We can finally recast this into the overall selection function, dubbed '*effective selection function*' when it accounts for both the probability to select a star from the photometric sample and for the probability to see a star given dust extinction, plotted in Figure IV.3,

$$S(l_i, b_i, D) = S_i \times f_i(D \mid \text{field i}). \tag{IV.6}$$

This is one of the three terms to cast in Eq. IV.1, and we are left with the two others: global model for the Galactic disk, and normalizing integral.

$$\ln\left(\Sigma_{\mathrm{SFH}}(R_0, \tau)/M_\odot \ \mathrm{kpc}^{-2} \ \mathrm{Gyr}^{-1}\right) + \mathrm{const}$$
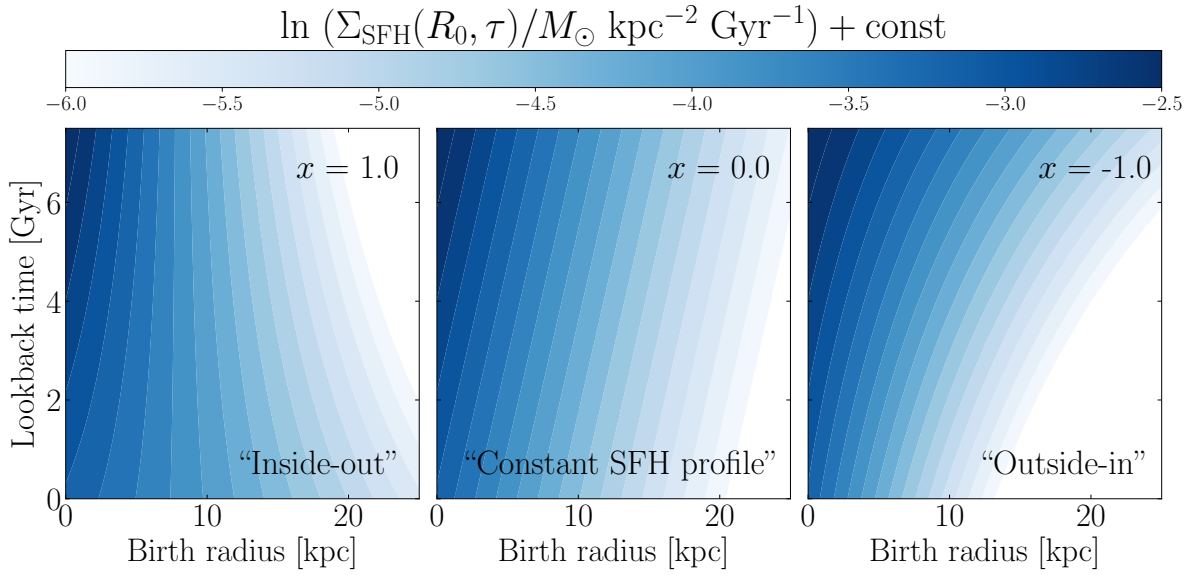
Figure IV.4: Model star formation rate as a function of time and birth Galactocentric radius for different scenarios considered here. We show the star formation rate surface density $\Sigma_{\mathrm{SFR}}(R_0, \tau \mid \tau_{SFR}, \tau_m, x)$, normalized to yield unit total stellar mass, as a function of birth radius R_0, lookback time τ and inside-out growth degree x as defined in Eq. IV.11. The panels reflect star formation histories for different 'inside-out growth parameters' x, from left to right: strong inside-out growth ($x = 1$) that would predict a flat star formation history at 8 kpc, uniform star formation history ($x = 0$), and strong outside-in growth, where the disk formed stars initially on a larger scale length than at present.

IV.3.2 Global Model for the Galactic Disk Evolution

We aim to model the Galactic disk in terms of the distributions $p(\tau, [\mathrm{Fe/H}], R, Z \mid \mathbf{p_m})$ of ages, metallicities, Galactocentric radii and heights above the plane. To fit the large data set efficiently, we build the different model aspects (star formation history, enrichment, radial mixing) from parametrized functional families. These are not designed to describe the exact physics in a self-consistent manner, but are physically plausible, fast to compute and have parameters that can be physically interpreted. This methodology permits us to disentangle different effects at play and measure the scales on which they happen. Applying the probabilistic chain rule and marginalizing over the birth Galactocentric radius R_0, we introduce the differ-

ent model aspects:

$$
\begin{aligned}
p(\tau, [\text{Fe/H}], X, Y, Z \mid \mathbf{p_m}) \\
&= \int p(R_0, \tau \mid \mathbf{p_m}) p([\text{Fe/H}] \mid R_0, \tau, \mathbf{p_m}) \\
&\times p(X, Y, Z \mid R_0, \tau, \mathbf{p_m}) \mathrm{d}R_0.
\end{aligned}
\tag{IV.7}
$$

The first term in the integral is the birth radius-age distribution of stars and is closely related to the star formation history, (subsection IV.3.2.1). The second term is the distributions of metallicity in the star forming gas as a function of time, which we adopt from Frankel et al. (2018) and re-fit. The last term is the spatial density resulting from radial orbit migration and vertical heating. It can be split into a radial component (the main focus here) and a vertical component, which depends on the distance from the Galactic mid-plane Z:

$$
\begin{aligned}
p(X, Y, Z \mid R_0, \tau, \mathbf{p_m}) &= p(X, Y \mid R_0, \tau, \mathbf{p_m}) \\
&\times p(Z \mid R_0, R, \tau, \mathbf{p_m}).
\end{aligned}
\tag{IV.8}
$$

The first term on the right hand side is the present-day surface density of stars of true age τ and birth radius R_0 (subsection IV.3.2.2), and the second term is the present-day vertical profile of the disk resulting from the vertical heating of stellar orbits between their birth radius and their present-day radius over time (subsection IV.3.2.3).

IV.3.2.1   Radial Dependent Star Formation History

We model the distribution of stars at birth as

$$
\Sigma_{\text{SFR}}(R_0, \tau \mid \mathbf{p_m}) = \Sigma(R_0 \mid \mathbf{p_m}) \text{SFH}(\tau \mid R_0, \mathbf{p_m}),
\tag{IV.9}
$$

where the time integrated surface density profile at birth is an exponential in birth radius R_0

$$\Sigma(R_0 \mid \mathbf{p_m}) \propto \exp\left(-\frac{R_0}{R_d}\right), \tag{IV.10}$$

and the radially-dependent normalized star formation history SFH is a function of age τ

$$\begin{aligned} \text{SFH}(\tau \mid R_0, \mathbf{p_m}) &= c(R_0, \mathbf{p_m}) \\ &\times \exp\left[\frac{1}{\tau_{SFR}}\left((1 - x\frac{R_0}{8\text{kpc}})\tau - \tau_m\right)\right]. \end{aligned} \tag{IV.11}$$

The inside-out growth is encoded in the dimensionless parameter x. If $x = 0$, the star formation time-scale is constant across the disk: no inside-out growth. If $x > 0$, stars form on a shorter time-scale in the inner disk than in the outer disk: there is inside-out growth. If $x < 0$, the star formation time-scale decreases to the outer disk: this would be outside-in growth. We fit for x by maximizing the likelihood, without imposing any prior. The values taken by $\Sigma_{SFR}(R_0, \tau \mid \mathbf{p_m})$ for three different values of x (1, 0 and -1) are illustrated in Figure IV.4. More generally, x sets the strength of the linear dependency of the star formation history with Galactocentric radius. For positive x and τ_{SFR}, there is always a Galactocentric radius R_{SFR0} such that the star formation rate is a decreasing function of time inside R_{SFR0}, and is an increasing function of time outside R_{SFR0}. In the particular case where $x = 1$, the star formation history is constant at 8 kpc, decreasing in the inner 8 kpc, and increasing in the outer 8 kpc. This is illustrated in the left panel of Figure IV.4, where at the radius $R_0 = 8$ kpc, the contour lines are vertical. Finally, the normalization constant $c(R_0, \mathbf{p_m})$ is such that the SFH in Eq. IV.11 is normalized between 0 and τ_m. The model parameters to fit for are $\{\tau_m, \tau_{SFR}, x, R_d\}$. This equation is related to the first term of Eq. IV.7 through

$$p(R_0, \tau \mid \mathbf{p_m}) = 2\pi R_0 \, \Sigma_{SFR}(R_0, \tau \mid \mathbf{p_m}). \tag{IV.12}$$

IV.3.2.2 Radial Orbit Migration

Since the present-day Galactocentric radii of stars may be different from their birth
positions, we model the effect of radial orbit migration in order to 'rewind' back
to the birth properties of stars. We use the radial orbit migration prescription from
Frankel et al. (2018) for the probability of a star moving from birth radius R_0 to
current radius R in a time τ. This is modeled as a global diffusion process with a
diffusion strength $\sigma(\tau) = \sigma_{\text{Lz12}}\sqrt{\tau/7\,\text{Gyr}}$,

$$p(R \mid R_0, \tau, \mathbf{p_m}) = N(\mathbf{p_m}, \tau, R_0)\exp\left(-\frac{(R - R_0)^2}{2\,\sigma^2(\tau)}\right) \tag{IV.13}$$

with $N(\mathbf{p_m}, \tau, R_0)$ a normalization constant. We re-fit for σ_{Lz12}.

The surface density profile of migrated stars of age τ and from birth radius R_0 is

$$p(X, Y \mid R_0, \tau, \mathbf{p_m}) = \frac{1}{2\pi R}p(R \mid R_0, \tau, \mathbf{p_m}), \tag{IV.14}$$

and is the first term in Eq. IV.8.

IV.3.2.3 Vertical Distribution of Stars

Since the present work focuses on the radial structure of the Milky Way disk, we are
essentially not interested in its vertical structure. However, we must not ignore it
as the survey selection function is three dimensional. We therefore adopt a descrip-
tion for the vertical profile that is good enough to characterize the vertical heating
history of the disk, and for which we only fit a single parameter.

The Milky Way disk scale height depends on the ages of stellar populations,
and the vertical profile of populations of given age flares (e.g., Mackereth et al.,
2017; Bovy et al., 2016a). We model the vertical structure of the Milky Way disk as a
function of age and Galactocentric radius, using the approximation of an isothermal

disk and the harmonic limit (e.g., Binney & Tremaine, 2008):

$$p(Z \mid R, R_0, \tau, \mathbf{p_m}) =$$
$$\frac{1}{2h_z(R, R_0, \tau)} \mathrm{sech}^2 \left(\frac{Z}{h_z(R, R_0, \tau)} \right),$$
(IV.15)

where the scale height is modeled as

$$h_z(R, R_0, \tau) = a_z \sqrt{\frac{2\overline{J_z}(R, R_0, \tau)}{\nu(R)}}.$$
(IV.16)

We fit for the dimensionless parameter a_z and adopt the terms in the square root from the literature: $\overline{J_z}(R, R_0, \tau)$ is the mean vertical action of stars of age τ born at R_0 and now at Galactocentric radius R. Ting & Rix (2019) have studied the vertical heating history of the Galactic disk using an APOGEE red clump data set and Gaia data (Gaia Collaboration et al., 2018b; Lindegren et al., 2018), and provided a functional form for $\overline{J_z}(R, R_0, \tau)$, which we adopt here. We calculate the vertical frequency ν such that $\nu^2 = \frac{\partial^2 \Phi}{\partial^2 z}$ using the MWPotential2014 potential of the Galpy python package (**?**), which is the same gravitational potential Φ used by Ting & Rix (2019) to infer the orbital actions of their data.

IV.3.2.4   Chemical Evolution

We model the chemical evolution of the gas as in Frankel et al. (2018): the metallicity of a star at birth is modeled as a simple function of its birth Galactocentric radius R_0 and time after birth τ:

$$[\mathrm{Fe/H}] = F_m - (F_m + \nabla[\mathrm{Fe/H}] R^{\mathrm{now}}_{[\mathrm{Fe/H}]=0}) f(\tau)$$
$$+ \nabla[\mathrm{Fe/H}] R$$
(IV.17)

with the time dependency

$$f(\tau) = \left(1 - \frac{\tau}{12\,\mathrm{Gyr}} \right)^{\gamma_{[\mathrm{Fe/H}]}}.$$
(IV.18)

We fit for the model parameters $\{\nabla[\text{Fe/H}], R^{\text{now}}_{[\text{Fe/H}]=0}, \gamma_{[\text{Fe/H}]}\}$ and keep $F_m = -1$ dex fixed. This chemical evolution model makes the following assumptions:

- there is a tight, unique relation between the birth location and time and the metallicity of a star,

- there is always a negative radial metallicity gradient in the ISM (modeled through $\nabla[\text{Fe/H}]$)

- at any Galactocentric radius, the [Fe/H] of the ISM only increases with time (modeled through the exponent $\gamma_{[\text{Fe/H}]}$).

These assumptions are supported by several chemical evolution models for the late evolution of the Milky Way disk (the past 8 Gyr) after the last major merger (e.g. Schönrich & Binney, 2009b; Grisoni et al., 2018b). Since this model is purely parametric and fitted to the data, it has the important advantage of bypassing the large uncertainties currently present in chemical evolution models, for example the coupling between the star formation history, possible gas inflows, outflows, radial flows, enrichment sources, supernovae progenitors, supernovae models and nucleosynthesis yields. However, the shortcoming of this model is that it does not contain a self-consistent link between the chemical evolution description and the star formation history. Our approach comes closer to 'weak chemical tagging', where $[\text{Fe/H}](R_0, \tau)$ is used to tag stars to their possible birth radius (e.g. Minchev et al., 2018; Schönrich & Binney, 2009b; Sanders & Binney, 2015).

IV.3.2.5   Accounting for an "Old" Disk Component

The evolution model presented above may not be valid at early times in the evolution of the Milky Way; yet, the size-able age uncertainties mean that we have to incorporate the existence of an "old" (still low-α) disk component. We aim to introduce an uninformative model for this old low-α disk by presuming there is an old star fraction ϵ in our data set with an uniform age distribution between τ_m and 12 Gyr, where τ_m remains part of the formal model fit. After some experimentation, we have adopted empirically $\epsilon = 0.05$, as this leads to astrophysically sensible τ_m.

We model the old star metallicity distribution as a Gaussian centered on solar metallicity with 0.2 dex spread (inspired from Frankel et al. (2018)), the radial distribution as an exponential of scale length R_{old} for which we fit, and the vertical distribution as a *sech2* function of scale height $h_{\text{old}} = 0.85$ kpc (which is roughly consistent with the local scale height of old stars (Mackereth et al., 2017)). We do not fit for the vertical scale height of the older stars, but instead use prior knowledge that old stars have generally dynamically hotter orbits (so greater scale heights) than younger stars. This makes our separation between 'young' and 'old' better informed in the presence of large age uncertainties at large ages.

IV.3.3 Model for Age Uncertainties

To account for age uncertainties, we convolve the evolution model with a noise model:

$$
\begin{aligned}
p(\tau_{\text{obs}}, \mathcal{D}' \mid \mathbf{p_m}) = & \\
& \int_0^{\tau_m} p(\tau, \mathcal{D}' \mid \mathbf{p_m}) p_{\text{obs}}(\tau_{\text{obs}} \mid \tau, \sigma_{\log_{10}\tau}) \mathrm{d}\tau
\end{aligned}
\tag{IV.19}
$$

where here $\mathcal{D}'$ is all assumed noise-free observables (position and metallicity, see Table IV.1), and $\sigma_{\log_{10}\tau}$ is our noise parameter. We assume that age uncertainties are Gaussian in log age with a spread of $\sigma_{\log_{10}\tau} = 0.15$ dex, which we calculated by measuring the standard deviation of the difference in inferred log age and APOKASC2 test set. $p_{\text{obs}}\left(\log_{10}(\tau_{\text{obs}}) \mid \tau, \sigma_{\log_{10}\tau}\right)$ represents the probability of measuring an age τ_{obs} given the true age τ:

$$
p_{\text{obs}}\left(\log_{10}(\tau_{\text{obs}}) \mid \tau, \sigma_{\log_{10}\tau}\right) \sim \mathcal{N}\left(\log_{10}(\tau), \sigma_{\log_{10}\tau}\right). \tag{IV.20}
$$

The integral in Eq. IV.19 must be computed numerically for each of the 5381 stars, which makes the fitting procedure computationally expensive.

IV.3.4 Normalization of the Probability Density Function: Survey Volume

The probability density function must be normalized over the observables. The survey volume, as defined in Equation IV.2, is

$$
\begin{aligned}
V_S(\mathbf{p_m}) &= \int_{\mathcal{D}''} p(\mathcal{D}'' \mid \mathbf{p_m}) S(l,b,D) \mathrm{d}\mathcal{D}'' \\
&= \sum_{\mathrm{i}}^{\mathrm{fields}} \iiint p(\tau, R_0, X, Y, Z \mid \mathbf{p_m}) S_i(D) \Omega_{\mathrm{i}} D^2 \mathrm{d}D \mathrm{d}R_0 \mathrm{d}\tau,
\end{aligned}
\tag{IV.21}
$$

with $\mathcal{D}'' = \{l, b, D, R_0, \tau\}$ and $\Omega_{\mathrm{i}} = \iint_{\mathrm{field\ i}} \cos(b) \mathrm{d}l \mathrm{d}b$ the solid angle of plate i. In the second line of Eq. IV.21, we sum over fields instead of integrating over the entire sky (S is zero outside the fields), and we have performed the integral over (l, b) in each field assuming the density varies slowly across the (small) angular size of the field. We have also implicitly integrated over metallicity as $\int p([\mathrm{Fe/H}] \mid R_0, \tau) \mathrm{d}[\mathrm{Fe/H}] = 1$ and the selection function is assumed independent of metallicity. We compute the sum of the remaining 3D integrals using trapezoidal integration on a regular grid of $[D, R_0, \tau]$ with 42, 38 and 36 points in each dimension respectively. $V_S(\mathbf{p_m})$ is a function of the model parameters only, so is only evaluated once per optimization step and not for each star.

IV.3.5 Constructing the Likelihood

We can now cast the model aspects back into Eq. IV.7, and build Eq. **??** from Equations IV.3 and IV.6. In practice, our model is a mixture of the evolution model and the old, uninformative model:

$$
\begin{aligned}
p_{\mathrm{tot}}(\mathcal{D}_i \mid \mathbf{p_m}, \mathrm{selection}) =& (1 - \epsilon) \cdot p(\mathcal{D}_i \mid \mathbf{p_m}, \mathrm{selection}) \\
&+ \epsilon \cdot p_{\mathrm{old}}(\mathcal{D}_i \mid \mathbf{p_m}, \mathrm{selection}),
\end{aligned}
\tag{IV.22}
$$

with an 'old fraction' $\epsilon = 5\%$. Assuming all measurements are independent, we construct the log likelihood $\mathcal{L}$ that the model parameters $\mathbf{p_m}$ generated the data $\mathcal{D}$

from our model

$$\mathcal{L}(\mathbf{p_m}, \{\mathcal{D}\}) = \sum_i \ln p_{\text{tot}}(\mathcal{D}_i \mid \mathbf{p_m}, \text{selection}). \qquad (\text{IV.23})$$

To optimize calculations, we compute the survey volume once per optimization step as it is not a function of the observables. We perform a maximum likelihood estimate of the parameters $\mathbf{p_m}$ of the global model for all the 5381 stars. We are mainly interested in three parameters: the star formation time-scale, the inside-out growth parameter x and the scale length of stars at birth R_d. However, we fit for all ten parameters in the model (summarized in Table IV.2) because the global model needs a good description of the Milky Way disk in all aspects in order to describe inside-out growth correctly.

IV.4   Results

The parameter values that maximize the likelihood are presented in Table IV.2, where the uncertainties quoted are determined from 10 samples of bootstrapped data. We comment below the direct implications and describe the main tests carried to verify the results.

IV.4.1   Inside-out Growth

We quantify the radial dependence of the star formation history with $x = 0.75$ for the Milky Way's low-α disk. The resulting star formation history is illustrated in Figure IV.5. According to this fit, the star formation processes that generated our data set started about $\tau_m = 7.5$ Gyr ago. This maximum age differs from the measured age of the oldest star in the data set because (1) a fraction of old stars constrain the old component of the model more than the young one, and (2) this parameter is in units of the dummy variable 'true age' of the model, which is convolved over age uncertainties. Therefore, τ_m is different from a best fit that would not account for age uncertainties, where it would take the value of the oldest
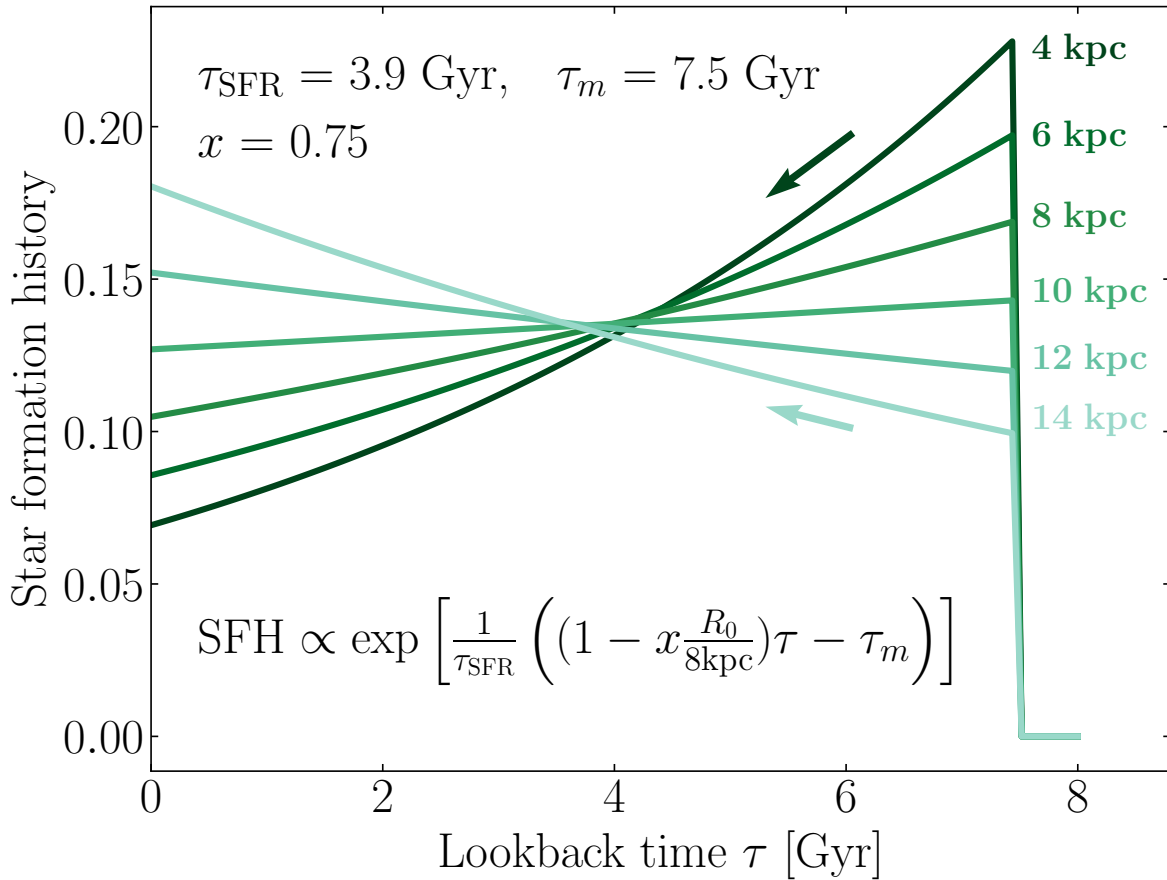
Figure IV.5: Star formation history SFH($R_0 \mid \tau$) implied by the best fit model at different Galactocentric birth radii R_0 (from dark to light: 4, 6, 8, 10, 12 and 14 kpc). The best fit model has parameters $x = 0.75$, $\tau_m = 7.5$ Gyr and $\tau_{SFR} = 3.9$ Gyr. This yields a star formation rate decreasing with time in the inner disk (dark green arrow), flat at 10.5 kpc, and increasing with time in the outer disk (light green arrow).

star of the 'young sample' (where the 'young sample' would be defined as the 95% youngest stars of the APOGEE sample because of our split in young and old components, see Section IV.3.2.5).

The best fit value of x implies that the star formation rate has been constant at ~ 10.5 kpc, a decreasing function of time in the inner ~ 10.5 kpc, and an increasing function if time in the outer ~ 10.5 kpc. This means that the Milky Way disk is still forming stars, with a slower decay in the outer disk than in the inner disk. The star formation history decayed slowly in the Solar neighbourhood.

Parameter	$\mathbf{p_m}$	best fit
Inside-out growth	x	0.75 ± 0.17 (0.69)[a]
Star formation time-scale	$\frac{\tau_{SFR}}{Gyr}$	3.9 ± 1.5 (1.4)
Star formation onset	$\frac{\tau_m}{Gyr}$	7.5 ± 0.5 (7.6)
Disk scale length	$\frac{R_d}{kpc}$	3.1 ± 0.4 (2.9)
Radial orbit migration	$\frac{\sigma_{Lz12}}{kpc}$	3.9 ± 0.2 (3.7)
Radius of solar [Fe/H]	$\frac{R^{now}_{[Fe/H]=0}}{kpc}$	8.3 ± 0.3 (8.9)
Enrichment exponent	$\gamma_{[Fe/H]}$	0.19 ± 0.03 (0.212)
Metallicity gradient	$\frac{\nabla[Fe/H]}{dex\ kpc^{-1}}$	-0.073 ± 0.002 (-0.078)
Old disk scale length	$\frac{R_{old}}{kpc}$	1.3 ± 0.9 (2.2)
Vertical adaptive scale	a_z	0.85 ± 0.03 (0.79)

[a] Numbers in parentheses are fits using the Bayestar19 extinction map in
240 fields and 7600 stars as a check described in subsection IV.4.3.2.

Table IV.2: Maximum Likelihood Estimates of $\mathbf{p_m}$

IV.4.2   Other Parameters

Even if the present work focuses on the radius-dependent star formation history of the Milky Way disk, the processes determining the evolution of the Milky Way are multiple and complex. We therefore constructed a global model to account for the effect of several of them, in particular radial orbit migration and chemical evolution.

We find a radial orbit migration strength of about $\sigma_{RM} = 3.9 \; kpc\sqrt{\tau/7\ Gyr}$. This value is greater than, but consistent with, the amount of radial migration in Frankel et al. (2018) who found $\sigma_{RM} \approx 3.4 \; kpc\sqrt{\tau/7\ Gyr}$. The difference results from the different age sets used between that work and the present study. The current age catalog is, on average, younger. So the stars have had less apparent time to migrate the same distance, which pushes the radial orbit migration strength up accordingly. The effects of different age catalogs is discussed more extensively in Sections IV.4.3.4 and IV.6.

IV.4.3   Tests

We test the robustness of the results to various numerical approximations and data uncertainties, and discuss the most important aspects below.
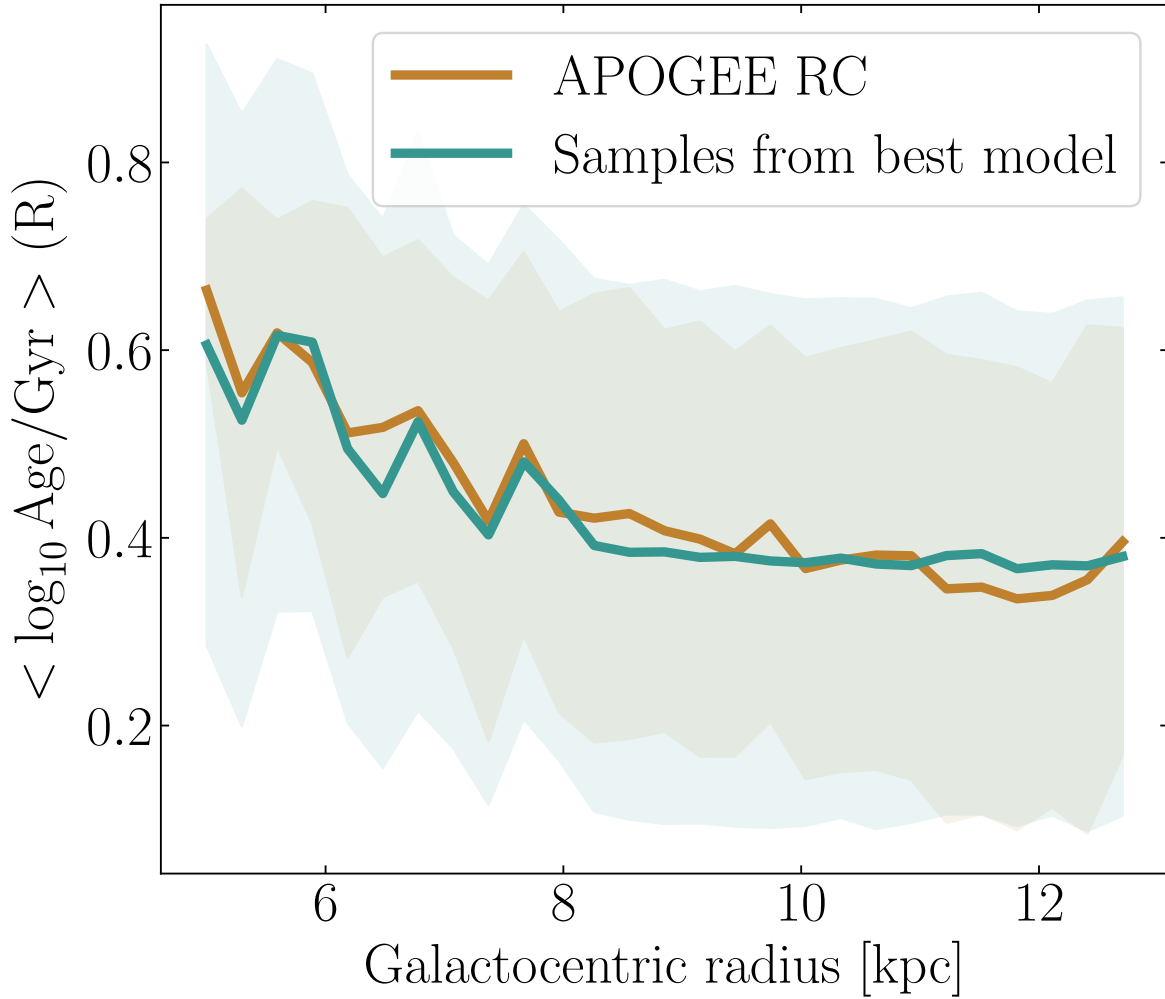
Figure IV.6: Radial profile of the stellar age distribution in the Galactic disk. The observed data are shown brown, and samples from the best fit model, after applying the APOGEE selection function, are shown in green; the thick lines reflect the mean age and the filled areas are the age dispersion. The jaggedness of the median age is a consequence of the spatially complex selection function, not an indication of spatially discontinuous star formation. This is why the model (green), combined with the APOGEE selection function, is able to reproduce these features even with a smooth star formation history. This Figure illustrates that the observed, present-day age distribution as a function of radius, can be modeled well by our model.

IV.4.3.1 Basic Tests

We perform a series of simple tests to ensure that (1) model prediction in data space compare well to our data set, (2) a density model recovers similar work in the literature, (3) integrals are computed with the necessary level of accuracy, (4) the optimization scheme recovers parameters correctly.

1. To verify that the fitting procedure has worked, we produce a mock data
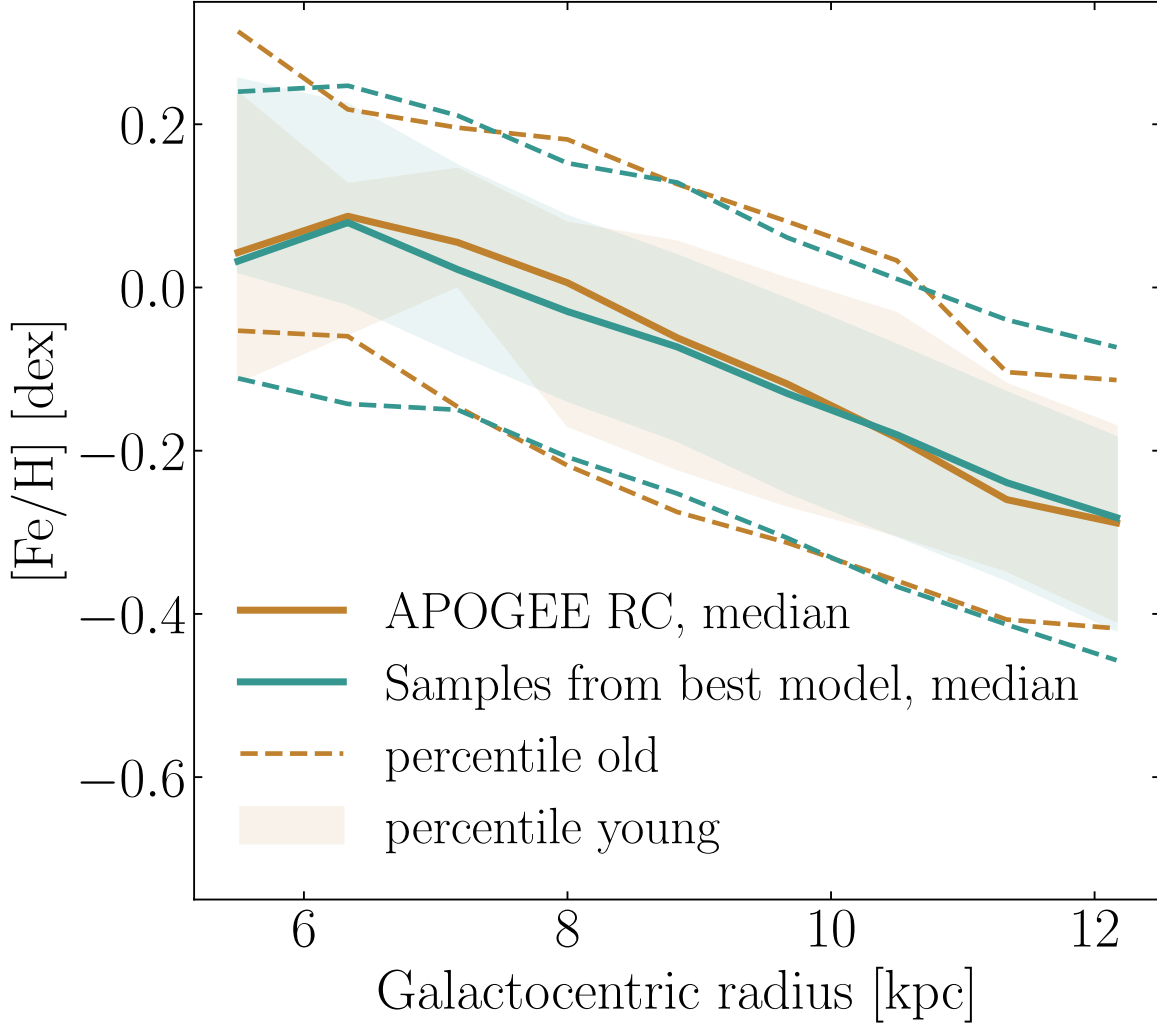
Figure IV.7: Radial metallicity profile of the observed data (brown) and samples from the best model (green), analogous to Fig.IV.6. The solid lines are the median metallicity profiles using all stars, and using a best fit metallicity gradient of -0.073 dex kpc^{-1} (see Table IV.2). The 16% and 84% percentiles of two age bins are also plotted: the shaded area for stars younger than 1.5 Gyr, and the dashed lines for stars with ages $2.5 < \tau_{obs} < 5$ Gyr. The metallicity scatter increases with age due to radial orbit migration, and seems well reproduced by the model. The slight differences in the inner disk are expected because there are few data points at radii less than 7 kpc. Our model reproduces well both the metallicity gradient and the age-dependent metallicity scatter.

set from the best fit parameters using the APOGEE selection function and compare it to the real data. The mass-weighted age profile is well recovered, but the predicted age scatter is greater than observed (see Fig. IV.6 and Section IV.6.3). Overall, the best fit evolution model reproduces well the observed scatter in age-metallicity at given Galactocentric radius, as shown in Fig. IV.7. The mean metallicity profile is well reproduced, indicating that our parametric prescription for the gradual enrichment of the gas was well fitted. In Figure IV.7, there is an apparent flattening of the metallicity profile at $R < 7$ kpc, both in the model and in the data. In the present work, these are purely due to selection effects, since our chemical evolution model has a constant metallicity gradient in space and in time. The inner disk APOGEE fields tend to point to high Galactic latitudes away from the mid-plane (Fig. IV.3). Since there are vertical metallicity gradients rising from vertical heating of older, metal-poorer stars, the data set lacks the metal rich stars from the inner mid-plane, underrepresented due to the spatial selection. Of course, this is not an issue in our case because these effects are fully accounted for in our model. But it highlights the importance of accounting carefully for selection effects when using data from surveys to draw conclusions on the evolution of the Galaxy.

2. We set out a model for the 3D density of the Galactic disk $p(X, Y, Z \mid [\text{Fe/H}], \tau)$, as in Bovy et al. (2016a); Mackereth et al. (2017). Qualitatively, fitting for the scale lengths and heights in age-metallicity bins gave consistent results with Mackereth et al. (2017), where at given age, the distribution of metal-rich stars peak in the inner disk and those of metal-poor stars peak in the outer disk. And at given metallicity, the distributions of old stars are in broader 'donut-like' structures than those of young stars.

3. We verify that the normalizing integrals of our global model were evaluated with enough accuracy. Varying the ranges and regularity of the integration grids, we find that increasing the accuracy further does not influence the best estimate results presented here.

4. To ensure that the optimization scheme (Nelder-Mead algorithm) does not get stuck in local maxima, we optimize the likelihood several times, with different initial parameters. Additionally, we check that the optimization scheme was able to recover the true parameters. We sample 5400 mock data points with various parameter values (as well as the best fit) and add noise to their ages from our noise model, Eq. IV.20. We fit these data, and recover the parameters with good precision. The enrichment parameters used to tag birth radii, and the radial orbit migration strength are recovered to 4%, τ_m is recovered to 0.5%, x to 7% and τ_{SFR} to 15% (depending how much noise is added to the ages, here for $\sigma_{\log_{10} \tau} = 0.15$ dex). The scale length of the disk is recovered to 3% and a_z to 0.9%.

IV.4.3.2 Modeling Extinction

We verify the consistency of the effective selection function of this work (Eq. IV.6), using the Bayestar17 extinction map (Green et al., 2018), with the more recent extinction map Bayestar19 (Green et al., 2019). Since we have excluded all the APOGEE fields where the median extinction of the APOGEE sample is greater than $A_H = 0.6$, the Bayestar17 map is largely sufficient for our description of the disk in the 142 remaining disk fields and yields the same effective selection function as the Bayestar19 map. However, the effective selection function differs significantly in the Galactic mid-plane where there are more extinguished fields, which we have excluded. Assuming we can trust the Bayestar19 dust map for such fields, we have fitted the parameters again using the 7600 stars present in the 213 disk fields including those high extinction fields. The best fit parameters are listed in parentheses in Table IV.2. We find a similar estimate of the disk scale length R_0, which is the parameter that would have been most affected by variations in the effective selection function (direct density modeling). The star formation time-scale τ_{SFR} changes significantly after including more stars from the inner disk (due to co-variances with the scale length of the old disk component and the fact that the data set has changed but not our outlier fraction ϵ), but the inside-out growth parameter x remains strongly positive.

IV.4.3.3   Modeling Age Uncertainties

Stellar ages are challenging to determine. They are modeled quantities rather than direct observables, so using stellar ages relies on assumptions in the underlying stellar evolution models. Ages are heteroscedatic, their uncertainties not well quantified, and their systematic behaviors unknown. In the present work, we assume that asteroseismic ages are the ground truth, and that age errors arise when mapping from stellar spectra to asteroseismic ages through data-driven methods. For the data set we have used, these errors are approximately constant in log age, and the standard deviation of log age on a test set (APOKASC2) is roughly 0.15 dex in decimal logarithm, (Ting & Rix, 2019). We used a noise model based on this value, where the measured log age is normally distributed around the true value with a 0.15 dex spread (Eq. IV.20). This assumes that the neural network used to map stellar spectra to log age produces Gaussian errors of 0.15 dex.

To benefit from the direct use of stellar ages, we need to test and understand the impact of the (unknown) uncertainties on our conclusions. We test the robustness of the results to the assumed noise model by varying the value of this scatter between 0.12 and 0.17 dex, and optimizing the likelihood with these new values. We find noticeable changes in the total age of the low-α disk (parameter τ_m) and a (weak) dependency on the inside-out growth parameter x that takes values between 0.6 (underestimate errors) and 0.82 (overestimate errors). This leaves our conclusions on inside-out growth unchanged (with a strongly positive x), but it affects the comparisons between model predictions and the data set for old stars. So the best fit parameter τ_m should not be seen as the age of the Milky Way disk, but rather as the maximum age at which we trust our model - based on the age scale and assumed uncertainties of our data.

IV.4.3.4   Different Age Determination Methods

In the era of large surveys and data-driven methods, there are at present multiple catalogs of parameters derived for the same stars in large homogeneous data sets. The values inferred from different methods have systematic differences, which are

Age set	x	R_{const}
Ting18	0.75	11 kpc
Ness16	0.62	12 kpc
Ness18	0.50	16 kpc
Ness19	1.1	8 kpc
Sanders18	-0.3	–

Table IV.3: Inside-out results using different ages

sometimes significant. It is central to realize how these systematics influence our understanding of Galaxy evolution. We test a total of five age catalogs (described in details in Appendix IV.8), on the exact stars that we presented in Section IV.2 (with some minor loss during the cross-match), keeping metallicity and position the same and changing only the age data column in the likelihood optimization. As expected, the best fit values changed between age sets, see Table IV.3 where the best fit parameter x is summarized, as well as the Galactocentric radius at which the star formation rate is a constant in time R_{const}. The first data (which we will refer to as 'Ting18') set was used for the analysis described above. The ages of the other sets were derived either using *The Cannon* (Ness et al., 2015, 2016, 2019b) or a combination of data-driven mapping from abundances to ages and stellar evolution models (Das & Sanders, 2019; Sanders & Das, 2018). and are named from these references (see Table IV.3).

These five data sets, composed of the same stars but with different age estimates, lead to five different best fit values for inside-out growth x due to systematic differences between methods. These differences in inside-out growth best fit arise naturally from the different radial age gradients present in each data set: the data set containing the strongest age radial gradient (Ness19) leads to the strongest inside-out growth best value ($x = 1.1$), and the data that show the weakest age gradient (or the least negative, Sanders18) also has the least positive inside-out growth ($x = -0.3$). Apart from the Sanders18 age set, all data are consistent with an inside-out growth formation scenario for the Milky Way disk, with some slight difference on the decay of star formation with Galactocentric radius. We found that the Sanders18 age set might over estimate stellar ages at large distance: this is the only method making direct use of Gaia parallaxes, and comparing these ages to the

four other spectroscopic ages (with no known bias with distance) shows systematic differences as a function of distance. The systematic zeropoint issues with the Gaia parallaxes are now well studied (Leung & Bovy, 2019) which bias the ages via the the strong mass-luminosity degeneracy for giant stars. Folding this distance bias with the APOGEE spatial selection function can produce an inversion of the overall age gradient in the data set.

IV.4.3.5 Comparisons with Literature Results

The test presented above consists in comparing inference results from the same stars, of the same population (red clump), but using ages derived from different methods. In complement, we now use the best fit parameters from these five age sets to make predictions that can be compared with literature. We compare the model predictions to the age distributions from Xiang et al. (2018), who measured ages from turn off and sub-giant LAMOST stars (Cui et al., 2012) with a 0.12 dex precision on log age. They corrected for selection effects, and derived selection-corrected age histograms in Galactocentric radius bins. To compare, we simulate this procedure. We sample stars of all populations (not just red clump) from our best fit evolutionary model and select them in Galactocentric radius bins as in Xiang et al. (2018). We then add 0.12 dex of noise to the ages, to emulate their age histograms. We find that the best fit parameters obtained from the Ting18 sample (the ages we have focused on during the analysis) are more consistent with the trends in Xiang et al. (2018) than those from the other age sets, at young ages (where it matters and where the data are constraining). The model predictions and those of Xiang et al. (2018) differ significantly at large ages: we under predict the number of old stars. This could come from that our model is mostly constrained by young stars, and that we only model the low-α disk, whereas Xiang et al. (2018) derived these age histograms considering all stars.

IV.4.3.6   Inside-out Model Variants

We test several models for the distribution of $\Sigma(R_0, \tau)$ in order to (1) see whether the general result 'the Milky Way disk grew from inside-out' is robust to model variations and to our definitions, and (2) set out to understand what the best description for inside-out growth is. We describe two of them below.

(1) Time-varying Disk Scale length   We first build a model of a birth surface density profile with a time varying scale length, where

$$\Sigma(R_0, \tau) = \text{SFH}(\tau)\Sigma(R_0 \mid \tau), \tag{IV.24}$$

inspired by that in Frankel et al. (2018). The star formation history is simply a universally-decreasing exponential, where stars started forming 12 Gyr ago on a time-scale τ_{SFR}, and $\Sigma(R_0 \mid \tau)$ is an exponential profile of the disk with a varying scale length $R_d(\tau) = R_{d,0}(1 - \alpha_{R_{\text{exp}}} \frac{\tau}{8\text{Gyr}})$. The fitted parameter quantifying inside-out growth is $\alpha_{R_{\text{exp}}}$. The fit results in overly strong inside-out growth, $\alpha_{R_{\text{exp}}}$ going to 1 (which confirms and amplifies the inside-out growth results found here). But this model is conceptually deceiving: integrated over time, it predicts an overall disk with a profile that deviates significantly from the expected exponential for disk galaxies. Additionally, this model is restrictive: by construction, it is (1) unable to describe outside-in growth in a physically plausible way, (2) unable to describe very strong inside-out growth, which would result in stars born with a negative scale length.

(2) Radius-varying Star Formation Peak   We test another model, where inside-out growth is not described by a radially-varying star formation time-scale as in equation IV.11, but rather with a radially-dependent star formation peak. This raises the question of what inside-out growth is: do stars form on a longer time-scale at large radii, or does star formation begin later at large radii? Unfortunately, the second question, 'when do stars begin to form?' requires data that are constraining at large ages, which are currently not available due to the red clump selection. The

best fit parameters are not in contradiction with inside-out growth and samples from that model reproduce the observed data better than the model we chose to show in this analysis. But the fitting procedure is unfortunately not more conclusive in a quantifiable way. This is because age errors at large ages are so large, and old data are so sparse, that our likelihood function is almost flat in the parameter quantifying the radial dependency in the star formation peak.

IV.5   Astrophysical Implications

We have constructed and constrained a model that describes how the Milky Way's low-α disk may have built up and grown over time. We discuss below the implications in the more general context of the formation and evolution of galactic disks, and show that under the assumptions of this work, the Milky Way is typical in this aspect.

For external galaxies, there exist two families of observational constraints for inside-out growth. Redshift-size relations are obtained by measuring the size of the visible disks (half-light radius, or effective radius), assuming exponential or de Vaucouleur (de Vaucouleurs, 1948) profiles. These observations reflect the overall size of galaxies of fixed stellar mass (derived from their observed light) at given lookback times, and show that on average, disks were smaller in the past. Since these observations are made on populations of galaxies of a given stellar mass at all redshifts, they do not reflect the time evolution of individual galaxies (especially as, due to star formation, the stellar mass of a galaxy should in principle increase with time). In this picture, a star-forming disk galaxy's stellar mass and size should grow with time. Interpreting the evolution of scaling relations with time requires modeling (e.g., Mo et al., 1998).

On the other hand, galactic archaeology approaches have studied the present-day positions of different populations of stars in individual galaxies, including the Milky Way. But stellar ages have large uncertainties, and present-day stars Galactocentric radii are not their birth radii. If stellar ages indicated the lookback time at which stars formed, and if present-day stellar positions reflected well their birth po-
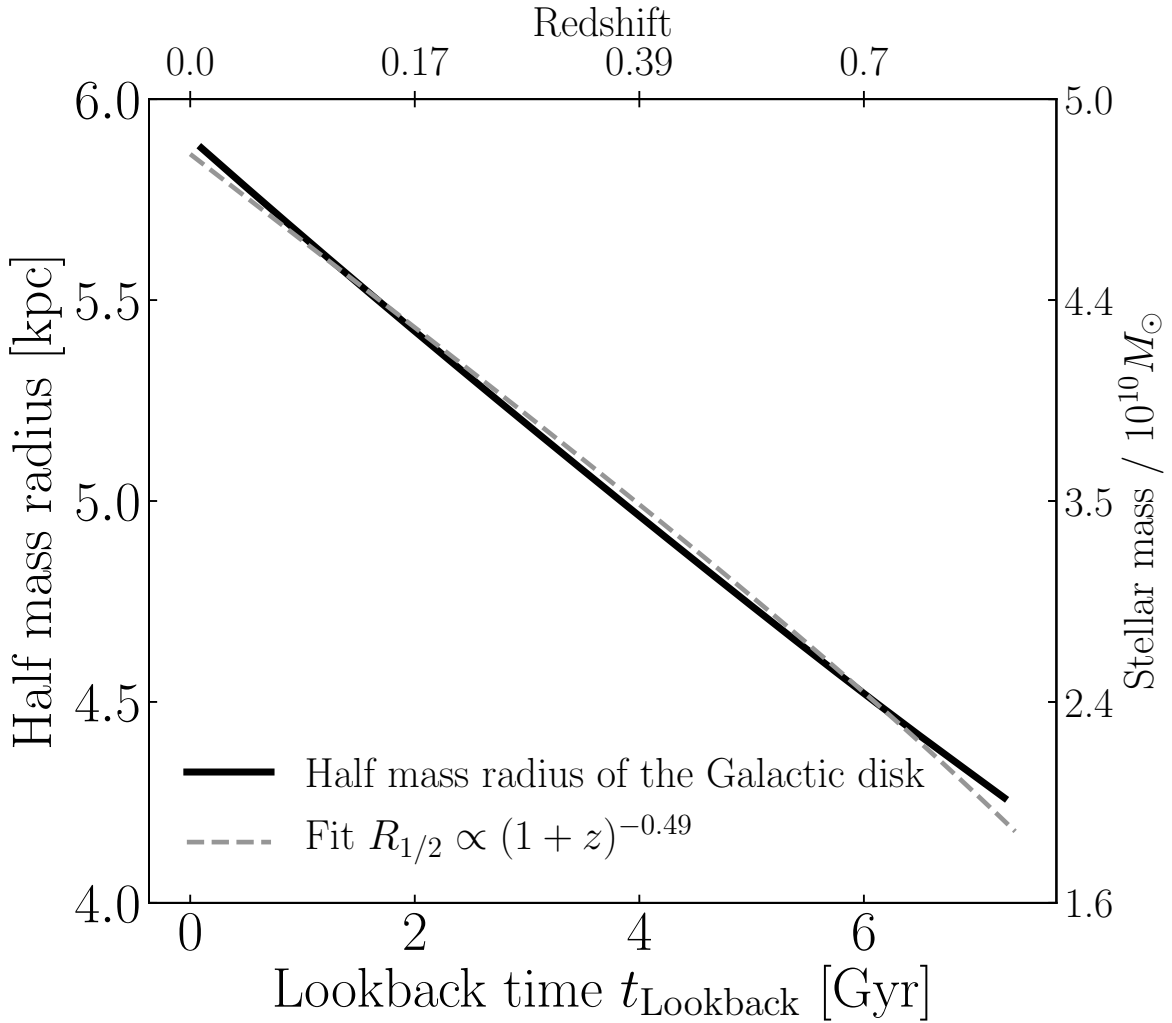
Figure IV.8: Size evolution of the Milky Way's low-α stellar disk over the past 7 Gyr, according to the best fit model (as computed in Eq. IV.26). The disk has grown by 43% its size 7.5 Gyr ago. The dashed grey line is an approximation of this evolution by $R_{1/2} \propto (1+z)^{\alpha}$ with $\alpha = -0.49$. The stellar mass as a function of lookback time (as computed in Eq. IV.27) is illustrated on the right hand side y axis.

sitions, this approach would provide a direct knowledge of the formation of galactic disks. But under extensive radial orbit migration and diffusion, information on stellar birth sites, and therefore local star formation histories, is lost.

Measured mass weighted age gradients are small. For instance, Goddard et al. (2017) found mass weighted age gradient on average consistent with zero. This is in apparent contradiction with the picture provided by redshift-size relations, implying that old stars should be more centrally concentrated if stars were not

radially redistributed in some way. If these differences are physical (and not due to measurement systematics), two scenarios can reconcile these observations: (a) either star formation is constant across disks, and disks grow in size due to redistribution of stars or mergers for non isolated galaxies, or (b) star formation moves outwards with time but radial orbit migration erases the traces of it, such that present-day studies only see the weak remnants of formation gradients. Our present model for the Milky Way disk allowed both pictures to exist through the parameter x, that would be zero in (a) and positive in (b). The data preferentially constrained it towards (b) since the best fit $x = 0.75$.

Below, we use the best fit model to predict (1) the evolution of the half-mass radius of the Milky Way disk with time, (2) the evolution of its surface brightness profile and its half-light radius, to compare to redshift-size relations, and (3) the present-day positions of stars of different ages.

IV.5.1   Evolution of the Disk Half-mass Radius

We use the best fit model to predict the size of the Milky Way disk at different times in the past. Accounting for inside-out growth and radial redistribution of stars, we compute the radius containing half of the total disk mass,

$$M(< R_{1/2}) = M_{tot}/2, \tag{IV.25}$$

as a function of lookback time $R_{1/2}(t_{\text{lkback}})$ by solving numerically for the radius $R_{1/2}(t_{\text{lkback}})$ enclosing half of the total disk stellar mass M_{tot}.

The stellar mass $M(< R_{1/2})$ contained within $R_{1/2}$ is defined as

$$
\begin{aligned}
M(<R_{1/2}, t_{\text{lkback}}) = M_{tot} &\int_0^{R_{1/2}} \int_0^\infty \int_{t_{\text{lkback}}}^{\tau_m} p(R_0) \\
&\times p(\tau \mid R_0) p(R \mid R_0, \tau - t_{\text{lkback}}) \mathrm{d}\tau \mathrm{d}R_0 \mathrm{d}R,
\end{aligned}
\tag{IV.26}
$$

where t_{lkback} is lookback time, τ is time from now (dummy lookback time in the integral, marking the birth of stars) and the quantity $\tau - t_{\text{lkback}}$ is the age of stars at lookback time t_{lkback} and is used to compute the radial migration term $p(R \mid R_0, \tau -$

t_{lkback}). The evolution of the half-mass radius for the best fit model is illustrated by the black solid line in Figure IV.8. The size of the disk has evolved almost linearly in time from about 4.2 kpc 7.5 Gyr ago to about 5.9 kpc today. This implies an almost constant growth rate of $\dot{R}_{1/2} = 0.2$ kpc Gyr^{-1}. The associated time-scale of radial disk growth is $\tau_R = R_{1/2}/\dot{R}_{1/2} = 30$ Gyr. This compares well with the findings of Pezzulli et al. (2015), who measured $\dot{R}_{1/2}$ using star formation and $R_{1/2}$ assuming an exponential surface density profile of about 30 disk galaxies and quote the same growth time-scale. There may be differences by factors of a few due to systematic uncertainties or the definition of a disk size used (half-mass radius, half-light radius, or exponential scale length).

Using $\Omega_\Lambda = 0.7$, $\Omega_m = 0.3$, $H_0 = 70$ km s^{-1} Mpc^{-1}, the half-mass radius obtained from Eq. IV.26 is well approximated by a function of redshift z as $R_{1/2} \propto (1+z)^\alpha$, with $\alpha = -0.49$. This seems globally consistent with redshift-size measurements of external disk galaxies. Franx et al. (2008) find an average relation for galaxies of stellar mass $M_\star > 2.5 \times 10^{10} M_\odot$ with $\alpha = -0.6 \pm 0.1$ and Trujillo et al. (2006) find $\alpha = -0.40 \pm 0.06$ for late type galaxies of stellar mass $M_\star > 3 \times 10^{10} M_\odot$. This approximation of the half-mass radius is illustrated by the grey dashed line in Figure IV.8. However, this direct comparison is only approximate: the literature relations were fitted for galaxy populations of given stellar mass, whereas this work predicts the evolution of the half-mass radius of the Milky Way at different times of its evolution, including its growth in stellar mass. We propose to compensate for these differences in the next subsection.

IV.5.2   Evolution of the Half-light Radius: Comparing to Redshift-Size Relations

In external galaxies, the physical half-mass radius is not a direct observable. It is often assumed that stellar light at different wavelengths traces stellar mass of different populations, and the half-light radius is used as a proxy for the disk size. We predict the surface brightness profile and the half-light radius that would be measured at different lookback times and in different photometric bands, roughly
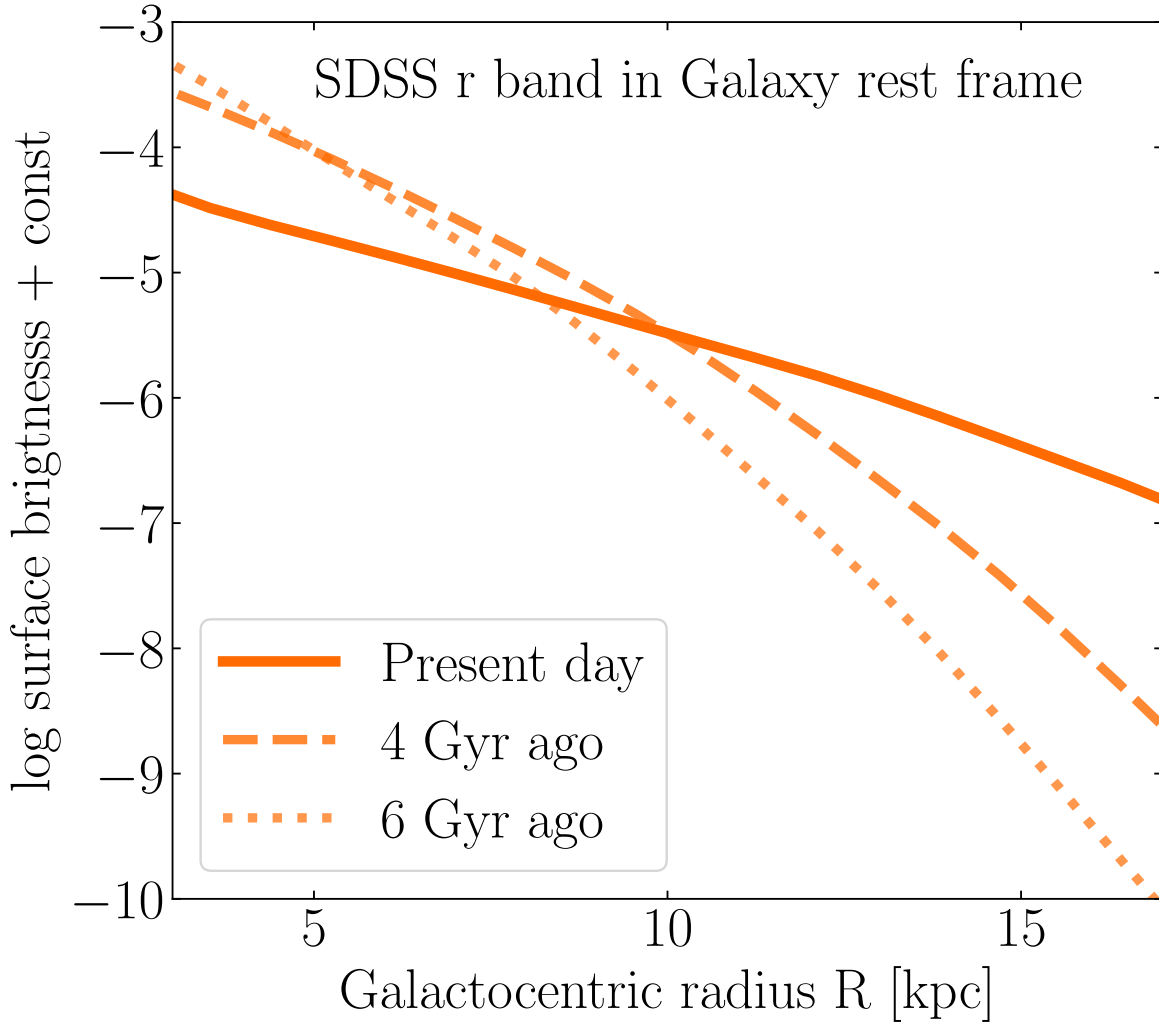
Figure IV.9: Predicted SDSS r band surface brightness profile for the Galactic disk at three different lookback times. This illustrates the inside-out growth of the stellar disk implied by our model fit.

emulating observations of the Milky Way at different redshifts. For this purpose, we use grids based on the single stellar population synthesis code E-MILES SEDs (Vazdekis et al., 2010, 2012; Ricciardelli et al., 2012) to predict the mass-to-light ratio of a single stellar population of given age and metallicity. Assuming a Kroupa initial mass function (Kroupa, 2001), we use the best fit model to predict the distributions of $p(\tau, [\text{Fe/H}], R \mid \mathbf{p_m}, t_{\text{lkback}})$ at given lookback time to estimate the stellar mass density at radius R (up to a normalization constant). The resulting surface brightness profiles in the SDSS-r band are plotted as an example in Figure IV.9. Qualitatively, the trends are similar in other bands. Generally, blue bands are spa-
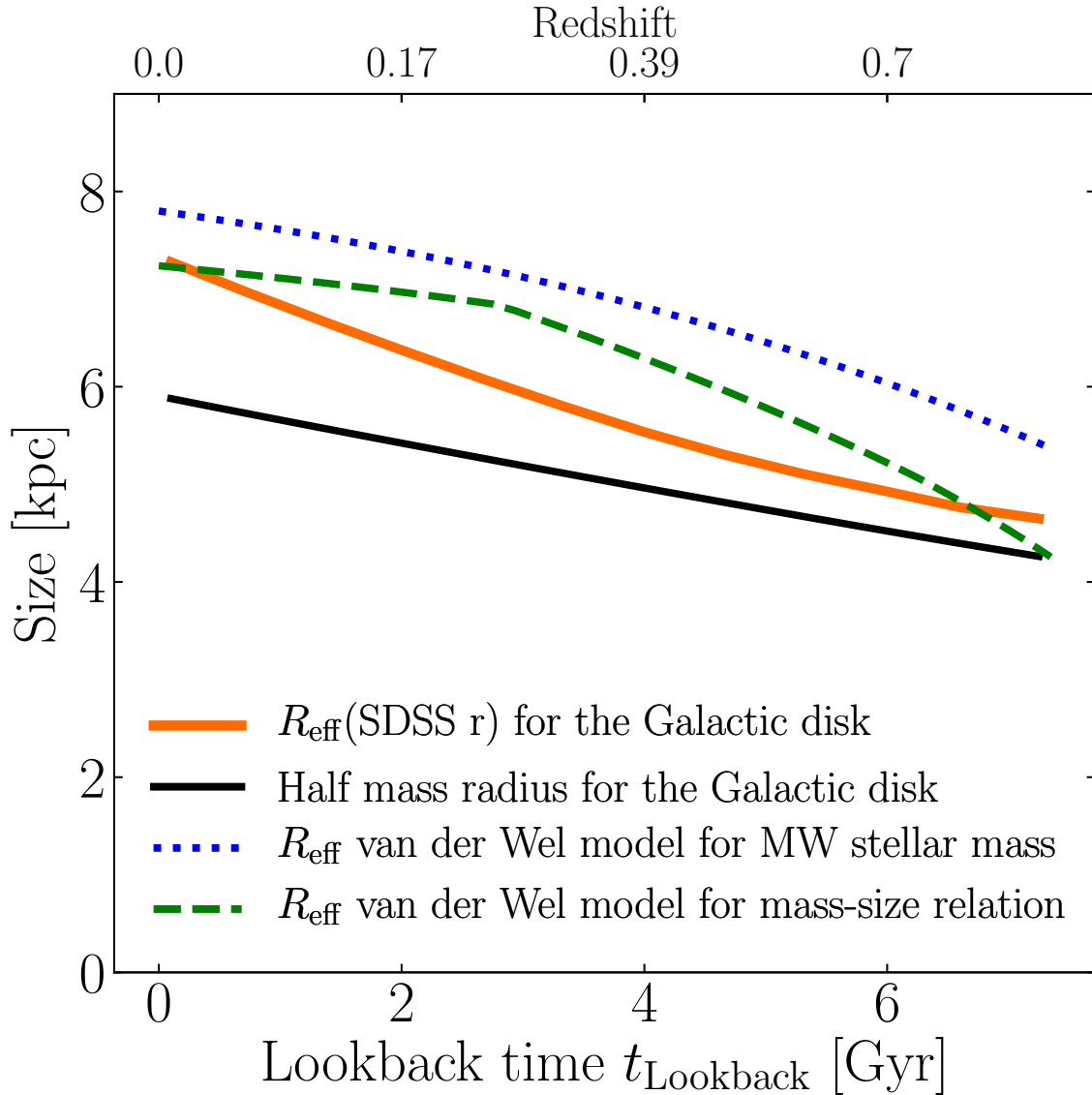
Figure IV.10: Predicted half-light radius as a function of lookback time for the Milky Way disk (thick orange), compared with that of other galaxies (green and blue). The blue dotted line is a prediction from the van der Wel et al. (2014) model for Milky Way mass redshift-size relations, as an element of comparison. It is different from the evolutionary track of a single galaxy, because galaxies grow in stellar mass and size (whereas the van der Wel et al. (2014) blue line is at fixed stellar mass). The green dashed line shows the the same prediction of the van der Wel et al. (2014), but including the evolution of the stellar mass of the Galaxy as in Eq. IV.27. It leads to a redshift-size evolution close to our inference for the Milky Way.

We include the half-mass radius (from Fig. IV.8) in black as a reference.

tially more extended and red more centrally concentrated. This is expected because shorter wavelengths are better tracers of young populations.

From these surface brightness profiles, we solve a similar equation to Eq. IV.26 for the half-light radius, illustrated by the thick orange line in Fig. IV.10. The half-light radius is greater than the half-mass radius, in particular at late times, when the young stars dominating the light are spatially more extended than the overall stellar population. This compares well with the model of van der Wel et al. (2014), who fitted a model to galaxies at different redshifts (illustrated in dotted blue in Fig. IV.10 for galaxies of stellar mass $M_\star \approx 5 \times 10^{10} M_\odot$). However, this only serves as an element of qualitative comparison. This model fitted the size of galaxies of $\sim$ Milky Way stellar mass at different redshifts. But the stellar mass of the Milky Way has grown with time. Therefore, the comparison holds best at $z = 0$. At higher redshifts, one should compare to the sizes of galaxies of smaller stellar mass, which should also be smaller than the blue dotted line that Fig. IV.10 predicts.

van der Wel et al. (2014) have also fitted the evolution of the total stellar mass $M_\star$ - size R_{eff} relation as a function of redshift z. With our best fit model of the evolution of the stellar mass of the Milky Way, we can use the van der Wel et al. (2014) fits to predict the corresponding size. Assuming that the total stellar mass of the Milky Way is the sum of the bulge mass M_b and that of the disk, and assuming that the bulge mass has been constant over the past 8 Gyr (because the bulge is relatively old compared to the disk (Bland-Hawthorn & Gerhard, 2016)), we consider the total Milky Way stellar mass as

$$M_\star(t) = M_b + M_d(t). \tag{IV.27}$$

We assume a bulge stellar mass of about $1.5 \times 10^{10} M_\odot$ (Bland-Hawthorn & Gerhard, 2016) and the fraction of mass in the bulge about 30% at present. The evolution of the stellar mass is illustrated in Fig. IV.8.

Following van der Wel et al. (2014), we assume a stellar mass–size relation of the form

$$R_{\mathrm{eff}}(z) = A(z) \left(\frac{M_\star(z)}{5 \times 10^{10} M_\odot} \right)^{\alpha(z)}, \tag{IV.28}$$

where $A(z)$ and $\alpha(z)$ were measured by van der Wel et al. (2014) at different red-

shifts. We interpolate these values linearly as a function of redshift and compute the corresponding value of $R_{\text{eff}}(z)$ and our predicted Milky Way's stellar mass as a function of time. The resulting size as a function of lookback time (or redshift) is illustrated with the dashed green line in Figure IV.10, and compares well with our predicted evolution of the half-light radius of the Milky Way.

IV.5.3 Present-day Scale lengths of Stellar Populations

In nearby galaxies, it is common to determine the spatial distribution of stars of different populations (e.g., Gogarten et al., 2010). When old stellar populations are found more centrally concentrated than the young ones, this is interpreted as the result of inside-out growth.

   We compute these quantities in two cases: (a) for our Milky Way best fit, and (b) for our best fit excluding radial migration (i.e. finding the half-mass birth radii). (b) does not lead to a scale length that is possibly observable today if stars migrate, but decouples the contributions of the star formation history and radial orbit migration to the growth of the disk. To compute these, we perform a Monte Carlo simulation sampling ages, present-day Galactocentric radii and Galactocentric radii at birth for stars from the best fit model. For each sample, we compute the present-day radius $R_{1/2}(\tau \approx t_{\text{lkback}})$ containing half of the mass of stars at given age, and similarly for the birth radius $R_{0,1/2}(\tau \approx t_{\text{lkback}})$. These two quantities are plotted in purple in Figure IV.11.

   We find a significant difference in the half-mass radius of different stellar populations that have migrated (solid purple in Fig. IV.11) and those that have not (dashed purple). In the limits of our modeling, we can argue that if we were to observe the Milky Way present-day stellar populations in order to constrain inside-out growth, and assume its stars do not redistribute radially, we would overestimate the scale length at birth of old stars by about 1 kpc, and therefore underestimate the amount of inside-out growth. This is a caveat for galactic archaeology approaches that cannot be neglected for disk galaxies with significant radial orbit migration. For the Milky Way, this can be overcome by detailed modeling, because one can measure a physical scatter in the age-metallicity distributions, and interpret it as an
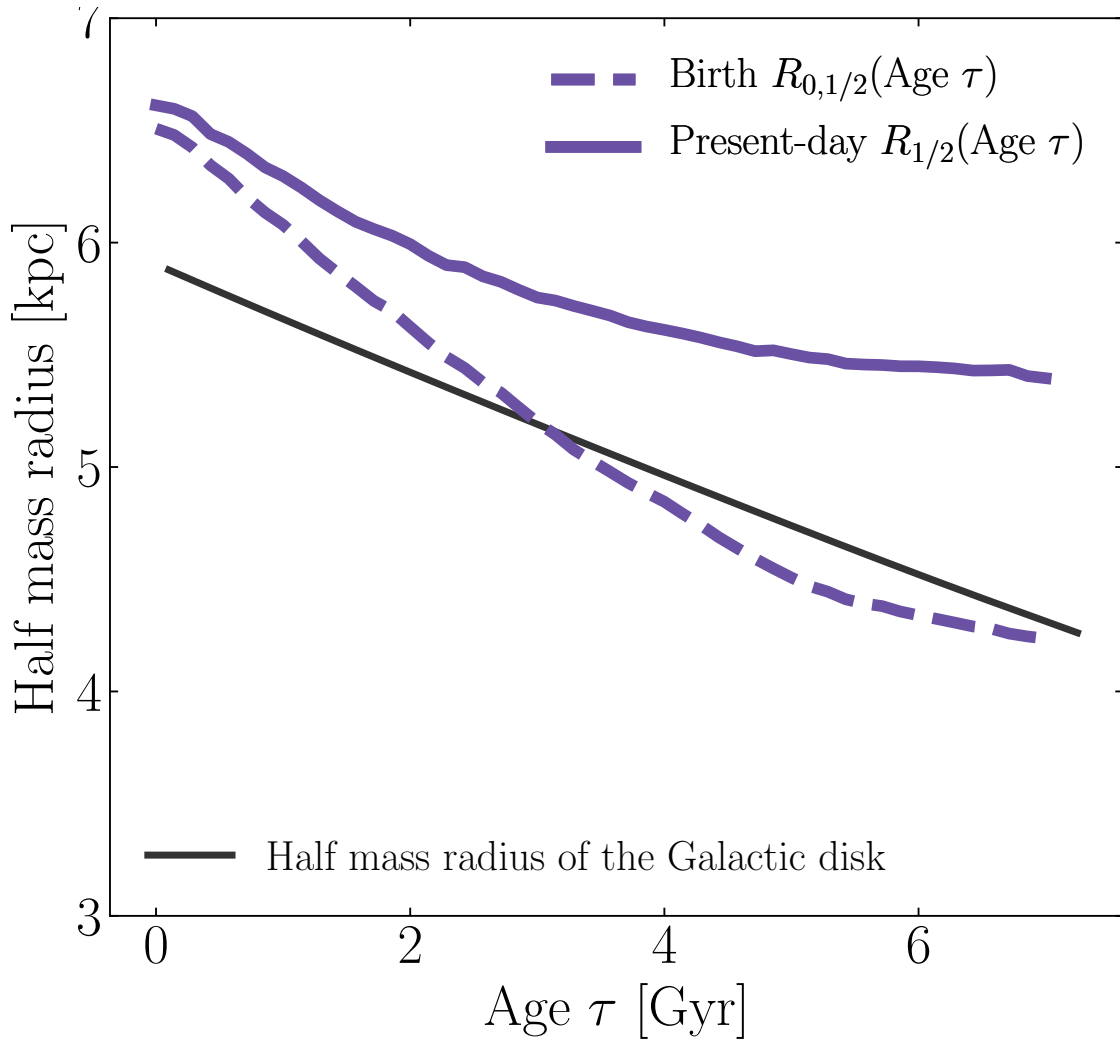
Figure IV.11: The present-day half-mass radii of stars with ages τ, $R_{1/2}(\tau)$, compared to the star formation scale length a time τ ago. We show $R_{1/2}(\tau)$ from the best fit model with solid purple and compare it to the analogous, hypothetical radii expected in the absence of radial orbit migration (dashed purple). As a reference, we overplot the overall size evolution of the disk at different lookback times in solid black. Radial mixing leads to a moderate present-day dependence of $R_{1/2}$ on age, even in the presence of distinct inside-out growth in the star formation history.

effect of radial orbit migration. However, for external galaxies, the question is more challenging as only integrated properties are derived (the mean, but not the scatter). Therefore, the present-day distributions of stellar populations can be a weak diagnostic for inside-out growth, giving only lower limits.
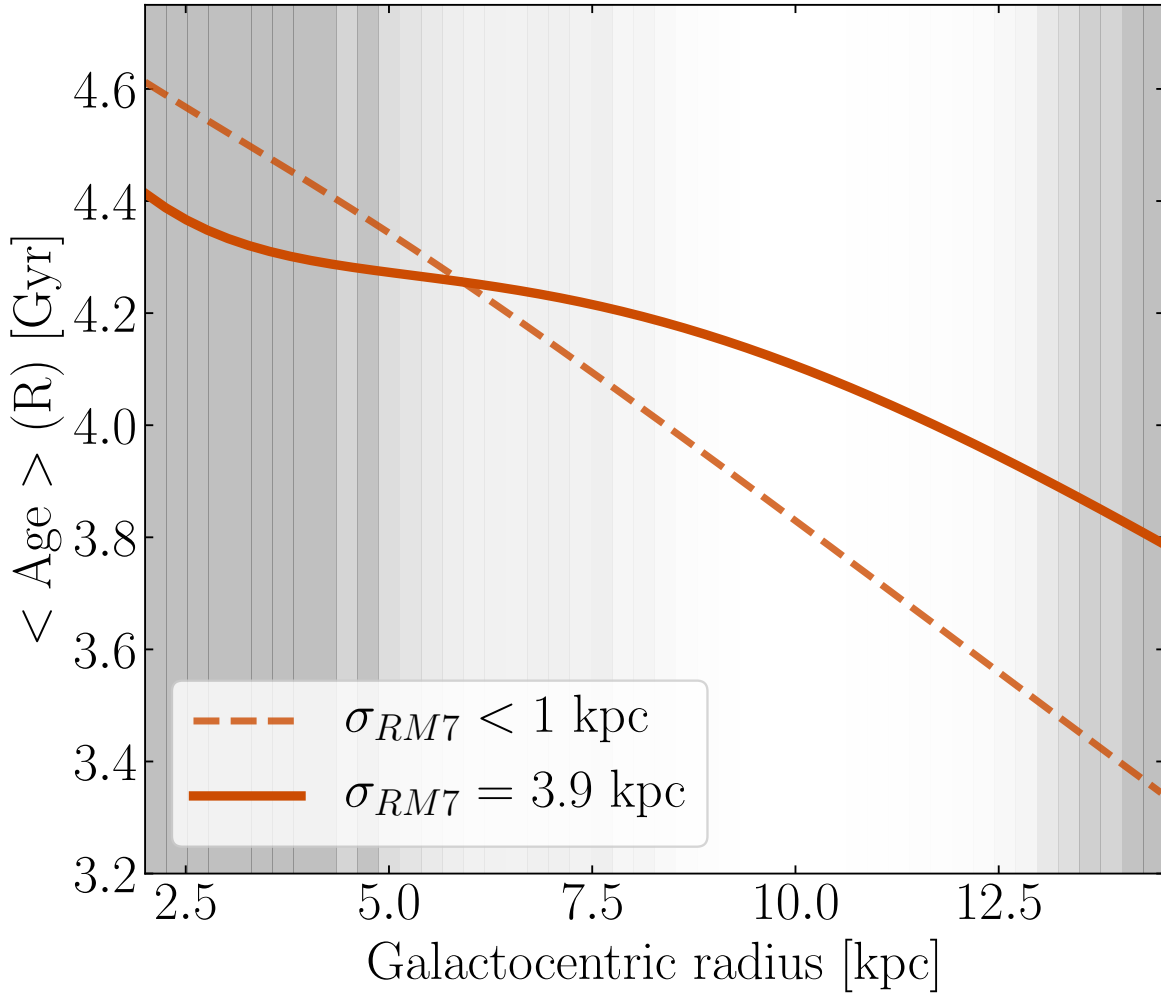
Figure IV.12: Radial profile of the mean stellar age in the Galactic disk, determined through our model fit (solid line, for $\sigma_{RM7} = 3.9$ kpc computed using Equation IV.29). This is compared to the hypothetical case of 'no radial orbit migration' (dashed line), where stars stay at their birth radii (also determined from our model fit). Age gradients resulting from the distinct inside-out growth that the best model implies are severely weakened by radial orbit migration. Areas containing few data to constrain our model at their present-day Galactocentric radii are shaded in proportions of the Galactocentric radius histogram in Fig. IV.2 on a logarithmic scale.

IV.5.4 Weakening of Age Radial Gradients

Age gradients are expected to result from inside-out growth: if stars formed on shorter time-scales in the inner disk than in the outer disk, then the proportions of old stars should be larger in the inner disk than in the outer disk. But in external galaxies, the mass weighted age gradients seen in MaNGA seem weak for a large number of disk galaxies (Goddard et al., 2017; Bundy et al., 2015).

We compute the expected mass weighted age profile from our model and the

best fit parameters with

$$\langle \text{Age} \rangle (R) = \iint \tau \cdot p(R_0, \tau \mid R) \mathrm{d}R_0 \mathrm{d}\tau, \tag{IV.29}$$

and illustrate it in Figure IV.12 for two cases: no radial migration (where we take $\sigma_{\text{Lz12}} < 1$ kpc), and our best fit radial migration. We find that, in the 'no migration' case, the best fit star formation history produces an age gradient that is already weak, with only about -0.1 Gyr kpc^{-1}. But in addition, radial orbit migration weakens severely this gradient. Therefore, it is possible for a galaxy to have grown from inside-out without exhibiting strong age radial gradients, making present-day age gradients a poor diagnostic of inside-out growth.

IV.6 Limitations of our Methodology

Even though the present method is promising for later studies of Galaxy evolution, we state below important shortcomings that should be addressed in the future.

IV.6.1 Inevitable Limitations: Direct Use of Ages

The direct use of ages in global models for the Galactic archaeology field is new and can only be as powerful as the ages are good. Since our method relies *directly* on stellar age measurements, the results are directly affected by any systematics in age determination methods (see Section IV.4). These systematics are numerous and unknown; and age uncertainties are large and heteroscedatic. Age determination methods differ by their complexity. Data-driven methods depend strongly on the reliability of their training sets, those using luminosity and distances may induce large scale spatial biases, affecting our understanding of Galaxy evolution. To estimate the extent of these limitations, we have considered several data-driven age catalogs, and presented the results for the fit on the Ting18 sample (Ting & Rix, 2019). Even though this data set has its short comings, such as an unexpectedly small fraction of old stars, it showed more reliability than the three others in the several aspects:

- the precision of the determined ages on a test set on APOKASC 2 red clump stars was the highest with 0.15 dex scatter in log age;

- model predictions using the best fit on these data compared better than those the three other data sets to independent work on selection-corrected age histograms using LAMOST turn off stars;

- the age determination method (spectroscopic ages) has no known dependencies on distance measurement, so there should not be age biases with distance, which is of fundamental importance to study inside-out growth through the spatial structure of ages;

- the training of the neural networks that determined these ages was done only on red clump stars, so the neural networks were not learning possibly undesired information from other stellar evolutionary stages.

Inevitably, the present results are bound to all assumptions that were made by using this data set and by modeling its age uncertainties.

IV.6.2   Limitations from the Data Selection

This work made exclusive use of red clump stars, because they are excellent standard candles, they are bright and they are abundant in the Galactic disk. However, this stellar population is younger than the underlying mean population, with an age distribution that peaks at 2 Gyr and that has few stars older than 5 Gyr (see Fig. IV.1). This introduces two shortcomings. First, most of the information constraining our model lies between 1 - 4 Gyr. Therefore, our model describes best the most recent evolution of the Galactic disk, but not earlier times when the physical processes of disk formation were supposedly faster. Secondly, we corrected for population selection biases by modeling their age distribution (or, more accurately, the relative mass of stars on the red clump evolutionary stage, at given age and assuming an initial mass function). This was based on theoretical expectations of a star's lifetime on the core helium burning stage, which is only constrained by theoretical models of stellar evolution.

In order to constrain the evolution of the disk at earlier times, and reduce stellar population effects on ages, we should turn to a different stellar population with more old stars, for example RGB stars for which distances are known precisely (Hogg et al., 2018; Leung & Bovy, 2019). But this would introduce more technical difficulties that are not straightforward to overcome: using standard candles limits the number of integrals to evaluate in magnitude-limited selection functions, bringing computational expenses down. However, the lack of old stars in our red clump data set, and the large age uncertainties at large ages, made us unable to build and constrain a more adequate model for the early behavior of star formation. This question is left to be addressed in the future.

Additionally, due to the spatial selection of stars in our survey, most of the stars we have used lie in the outer disk (5-14 kpc, but with few stars between 5 and 7 kpc, see Fig. IV.2). Since these are the data constraining our model, our results describe best the outer disk of the Milky Way. But the inner low-α disk should contain additional information on inside-out growth in its spatial-age-metallicity distributions, unless it had a different formation scenario (as argued in e.g. Haywood et al., 2019b). As shown in the test of subsection IV.4.3.2, including more APOGEE fields with data from the inner disk mid-plane affects some parameters, for example the star formation time-scale τ_{SFR} and the inferred scale length of our outlier model (old component). We have kept consistency with the data set used in Frankel et al. (2018), but we plan to turn to APOGEE DR16 and the inner Galaxy in future work.

IV.6.3   Model Shortcomings

To construct a parametric model for the Galactic disk, we have made several assumptions. The core of this model, a radially-dependent star formation history, was built to satisfy the following properties: (1) be qualitatively plausible; (2) be sufficiently flexible to allow the 'no inside-out growth', 'inside-out growth' and 'outside-in growth' scenarios to exist, and to be fit; (3) be a global decreasing exponential in the case of 'no inside-out growth', and (4) be such that our data can constrain it.

The functional form presented in Eq. IV.11 satisfies the properties (2)-(4), and is

good with (1) on average. However, it proposes a rather simplistic description of the star formation history: star formation begins at the same time over the entire disk and the only parameter quantifying inside-out growth is the time-scale regulating the star formation. By definition, such a functional form produces an age distribution that has a large variance, and our model does not reproduce exactly the age distribution of the data at given Galactocentric radius. This can be seen in Fig. IV.6, where our model predicts the mean age profile correctly, but overestimates the standard deviation, and is skewed at large ages. We have experimented with different functional forms for the star formation history, where star formation rises at different times at different Galactocentric radii (see Section IV.4). Samples from such a model compared much better to the observed data than those from the model we have chosen to present. But due to the lack of old stars in our data set, and large age uncertainties at large ages, we were not able to fit this model reliably (and condition (4) was violated).

In order to improve the description of the data in a physically sensible way, it will be important in the future to introduce realistic parametric models inspired by simulations.

IV.7   Summary and Future Prospects

We have built a model to constrain the degree of inside-out growth of the Milky Way disk. Applied to APOGEE red clump stars, the model fit leads to significant inside-out growth and has several implications. In this modeling context, we find that

- the model fit implies a growth rate of the stellar disk of 0.2 kpc Gyr^{-1} and a present-day half-mass radius of 5.9 kpc, resulting from a 43% growth over the past 7.5 Gyr;

- comparing the half-mass and half-light radii with redshift-size relations and with the evolution of the mass-size relations of other galaxies shows that the Milky Way is a rather typical disk galaxy in terms of present-day mass and

size, but also in terms of global mass-size evolution. We fitted the evolution of the Milky Way's half-mass radius $R_{1/2} \propto (1+z)^{-0.49}$);

- important radial redistribution of stars erases present-day evidence for the past history of the disk, including the spatial variations of the star formation history and therefore inside-out growth. This implies that a local age histogram differs from a local star formation history as local stars may have been born at different Galactocentric radii and stars formed locally may have migrated to different radii;

- present-day age gradients can be a poor diagnostic for inside-out growth if radial orbit migration is strong and makes population studies in external galaxies challenging as assessing the strength of radial orbit migration is more difficult (the physical scatter in age-metallicity resulting from radial orbit migration is not accessible through integrated light). Indirect possibilities to assess radial mixing strength in external galaxies and their impact on the stellar age structure are, for example, dynamical studies as in Gogarten et al. (2010).

This methodology builds on a large data set, with extended spatial coverage and for which stellar ages are known, combined with a forward model with parameters physically understandable. This allows to quantify the amount of inside-out growth in the Milky Way disk. However, there are clear limitations to outcome: the data set we have used is overall young (whereas the evolution of the disk was possibly faster at early times), which allows us to fit the recent evolution of the disk well but not earlier times. In addition, the results are bound to all assumptions made while constructing this model.

To confirm and improve these results, reliable age estimates of stellar populations that cover wide age and Galactocentric radius ranges are needed. Red clump stars are excellent distance indicators, but have poor age estimates and are younger than the underlying population. We showed that five different age sets for our red clump stars lead to five different estimates of the degree of inside-out growth, which is a general problem for Galactic archaeology.

With a data set with precise distances (e.g., Hogg et al., 2018; Leung & Bovy,

2019) and less prone to population selection effects, it should be feasible to improve the inside-out growth model for a better description of the build up of the Milky Way disk and inspire the model construction from numerical simulations, to benefit from direct physical insights. But these requires more computational issues to overcome.

Acknowledgements

The following softwares were used during this research: Astropy (Astropy Collaboration et al., 2013), Matplotlib (Hunter, 2007).

IV.8   Inside-out growth inference using different age sets

As part of the analysis, we explore the effect of age determination methods on the results. We repeat the analysis keeping the same stars, the same [Fe/H] and position columns, but changing the age column using five different age sets described below. We find that the overall inside-out growth scenario is robust to age systematics, but the details can change quantitatively. We describe the detailed procedure and results for each age set below.

Ness16   We use ages derived with *The Cannon* (Ness et al., 2015, 2016) trained on spectra and masses of APOKASC1 stars (Pinsonneault et al., 2014), and derived log age with a precision of 0.2 dex. Adapting our noise model from Eq. IV.20 with $\sigma_{\log \tau} = 0.2$, and optimizing the likelihood, we find a value for the parameter x of 0.62, which is roughly consistent with our results with the Ting age set: the star formation time-scale decreases slowly towards the outer disk and flattens at $R_0 = 12$ kpc. Additionally, the best fit parameters of the other model aspects are consistent with the work in Frankel et al. (2018), who used this data set. In particular, the value of the radial orbit migration term was exactly the same: a mixing scale of 3.6 kpc after 8 Gyr. This confirms the robustness of this result, and suggests that our new model aspects and APOGEE selection function are incorporated correctly.

Ness18   This data set also used *The Cannon*, trained on APOKASC2 spectra and masses. We apply the same noise model as for the Ness16 data set. The best fit inside-out parameter for this data set is $x = 0.50$, which means that the star formation rate depends more weakly on Galactocentric radius, and goes as $1 - 0.5 R_0/8$ kpc. According to this fit, the star formation rate is as slowly decreasing function of time throughout the disk until $R_0 = 16$ kpc.

Ness19   Ness et al. (2019b) used empirical tight age-abundance relations, and trained *The Cannon* to map from precise abundances measurements for 17 elements

to APOKASK2 age estimates. This procedure was applied to the low-α red clump sample of Ting et al. (2018b), and yields ages with a precision $\sigma_\tau = 1.6$ Gyr. The resulting distribution of observed ages resembles most that of the Ting18 sample compared to the other age sets. We modified our noise model accordingly with $p(\tau_{\mathrm{obs}} \mid \tau, \sigma_\tau) \sim \mathcal{N}(\tau, \sigma_\tau)$. The best fit parameter for the inside-out growth on this data set is $x = 1.1$, which implies that the star formation history at 8 kpc has been constant over the past 7.5 Gyr.

Sanders18   We also used the ages presented in Sanders & Das (2018), using the method outlined in Das & Sanders (2019). This method consists of an initial data-driven stage to measure stellar mass from APOGEE spectroscopy as in Ting & Rix (2019) and Ness et al. (2016), but using the information contained in the abundances directly rather than the full spectrum. A second stage compares the derived mass, spectroscopic parameters, photometry and Gaia parallaxes to a set of isochrones folded with a Galactic prior. We first re-run the age determination procedure, removing the priors on the ages. The fit to the data leads to $x = -0.3 < 0$, favouring weak outside-in growth. A key difference between this age determination method and the previous ones is that the luminosity and parallaxes of the stars were explicitly used to derive the stellar masses. This could introduce a bias with distance or extinction, in particular at large distances where the distance information from the parallax is modest and the extinction may be significant. When comparing these ages with all of the previous ones (Ting18, Ness16, Ness18, Ness19), which are not distance-dependent, we find systematic differences that are function of distance: compared to the other data sets, these ages tend to be overestimated at large distances leading to a contaminating population of old stars at large distances. In our case, due to selection effects, distant stars are mainly located in the outer disk. This produced a general trend with older stars at larger distances and larger Galactocentric radii, weakening (and inverting, in some parts) the already quite weak radial age gradient that contains information about inside-out growth in the data set (see Fig. IV.6).

Chapter V

Discussion

Contributions   Although this chapter was not published as an article, many people contributed to it through regular interactions and discussions with me. The written part of this discussion is, of course, my own processing and analysis of different aspects touched by this thesis, but arose through various discussions.

- Yuan-Sen Ting shared ideas and enthusiasm about (1) modelling multiple elemental abundances in the Galactic disk, not just metallicity; and (2) the statistical methods outlined in the discussion.

- Hans-Walter Rix contributed to my scientific maturity through regular interactions, and finding sensible compromises between technical or mathematical problems.

- Jason Sanders gave practical counselling with the stellar dynamics in simulation outputs and scientific insight.

- Tobias Buck provided data and practical help with NIHAO simulation output.

- Annalisa Pillepich provided data, practical help and a scientific insights with TNG50 simulation output.

- Martina Donnari provided a list of flags to Milky Way-like galaxies in the TNG50 simulation.

- Ivan Minchev and Friedrich Anders shared their experience and ideas.

Science question Even though it is near isolation, the Milky Way is a dynamic organism in permanent formation and evolution. It has evolved and seen long-lasting changes in its structural properties. Over the past 7-8 Gyr, internal processes drove the secular evolution of the Milky Way's disk, shaping its radial profile to what we observe now through the stellar distributions of $\{[\text{Fe/H}], \tau, \vec{x}, \vec{v}\}$. The explorations carried out in the previous chapters show that the orbital changes of stars follow a very specific pattern: they are strong, but mostly cold such that stellar orbits remain approximately circular. This can provide tight constraints on the nature of the drivers of secular evolution. In this chapter, I synthesize the results of this thesis, discuss their limitations, and explore the nature of the internal processes driving secular evolution, with cosmological simulations.

V.1   The Secular Evolution of the Milky Way as a Galaxy

The previous three chapters introduced a phenomenological approach to measure the orbital changes of stars in the Galactic disk. The two most important assumptions underlying this thesis are

1. Stars change orbit; and the orbital changes are slow and diffusive. The analysis focused on measuring how strong these orbital changes are, without asking what the *nature* or *origin* of the drivers are.

2. The birth orbit of a star is imprinted in the chemical abundance patterns in its atmosphere: the abundances of stellar atmosphere reflect those of the gas from which they formed, and this abundance patttern varied as a function of time and position in the Galactic disk, allowing us to find stars' birth orbits through 'weak chemical tagging'.

Based on these assumptions, in the previous three chapters, we build incrementally and fit a model for the evolution of the Milky Way's disk, relating birth orbits to present-day orbits through birth abundances and an evlution model, $p([\text{Fe/H}], L_{z,0}, L_z, J_R, \tau | \mathbf{p_m})$.

The three main results obtained in this thesis are:

1. The stars in the Milky Way disk undergo strong dynamical secular evolution: stars mix in radius on scales of $\sqrt{\langle (R - R_0)^2 \rangle} = 3.5\sqrt{\tau/8\text{Gyr}}$.

2. This dynamical evolution is mostly cold and dominated by diffusion in angular momentum, implying a dynamical memory loss of star's birth conditions. The diffusion in L_z and J_R goes at the rates

$$
\begin{aligned}
\sqrt{\langle (L_z - L_{z0})^2 \rangle} &\approx (619 \text{ kpc km/s}) \left(\frac{\tau}{6 \text{ Gyr}} \right)^{0.5}, \\
\sqrt{\langle (J_R - J_{R0})^2 \rangle} &\approx (63 \text{ kpc km/s}) \left(\frac{\tau}{6 \text{ Gyr}} \right)^{0.6}.
\end{aligned}
\tag{V.1}
$$

3. Rewinding stars to their birth conditions thanks to the chemical memory they retained (stars' atmospheric abundances should reflect, to some extent, the abundances of the gas they were born from), allowed us to conclude that its disk likely grew from inside-out, by about 40% over the past 7 Gyr: this makes the Milky Way follow well the redshift-size evolutions seen for other galaxies of its mass.

The physical processes that are thought to play an important role in the secular evolution of the disk arise from the presence of non axisymmetries (Sellwood, 2014) a long-lived bar in the inner 5 kpc, and fleeting spiral perturbations that exert torques on the stars and change their angular momenta. The Milky Way is typical in this aspect: most disk galaxies exhibit similar non-axisymmetries, and those axisymmetries are what simulations have shown to redistribute stars' orbits by large amounts. If this process is typical and generalizable, this could validate the argument proposed in Herpich et al. (2017): strong L_z diffusion could lead disk profiles to near-exponential surface brightness profiles. This diffusion process leads stars to lose dynamical memory of their birth conditions, erasing the dynamical clues about

their formation processes. Therefore, a star on a circular orbit at a given radius to-day may well have been born several kpc away from its present-day position. For example, the Sun was likely born ∼1 kpc away from its present-day orbit as seen in Chapter III.

Rewinding stars to their birth orbits in Chapter IV showed that its disk likely grew from inside-out. Comparing the surface brightness profile, and the size, one would measure for the Milky Way at different redshifts, to actual redshift-size measurements of external galaxies showed that the Milky Way likely had a typical growth over the past 6-7 Gyr: the Milky Way not only obeys present-day scaling relations, but likely also did in the past [1].

V.2   Methodology Extensions and Science Questions

The method presented in this thesis sucessfully used datasets of $\sim 10^4$ stars, and extracted quantifiable information and knowledge about the Milky Way's disk: the evolution of its size, the scales of global stellar redistributions in orbit space, the rate at which stars formed an when. However, it presents limitations in three aspects:

1. This method was applied successfully to a relatively small dataset (about 10,000 stars). But we have now and will have in the future sample sizes larger by factors from 10 to 100. These bring new challenges, in particular the optimization of the fitting algorithm and statistical technique.

2. It is a purely descriptive approach of the physical evolution of the Galactic disk, and some aspects that are covariant need physical insights and motivations.

3. The physical assumptions this thesis is based on (axisymmetry, equilibrium) are only assumptions, and the quality of the data that we are currently reaching now allow us to largely see deviations from them.

---

[1]Though there would be additional work to do for better apple-to-apple comparisons with external galaxies, Chapter IV only was an exploration.

We need an improvement of the physical description of the sytem and of the satistical methods. I detail the limitations and discuss some possible actions to take below.

V.2.1 Statistical Inference and Modelling

V.2.1.1 Inference

As the size of datasets increase, the required precision for calculating the likelihood functions increases; and the computation time to evaluate likelihoods also increases. With the method used in this thesis – build a parametric model, a likelihood function, a posterior and sample the posterior with Markov Chain Monte Carlo, MCMC – sampling posteriors from the likelihood functions might reach computational limitations soon if not optimized. Currently, a typical optimization time was of a few hundreds of core hours. Improving statistical methods or using different ones may be needed in the future if one wants to model samples of a size of a million.

One approach that could be interesting to pursue, practically, is variational inference. Instead of sampling the model parameters from the posterior ($p_{\mathrm{pos}}(\mathbf{p_m})$) via MCMC sampling, one could *approximate* the posterior with a different function that is practically easy to sample from (e.g. a multivariate Gaussian), $q_{\mathrm{pos}}(\mathbf{p_m})$. One could then sample points from the approximate q_{pos}, and ask the question: 'what set of parameters $\mathbf{p_m}$ make q_{pos} as close as possible to the target disribution p_{pos}?'. This is effectively done by minimizing the KL (Kullback-Leibler) divergence between p_{pos} and q_{pos}.

I have not pursued this direction in this thesis, appart from doing a few one-dimensional tests, but discussed it with collaborators (specifically Yuan-Sen Ting) as a possible improvement for the future.

V.2.1.2 Modelling: the 'nuisance' aspects

Some aspects of the Milky Way model introduced in this thesis were purely descriptive and considered as a nuisance: the chemical enrichement part of the model served only as a 'weak chemical tagging' strategy, to rewind stars to their birth or-

bits. But this part of the model only was a 3-parameter functional form: this is not very flexible, might not reflect the complexities involved in the chemical enrichment in the Milky Way. Any inadequacy in this model aspect may well bias the best fit secular evolution part of the model.

The model could and perhaps should be much more flexible. To add more degrees of freedom to a function, one way is to add model parameters and the other is to add nonlinearities. Adding both parameters and nonlinearities is also feasible, for example by constructing a neural network that, from the birth orbit and the birth time of a star, predicts its present-day abundances.

This approach would be extremely interesting because it would open new modelling avenues. In particular, it would allow to preform suitable multi-abundance fits: the chemical enrichment model would then take as input the birth orbit and birth time of stars, and predict all abundances (or abundances that can be obtained from the observations) at once. I have explored modelling along these lines in a simplified manner, including three elements in the model ([Fe/H], [Mg/H] and [Si/H], instead of only [Fe/H]). This was done not by adding three model parameters per new element. Globally, the fit to the data went well and gave plausible results: the best fit model could predict well that alpha elements were produced faster at early times, and elements produced mostly in type Ia supernovae were produced mostly at later times. However, the model fits were not robust, and this could certainly improve with a more flexible chemical enrichment model. With a full $p([\vec{X/H}], \tau, L_z, J_R, J_z | \mathbf{p_m})$, we could (1) find the set of birth orbits and abundances that *minimize* the present-day observed scatter n serveral elemental abundances, by assuming the interstellar medium is well mixed at all times (this is essentially what was done in my thesis but I lacked degrees of freedoms), (2) measure the radial and time dependence of orbital changes, (3) learn chemical evolution: what are the relevant processes, timescales and yields involved in chemical enrichment?

V.2.2   Physical Limitations

Along this thesis, I presented radial migration as a process arising due to resonant scattering with non-axisymmetric structures. However, the statistical model for the

Milky Way disk that I have build only presumed that 'a global process causes stars to diffuse in angular momentum in the disk, at all times, and at all locations', but did not 'know' the dynamical processes causing stars to change orbit, it .

These assumptions are clearly limiting the description of the Galactic disk, the interpretation of stellar orbital changes, and the information we can extract from the dataset. Therefore, it is important to *understand* the physical processes at play in the secular evolution of disk galaxies in order to better describe them and measure their impact. In particular, is angular momentum change really driven by the corotation resonances? What is the lifetime and pattern speed of the fleeting spirals that caused them? Is the lifetime of the spirals short enough, and their formation and decay stochastic enough for radial migration to actually be a random walk? To which extent do internal processes actually dominate the disk, in contrast to external processes and the possible influence of satellites? Do satellites play any role in triggering disk instabilities and causing spirals to form?

Unfortunately, dynamics are difficult to trace from the Milky Way's present-day data themselves: measuring accelerations, torques, mass densities with our incomplete view of the disk has not been achieved (and also because we have observed the disk over durations negligible compared to the orbital time). Furthermore, data from external galaxies are difficult to interpret, but there are ongoing efforts in galaxies where the stars are resolved, trying to link global stability and stellar kinematics (e.g. Sellwood et al., 2019).

Simulations of disk galaxies can provide the required physical guidance for this modelling. In particular, the recent improvements of cosmological N-body simulations provide an interesting framework where the resolution is high enough to investigate and disentangle both the internal and external dynamical processes. I present in the next section a preliminary investigation of the physical processes at play in the secular evolution of simulated disk galaxies.

> The method presented in this thesis could benefit from methodology extensions. In particular, the statistical methods will need optimization or a different technique to keep up with the increasing amounts of data (whose size can be larger by facors 10 or 100). As most aspects of galaxy evolution are covariant or partially degenerate, getting physical insight from simulations to improve the model will be crucial.

V.3 Physical Input from Simulations

I have started to enlist numerical cosmological simulations to better understand what the drivers of secular evolution are, to disentangle them, and to come to a better description of secular changes in disk galaxies. Specifically, I studied two disk galaxies from two different state of the art simulation suites: NIHAO-UHD (Buck et al., 2020) and TNG50 (Pillepich et al., 2019). This is the begining exploration of a still on-going work, and the discussion will remain very qualitative.

V.3.1 Simulated Galaxies

Many cosmological galaxy formation simulations exist. Here, we need not only high physical resolution, but also frequent (~ 10 Myr) simulation outputs, which is rare for practical reasons. To understand the processes driving secular evolution in disk galaxies in a broad context, we need simulations with

- physical conditions that reflect reality, i.e. cosmological simulations,

- both stars and gas (hydrodynamical simulations)

- fequent outputs to resolve the timescales of the dynamical effects (e.g., period of a central bar, short-lived spiral structures, etc.)

With these requirements, we study two simulated galaxies introduced briefly below.

NIHAO-UHD is an ultra high definition re-run of the NIHAO SPH zoom in simulations (Buck et al., 2020). One of the re-ran galaxies (g2.79e12) has a bar, a disk a halo mass of $M_{200} = 3.13 \times 10^{12} M_\odot$ and a stellar mass of $M_\star = 15.9 \times 10^{10} M_\odot$, and an exponential scale length of about 5.5 kpc. This simulation was re-ran for the last 1 Gyr with output times every ~ 7 Myr.

Illustris TNG50 is a high resolution cosmological simulations ran in a 50 Mpc periodic box. Milky Way-like galaxies (in halo mass range and disky shape requirements) were extracted in Donnari et al. 2020 (in prep). A subbox of the TNG50 simulation has output data with high time cadence (every ~ 7 Myr) for the whole run in the simulation. In this subbox, one galaxy is flagged as Milky-Way like, and we focus on this galaxy here. It has a mass of $M_{200} = 10^{12} M_\odot$ and stellar mass of $2.5 \times 10^{10} M_\odot$. This galaxy has no bar at redshift $z = 0$ (but it appears it could have hosted a bar in the past), and it has a few satellites.

These two simulated galaxies complement each other (bar / no bar) and were computed with different physical recipes (SPH / mesh), so they give a wide dynamical range of different apects to explore.

V.3.2   What Drives the Dynamics?

Stars in a galaxy feel net gravitational forces and torques irrespectively of what generates them. At a given position, as star feels the net effect of all structures around it, therefore a simple map of the surface density of the different structures in the galactic disk is not informative to know how they affect stellar orbits. In order to disentangle the possibe drivers of the secular evolution in disk galaxies, we need to map the different structures present in and around the galaxies, and quantify the strength of the forces they apply on the star particles, for how long, and how often. A large fraction of the literature body focused on the effect of spiral arms on the stars' orbits, by designing stellar N-body experiments (e.g. Sellwood, 1987). In these simulations, stellar spiral arms form from dynamical instabilities, and perturb the orbits of other stars. However, disk galaxies like the Milky Way may also contain gas, and accounting for the presence of gas, its reactions to supernovae feedback and its dynamics is important. Stars respond to a spiral perturbation, and

the material the spiral is made of also responds to the new stellar arrangement. If the material making the spiral is external to the star system and behaves differently (for example, gas), then the dynamics can be different. The simulations introduced now contain dark matter particles, stars (collisionless) and gas (not collisionless).

On the observational side, most constraints on the evolution rate of disk galaxies consisted in measuring torques from the mass density of stars in external galaxies (e.g., Foyle et al., 2010). But if the torques arising from the gas were to be important and unobserved, this could bias the estimates of secular evolution rates. Foyle et al. (2010) report that only 8 out of 24 spiral galaxies in their sample have torques strong enough to redistribute angular momentum over a Hubble time, but this estimate only accounts for torques arising from the stellar distribution.

In the simulation, one can measure the surface density of particles (of star, gas or both) by summing the mass on a spatial grid. To approximate the gravitational potential generated by these in the midplane of the disk, one can then use a Green's function,

$$\Phi_{\text{pot}}(R, \phi) = -G \iint \frac{\Sigma(R', \phi')R'}{\sqrt{R^2 + R'^2 - 2RR' \cos(\phi' - \phi)}} dR' d\phi', \qquad \text{(V.2)}$$

with G the gravitational constant, Σ the surface density, and R the galactocentric radius. This integral is in practice summed over a grid in log radius and azimuth (ϕ). We have verified that this approximate potential is in quantitative agreement with the potential calculated by the simulation. It is smoother due to the binning, but allows us to disentangle contributions from the stars and from the gas, which is insightful. To approximate the torques, one can approximate the potential as a Fourier series of modes m in azimuth ϕ, and take the ϕ derivative,

$$T(R, \phi) = \frac{\partial \Phi_{\text{pot}}}{\partial \phi}(R, \phi). \qquad \text{(V.3)}$$

This procedure produces each panel of Figures V.1 and V.2. For the NIHAO galaxy, the surface density (top panel) clearly shows that (1) the galaxy contains a bar at its center, dominated by the stars (left panel). But the rest of the stellar distribution

seems smooth in the outer disk. The middle panel shows the gas, where clear, detailed structures emerge. The stars dominate (2nd and 3rd rows) most of the disk (but not all) in mass density as well as in depth of the potential well. However, the gaseous structures are more extended radially and more clumpy than the stellar structures, which allows them dominate the torques in the outer disk of the galaxy. The stars in the bar shows an important role: they induce a long-lived quadrupole (bottom left panel). All combined, these agents drive the evolution of the disk. Figure V.2 shows the same decomposition for the TNG50 galaxy. We see directly that it is barless, the stars also dominate in mass and in potential, but not everywhere in the torques: stars dominate the torques at the center, and gas dominates in the outskirts. But the strength and spatial location of the torques is not sufficient to infer the dynamical evolution of the disk: the location of resonances with the orbital motion of the stars will be highly important. This can be achieved if we infer the speeds at which they rotate compared to the stars.

## V.3.3   Characterizing the Non-axisymmetric Structures

To characterize the strength and geometry of non-axisymmetries in density space, we can take a Fourier transform of the surface density in the disk of the simulated galaxy. At a given galactocentric radius R,

$$\hat{\Sigma}(\vec{k}, R) = \frac{1}{\Sigma_0(R)} \iint \Sigma(R, \phi) e^{-i\vec{k}.\vec{x}} b(R, t) d\vec{x}, \tag{V.4}$$

where $\vec{k} = (-m, \omega)$, $\vec{x} = (\phi, t)$ and Σ_0 is the azimuthally averaged density (which corresponds to the axisymmetric component of the density, or the $m = 0$ mode). The term $b(R, t)$ is a binning/window function: these Fourier transforms are taken at a given Galactocentric radius in the disk, so in a radial bin. The simulation is not really periodic in time, or it may be physically appropriate to focus on a specific time window in the simulation (in practice I have used a Hann function). For a bar, the strongest mode will be $m = 2$, and weaker components will appear at even modes. For a spiral arm with four arms, the strongest mode will be $m = 4$, etc.. The frequency ω of the perturbations of mode m is related to its pattern speed (i.e.
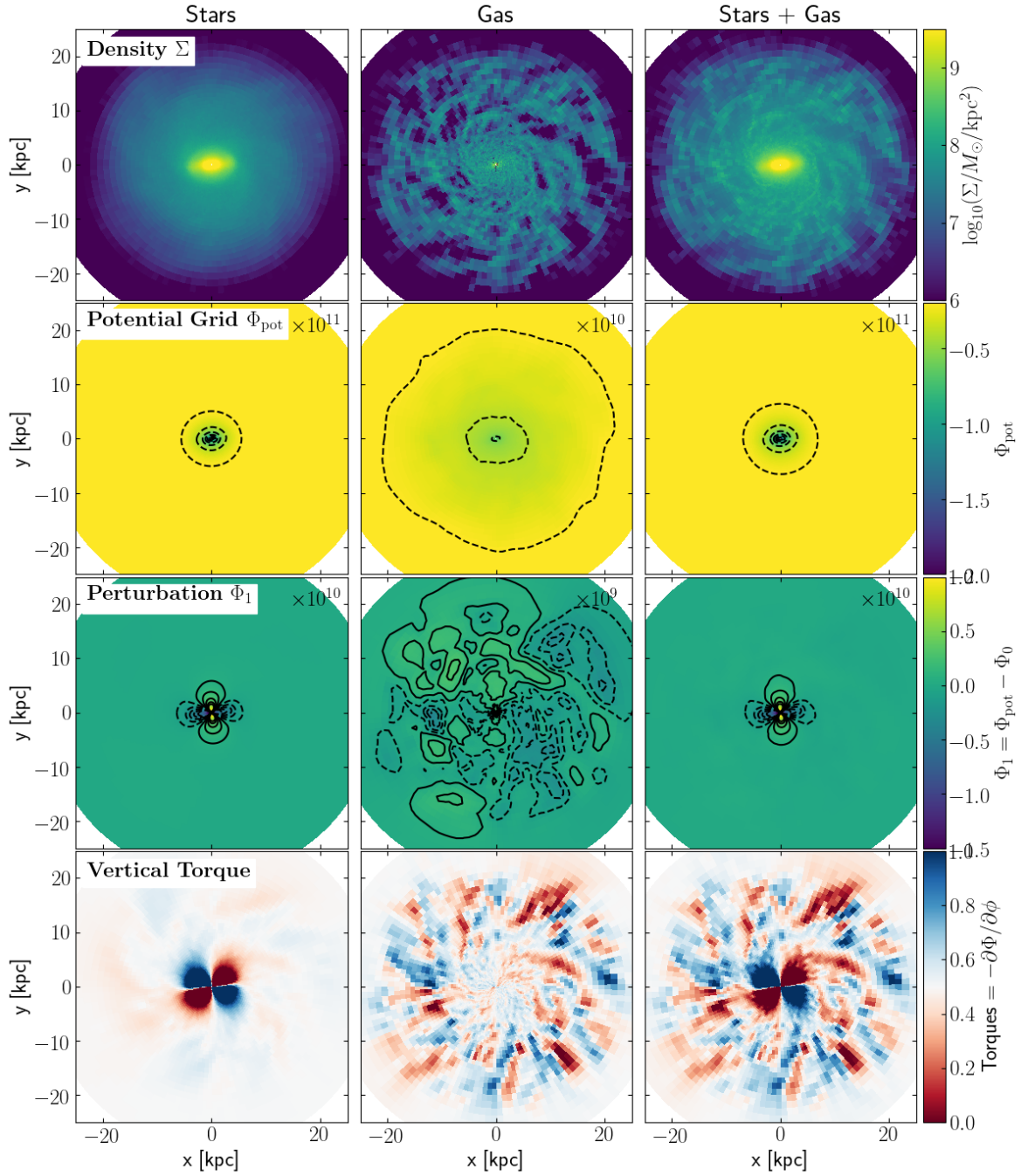
Figure V.1: Decomposition of the NIHAO disk galaxy in surface density (1st row), potential (2nd row), non-axisymmetric components of the potential (3rd row), and vertical component of the torques (4th row). This decomposition was made for star particles only (left), gas particles only (middle), all baryonic particles (stars + gas, right).
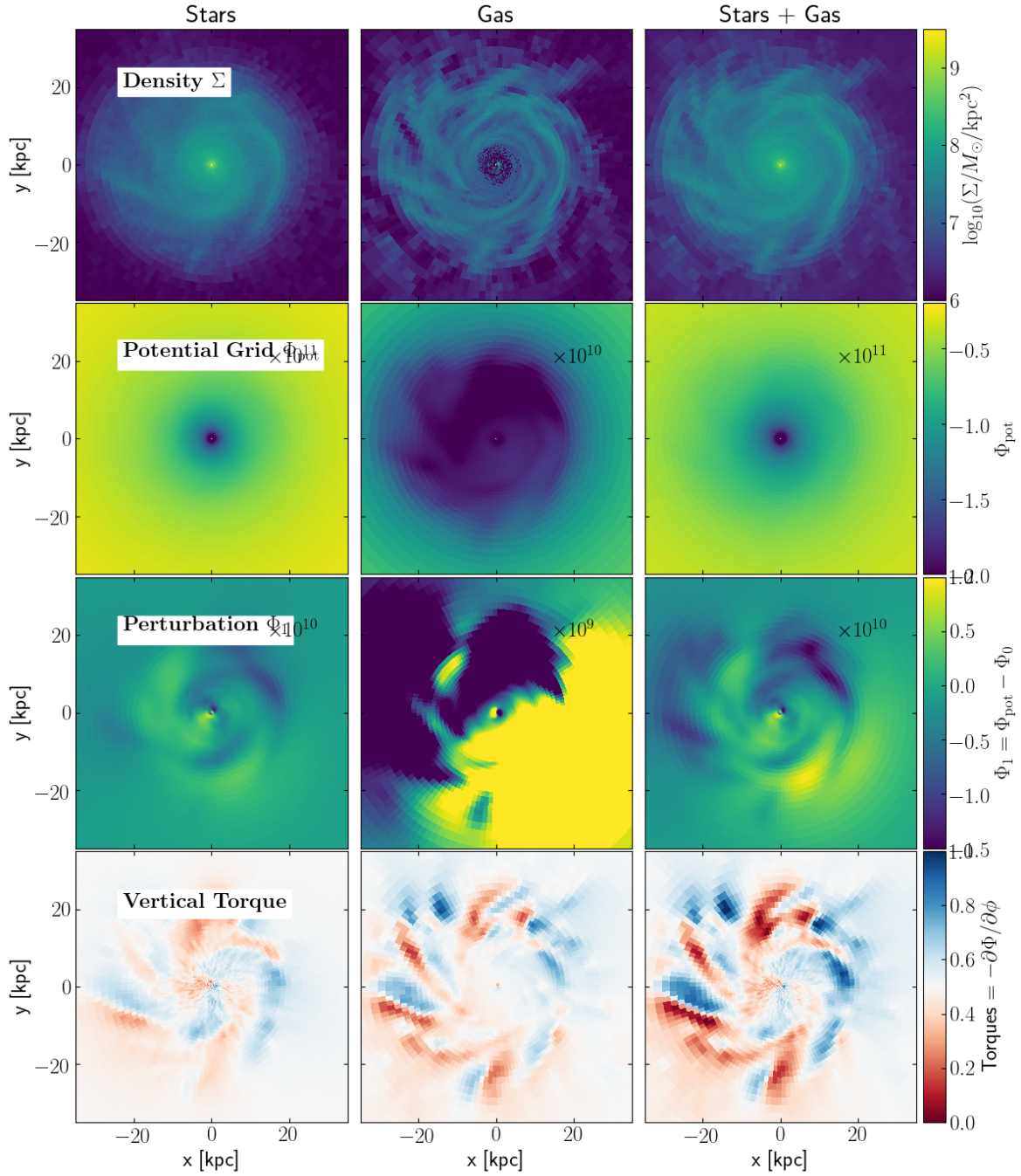
Figure V.2: Decomposition of the TNG50 Milky Way-like disk galaxy in surface density (1st row), potential (2nd row), non-axisymmetric components of the potential (3rd row), and vertical component of the torques (4th row). This decomposition was made for star particles only (left), gas particles only (middle), all baryonic particles (stars + gas, right).
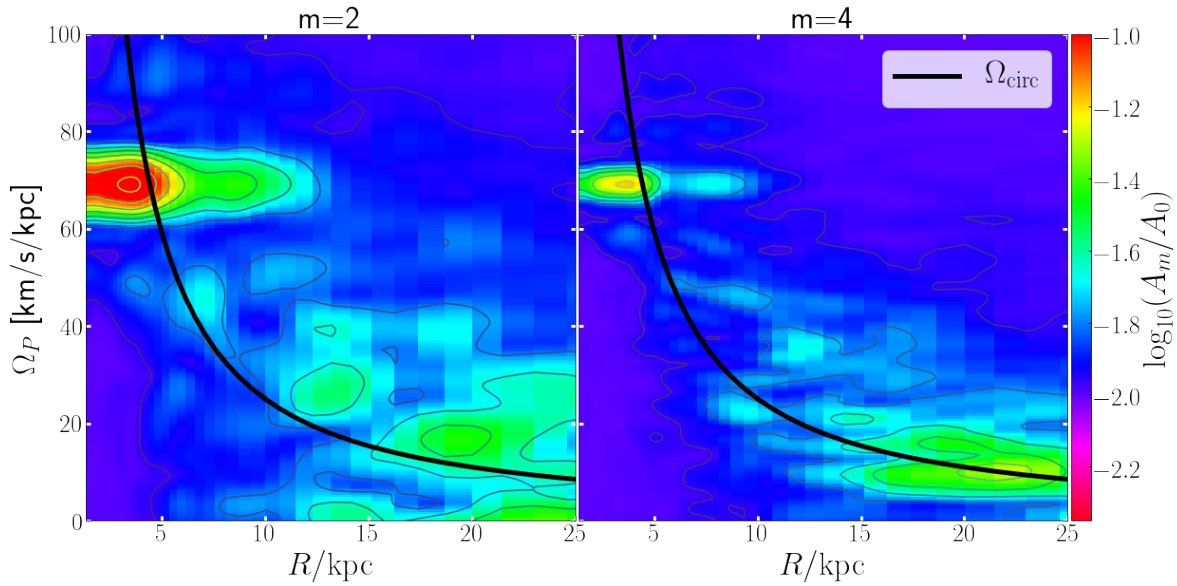
Figure V.3: Power spectrogram in density space for the $m = 2$ and $m = 4$ modes of the NIHAO galaxy. The color code shows the strength of the Fourier components. The black line shows the circular velocity curve for the stars. The color code was voluntarily saturated. The bar dominates in the inner 5kpc (in red) with a pattern speed of about 70 km/s/kpc. The outer disk contains more, weaker, structures that seem to rotate much slower and stay close to the circular velocity curve. A structure rotating at the same speed as the star will be co-rotating with them and create important resonances.

the speed at which the overdensity rotates, Ω_P) by $\omega = m\Omega_P$. The strength of the density signal will be the amplitude,

$$P(\omega, m, R) = \sqrt{\mathrm{Re}^2(\hat{\Sigma}) + \mathrm{Im}^2(\hat{\Sigma})}. \tag{V.5}$$

This method was first outlined in Sellwood & Athanassoula (1986) and used in a number of simulation work to characterize the strength of non-axisymmetries (Masset & Tagger, 1997; Quillen et al., 2011; Hilmi et al., 2020).

As a first example, $P(\Omega, m, R)$ is shown for the NIHAO galaxy for $m = 2$ and $m = 4$ modes in Figure V.3. The inner 5 kpc are dominated dominated by the bar rotating at about 70 km/s/kpc, from which a spiral arm of similar speed seems start. Beyond 10 kpc, the disk is dominated by lower mass structures of lower rotation speeds. These considerations are important and, in principle, permit to find the locations of resonances of the different structures with the stars. For example, the corotation of the bar with the stars is located at about $R = 5$ kpc for this galaxy. Another structure in the outer disk seems to corotate with the stars at about 10 kpc.
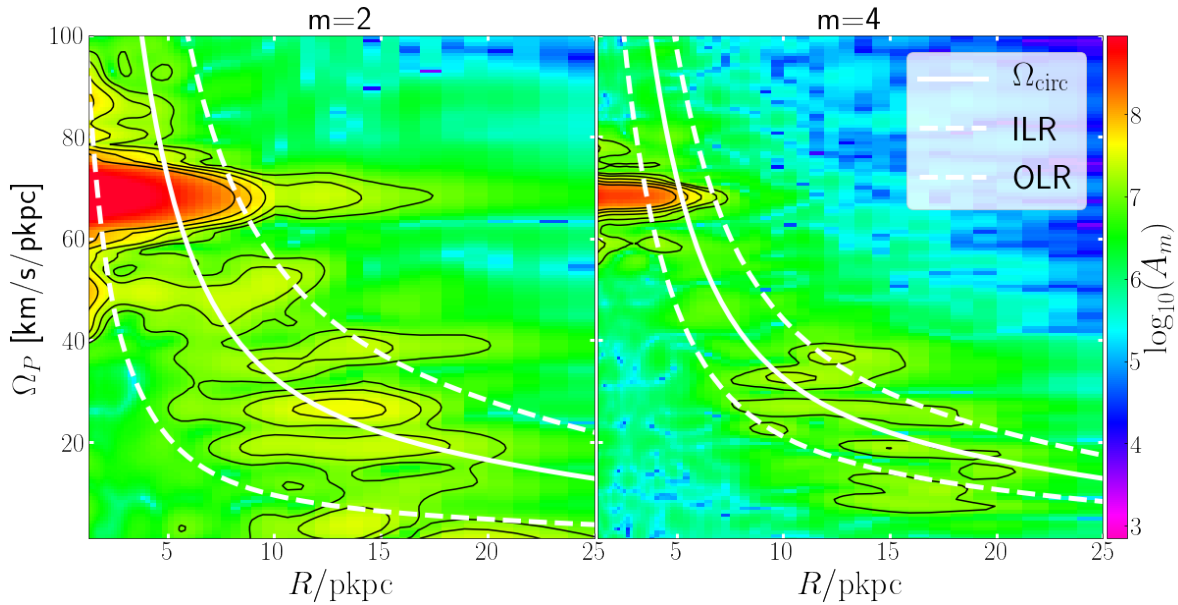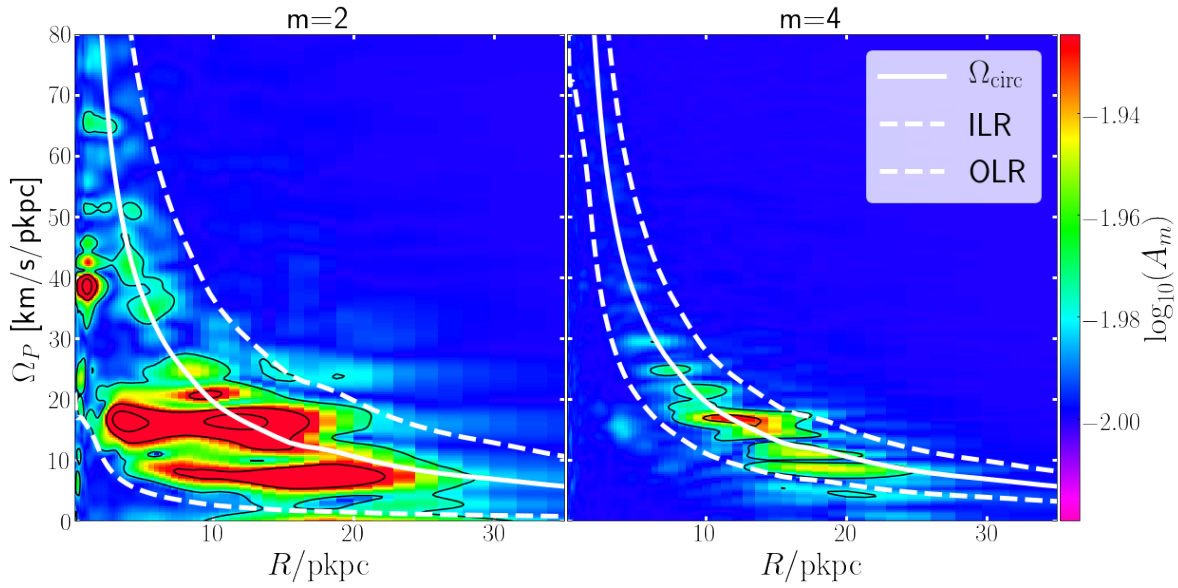
Figure V.4: Power spectrogram of the potential Φ_{pot} for the $m = 2$ and $m = 4$ modes of the NIHAO galaxy. The white solid line show the circular angular velocity curve in the axisymmetrized potential of the galaxy, and the two white dashed lines correspond respectively to the inner and outer Lindblad resonances. The color code is in arbitrary units of potential. Clearly, the bar potential influence extends much further out than its spacial density and perturbing structures are smoother.

But from this analysis, we cannot disentangle which structure is most important in driving the orbits of stars at 10 kpc: does the star feel more the faster-rotating bar, or the structure it corotates with?

These calculations are performed in the space of mass density, or surface density. But to relate these to the motion of the stars and the overall secular evolution of the galactic disk, it is more meaningful to work in the space of potential, or torques, which is what stars actually feel. The results can be different from what we see in surface density since in potential space, different structures of different strengths and speed can reach, and influence, different radii.

In Fig V.4, we illustrate the resulting power spectrogram in potential space for the NIHAO galaxy. The bar potential extends much further out its actual size and its quadrupole dominates the inner 10 kpc of the galaxy in strength. Regarding the spirals arms, which rotate slower and are stronger in the outer disk, much of the strength is confined between the inner and outer Lindblad resonances. The spirals appear on the spectrograms as horizontal stripes, indicating a solid body-like behavior (a structure rotates at the same speed at all radii), and are strongest

Figure V.5: Power spectrogram of the potential Φ_{pot} for the $m = 2$ and $m = 4$ modes of the TNG50 galaxy. The white solid line show the circular angular velocity curve in the axisymmetrized potential of the galaxy, and the two white dashed lines correspond respectively to the inner and outer Lindblad resonances. The color code is in arbitrary units of potential. As for the NIHAO simulation, much of the power is expressed as solid body rotators between inner and outer Lindblad resonances.

near the corotation resonance, which is the process boosting radial migration of stars without much heating.

The TNG50 galaxy's power spectrogram in potential is illustrated in Fig. V.5. It also shows perturbations that are solid bodies (horizontal stripes), rotating with multiple pattern speeds. Their strengths also extend between the inner and outer Lindblad resonance, with much of the strength at corotation, where radial migration is effective. We can further quantify the drivers of secular evolution, by splitting the contributions from the star particles and those from the gas particles, respectively in the top and bottom panels of Figure V.6. Non-axisymmetric features made of stars dominate the inner disk of the galaxy, whereas the gas torques are stronger in the outer disk.
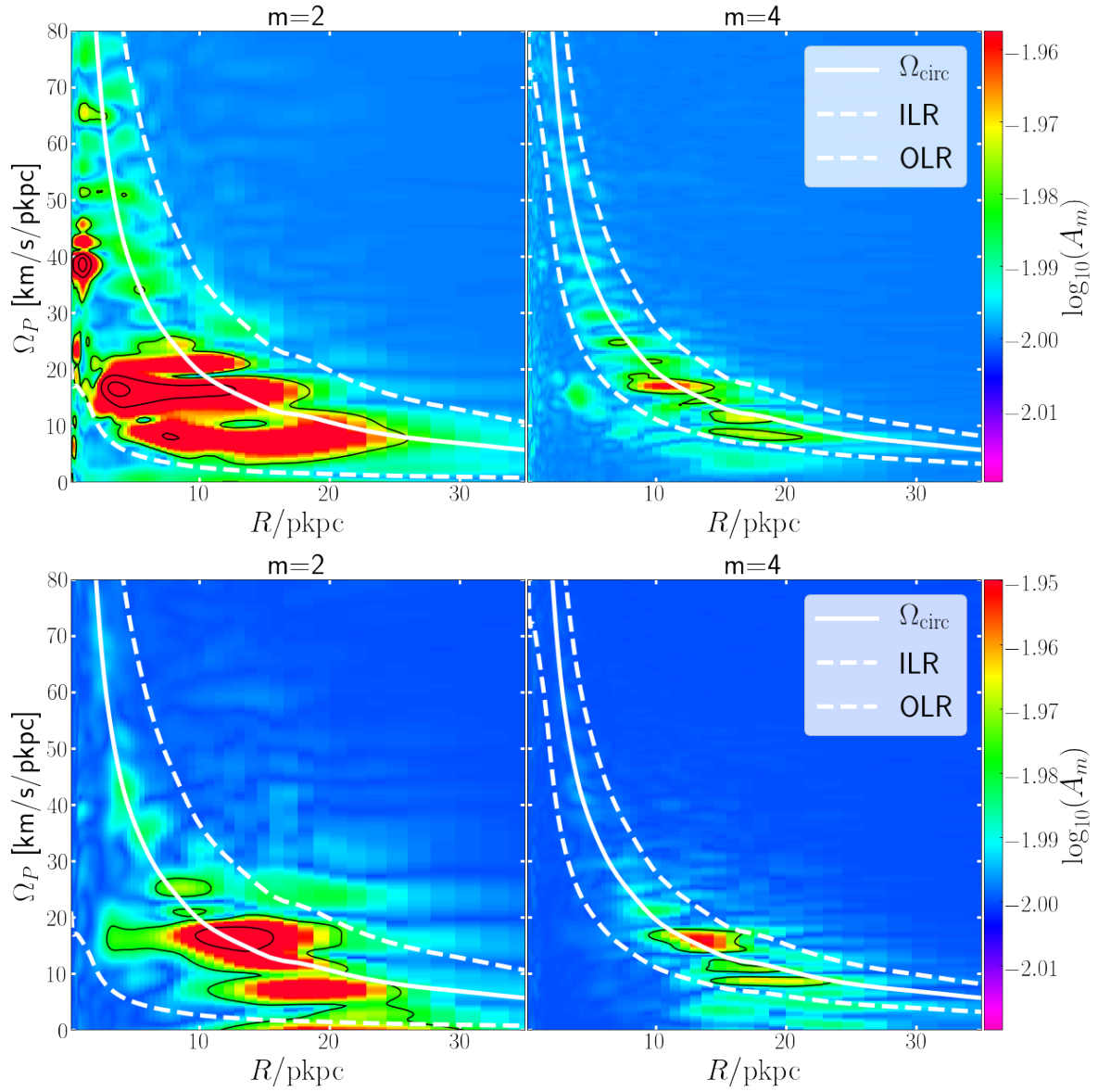
Figure V.6: Top: power spectrogram of the potential generated by the stars $\Phi_{\text{pot},\star}$ for the $m = 2$ and $m = 4$ modes of the TNG50 galaxy. The white solid line show the circular angular velocity curve in the axisymmetrized potential of the galaxy, and the two white dashed lines correspond respectively to the inner and outer Lindblad resonances. The color code is in arbitrary units of potential. As for the NIHAO simulation, much of the power is expressed as solid body rotators between inner and outer Lindblad resonances. Bottom: same for the gas.

> Decomposing simulated galactic disks into torque maps driven by stars and gas, and non-axisymmetries by mode and pattern speed, we see that (1) much of the non-axisymmetric strength of fleeting spirals occurs near the corotation resonance, which is the main driver of radial migration, and (2) the gas here contributes to at least half of the torques driving secular evolution.

V.4 How Do Stars Change Orbits?

As the galaxies in these simulations are clearly not axisymmetric nor time-independent, the stellar orbits will evolve. Understanding this orbit evolution in the simulation can set a basis for physically-motivated improvements of the modelling for the Milky Way's disk. We choose to characterize stars' orbits in the simulation with assumptions identical to the Milky Way: we use axisymmetric actions to describe stellar orbits. We will then trace how stellar actions evolve with time as a function of their initial phase space in the disk, and propose possible applications to Galactic disk statistical modelling.

V.4.1 Characterizing Stellar Orbits

To characterize the orbital changes of stars, we can use the cylindrical axisymmetric actions already introduced Chapters I and III (L_z, J_R, J_z). To compute the actions, the potential of the simulation is first approximated with a symmetrical potential for each snapshot. The dark matter particles, whose distribution is the closest to spherical distribution (except for possible satellites), is approximated with a spherically symmetric potential (multipole expansion). The stars and gas are distributed mostly inside the plane of the galaxy, so the cylspline expansion approximates well the potential they create. This is done using the AGAMA package (Vasiliev, 2019). As for the observed Milky Way, actions are then calculated using the Staeckel fudge (also implemented in AGAMA).
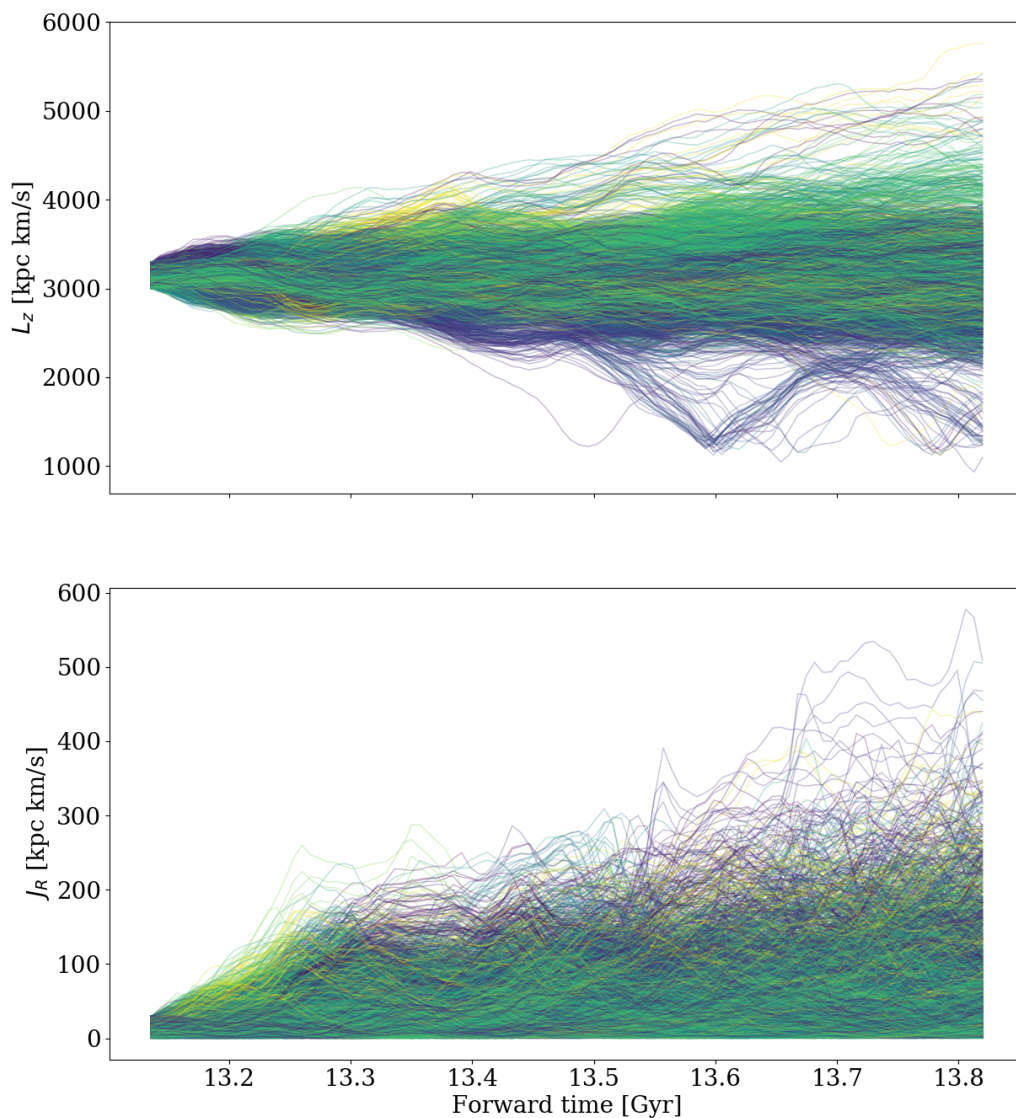
Figure V.7: Trajectories of stars initially selected in small phase space volume as a function of time, showing that stars change orbit significantly and in a complex way. The color indicates the initial phase of the particles, and shows that over 1 Gyr, some star particles continue to have a coherent motion and do not phase mix as quickly.
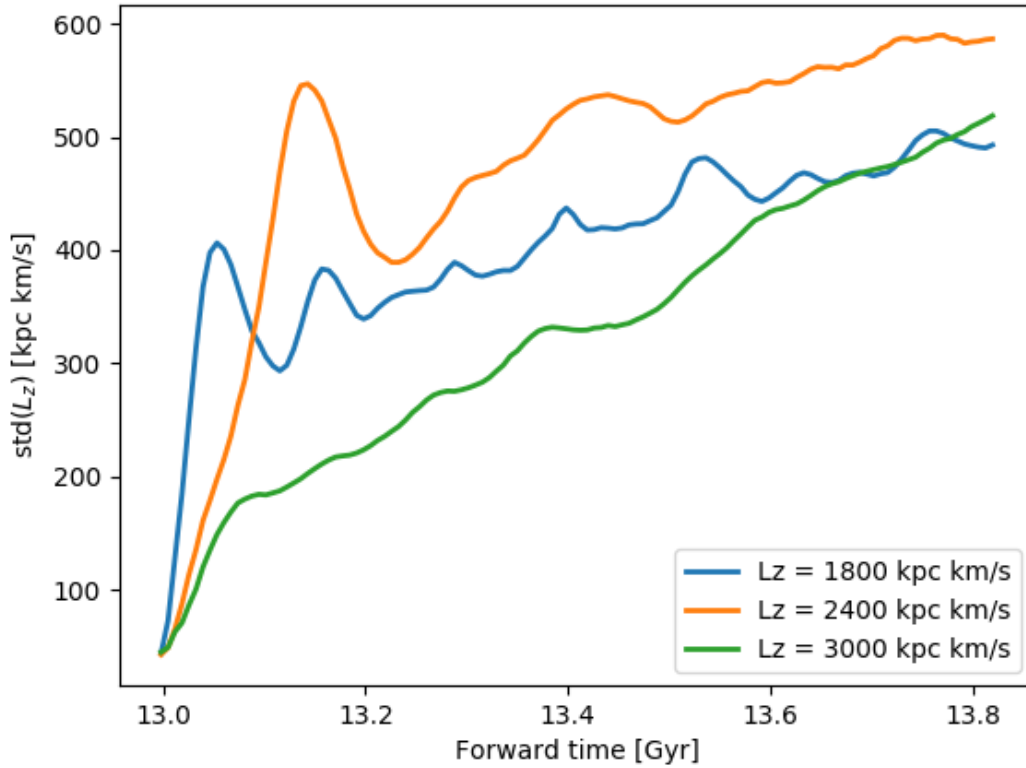
Figure V.8: Spread in angular momentum as a function of time for stars initally selcted in a small phase space volume in the NIHAO galaxy. The three colors indicate a position in the disk: blue for inner disk where the bar dominates the potential, green for the outer disk (where the non-axisymmetric potential is dominated by spiral arms), and orange in between.

V.4.2   Characterizing Orbital Changes

To quantify the changes of stellar orbits, we select a set of stars in a small volume in phase space, and track their actions as a function of time (Figure V.7) for the final 1 Gyr of the NIHAO simulation run (this section only treats the NIHAO galaxy, for time reasons). This approach is very different from the obsevational approaches used in the Milky Way and other galaxies, which consider present-day stellar properties as a function of their age, and make assumptions on their birth orbits. The simulation allows us to track stars as a function of forward time. If the galaxy were axisymmetric, stellar actions would not change, star particles would remain on their orbit, and Figure V.7 would show a set of horizontal lines. Instead, we observe a complex structure in these patterns. Some variations in the actions seem
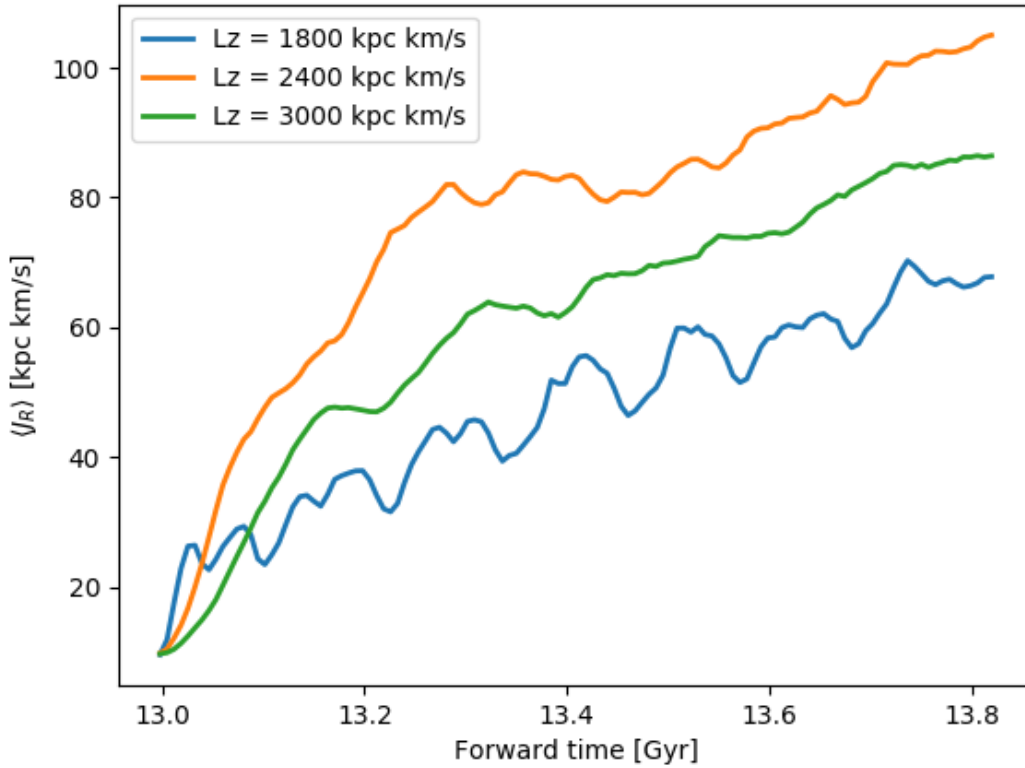
Figure V.9: Mean radial action as a function of time for stars initally selcted in a small phase space volume in the NIHAO galaxy. The three colors indicate a position in the disk: blue for inner disk where the bar dominates the potential, green for the outer disk (where the non-axisymmetric potential is dominated by spiral arms), and orange in between.

periodic, some seem to be closer to a random walk, and the space in $L_z - J_R$ of stars initially occupying a small volume is expanding. Additionally, not all stars phase mix and not at the same speed: some particles remain comoving (see coherent lines of similar colors) while some particles phase mix and disperse more quickly.

The way in which orbits change is a function of position in the disk. The stars selected inside the bar region ($L_z \approx 2000$ kpc km/s) show a very strong oscillatory behavior as they are influenced by a strong, long-lived bar, whereas stars selected in the outer disk will show a motion closer to random. This can be expressed by showing, for example, the action spread of these stars as a function of time. Figures V.8 and V.9 show this with in addition, stars selected in two different regions of the disk. In all regions, the action dispersion increases quickly with time for about 100-

200 Myr before reaching slower changes. The closer to the bar region, the faster the initial spread increase is (blue line rises faster than orange line, etc.). This reflects the fact that in a non-axisymmetric potential, actions as calculated here, assuming axisymmetry, are periodic functions of time. After a few dynamical periods, the spread in angular momentum in the bar region stops increasing (as typical for periodic motions, and stars in the bar region tend to remain there), whereas that of the stars outside the bar continues to increase. We saw in the previous section that stars outside the bar receive torques from from nearly corotating fleeting spirals (as shown in the powe spectrograms), so that they continue to migrate and spread radially.

V.4.3   Possible Applications to Milky Way Modelling

The analysis presented above is only preliminary and qualitative, but we can already draw conclusions to improve physically the forward model this thesis is based on.

V.4.3.1   Modelling Orbit Evolution

This first, simple, exploration leads to a possible modification that could be adopted in the radial migration model I presented in this thesis. The current model assumes that all stars migrate and diffuse equally efficiently in angular momentum $p_{\text{orbit}} = p(L_z|L_{z,0}, \tau)$. This could be easily replaced by a migration probability based on stellar positions in phase space (and possibly conditionned on other quantities, e.g., radial action).

$$
\begin{aligned}
p_{\text{orbit}} &= p(\text{migrate by resonance scattering}|L_{z,0}, \tau)\,p(L_z|L_{z,0}, \tau, \text{res}) \\
&\quad + p(\text{different scattering}|L_{z,0}, \tau)\,p(L_z|L_{z,0}, \tau, \text{not res}) \\
&\quad + ... \\
&= \sum_{\text{process}} p(\text{process dominates}|L_{z,0}, \tau)\,p(L_z|L_{z,0}, \tau, \text{process}).
\end{aligned}
\tag{V.6}
$$

Disentangling different processes and accounting for them may (1) eventually lead to a better description of the Galactic disk, (2) lead to a better measurement of the strength of radial migration, (3) make a small step towards dynamics (relating structures to processes, and processes to kinematics, rather than just describing kinematics). Including different scattering processes, and considering the joint changes of distributions in angular momentum and radial action, may also help to disentangle the effects from different resonances: stars can then be scattered in the $L_z - J_R$ plane (1) only along the L_z direction at corotation, (2) with defined slopes of l/m with $l, m \in \mathbb{N}$ at the Lindblad resonances with m-fold structures, and (3) with different or no correlations with different processes (excitation by satellites, scattering with giant molecular clouds, etc.). Disentangling the global strength of different resonances may help uncovering better the heating history of the Galactic disk.

V.4.3.2 Distribution Functions for Selected Data in Non-axisymmetric Potentials

In regions of the Galactic disk where the bar quadrupole is important, stars deviate significantly from a circular orbit. Their angular momentum is a periodic function of time and so is their radial action. Therefore, the mean angular momentum and radial action at a given position in the disk will be a function of the phase between stars and ther bar structure. Since star surveys are centered on the Sun, and data collection happens around the Sun, most of our current data is selected in azimuth. A consequence is that the mean actions (or the full distribution functions) of our data at a given galactocentric radius may not reflect the mean actions (or the full distribution functions) of all stars in the Galactic disk at given Galactocentric radius. Not accounting for the presence of non-axisymmetric structures may bias our inferred Galactic parameters, and so we should correct our models for the distribtion functions to account for these (e.g., Trick et al., 2017). This is left for future work.

V.5   Summary and Future Work

This section laid out a proposal for exploring how to best relate the orbital changes of stars to their main drivers, in order to come to a better physical understanding of the evolution of the Milky Way. The main conclusions so far are

- Both in the Milky Way and in these two simulated galaxies, redistribution in angular momentum dominates over the growth of radial action. Migration is 'cold'.

- In the simulation, most structures in the galactic disk can be described by a set of solid bodies, which have their peak strength (in *potential*) at the corotation resonance, where angular momentum redistribution is the strongest and also the coldest. Several structures rotating at different speeds are spread over the disk, such that stars at different radii or locations will have the opportunity to migrate large distances. This qualitatively explains why radial migration is cold.

- Radial migration is not a purely diffusive process. After their birth, stars become quickly perturbed by the gravitational non-axisymmetries present in the disk (bar, spirals).

- The gas in these disk galaxies seems to play an important role in exerting torques and exchanging angular momentum with the stars. It will be interesting to study how these exchanges affect the dynamics of the gas itself (e.g. to fuel the center of the Galaxy, private discussion with Ralf Klessen).

- As these structures form and decay stars undergo a finite set of migration events, as defined with the 'corotation resonance trapping'.

- In a non-axisymmetric potential, the axisymmetric actions are oscillating along the orbits of stars. These oscillations produce an important scatter in the action measurement at a given time, that should not be confused with the scatter produced by the longer term secular evolution.

Pursuing this study over more simulated galaxies with systematic quantification of the global torques exerted on the stars, the degree of recurrence of the spiral structures and their pattern speeds and how these are related to stellar orbits will be important to build more physically motivated models for our Galaxy.

Chapter VI

Conclusions and Outlook

Understanding galaxy formation and evolution is central to astrophysics. Our galaxy, the Milky Way is a typical spiral galaxy that presents the unique opportunity to study galaxy formation and evolution in immense detail, from the inside. We can then understand universal processes shaping galaxies.

Most disk galaxies, even the isolated ones, are constantly evolving. Internal processes then play an important role in shaping and structuring disks. In particular, non-axisymmetries such as bars and recurrent spiral arms have a great influence on the orbits of stars. Most processes affecting disk galaxies, such as star formation, chemical enrichment, and secular evolution happen simultaneously and on similar time-scales, such that the entire disk is both in constant *formation* and in constant *evolution*. For external galaxies where stars are not resolved individually, these processes are difficult to disentangle. This thesis took the approach to use the Milky Way as a global model organism, and study its structure in details, using the multi-dimensional information available for many of its individual stars $p([\text{Fe/H}], \tau, \vec{x}, \vec{v})$ around us, to reconstruct the past history of the Galactic disk.

We found that the Milky Way disk, even though it seems cold, has undergone strong dynamical evolution. The Galactic disk likely grew from inside-out, following closely the mass-size relation observed in external galaxies down to redshift $z = 1$. After their formation, stars redistributed greatly in angular momentum while keeping the disk mostly cold. This long-term dynamical evolution is thought

to be dictated by fleeting spiral arms near the corotation resonance. Looking at two galaxies from state of the art cosmological simulations, we have shown that such fleeting spirals are common over the entire disk and are strongest near the corotation resonance, which supports this scenario.

The Galactic disk is still evolving at present. Spiral perturbations are currently forming and decaying and the bar is influencing the stars over a large part of the disk. And these complex dynamical effects are now visible and measureable in the kinematics of the high quality data collected by SDSS-IV, GALAH, LAMOST and the Gaia space mission (e.g. Trick et al., 2019a; Hunt et al., 2019; Monari et al., 2019), and the present framework is not well suited to study these structures that will become even sharper in the next generations of surveys. This method should be improved in the futre, by considering the dynamical effects of non-axisymmetric structures, gaining physical insight from simulations to be more physically plausible, and using a better statistical strategy to optimize fits to large datasets.

Acknowledgements

- Christian Fendt and Huong Witte-Nguy, thank you for managing the IMPRS program and for your availability and support.

- Nadine Neumayer, thank you for these numerous stimulating lunches. I missed them in home office mode. Thank you for the support and for being so inspiring! And I will keep excellent memories of our (re)-submission parties with Alina!

- Andy Gould, talking with you and selling you my ideas over coffee break or hiking down the hill was always a good test to see whether they were 'bad' or not: thank you.

- I thank the IT support for making sure that (1) I could have most of the computing facilities I needed, ad (2) without me blowing up my computer!

- I wish to thank the Human Resources and Travel departments for being hepful with the paper-work and keeping the institute and my environment on track.

- There would have been many 'accidents' without the support of

    - Diane Feuillet - for saving me from various difficult situations involving elevators and bearing my execrable mood over talk trips, and for always being so calm and ressourceful.
    - Sven Buder - also for saving me from an elevator in Shanghai.
    - Joao A. S. Amarante, for saving me from numerous elevators in Shanghai.

- Francisco Aros, I thank you for the good breaks spent together filling our second stomach with icecream and hot chocolate! Thank you for helping me rehearse numerous talks and for your patience each time. I was sad that you left to Vienna.

- Alina Boecker, thank you for the support, our conversations, and the submission parties. I loved talking science with you in office or in forest, and am always impressed by your work! I am greateful that we had such a scientifically stimulating office.

- Melanie Kaasinen, I think you have seen me in all possible states and still managed to remain a friend. Thank you for being there, for all you support, and for your patience with all the talk rehearsing sessions we have had, and for the outdoor breaks that were so fun...

- Jean-Baptiste Vielfaure, thank you for this long-lasting friendship which contributed well to my development during this PhD adventure. Thanks for your unlimited support, for our regular skypes during which I have learned a lot about your work. Thank you for your hospitality and talk-preparation in Paris, and for awesome hiking breaks.

- My parents, you have been a great motivation and inspiration source in many ways. I thank you for accepting my choices, for your support and visits in Heidelberg to share this experience! Special thanks for driving me all the way from Toulouse to Heidelberg, for hiding candies in the car to make the trip more fun, and for driving me up to MPIA for my first day of financial independence. That will remain memorable!!

- My siblings Julie and Lisa, you have enriched my life and made it non-boring in so many aspects. I am grateful to have you. I enjoyed your visits here and the mind-refreshing effect they had, as well as your support.

- Papi et Mamie des Vosges, merci pour votre soutien, merci de m'avoir acceuillie si souvent chez vous (j'aurais aime venir plus), merci pour les confitures, les pates de coing, les tartes aux myrtilles si revigorantes, les promenades en foret, les champignons et surtout: merci d'avoir une si bonne sante.

Bibliography

Abolfathi, B., Aguado, D. S., Aguilar, G., et al. 2018, ApJS, 235, 42

Alam, S., Albareti, F. D., Allende Prieto, C., et al. 2015, ApJS, 219, 12

Anders, F., Chiappini, C., Minchev, I., et al. 2017, A&A, 600, A70

Asplund, M., Grevesse, N., Sauval, A. J., & Scott, P. 2009, ARA&A, 47, 481

Astropy Collaboration, Robitaille, T. P., Tollerud, E. J., et al. 2013, A&A, 558, A33

Aumer, M., Binney, J., & Schönrich, R. 2016a, MNRAS, 462, 1697

—. 2016b, MNRAS, 462, 1697

Aumer, M., White, S. D. M., & Naab, T. 2014, MNRAS, 441, 3679

Avila-Reese, V., González-Samaniego, A., Colín, P., Ibarra-Medel, H., & Rodríguez-Puebla, A. 2018, ApJ, 854, 152

Barden, M., Rix, H.-W., Somerville, R. S., et al. 2005, ApJ, 635, 959

Beane, A., Sanderson, R. E., Ness, M. K., et al. 2019, ApJ, 883, 103

Bell, E. F., Papovich, C., Wolf, C., et al. 2005, ApJ, 625, 23

Belokurov, V., Erkal, D., Evans, N. W., Koposov, S. E., & Deason, A. J. 2018, MNRAS, 478, 611

Bender, R., Burstein, D., & Faber, S. M. 1992, ApJ, 399, 462

Bennett, M., & Bovy, J. 2019, MNRAS, 482, 1417

Bensby, T., Alves-Brito, A., Oey, M. S., Yong, D., & Meléndez, J. 2010, A&A, 516, L13

Bensby, T., Feltzing, S., & Oey, M. S. 2014, A&A, 562, A71

Bergemann, M., Ruchti, G. R., Serenelli, A., et al. 2014, A&A, 565, A89

Bernard, E. J., Ferguson, A. M. N., Chapman, S. C., et al. 2015, MNRAS, 453, L113

Binney, J. 2010, MNRAS, 401, 2318

—. 2012, MNRAS, 426, 1324

Binney, J., Gerhard, O., & Spergel, D. 1997, MNRAS, 288, 365

Binney, J., & Tremaine, S. 2008, Galactic Dynamics: Second Edition (Princeton University Press)

Bird, J. C., Kazantzidis, S., Weinberg, D. H., et al. 2013, ApJ, 773, 43

Bland-Hawthorn, J., & Gerhard, O. 2016, ARA&A, 54, 529

Bland-Hawthorn, J., Krumholz, M. R., & Freeman, K. 2010, ApJ, 713, 166

Blitz, L., & Spergel, D. N. 1991, ApJ, 370, 205

Boecker, A., Alfaro-Cuello, M., Neumayer, N., Martín-Navarro, I., & Leaman, R. 2020, ApJ, 896, 13

Boissier, S., Gil de Paz, A., Boselli, A., et al. 2008, ApJ, 681, 244

Bonanno, A., Schlattl, H., & Paternò, L. 2002, A&A, 390, 1115

Bovy, J. 2015, ApJS, 216, 29

—. 2016, ApJ, 817, 49

Bovy, J., Leung, H. W., Hunt, J. A. S., et al. 2019, MNRAS, 490, 4740

Bovy, J., & Rix, H.-W. 2013, ApJ, 779, 115

Bovy, J., Rix, H.-W., Green, G. M., Schlafly, E. F., & Finkbeiner, D. P. 2016a, ApJ, 818, 130

Bovy, J., Rix, H.-W., Liu, C., et al. 2012, ApJ, 753, 148

Bovy, J., Rix, H.-W., Schlafly, E. F., et al. 2016b, ApJ, 823, 30

Bovy, J., Nidever, D. L., Rix, H.-W., et al. 2014, ApJ, 790, 127

Brammer, G. B., van Dokkum, P. G., Franx, M., et al. 2012, ApJS, 200, 13

Brook, C. B., Kawata, D., Gibson, B. K., & Freeman, K. C. 2004, ApJ, 612, 894

Brook, C. B., Kawata, D., Martel, H., Gibson, B. K., & Bailin, J. 2006, ApJ, 639, 126

Brook, C. B., Stinson, G. S., Gibson, B. K., et al. 2012, MNRAS, 426, 690

Brunetti, M., Chiappini, C., & Pfenniger, D. 2011, A&A, 534, A75

Buck, T., Obreja, A., Macciò, A. V., et al. 2020, MNRAS, 491, 3461

Buitrago, F., Trujillo, I., Conselice, C. J., et al. 2008, ApJ, 687, L61

Bundy, K., Bershady, M. A., Law, D. R., et al. 2015, ApJ, 798, 7

Carlberg, R. G., & Sellwood, J. A. 1985, ApJ, 292, 79

Casagrande, L., Schönrich, R., Asplund, M., et al. 2011, A&A, 530, A138

Chan, V. C., & Bovy, J. 2020, MNRAS, 493, 4367

Chiappini, C., Matteucci, F., & Romano, D. 2001, ApJ, 554, 1044

Conselice, C. J. 2014, ARA&A, 52, 291

Coronado, J., Rix, H.-W., & Trick, W. H. 2018, MNRAS, 481, 2970

Courteau, S., Dutton, A. A., van den Bosch, F. C., et al. 2007, ApJ, 671, 203

Courtes, G. 1982, Astrophysics and Space Science Library, Vol. 92, An Integral Field Spectrograph (IFS) for Large Telescopes, ed. C. M. Humphries, 123

Cui, X.-Q., Zhao, Y.-H., Chu, Y.-Q., et al. 2012, Research in Astronomy and Astrophysics, 12, 1197

Daniel, K. J., Schaffner, D. A., McCluskey, F., Fiedler Kawaguchi, C., & Loebman, S. 2019, ApJ, 882, 111

Daniel, K. J., & Wyse, R. F. G. 2018, MNRAS, 476, 1561

Das, P., & Sanders, J. L. 2019, MNRAS, 484, 294

de Salas, P. F., Malhan, K., Freese, K., Hattori, K., & Valluri, M. 2019, J. Cosmology Astropart. Phys., 2019, 037

de Vaucouleurs, G. 1948, Annales d'Astrophysique, 11, 247

Deason, A. J., Fattahi, A., Belokurov, V., et al. 2019, MNRAS, 485, 3514

Drimmel, R. 2000, A&A, 358, L13

Edvardsson, B., Andersen, J., Gustafsson, B., et al. 1993, A&A, 275, 101

Eggen, O. J., Lynden-Bell, D., & Sandage, A. R. 1962, ApJ, 136, 748

Eilers, A.-C., Hogg, D. W., Rix, H.-W., et al. 2020, arXiv e-prints, arXiv:2003.01132

Eilers, A.-C., Hogg, D. W., Rix, H.-W., & Ness, M. K. 2019, ApJ, 871, 120

Elmegreen, B. G., & Elmegreen, D. M. 2019, ApJS, 245, 14

Elmegreen, B. G., & Struck, C. 2013, ApJ, 775, L35

—. 2016, ApJ, 830, 115

Erwin, P. 2018, MNRAS, 474, 5372

Fall, S. M., & Efstathiou, G. 1980, MNRAS, 193, 189

Feltzing, S., Bowers, J. B., & Agertz, O. 2020, MNRAS, arXiv:1907.08011

Ferguson, H. C., Dickinson, M., Giavalisco, M., et al. 2004, ApJ, 600, L107

Feuillet, D. K., Bovy, J., Holtzman, J., et al. 2016, ApJ, 817, 40

Flynn, C., Holmberg, J., Portinari, L., Fuchs, B., & Jahreiß, H. 2006, MNRAS, 372, 1149

Foreman-Mackey, D. 2016, The Journal of Open Source Software, 24, doi:10.21105/joss.00024

Foreman-Mackey, D., Hogg, D. W., Lang, D., & Goodman, J. 2013, PASP, 125, 306

Foyle, K., Rix, H.-W., & Zibetti, S. 2010, MNRAS, 407, 163

Frankel, N., Rix, H.-W., Ting, Y.-S., Ness, M., & Hogg, D. W. 2018, ApJ, 865, 96

Frankel, N., Sanders, J., Rix, H.-W., Ting, Y.-S., & Ness, M. 2019, ApJ, 884, 99

Frankel, N., Sanders, J., Ting, Y.-S., & Rix, H.-W. 2020, ApJ, 896, 15

Franx, M., van Dokkum, P. G., Förster Schreiber, N. M., et al. 2008, ApJ, 688, 770

Fraternali, F., & Tomassetti, M. 2012, MNRAS, 426, 2166

Freeman, K., & Bland-Hawthorn, J. 2002, ARA&A, 40, 487

Freeman, K. C. 1970, ApJ, 160, 811

—. 1987, ARA&A, 25, 603

Gaia Collaboration, Brown, A. G. A., Vallenari, A., et al. 2018a, ArXiv e-prints, arXiv:1804.09365

—. 2018b, A&A, 616, A1

Gallazzi, A., Charlot, S., Brinchmann, J., White, S. D. M., & Tremonti, C. A. 2005, MNRAS, 362, 41

García-Benito, R., González Delgado, R. M., Pérez, E., et al. 2017, A&A, 608, A27

Genovali, K., Lemasle, B., Bono, G., et al. 2014, A&A, 566, A37

Gilmore, G., & Reid, N. 1983, MNRAS, 202, 1025

Giovanelli, R., Haynes, M. P., da Costa, L. N., et al. 1997, ApJ, 477, L1

Girardi, L. 2016, ARA&A, 54, 95

Girardi, L., & Salaris, M. 2001, MNRAS, 323, 109

Goddard, D., Thomas, D., Maraston, C., et al. 2017, MNRAS, 466, 4731

Gogarten, S. M., Dalcanton, J. J., Williams, B. F., et al. 2010, ApJ, 712, 858

González Delgado, R. M., Pérez, E., Cid Fernandes, R., et al. 2014, A&A, 562, A47

Grand, R. J. J., Kawata, D., & Cropper, M. 2012, MNRAS, 421, 1529

—. 2015, MNRAS, 447, 4018

Grand, R. J. J., Springel, V., Kawata, D., et al. 2016, MNRAS, 460, L94

Grand, R. J. J., Gómez, F. A., Marinacci, F., et al. 2017, MNRAS, 467, 179

Grand, R. J. J., Bustamante, S., Gómez, F. A., et al. 2018, MNRAS, 474, 3629

Gravity Collaboration, Abuter, R., Amorim, A., et al. 2019, A&A, 625, L10

Green, G. M., Schlafly, E., Zucker, C., Speagle, J. S., & Finkbeiner, D. 2019, ApJ, 887, 93

Green, G. M., Schlafly, E. F., Finkbeiner, D., et al. 2018, MNRAS, 478, 651

Grisoni, V., Spitoni, E., & Matteucci, F. 2018a, ArXiv e-prints, arXiv:1805.11415

—. 2018b, MNRAS, 481, 2570

Grogin, N. A., Kocevski, D. D., Faber, S. M., et al. 2011, ApJS, 197, 35

Hall, O. J., Davies, G. R., Elsworth, Y. P., et al. 2019, MNRAS, 486, 3569

Halle, A., Di Matteo, P., Haywood, M., & Combes, F. 2015, A&A, 578, A58

Hawkins, K., Leistedt, B., Bovy, J., & Hogg, D. W. 2017, MNRAS, 471, 722

Hayden, M. R., Bovy, J., Holtzman, J. A., et al. 2015, ApJ, 808, 132

Hayden, M. R., Recio-Blanco, A., de Laverny, P., et al. 2018, A&A, 609

Haywood, M. 2008, MNRAS, 388, 1175

Haywood, M., Di Matteo, P., Lehnert, M. D., Katz, D., & Gómez, A. 2013, A&A, 560, A109

Haywood, M., Lehnert, M. D., Di Matteo, P., et al. 2016, A&A, 589, A66

Haywood, M., Snaith, O., Lehnert, M. D., Di Matteo, P., & Khoperskov, S. 2019a, A&A, 625, A105

—. 2019b, A&A, 625, A105

Heiter, U., Soubiran, C., Netopil, M., & Paunzen, E. 2014, A&A, 561, A93

Helmi, A., Babusiaux, C., Koppelman, H. H., et al. 2018, Nature, 563, 85

Herpich, J., Tremaine, S., & Rix, H.-W. 2017, MNRAS, 467, 5022

Hilmi, T., Minchev, I., Buck, T., et al. 2020, MNRAS, arXiv:2003.05457

Ho, I. T., Seibert, M., Meidt, S. E., et al. 2017, ApJ, 846, doi:10.3847/1538-4357/aa8460

Hogg, D. W., Eilers, A.-C., & Rix, H.-W. 2018, arXiv e-prints, arXiv:1810.09468

Holtzman, J. A., Hasselquist, S., Shetrone, M., et al. 2018, AJ, 156, 125

Hubble, E. 1929, Proceedings of the National Academy of Science, 15, 168

Hubble, E. P. 1926, ApJ, 64, 321

Hunt, J. A. S., Bub, M. W., Bovy, J., et al. 2019, MNRAS, 490, 1026

Hunter, J. D. 2007, Computing In Science & Engineering, 9, 90

Indebetouw, R., Mathis, J. S., Babler, B. L., et al. 2005, ApJ, 619, 931

Jeans, J. H. 1961, Astronomy and cosmogony

Jørgensen, T. G., & Church, R. P. 2020, MNRAS, 492, 4959

Kauffmann, G., White, S. D. M., & Guiderdoni, B. 1993, MNRAS, 264, 201

Kauffmann, G., Heckman, T. M., White, S. D. M., et al. 2003, MNRAS, 341, 33

Kawata, D., Grand, R. J. J., Gibson, B. K., et al. 2017a, MNRAS, 464, 702

Kawata, D., Grand, R. J. J., Gibson, B. K., et al. 2017b, MNRAS, 464, 702

Kokaia, G., & Davies, M. B. 2019, MNRAS, 489, 5165

Kormendy, J. 1977, ApJ, 217, 406

—. 1979, ApJ, 227, 714

Kormendy, J., Drory, N., Bender, R., & Cornell, M. E. 2010, ApJ, 723, 54

Kreckel, K., Ho, I. T., Blanc, G. A., et al. 2019, ApJ, 887, 80

Kroupa, P. 2001, MNRAS, 322, 231

Kruijssen, J. M. D., Pfeffer, J. L., Reina-Campos, M., Crain, R. A., & Bastian, N. 2018, MNRAS, 1537

Krumholz, M. R., & Ting, Y.-S. 2018, MNRAS, 475, 2236

Kubryk, M., Prantzos, N., & Athanassoula, E. 2013, MNRAS, 436, 1479

—. 2015, A&A, 580, A126

Lacey, C. G. 1984, MNRAS, 208, 687

Laney, C. D., Joner, M. D., & Pietrzyński, G. 2012, MNRAS, 419, 1637

Larson, R. B. 1976, MNRAS, 176, 31

Leung, H. W., & Bovy, J. 2019, arXiv e-prints, arXiv:1902.08634

Lin, D. N. C., & Pringle, J. E. 1987, ApJ, 320, L87

Lindegren, L., Hernández, J., Bombrun, A., et al. 2018, A&A, 616, A2

Loebman, S. R., Debattista, V. P., Nidever, D. L., et al. 2016, ApJ, 818, L6

Luck, R. E., Kovtyukh, V. V., & Andrievsky, S. M. 2006, AJ, 132, 902

Luck, R. E., & Lambert, D. L. 2011, AJ, 142, 136

Lynden-Bell, D., & Kalnajs, A. J. 1972, MNRAS, 157, 1

MacArthur, L. A., Courteau, S., Bell, E., & Holtzman, J. A. 2004, ApJS, 152, 175

Mackereth, J. T., Bovy, J., Schiavon, R. P., et al. 2017, MNRAS, 471, 3057

Mackereth, J. T., Bovy, J., Leung, H. W., et al. 2019, MNRAS, 489, 176

Majewski, S. R., Zasowski, G., & Nidever, D. L. 2011, ApJ, 739, 25

Majewski, S. R., Schiavon, R. P., Frinchaboy, P. M., et al. 2017, AJ, 154, 94

Malhotra, S., Spergel, D. N., Rhoads, J. E., & Li, J. 1996, ApJ, 473, 687

Maoz, D., Mannucci, F., & Nelemans, G. 2014, ARA&A, 52, 107

Martig, M., Fouesneau, M., Rix, H.-W., et al. 2016, MNRAS, 456, 3655

Martínez-Barbosa, C. A., Brown, A. G. A., & Portegies Zwart, S. 2015, MNRAS, 446, 823

Masseron, T., & Gilmore, G. 2015, MNRAS, 453, 1855

Masset, F., & Tagger, M. 1997, A&A, 322, 442

Masters, K. L., Lintott, C. J., Hart, R. E., et al. 2019, MNRAS, 487, 1808

Matteucci, F., & Francois, P. 1989, MNRAS, 239, 885

McMillan, P. J., & Binney, J. J. 2013, MNRAS, 433, 1411

Merrifield, M. R., Rand, R. J., & Meidt, S. E. 2006, MNRAS, 366, L17

Minchev, I., Chiappini, C., & Martig, M. 2013, A&A, 558, A9

Minchev, I., & Famaey, B. 2010a, ApJ, 722, 112

—. 2010b, ApJ, 722, 112

Minchev, I., Famaey, B., Combes, F., et al. 2011, A&A, 527, A147

Minchev, I., Famaey, B., Quillen, A. C., et al. 2012a, A&A, 548, A127

—. 2012b, A&A, 548, A126

Minchev, I., Martig, M., Streich, D., et al. 2015, ApJ, 804, L9

Minchev, I., Anders, F., Recio-Blanco, A., et al. 2018, MNRAS, 481, 1645

Minchev, I., Matijevic, G., Hogg, D. W., et al. 2019, MNRAS, 487, 3946

Mo, H., van den Bosch, F. C., & White, S. 2010a, Galaxy Formation and Evolution

—. 2010b, Galaxy Formation and Evolution

Mo, H. J., Mao, S., & White, S. D. M. 1998, MNRAS, 295, 319

Monari, G., Famaey, B., Siebert, A., Wegg, C., & Gerhard, O. 2019, A&A, 626, A41

Morgan, W. W., Whitford, A. E., & Code, A. D. 1953, ApJ, 118, 318

Mosleh, M., Tacchella, S., Renzini, A., et al. 2017, ApJ, 837, 2

Muñoz-Mateos, J. C., Boissier, S., Gil de Paz, A., et al. 2011, ApJ, 731, 10

Muñoz-Mateos, J. C., Gil de Paz, A., Boissier, S., et al. 2007a, ApJ, 658, 1006

—. 2007b, ApJ, 658, 1006

Navarro, J. F., Frenk, C. S., & White, S. D. M. 1996, ApJ, 462, 563

Nelder, J. A., & Mead, R. 1965, Computer Journal, 7, 308

Nelson, D., Pillepich, A., Springel, V., et al. 2019, MNRAS, 490, 3234

Ness, M., Hogg, D. W., Rix, H.-W., Ho, A. Y. Q., & Zasowski, G. 2015, ApJ, 808, 16

Ness, M., Hogg, D. W., Rix, H.-W., et al. 2016, ApJ, 823, 114

Ness, M., Bird, J., Johnson, J., et al. 2019a, arXiv e-prints, arXiv:1907.05422

Ness, M. K., Johnston, K. V., Blancato, K., et al. 2019b, ApJ, 883, 177

Ness, N., Rix, H.-W., Hogg, D. W., et al. 2017, Arxiv preprint

Nieva, M. F., & Przybilla, N. 2012, A&A, 539, A143

Nordström, B., Mayor, M., Andersen, J., et al. 2004, A&A, 418, 989

Oort, J. H., & Muller, C. A. 1952, Monthly Notes of the Astronomical Society of South Africa, 11, 65

Paszke, A., Gross, S., Chintala, S., et al. 2017, in NIPS-W

Peebles, P. J. E. 1969, ApJ, 155, 393

Pérez, E., Cid Fernandes, R., González Delgado, R. M., et al. 2013, ApJ, 764, L1

Peterken, T., Merrifield, M., Aragón-Salamanca, A., et al. 2020, MNRAS, 495, 3387

Pezzulli, G., Fraternali, F., Boissier, S., & Muñoz-Mateos, J. C. 2015, MNRAS, 451, 2324

Pietrukowicz, P., Kozłowski, S., Skowron, J., et al. 2015, ApJ, 811, 113

Pilkington, K., Few, C. G., Gibson, B. K., et al. 2012, A&A, 540, A56

Pillepich, A., Nelson, D., Springel, V., et al. 2019, MNRAS, 490, 3196

Pinsonneault, M. H., Elsworth, Y., Epstein, C., et al. 2014, ApJS, 215, 19

Pinsonneault, M. H., Elsworth, Y. P., Tayar, J., et al. 2018, ApJS, 239, 32

Planck Collaboration, Ade, P. A. R., Aghanim, N., et al. 2016, A&A, 594, A13

Przybilla, N., Nieva, M.-F., & Butler, K. 2008, ApJ, 688, L103

Quillen, A. C., Dougherty, J., Bagley, M. B., Minchev, I., & Comparetta, J. 2011, MNRAS, 417, 762

Reid, M. J., & Brunthaler, A. 2004, ApJ, 616, 872

Rezaei Kh., S., Bailer-Jones, C. A. L., Hanson, R. J., & Fouesneau, M. 2017, A&A, 598, A125

Ricciardelli, E., Vazdekis, A., Cenarro, A. J., & Falcón-Barroso, J. 2012, MNRAS, 424, 172

Riess, A. G., Macri, L., Casertano, S., et al. 2009, ApJ, 699, 539

Rix, H.-W., & Bovy, J. 2013, A&A Rev., 21, 61

Rodríguez-Puebla, A., Primack, J. R., Avila-Reese, V., & Faber, S. M. 2017, MNRAS, 470, 651

Roškar, R., Debattista, V. P., Quinn, T. R., Stinson, G. S., & Wadsley, J. 2008a, ApJ, 684, L79

—. 2008b, ApJ, 684, L79

Roškar, R., Debattista, V. P., Stinson, G. S., et al. 2008c, ApJ, 675, L65

Rubin, V. C., & Ford, W. Kent, J. 1970, ApJ, 159, 379

Ruiz-Lara, T., Few, C. G., Florido, E., et al. 2017, A&A, 608, A126

Sacchi, E., Cignoni, M., Aloisi, A., et al. 2019, arXiv e-prints, arXiv:arXiv:1905.00020

Sánchez, S. F., Kennicutt, R. C., Gil de Paz, A., et al. 2012, A&A, 538, A8

Sánchez-Menguiano, L., Sánchez, S. F., Kawata, D., et al. 2016, ApJ, 830, L40

Sanders, J. L., & Binney, J. 2015, MNRAS, 449, 3479

Sanders, J. L., & Das, P. 2018, MNRAS, 481, 4093

Sanders, J. L., Smith, L., & Evans, N. W. 2019, MNRAS, 488, 4552

Schaye, J., Crain, R. A., Bower, R. G., et al. 2015, MNRAS, 446, 521

Schechter, P. 1976, ApJ, 203, 297

Schönrich, R., & Binney, J. 2009a, MNRAS, 396, 203

—. 2009b, MNRAS, 399, 1145

Schönrich, R., Binney, J., & Dehnen, W. 2010, MNRAS, 403, 1829

Schönrich, R., & McMillan, P. J. 2017a, MNRAS, 467, 1154

—. 2017b, MNRAS, 467, 1154

Sellwood, J. A. 1987, ARA&A, 25, 151

—. 2014, Reviews of Modern Physics, 86, 1

Sellwood, J. A., & Athanassoula, E. 1986, MNRAS, 221, 195

Sellwood, J. A., & Binney, J. J. 2002, MNRAS, 336, 785

Sellwood, J. A., Shen, J., & Li, Z. 2019, MNRAS, 486, 4710

Sérsic, J. L. 1963, Boletin de la Asociacion Argentina de Astronomia La Plata Argentina, 6, 41

Shen, S., Mo, H. J., White, S. D. M., et al. 2003, MNRAS, 343, 978

Shetty, S., Bershady, M. A., Westfall, K. B., et al. 2020, arXiv e-prints, arXiv:2006.02071

Silva Aguirre, V., Bojsen-Hansen, M., Slumstrup, D., et al. 2018, MNRAS, 475, 5487

Skrutskie, M. F., Cutri, R. M., Stiening, R., et al. 2006, AJ, 131, 1163

Snaith, O., Haywood, M., Di Matteo, P., et al. 2015, A&A, 578, A87

Solway, M., Sellwood, J. A., & Schönrich, R. 2012, MNRAS, 422, 1363

Somerville, R. S., & Davé, R. 2015, ARA&A, 53, 51

Somerville, R. S., Barden, M., Rix, H.-W., et al. 2008, ApJ, 672, 776

Soubiran, C., Bienaymé, O., Mishenina, T. V., & Kovtyukh, V. V. 2008, A&A, 480, 91

Stinson, G. S., Bovy, J., Rix, H.-W., et al. 2013, MNRAS, 436, 625

Ting, Y.-S., Conroy, C., & Goodman, A. 2015, ApJ, 807, 104

Ting, Y.-S., Conroy, C., Rix, H.-W., & Cargile, P. 2018a, ArXiv e-prints, arXiv:1804.01530

—. 2019, ApJ, 879, 69

Ting, Y.-S., Hawkins, K., & Rix, H.-W. 2018b, ApJ, 858, L7

Ting, Y.-S., & Rix, H.-W. 2019, ApJ, 878, 21

Ting, Y.-S., Rix, H.-W., Bovy, J., & van de Ven, G. 2013, MNRAS, 434, 652

Toyouchi, D., & Chiba, M. 2018, ApJ, 855, 104

Tremonti, C. A., Heckman, T. M., Kauffmann, G., et al. 2004, ApJ, 613, 898

Trick, W. H., Bovy, J., D'Onghia, E., & Rix, H.-W. 2017, ApJ, 839, 61

Trick, W. H., Coronado, J., & Rix, H.-W. 2019a, MNRAS, 484, 3291

Trick, W. H., Fragkoudi, F., Hunt, J. A. S., Mackereth, J. T., & White, S. D. M. 2019b, arXiv e-prints, arXiv:1906.04786

Trujillo, I., Förster Schreiber, N. M., Rudnick, G., et al. 2006, ApJ, 650, 18

Tully, R. B., & Fisher, J. R. 1977, A&A, 54, 661

van der Kruit, P. C., & Searle, L. 1982, A&A, 110, 61

van der Wel, A., Franx, M., van Dokkum, P. G., et al. 2014, ApJ, 788, 28

van Dokkum, P. G., Leja, J., Nelson, E. J., et al. 2013, ApJ, 771, L35

Vasiliev, E. 2019, MNRAS, 482, 1525

Vazdekis, A., Ricciardelli, E., Cenarro, A. J., et al. 2012, MNRAS, 424, 157

Vazdekis, A., Sánchez-Blázquez, P., Falcón-Barroso, J., et al. 2010, MNRAS, 404, 1639

Velazquez, H., & White, S. D. M. 1999, MNRAS, 304, 254

Vera-Ciro, C., D'Onghia, E., & Navarro, J. F. 2016, ApJ, 833, 42

Wan, Z., Guglielmo, M., Lewis, G. F., Mackey, D., & Ibata, R. A. 2020, MNRAS, 492, 782

Wang, L., Dutton, A. A., Stinson, G. S., et al. 2015, MNRAS, 454, 83

Wang, S., & Chen, X. 2019, ApJ, 877, 116

Webb, J. J., Price-Jones, N., Bovy, J., et al. 2019, arXiv e-prints, arXiv:1910.01646

White, S. D. M., & Frenk, C. S. 1991, ApJ, 379, 52

Wielen, R. 1977, A&A, 60, 263

Williams, B. F., Dalcanton, J. J., Dolphin, A. E., Holtzman, J., & Sarajedini, A. 2009, ApJ, 695, L15

Wuyts, E., Wisnioski, E., Fossati, M., et al. 2016, ApJ, 827, 74

Xiang, M., Shi, J., Liu, X., et al. 2018, ApJS, 237, 33

Yadav, R. K. S., Bedin, L. R., Piotto, G., et al. 2008, A&A, 484, 609

York, D. G., Adelman, J., Anderson, John E., J., et al. 2000, AJ, 120, 1579

Zahid, H. J., Geller, M. J., Kewley, L. J., et al. 2013, ApJ, 771, L19

Zaritsky, D., Kennicutt, Robert C., J., & Huchra, J. P. 1994, ApJ, 420, 87

Zasowski, G., Johnson, J. A., Frinchaboy, P. M., et al. 2013, AJ, 146, 81

Zasowski, G., Cohen, R. E., Chojnowski, S. D., et al. 2017, AJ, 154, 198

List of my Publications

Frankel, N., Rix, H.-W., Ting, Y.-S., Ness, M., & Hogg, D. W. 2018, ApJ, 865, 96

Frankel, N., Sanders, J., Rix, H.-W., Ting, Y.-S., & Ness, M. 2019, ApJ, 884, 99

Frankel, N., Sanders, J., Ting, Y.-S., & Rix, H.-W. 2020, ApJ, 896, 15